Challenges and opportunities at the interface between lithium metal and LLZO solid electrolyte



Marco Siniscalchi
St Cross College
University of Oxford

A thesis submitted for the degree of
Doctor of Philosophy
Michaelmas 2023

Acknowledgements

I would like to express my sincerest gratitude to Prof. Chris Grovenor and Prof. Susie Speller, whose guidance and mentorship have been instrumental throughout my academic journey. From day one, their trust in my abilities placed me in the optimal position to excel in my work, and I am beyond grateful for the freedom they gave me to shape my own research.

In addition, I would like to express my heartfelt appreciation to Prof. Mauro Pasta for his invaluable mentorship and to Prof. Rob Weatherup for his expert guidance in the realm of X-ray techniques.

My sincere thanks go out to my fellow DPhil students and colleagues who have made my time at Oxford a shared and enriching experience. I extend special gratitude to Stephen Turrell, Guillaume Matthews, and Junliang Liu for their continuous guidance and collaborative spirit. I am indebted to Josh Gibson, for the countless discussions on LLZO and for his invaluable assistance during our experiments at Diamond Light Source. I am immensely grateful to all the students who have been a part of my life, both within and outside the laboratories, with a special mention to Giulia, Shobhan, Max, Brigita, Mu.

Additionally, I would like to acknowledge Clara Barker, Nadia Abdul-Karim, and Esther Townsend for their outstanding efforts in keeping our labs running smoothly and for helping with my research.

My deepest appreciation goes to Dom, Michael, Axel, Clara, who have been my closest companions throughout this journey. They made my time at Oxford intellectually and emotionally enriching. I would also like to extend my thanks to my friends at St Cross College, Mirna, Sam, Tim, for their steadfast presence from the very beginning.

I take this opportunity to thank the members of the Oxford University Athletics Club, with whom I have shared countless training sessions and competitions over the years. True friendships were forged on the track.

My heartfelt thanks go to my family. To my parents, whom I admire greatly and whose unwavering guidance has been the foundation of this endeavor. To Paolo, Tuki, and Davide, who have always participated in my adventures. Your boundless support

every time I left home and your warm welcome when I returned meant the world to me.

To Silvia, who has stood beside me, always looking toward the future together. Your presence has been a constant source of strength and inspiration.

Abstract

Solid-state batteries show promise of improvements in battery energy density, power density and safety. However, numerous technological challenges must be overcome before realizing their full potential. This thesis focuses on addressing compatibility issues that arise at the interface between lithium metal anodes and LLZO, a widely adopted solid electrolyte. Interfacing two solid materials is a challenging task, especially when one, lithium metal, undergoes repeated depletion and replenishment during cell cycling. The primary experimental body of this study is divided into three chapters, each tackling challenges encountered at different stages of the Li/LLZO interface: assembly, lithium stripping, and lithium plating. These stages are thoroughly described in the introductory chapter 1, which provides an overview of the most pertinent existing literature. Then, chapter 2 details the wide array of processes and characterization techniques employed throughout this thesis, including a comprehensive analysis of the LLZO solid electrolyte pellets.

Chapter 3 delves into the challenges encountered during the assembly of the Li/LLZO interface. LLZO reacts when exposed to trace moisture and CO_2, forming a surface contamination layer primarily comprised of Li_2CO_3. The presence of Li_2CO_3, which exhibits lithiophobic properties, significantly complicates interfacing LLZO with lithium metal. Annealing or acid etching can be used to remove the LLZO surface contamination before assembly of the cell. This chapter employs near-ambient pressure X-ray photoelectron spectroscopy to extensively investigate LLZO surface reactivity in a glovebox environment, simulated using controlled H_2O and CO_2 gas dosing. It tracks the evolution of LLZO surface chemistry before, during, and after annealing or acid etching surface treatments, assessing their effectiveness in removing Li_2CO_3. A novel acid etching procedure is outlined, resulting in an optimal Li/LLZO interface.

Chapter 4 focuses on exploring the kinetics of lithium stripping. When the stripping current exceeds the rate of lithium diffusion in lithium metal, voids are formed at the anode side, reducing the contact area with LLZO. The addition of a small atomic percentage of magnesium in the lithium anode significantly alters the stripping behaviour and enhances the morphological stability at the interface with LLZO,

but the underlying reasons are not well understood. Initially, this chapter conducts a comprehensive characterization of the diffusion properties of lithium metal and LiMg alloy anodes using an isotope tracer method and secondary ion mass spectrometry. Subsequently, it examines the interface morphology after stripping using cryogenic plasma focused-ion beam. By comparing pure lithium and LiMg alloys, the chapter elucidates the relative importance of lithium diffusivity and interface morphology in determining the stripped capacity at the interface with LLZO.

Chapter 5 investigates the formation of lithium dendrites during plating, a primary challenge jeopardizing the adoption of solid-state batteries. Thin lithium filaments can grow from the plating electrode into the solid electrolyte through a concerted mechanism involving current intensification at the filament tip and mechanical cracking of the LLZO pellet. The root cause of this problem remains a subject of debate. In this chapter, the hot spots for dendrite initiation at the Li/LLZO are identified in the form of spallation cracks, and their morphology is studied with unprecedented resolution. Experimental evidence is presented supporting the possibility that lithium metal deposits within occluded LLZO porosity without a direct connection to the metallic anode, due to residual electronic conductivity of LLZO. The pressure buildup in such porosity leads to the development of surface spallation cracks, which act as hot spots for the concentration of both electrical field and mechanical stress, eventually leading to the propagation of dendrites. This chapter sheds light on the possible origin of lithium dendrites in LLZO.

In this thesis, the combination of highly dense solid electrolyte pellets and meticulous interface assembly with lithium metal is suggested as potential solution to enhance the performance of solid-state batteries, and chapter 6 outlines several promising directions for future research.

Statement of Originality

The work described in this thesis was undertaken in the Department of Materials at the University of Oxford under the supervision of Professor Chris Grovenor and Professor Susie Speller between October 2019 and June 2023.

No part of this thesis has been previously submitted for a degree at this or any other university. The work of others is duly acknowledged in the text and a list of references is provided at the end of the thesis.

Some of the work described here has been presented in the journal articles listed below or is in preparation for publication:

M. Siniscalchi, J. S. Gibson, J. Tufnail, J. Swallow, G. Matthews, J. Lewis, B. Karagoz, G. Held, R. S. Weatherup, Chris R. M. Grovenor, and S. C. Speller, *Removal and Reoccurrence of LLZO Surface Contaminants Under Glovebox Conditions*, in preparation.

M. Siniscalchi, J. Liu, J. S. Gibson, S. J. Turrell, J. Aspinall, R. S. Weatherup, M. Pasta, and Chris R. M. Grovenor, *On the Relative Importance of Li Bulk Diffusivity and Interface Morphology in Determining the Stripped Capacity of Metallic Anodes in Solid-State Batteries*, ACS Energy Lett. 2022, 7, 10, 3593–3599.

M. Siniscalchi, Y. Shi, G. Li, J. S. Gibson, R. S. Bonilla, S. C. Speller, and Chris R. M. Grovenor, *Initiation of Dendritic Failure of LLZO via Sub-Surface Lithium Deposition*, in preparation. Preprint available at `https://doi.org/10.21203/rs.3.rs-3223027/v1`.

List of Abbreviations

2D	Two dimensional
3D	Three dimensional
BCC	Body-centred cubic
CCD	Critical current density
CE	Counter electrode
CEI	Cathode electrolyte interface
EBIC	Electron beam induced current
EDS	Energy dispersive X-ray spectroscopy
EIS	Electrochemical impedance spectroscopy
FAST	Field assisted sintering technique
GB	Grain boundary
GEIS	Galvanostatic electrochemical impedance spectroscopy
GITT	Galvanostatic intermittent titration technique
ICP-OES	Inductively coupled plasma optical emission spectroscopy
LCO	$LiCoO_2$
LLZO	$Li_7La_3Zr_2O_{12}$
NAP-XPS	Near ambient pressure X-ray photoelectron spectroscopy
NMC	$LiNi_xMn_yCo_{1-x-y}O_2$
PEIS	Potentiostatic electrochemical impedance spectroscopy
PITT	Potentiostatic intermittent titration technique
PFIB	Plasma focused-ion beam
SEM	Secondary electron miscroscopy
SEI	Solid electrolyte interface
SHE	Standard hydrogen electrode
SIMS	Secondary ion mass spectrometry
SPS	Spark plasma sintering
UHV	Ultra-high vacuum
WE	Working electrode
XPS	X-ray photoelectron spectroscopy
XRD	X-ray diffraction

Contents

1 Introduction

1.1 Unlocking high performance with lithium metal anodes 1
1.2 Void formation during lithium stripping 9
1.3 Lithium dendrites during plating 16
1.4 LLZO as model solid electrolyte system 23
1.5 Aims and structure of the thesis 27

2 Experimental Methods

2.1 Spark plasma sintering of LLZO pellets 30
2.2 LLZO ionic and electronic conductivities 34
2.3 Casting LiMg alloys 36
2.4 Measuring Li diffusivity with PFIB-SIMS 41
2.5 Assembly and testing of solid-state cells 45
2.6 Serial sectioning of LLZO for three-dimensional visualization 49

3 The Removal and Reoccurrence of LLZO Surface Contaminants Under Glovebox Conditions

3.1 Introduction 54
3.2 Annealing in a glovebox environment 59
3.3 Acid etching in $HCl_{(aq)}$ 67
3.4 Acid etching in $HCl_{(Et_2O)}$ 71
3.5 Conclusions 73

4 On the Relative Importance of Li Bulk Diffusivity and Interface Morphology in Determining the Stripped Capacity of Metallic Anodes

4.1 Introduction 78
4.2 Lithium diffusivity measured by SIMS 84
4.3 Implications for solid-state batteries 87

4.4 Interface contamination 91
4.5 Conclusions 94

5 Initiation of Dendritic Failure of LLZO via Sub-Surface Lithium Deposition

5.1 Introduction 98
5.2 Spalling of LLZO during lithium plating 99
5.3 Locating the short-circuiting dendrite 106
5.4 Using magnesium to look for isolated lithium deposits 109
5.5 Current density dependency of the formation of spallations 114
5.6 Conclusions 118

6 Concluding Remarks and Outlook

A XPS and XANES data analysis

B Literature survey of lithium diffusivity in lithium alloys

Bibliography

List of Figures

1.1 Energy densities of lithium-ion batteries 3
1.2 Conventional lithium-ion cell versus solid-state cell 4
1.3 Electrochemical stability windows of common solid electrolytes 7
1.4 Challenges at the lithium/solid electrolyte interface 8
1.5 Void formation during lithium stripping 10
1.6 Balance between current density and lithium creep 13
1.7 Temperature dependent lithium stripping 14
1.8 Dendritic failure of solid electrolytes 18
1.9 Critical current density versus temperature 20
1.10 Internal lithium deposition 22
1.11 Performance of oxide and sulfide solid electrolytes 24
1.12 LLZO cubic crystal structure 25

2.1 Spark plasma sintering of LLZO pellets 31
2.2 LLZO pellet densities 32
2.3 XRD spectra of LLZO pellets 34
2.4 Ionic and electronic conductivity of LLZO 35
2.5 LiMg phase diagram 37
2.6 XRD and SEM characterization of Li and LiMg alloys 39
2.7 XPS depth profiling of Li and LiMg alloys 40
2.8 Schematic of the PFIB chamber 42
2.9 LiH correction applied to ion mass spectra 44
2.10 Thin film solution to Fick's second law 45
2.11 Typical EIS of a Li/LLZO/Li cell 47
2.12 Critical current density measurement 48
2.13 PFIB setup for automated serial sectioning 50
2.14 Segmentation procedure for 3D volume reconstruction 52

3.1 LLZO surface after air exposure 56
3.2 Removing lithiophobic surface contaminants via annealing 58

3.3 XPS survey spectrum of an LLZO pellet polished in air 60
3.4 Evolution of LLZO surface chemistry during annealing 62
3.5 Comparison between annealing at 600 °C and 750 °C 64
3.6 Lanthanum and zirconium chemical environments 65
3.7 Introducing LLZO in the 'glovebox' after $HCl_{(aq)}$ etching 68
3.8 LLZO surface SEM images after different $HCl_{(aq)}$ etching times 69
3.9 Comparison between annealing and $HCl_{(aq)}$ etching 70
3.10 Additional contamination during glovebox transfer 71
3.11 Electrochemical impedance spectroscopy of Li/LLZO/Li cells 72
3.12 Thermal conditioning of the Li/LLZO interface 74
3.13 Critical current density measurements 75

4.1 Schematic of Li/LLZO and LiMg/LLZO interfaces 80
4.2 Literature survey of Li diffusivity in Li alloys 82
4.3 Lithium diffusion profiles 84
4.4 Evolution of Li diffusion profiles in LiMg alloys with time 86
4.5 Starting EIS spectra of LLZO cells with negligible R_{int} 88
4.6 Stripping of Li and $Li_{0.9}Mg_{0.1}$ electrodes 89
4.7 Effect of glovebox atmosphere on Li diffusivity 92
4.8 Long exposure to optimal glovebox environment 93
4.9 Effective diffusivity at the metallic anode/LLZO interface 95

5.1 Tracking lithium dendrites with GEIS 100
5.2 Cycling of a Li/LLZO/Li cell with nearly zero starting R_{int} 102
5.3 Spallation cracks on the LLZO surface after lithium plating 103
5.4 Additional SEM images of spallations 104
5.5 Spallation cracks at the buried Li/LLZO interface 105
5.6 Indentations on the peeled lithium electrode surface 106
5.7 EBIC imaging of a surface spallation connected to the short-circuiting dendrite 107
5.8 Cross section of the spallation crack after EBIC 109
5.9 Macroscopic lithium-filled dendritic crack 110
5.10 Population density of surface spallation cracks with LLZO density . . 111
5.11 Different stages of the formation of surface spallations at the LiMg/LLZO interface 112
5.12 Spallation crack on the surface of Na β-Al_2O_3 114
5.13 LLZO spalling after 10 μAh cm^{-2} of plated capacity 115

5.14 Current dependency of the spalling process 116
5.15 Modeling internal lithium deposition in a pore 117

Chapter 1

Introduction

Traditional lithium-ion batteries are approaching their physicochemical limit. The growing demand for batteries with higher energy density, higher power and enhanced safety has recently sparked a resurgence of interest in solid-state batteries. Historically, solid-state research has focused on improving the ionic conductivity of solid electrolytes, yet ceramic solids now exhibit sufficient ionic conductivity. Hence, the new challenges lie instead at the interfaces between the electrolyte and the electrodes, in the mechanical properties across the device, and in the scalability of processing. Of particular interest is the behaviour at the interface between solid electrolytes and lithium metal anodes, which directly dictates the longevity, energy density and power density of solid-state batteries.

This introductory chapter provides an overview of the unique challenges associated with the interface between solid electrolytes and lithium metal. It elucidates how all the primary obstacles have their underlying origin in an inadequate solid-solid contact, which detrimentally impact the cell performance in many ways. This chapter also highlights potential solutions, although it explains that trade-offs are often necessary.

1.1 Unlocking high performance with lithium metal anodes

Lithium-ion batteries have become an integral part of our daily lives, enabling the widespread use of mobile electronic devices. As I write this thesis, more than six battery-powered devices are within my arm's reach, and a few battery packs, each containing an average of 7000 individual cylindrical cells, are parked in the street outside [1]. Batteries have revolutionized our world and continue to do so. In recent years, there has been a remarkable push to advance battery performance, driven by the

necessity to electrify the energy market and the transport sector, with an increasing number of scientific articles and patents published about this topic. However, we have reached a point where traditional lithium-ion batteries are nearing their limits in terms of energy density, which is the measure of how much energy a battery can store per unit weight or volume. This limitation impacts for instance the range of electric vehicles and how long mobile phones stay charged.

The energy density of a battery cell is equal to $Q \cdot V(t)$, where the specific capacity Q is defined as the amount of electronic charge per unit mass available to be extracted from the electrodes, and $V(t)$ is the voltage at which the electronic charge is extracted. Typically, secondary (i.e. rechargeable) lithium-ion cells consist of a graphite anode and of a Li-TM-O system as cathode, where TM is a transition metal, like cobalt in $LiCoO_2$ (LCO), or a combination of transition metals, like nickel, manganese, and cobalt in $LiNi_xMn_yCo_{1-x-y}O_2$ (NMC). Under open circuit conditions there is a potential difference $V(t)$ between anode and cathode related to the tendency for the redox reaction $Li^+ + e^- \rightleftharpoons Li^{neutral}$ to take place between the two electrode materials. For this reaction to occur there must be transport of Li^+ species from one electrode to the other, which can occur through the electrolyte, typically an electronically insulating liquid mixture of organic compounds containing a Li salt. If an external path is available for the electrons, the redox reaction can take place. Specifically, during the battery discharge process, Li^+ de-intercalate from the cathode (reduction), travel through the liquid electrolyte, and intercalate in the anode (oxidation). The electrons also flowing from cathode to anode in the external circuit can be used to power an external device. Thus the chemical energy stored in the electrode materials is converted into electrical energy. The opposite is true during charging, when Li^+ migrate in the other direction.

In a lithium-ion battery, Q is essentially the number of lithium ions that can be hosted in the electrodes, hence the energy density is a characteristic of the cell chemistry. The graphite - $LiCoO_2$ battery was first commercialized in 1991 by Sony [2]. Progressive improvements to the chemistry and microstructure, as well as to the manufacturing methods, led to its energy density increasing with a rate of 3 % year on year, as shown in Fig. 1.1. Nowadays, lithium-ion batteries with energy densities of 260 - 295 Wh kg^{-1} and 650 - 730 Wh L^{-1} are commercially available [3]. However, conventional batteries with graphite at the anode side possess a thermodynamically limited capacity (see Fig. 1.1), due to the limited number of lithium ions that can intercalate and de-intercalate in the material, and the demand for batteries with higher energy density means that new electrode materials are necessary if future

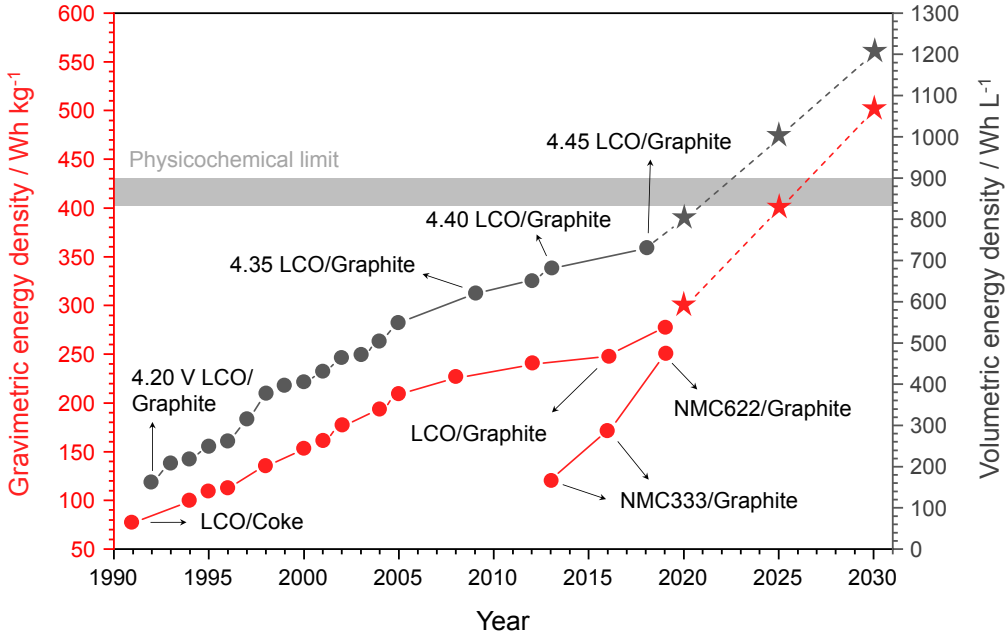


Figure 1.1. Energy densities of lithium-ion batteries. Trend of cell-level gravimetric and volumetric energy densities of lithium-ion batteries since their commercialization in 1991 and future targets ($\star$). Adapted with permission from [6, 7].

energy density targets of above 500 Wh kg^{-1} and 1200 Wh L^{-1} at the cell level are to be reached [4, 5].

To address this challenge, research has turned to alternative chemistries, with a particular focus on the material which can host the largest number of lithium ions per unit structure out of all the elements in the periodic table: lithium metal. Lithium has an unmatchable combination of light weight and small ionic radius, resulting in the largest theoretical specific capacity (3860 mAh g^{-1} versus 372 mAh g^{-1} for graphite). Alongside its low electrochemical redox potential of -3.04 V vs. SHE, a cell with an extremely large energy density can be constructed using a lithium metal anode [8]. However, using lithium metal in batteries has historically posed safety concerns, mainly associated with the inhomogeneous electrodeposition of lithium metal. Lithium metal grows in dendrites during electrodeposition (charging), which can reach the cathode and lead to short-circuits [9]. This represents a safety hazard, especially in the presence of a highly flammabile organic liquid electrolyte. Moreover, most liquid electrolytes are electrochemically unstable when exposed to the low redox potential of lithium, creating durability concerns. However, the interest in lithium metal as a possible anode material has been recently renewed, fueled by advances in electrolyte chemistries and progress in the understanding of the critical mechanisms of lithium electrodeposition [10].

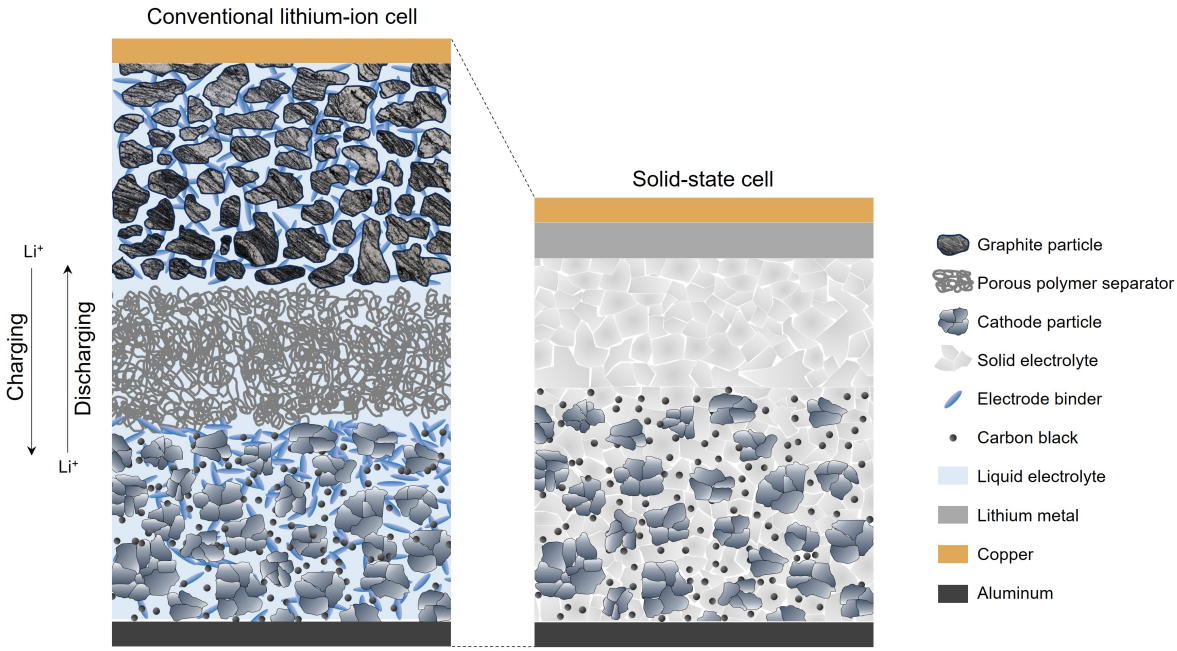


Figure 1.2. Conventional lithium-ion cell versus solid-state cell. Schematics of a conventional lithium-ion cell with a liquid electrolyte (left) and a solid-state cell with a lithium metal anode and a solid electrolyte (right). A conventional lithium-ion cell exhibits energy densities approximately of 270 Wh kg^{-1} and 700 Wh L^{-1}. A lithium metal solid-state cell would potentially achieve 500 Wh kg^{-1} and 1200 Wh L^{-1}.

In particular, to deal with the durability and safety concerns associated with lithium metal batteries, solid electrolytes have emerged as a potential solution [6]. Figure 1.2 shows a schematic of a conventional lithium-ion cell against a solid-state cell employing a lithium metal anode. As illustrated, the larger capacity of lithium metal anodes can reduce the overall thickness of the cell. The porous polymer separator and the liquid electrolyte in which it is soaked are replaced by a solid electrolyte, which should be of similar thickness. Solid electrolytes can offer several advantages over current liquid electrolyte systems, outlined as follows [11, 12]. Firstly, most solid electrolytes are non-flammable, reducing the risk of battery thermal runaway and electrolyte leakage. Secondly, they often exhibit greater electrochemical stability, meaning a decreased reactivity towards lithium metal anodes as well as high-voltage cathodes [13]. Additionally, solid electrolytes typically maintain functionality across a wider temperature range, potentially from -50 to 80 °C, where liquid electrolytes are susceptible to freezing, boiling or decomposition.

Furthermore, solid electrolytes function as single-ion conductors, with Li^+ ions being the sole mobile species. In contrast, in liquid electrolytes the anion of the lithium salt is also mobile and, when operated at high currents, a concentration gradient of the anion can be established, resulting in a strong electric polarization across the electrolyte and consequent voltage losses. The possibility of using higher currents in solid-state cells translates into higher projected power densities and ultimately into shorter charging times, which is especially relevant for electric vehicles. Moreover, because they do not suffer from such electric polarization within the electrolyte, solid-state cells can in principle include much thicker electrodes, potentially enhancing their energy density. Using a solid electrolyte also allows for bipolar stacking of the electrodes, which means a series internal connection of cells rather than parallel [14]. This saves on current collector material and further boosts battery energy density.

In addition to these benefits, as previously stated, the most significant advantage offered by solid electrolytes is their potential to prevent the growth of lithium dendrites by acting as mechanical barrier, which would enable the use of lithium metal anodes. In fact, it is believed that the employment of lithium metal anodes may only be feasible with a solid electrolyte [15]. Consequently, the commercialization of safe, high energy-density solid-state batteries is considered to be the primary pathway to outperform current lithium-ion technologies. As a result, extensive research efforts have been dedicated to developing new solid electrolyte materials. The major solid electrolyte chemistries can be broadly categorized as oxides, sulfides, halides, hydrides, phosphates, and polymers. Oxides and sulfides are the most widely studied chemistries and are compared later in this chapter. Readers are directed to relevant reviews for more details on each category [16, 17]. While the ideal solid electrolyte should possess all the aforementioned attributes, each material and category possesses its unique set of advantages and drawbacks.

Still, recent years have witnessed significant progress in enhancing the properties mentioned above. The Li^+ ionic conductivity of solid electrolytes now rivals that of liquid counterparts, with values reaching approximately 10^{-2} S cm^{-1} [18]. This achievement has marked a transformative milestone in the field and has intensified research efforts. The current focus is now shifting towards better understanding the intricate mechanisms of solid/solid interfaces within solid-state cells. These interfaces pose the foremost challenge and represent the real bottleneck in the progression of solid-state battery technology [19]. The main interfacial issues are reviewed in this chapter and can be classified into (i) side reactions, (ii) contact loss and (iii) lithium dendrites.

(i) Despite initial expectations of greater electrochemical stability of solid electrolytes, computational and experimental studies have demonstrated that the majority of them actually suffer from electrochemical instability, leading to similar issues as those for liquid electrolytes [20]. Figure 1.3 illustrates the computed electrochemical stability windows of the most common solid electrolytes. Solid electrolytes can undergo reduction when in contact with lithium metal, forming a 'solid electrolyte interface' (SEI), and they can be oxidised when in contact with high-voltage cathodes, forming a 'cathode electrolyte interface' (CEI). If the chemical species forming these interfaces exhibit high ionic conductivity and low electronic conductivity, they can act as a beneficial passivation layer that extends the operational stability window of the solid electrolyte. Conversely, interface compounds with low ionic conductivity create significant internal resistances for the movement of Li^+. Moreover, if they allow passage of electrons, further reaction may consume and completely degrade the solid electrolyte [21]. A general rule to increase electrochemical stability of solid electrolytes is to avoid chemistries containing cations with a high oxidation state that can be reduced in contact with lithium metal [22]. An absolute reduction stability against lithium metal is indeed observed in the nitride conductor Li_3N and anti-perovskite conductors Li_3OCl and $Li_3OBr_{0.5}Cl_{0.5}$, which however exhibit low ionic conductivities. However, even when computational studies predict slight instability of the solid electrolytes, they sometimes exhibit an apparent experimental stability, which has been attributed to the sluggish kinetics of reaction between the solid electrolyte and the electrode materials.

(ii) The solid/solid contact amongst the components of a solid-state cell is a fundamental prerequisite for the efficient Li^+ ion transport from one electrode to the other. However, achieving perfect contact is nearly impossible, differently from traditional cells where the liquid electrolyte can easily wet any interface. When assembling a solid-state cell, any interface is always uneven at the microscopic level, resulting in a true contact area smaller than the geometrical one. Moreover, both the lithium metal anode and common cathodes experience volume changes during cycling, further contributing to the formation of voids and to the delamination of electrodes. Inadequate physical contact results in high local current densities and inhomogeneous Li^+ kinetics at the electrode/electrolyte interface. As elucidated in this chapter, this is often the root cause of many issues affecting solid-state cells, ultimately limiting their rate performance and lifetime. The loss of contact at the interface between lithium metal and the solid electrolyte will be examined in more detail in section 1.2.

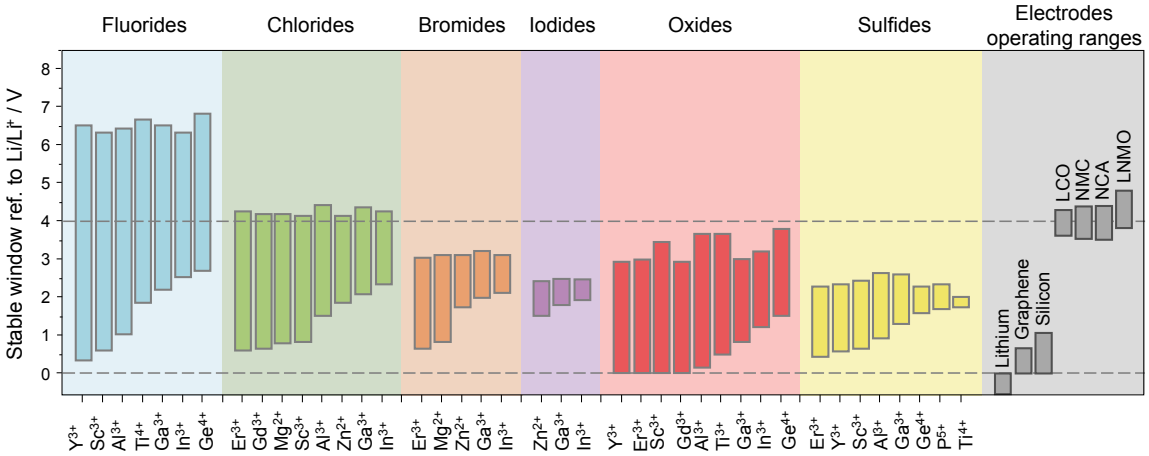


Figure 1.3. Electrochemical stability windows of common solid electrolytes. Calculated thermodynamic electrochemical windows of Li–M–X solid ternary compounds grouped according to the anion X. M is a metal cation at its highest common valence state. An ideal solid electrolyte should be stable at both the lithium metal potential of 0 V and the cathode potential typically of 4 V. Notice that oxide anion chemistries are the most stable in contact with Li metal. Adapted with permission from [20, 23].

(iii) Lithium dendrites can, surprisingly, grow through solid electrolytes. The term 'dendrite' is often used generically in the literature, without distinguishing between liquid and solid electrolyte systems, even though they exhibit different growth conditions and morphologies. In solid electrolytes, lithium dendrites typically take the form of thin filaments, which can fracture the electrolyte material and reach the cathode, leading to cell short-circuit and failure. The ability of a soft metal such as lithium to cause significant damage in mechanically robust ceramic materials is a central topic of discussion in the solid-state research community, and an ongoing debate exists about the mechanisms behind the formation of lithium dendrites. The different theories are reviewed in section 1.3, but in general dendrites appear to nucleate at defect points at the lithium/solid electrolyte interface, where current concentration can occur during plating, ultimately causing electrolyte cracking after a significant pressure build-up.

These interfacial challenges, summarized in the schematic in Fig. 1.4, result in the majority of solid-state cells reported in the literature showing energy and power densities below those of conventional lithium-ion batteries, falling far short of target values [24]. Possible solutions exist, as reported in Fig. 1.4. They include using artificial layers at the interfaces, carefully engineering pressure and temperature parameters during cycling, introducing small amounts of liquid electrolytes, etc. Given that various solid electrolytes possess different properties, the interfacial issues and

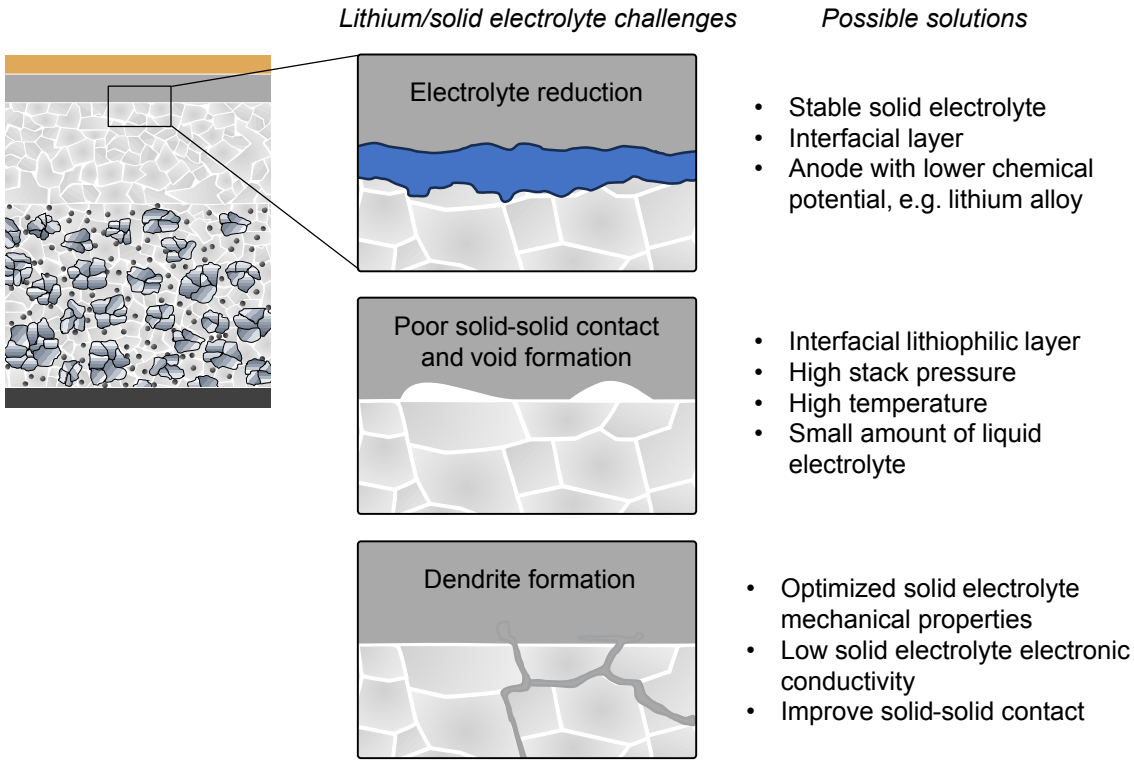


Figure 1.4. Challenges at the lithium/solid electrolyte interface. Most significant problems associated with the interface between a lithium metal anodes and a solid electrolyte. From top to bottom: reduction of solid electrolytes with insufficient electrochemical stability; poor solid-solid contact after assembly of the interface, and void formation during lithium stripping; formation of dendrites during lithium plating. Possible solutions to each issue are listed on the right.

potential solutions vary on a case-by-case basis. Multiple physical, chemical, and mechanical factors must be considered for each system.

While recognizing the issues associated with the cathode interface, this thesis primarily focuses on the interface between lithium metal and the solid electrolyte, which is of key importance. Therefore, the next two sections elaborate in detail on two of the most significant problems at the lithium/solid electrolyte interface, both of which hinder the commercialization of solid-state cells: void formation during stripping and dendrite growth during plating. These phenomena are a focal point in this thesis and have been respectively investigated in chapters 4 and 5 using an oxide solid electrolyte, LLZO, which is introduced in the final section of this chapter.

1.2 Void formation during lithium stripping

The elementary step of lithium stripping involves the transfer of a Li^+ ion across the lithium/solid electrolyte interface, leaving behind an electron $e^{'}(Li)$ and a vacant site $V_{Li}^{X}(Li)$ within the lithium metal. The ion occupies a vacant site $V_{Li^+}^{'}(SE)$ or, depending on the conduction mechanism, an interstitial site in the solid electrolyte near the interface [25]. This process can be described using Kroeger-Vink notation as follows:

$$Li_{Li}(Li) \rightleftharpoons [Li_{Li^+}^{X}(SE) - V_{Li^+}^{'}(SE)] + e^{'}(Li) + V_{Li}^{X}(Li) \tag{1.1}$$

To maintain contact between lithium and the electrolyte, the injected metal vacancy $V_{Li}^{X}(Li)$ must move away from the interface. The diffusion of the vacancy into the bulk of the lithium metal occurs in an opposite direction but at an equal rate to the diffusion of lithium atoms. This is schematically illustrated in Fig. 1.5a. When the diffusion of lithium atoms toward the interface is in local equilibrium with the injection rate of vacancies, the interface can maintain its morphological stability. If the injection rate of vacancies instead exceeds the rate of lithium atom diffusion, stripping will lead to a local loss of interfacial contact. As the total flux of lithium ions into the solid electrolyte, and consequently the flux of vacancies injected into the anode, remains constant during the stripping step, a local loss of contact results in an increased injection rate of vacancies at another contact location. This self-enhancing process ultimately leads to the exponential decrease in the contact area and subsequent increase in cell resistance, as shown in Figs. 1.5b and 1.5c.

The model from Schmalzried and Janek can be used to estimate the 'critical' stripping current density i_{crit}, below which morphological stability is maintained [27]. The equivalent flux of lithium vacancies j_V, exclusively driven by the concentration gradient of the vacancies $\nabla c_{V_{Li}}$ can be calculated according to:

$$j_V = \left(1 - \frac{c_V(\xi = 0)}{c_V^o}\right) c_V^o \sqrt{\frac{D_V}{\tau_V}} \tag{1.2}$$

Here, τ_V is the relaxation time for the establishment of the vacancy equilibrium concentration, c_V^o is the equilibrium bulk concentration of vacancies, $c_V(\xi = 0)$ is the Li vacancy concentration at the interface. D_V is the diffusion coefficient of metal vacancies, which is equal to the diffusion coefficient of lithium atoms in the bulk electrode. The critical stripping current density is $i_{crit} = z \cdot F \cdot j_V$ and, based on these equations, values in the range of i_{crit} = 50 - 200 μA cm^{-2} are calculated. This

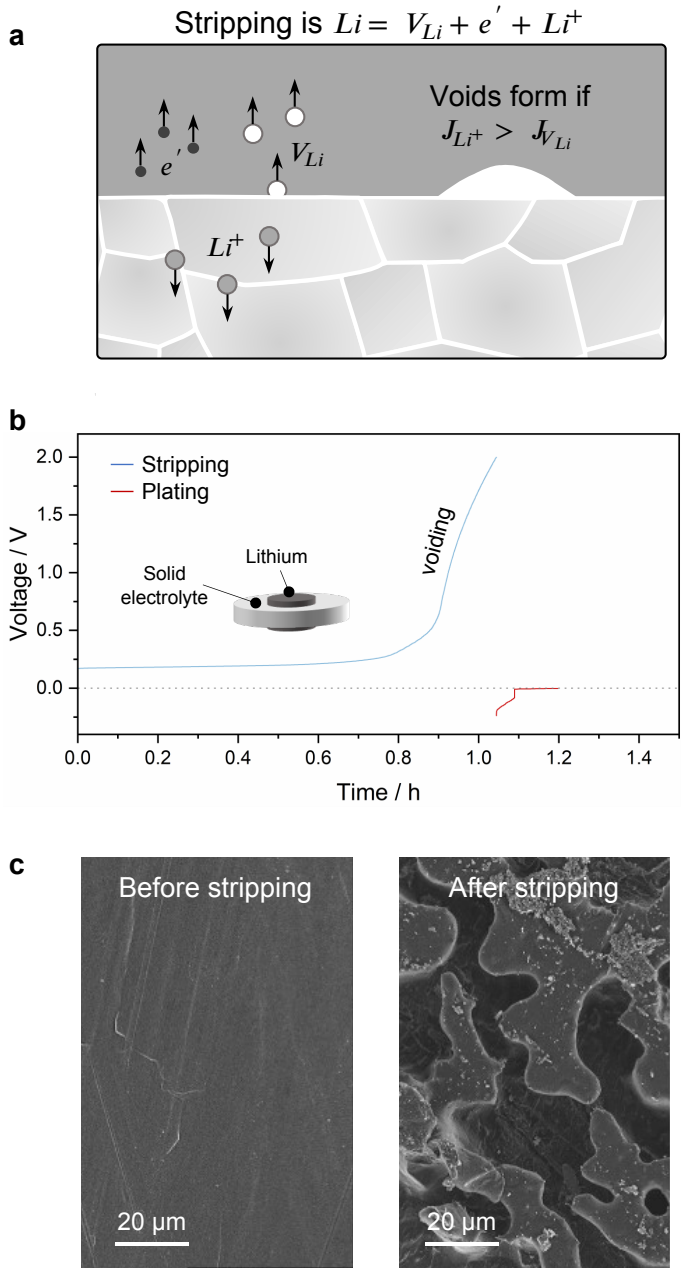


Figure 1.5. Void formation during lithium stripping. **a**, Schematic of the elementary step of charge transfer across the lithium/solid electrolyte interface. Voids form if the flux of lithium ions into the solid electrolyte exceeds the flux of vacancies (i.e. lithium atoms) within the lithium metal anode, $J_{Li^+} > J_{V_{Li}}$. **b**, Stripping and plating of a solid-state cell with lithium metal on each side. The increase in cell polarization is a sign of loss of interfacial contact due to void formation at the stripped lithium electrode. A dendritic short circuit occurs immediately upon plating due to current constriction effects. **c**, Peeled off lithium metal electrodes before and after stripping, adapted with permission from [26]. After stripping, extensive void formation is visible.

suggests that lithium self-diffusion alone is insufficient to transport lithium to the interface at a rate capable of supporting high power densities, typically considered as > 2 - 3 mA cm^{-2}.

Moreover, it important to recognize that there are multiple factors that lead to variations in the efficiency of vacancy injection along the interface and significantly influence the overall kinetics of the lithium/solid electrolyte interface. For instance, any metal/solid electrolyte interface is inherently heterogeneous, with microscopic contacts forming irregularly across the solid electrolyte. Additionally, lithium dissolution may preferentially occur at specific active sites on the lithium metal lattice, such has kink positions, grain boundaries and dislocations [28, 29, 30]. Uneven lithium dissolution can also result from irregularities on the solid electrolyte surface, such as defects and contamination. Therefore, it is a challenge to describe such interface with a model, which is necessarily a simplification of highly complex and intertwined mechanisms.

This interfacial inhomogeneity is not as much of a concern for liquid electrolyte systems, where voids formed by the dissolution of lithium ions into the electrolyte are immediately filled. However, in the case of solid-state cells, it is evident that the application of external stack pressure perpendicular to the lithium/solid electrolyte interface, a factor not accounted for in equation 1.2, is crucial to achieving commercially relevant stripping current densities exceeding 4 mA cm^{-2} [31]. This external pressure induces plastic deformation of lithium, thereby preserving or restoring good interfacial contact with the solid electrolyte.

Owing to a low melting temperature of 180 °C, lithium possesses a homologous temperature at room temperature of $T_H = {}^{T}/_{T_m} = {}^{298}/_{453} = 0.65$. Therefore, lithium exhibits high ductility (Young's modulus E $\sim$ 7.8 GPa and shear modulus G $\sim$ 2.8 GPa, though literature values slightly vary depending on the sample preparation method) [32], and creep predominantly governs its plastic deformation at room temperature [33]. Creep is a diffusion controlled, time-dependent plastic deformation occurring below the very low yield strength of lithium, which is $\sigma_y \sim 0.7$ MPa. This implies that relatively small stack pressures in the low MPa range are sufficient to mitigate interfacial void formation. However, the required stack pressure to enable stable operation varies with current density, stripped capacity and temperature.

Specifically, these dependencies can be determined by balancing the current density and creep according to Wang et al. [34]. Considering that the lithium stripping flux causes a change in the electrode thickness, such lithium flux and therefore the

stripping current density is analogous to a strain rate $\dot{\epsilon}_i$. Defining $\dot{\epsilon}_{creep}$ as the generalized form of the strain rate induced by creep, lithium/solid electrolyte interface stability is ensured when $\dot{\epsilon}_{creep} > \dot{\epsilon}_j$ [34]. This can be expressed as follows:

$$\dot{\epsilon}_{creep} = A\sigma^m \exp\left(-\frac{Q_c}{RT}\right) > \frac{iM}{\rho F l_0} = \dot{\epsilon}_j \tag{1.3}$$

where σ = stress, M = molar mass of lithium, i = current density, ρ = density of lithium, l_0 = lithium thickness, A = material parameter, Q_c = activation energy for creep power law, and m = power law exponent for creep. Creep in lithium metal has been experimentally shown to be controlled by dislocation climb, so $m = 0.66$ [32]. Consequently, a stress dependence on the current density as $\sigma \propto i^{0.15}$ may be expected at room temperature, leading to the introduction of the concept of 'critical' stack pressure, defined as the pressure level above which void formation is prevented. For example, Wang et al. observed a critical stack pressure of approximately 0.6 MPa at a current density of 0.1 mA cm^{-2} (see Fig. 1.6), which aligns with their model's predictions. However, higher current densities appear to require greater critical stack pressures than predicted by the model. For example, at 0.4 mA cm^{-2} a critical stack pressure above 2 MPa is required [34], and current densities exceeding 1 mA cm^{-2} demand pressures exceeding 10 MPa for stable cycling [35]. This highlights the complexity of theoretical predictions, as lithium creep also depends on microstructural properties such as the density of grain boundaries and dislocations, which are a function of the metal's mechanical history and service life. Therefore, complex processes which are not considered in the simplified model above might occur at higher stripping current densities. For further modeling of void formation, refer to Zhang et al. [36].

While the application of stack pressure is crucial for the stable operation of solid-state cells, practical engineering considerations and cost constraints argue against the use of excessively high pressures. Electric vehicle manufacturers, for instance, often establish an upper limit of 1 MPa. Furthermore, most ceramic solid electrolytes exhibit low fracture toughness, and excessive pressures can result in fracturing within these electrolytes. The resulting cracks can serve as favorable pathways for dendrite growth, as reported by Doux et al. [37]. Notably, many literature studies use millimetre-thick solid electrolytes, whereas achieving competitive energy density values necessitates solid electrolyte layers typically less than 50 - 100 μm thick [38]. Thus, applying stack pressure alone, while necessary, does not offer a viable solution.

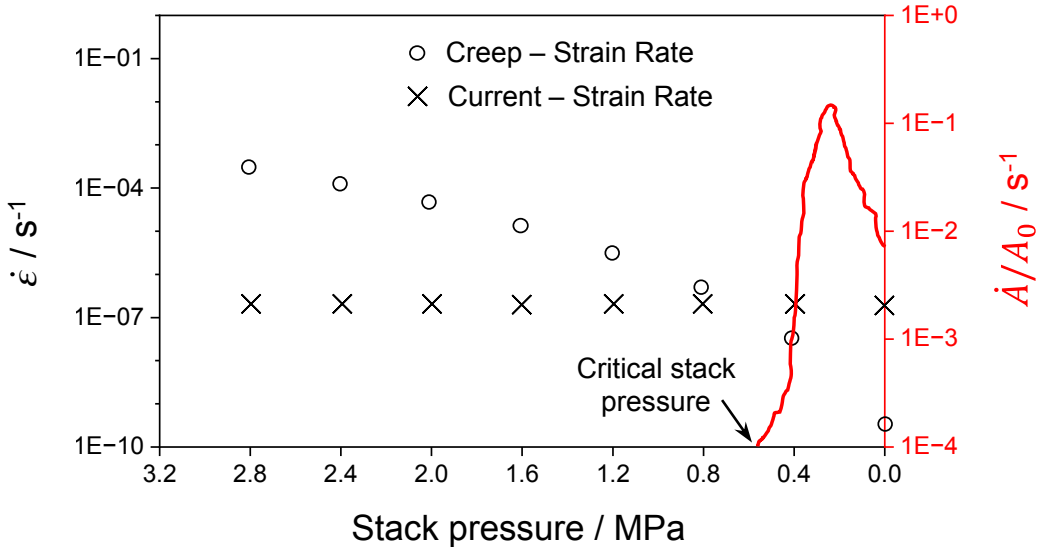


Figure 1.6. Balance between current density and lithium creep. Comparison of the pressure-induced strain rate, i.e. lithium creep (∘), and the current-induced strain rate (×) for cycling of a lithium metal symmetric solid state cell at 0.1 mA cm^{-2} and externally applied stack pressure. When decreasing the stack pressure, a point is reached at which the current-induced strain rate exceeds the pressure-induced strain rate, and unstable void growth occurs. This is evidenced by a decrease in the interfacial contact area. $\dot{A}/A_0$ represents the change in interfacial area with time. Adapted with permission from [34].

Another strategy to minimize void formation involves increasing temperature. Lithium diffusion follows an Arrhenius relation over a wide temperature range, resulting in exponentially higher diffusion at higher temperatures. In addition, temperature affects the elastic, plastic and viscous properties of lithium metal, rendering it softer and therefore reducing the critical stack pressure required. Higher temperatures also faciliate ionic transport within the solid electrolyte and enhance charge transfer across the interface. Systematic experimental studies have demonstrated significantly improved cycling behaviour at elevated temperatures [39, 40]. Figure 1.7 illustrates that the polarization of solid-state cells, a sign of void formation at the stripping lithium metal/solid electrolyte interface as previously discussed, can be delayed by increasing the temperature [41]. In fact, high rate stripping currents in the order of 500 mA cm^{-2} are possible using molten lithium electrodes [42]. In practical scenarios, a synergistic combination of both pressure and temperature is likely to be applied to the cells in most applications. For example, it has been observed that the critical current density for void formation increases from < 0.25 mA cm^{-2} at 25 °C to > 0.5 mA cm^{-2} at 80 °C when cycling under 1 MPa of stack pressure. However, under 5

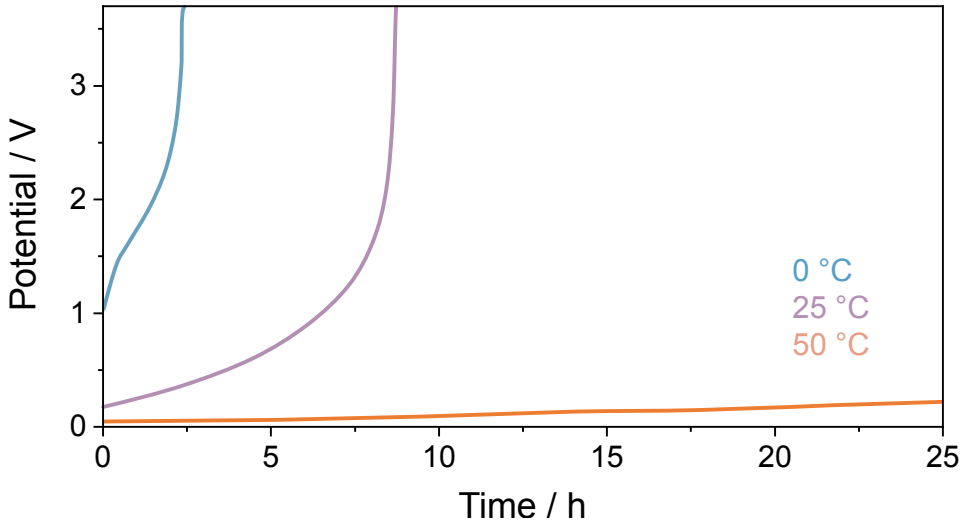


Figure 1.7. Temperature dependent lithium stripping. Potential profiles of lithium symmetrical solid-state cells during stripping at different temperatures. Delithiation of lithium metal anodes was performed with a stripping current density of 0.1 mA cm^{-2}. The cell polarization, induced by voiding at the lithium/solid electrolyte interface, is delayed at higher temperatures, so that a larger capacity can be stripped. Reproduced with permission from [41].

MPa of pressure, this increases to 2.5 mA cm^{-2} at 80 °C, approaching cycling rates of practical interest [43].

In an alternative approach, an interlayer is deposited at the lithium/solid electrolyte interface to circumvent the kinetic and morphological limitations associated with lithium metal. A wide variety of materials have proven effective as interlayers, though the exact effects are often not clearly defined in most reports, which are limited to a performance-based approach only. Generally, these interlayers are believed to modify lithium stripping dynamics by (i) acting as contact mediators during cell assembly, and (ii) changing lithium diffusion properties at the interface which can enhance the morphological stability. As contact mediators, these interlayers improve the wettability of lithium on the solid electrolyte, transitioning the interface from 'lithiophobic' to 'lithiophilic'. This results in improved effective interfacial contact and lower impedance of the as-assembled cells. It is worth noting that achieving these effects without interlayers is sometimes possible, by paying meticolous attention to a clean interface preparation [44]. For instance, chapter 3 will compare various treatments to achieve a pristine lithiophilic lithium/solid electrolyte interface, demonstrating its key importance for an improved cell performance.

Interlayers can also alter lithium diffusion properties at the interface with the solid

electrolyte. Building on the foundational work of Hiratani et al. [45], binary lithium alloys (e.g., with Si, Sn, Al, Mg, As, Bi, Zn, In, etc.) have been primarily used for this purpose. These alloys seemingly leverage enhanced lithium chemical diffusivity compared to lithium self-diffusivity in pure lithium metal, to effectively mitigate void formation by facilitating faster lithium flux from the bulk anode to the interface. However, the claim of faster lithium diffusivity in alloys is often either assumed or extrapolated from experiments conducted on liquid systems, which may not directly apply to solid-state cells. Chapter 4 delves deeper into this issue, challenging the assumption of enhanced lithium diffusivity in alloys. It will be demonstrated that, even in cases where alloys exhibit lower lithium diffusivity than pure lithium metal, voids do not form during stripping. Instead, the lithium concentration decreases in the interlayer region close to the solid electrolyte surface. As contact loss is prevented, the alloy anode can outperform pure lithium metal, especially at relatively small current densities. For a comprehensive examination of this topic, please refer to chapter 4, which focuses on the stripping behaviour of LiMg alloys.

Given the challenge of finding solid electrolytes with a wide electrochemical stability window, interlayers can also suppress the electrochemical decomposition of the solid electrolyte. This can be implemented at both the anode and cathode sides. Lithium alloys, with their lower chemical potential of lithium, can also achieve this effect at the anode side. However, this approach results in a trade-off, as it leads to a reduction in attainable energy density due to a diminished potential difference across the electrolyte. In general, the deposition of an additional interfacial layer can introduce new electrochemical and mechanical challenges, which tend to be specific for each system. These challenges may include interlayer dissolution into the anode or electrolyte, volume changes, and degradation during cycling. As a result, questions often arise concerning the long-term effectiveness of these interlayers. Furthermore, all concepts that introduce extra weight and occupy additional volume in the cell invariably decrease the gravimetric and volumetric energy density of the battery. Nevertheless, many studies demonstrating relatively high currents at low stack pressures incorporate interfacial layers between lithium metal and the solid electrolyte. However, interpreting experimental data can be complex due to the intricate effects interlayers may have on lithium mobility and interfacial mechanics.

A recent trend in addressing interfacial issues involves adding a small quantity of liquid electrolyte to the cell [46]. This hybrid system ensures that contact is maintained throughout cycling, offering a compromise in terms of safety and energy

density. It is worth noting that many solid-state batteries currently undergoing commercialization do contain some form of liquid or gel electrolyte [47].

Despite the awareness of void formation during stripping dates back to the pioneering work by Jow and Liang in the 1980s [28, 48, 49], efficiently addressing this challenge remains a difficult task. Understanding the physical, electrochemical, mechanical, and transport properties of lithium metal and common solid electrolytes is essential for comprehending interface phenomena and improving the rate performance of the lithium/solid electrolyte interface. According to Albertus et al., for lithium metal to outperform conventional graphite anodes, at least 5 mAh cm^{-2} of capacity need to be reversibly stripped and deposited at the interface with the solid electrolyte [31]. This corresponds to a 25 μm thick lithium layer. Overcoming void formation with realistic solutions when aiming for such high areal capacity remains one of the central obstacles in solid-state cell development.

1.3 Lithium dendrites during plating

In addition to the electrochemical stability of solid electrolytes and void formation during stripping, another major concern in solid-state cells is the formation of lithium dendrites. Early predictions based on modeling with liquid and polymer electrolytes have suggested that a sufficiently rigid solid electrolyte, with a shear modulus at least twice that of lithium metal, would effectively obstruct dendrite propagation [50]. However, metallic lithium has been detected penetrating various organic and inorganic solid electrolyte systems [51, 52]. In fact, experimental evidence suggests that the 'critical' current density beyond which lithium dendrites nucleate and propagate, can be significantly lower in solid electrolytes compared to liquid electrolytes, despite the rigidity of solid electrolytes. For example, critical current density values below 1 mA cm^{-2}, far below practically relevant cycling conditions, are usually found for ceramic solid electrolytes during room temperature operation. It is worth noting that the mechanisms governing ion transport, lithium deposition, and fracture mechanics in ceramic solid electrolytes differ fundamentally from those in polymer and liquid electrolytes [53]. As a result, the morphology of lithium dendrites also differs notably. The term 'dendrites' can be somewhat misleading, as the fractal structure typical of dendrites in liquid electrolytes is rarely observed in solid-state cells. Instead, thin lithium filaments rapidly propagate from the electroplating electrode into the solid electrolyte. These considerations suggest that the explanation for dendrite growth

may also be different from the kinetic-limited mechanism used to explain dendritic growth of lithium in liquid electrolytes [54].

Theoretical models of lithium deposition and growth, as well as numerous experimental studies, have attempted to explain the growth of dendrites in solid electrolytes, and they are summarized in this section. The prevailing theory proposes that metallic lithium propagation within a solid electrolyte originates from the uneven distribution of Li^+ ion current at the interface between lithium metal and the solid electrolyte. Current 'hot spots', where current intensifies due to geometrical or electrical factors, can manifest in various forms, including sharp defects, pores, grain boundaries, regions of poor interfacial contact, areas partially covered by contamination layers, etc [56, 57]. Some of these sites can exhibit higher lithium deposition rates. Since the lithium diffusivity within the anode bulk cannot sustain high current densities, not during stripping - as explained in the previous section - nor during plating, the plated lithium metal cannot be redistributed rapidly enough. This creates stress concentration and pressure build-up at these hot spots, potentially triggering stress-releasing mechanisms such as mechanical fracture of the solid electrolyte and/or plastic flow of the lithium anode within the solid electrolyte [58]. The plating current will intensify even further at these cracks, initiating a self-sustaining process that can rapidly propagate through the solid electrolyte. Concurrently, the cell resistance decreases as the lithium dendrite network advances through the solid electrolyte. When the dendrites ultimately reach the cathode side, a short-circuit occurs, leading to cell failure. Depending on the current density, a full short circuit can occur during a single plating step or over multiple plating-stripping cycles.

Figure 1.8a shows a schematic of lithium metal filling a surface flaw such as a microcrack or a pore, representing the initial stage of a lithium dendrite. The plating current density concentrates on the flaw area, inducing a pressure buildup. This pressure can be released either by lithium flow outside of the flaw or by crack growth into the solid electrolyte. In Fig. 1.8b, X-ray tomography is used to visualize the propagation of the dendritic crack during plating. This technique has often been used in the literature to locate the dendrites in solid electrolyte pellets and to investigate their morphology [55]. Figures 1.8c and d show optical and secondary electron microscopy (SEM) images of a solid electrolyte pellet after dendritic failure, where lithium filaments are visible stretching across the pellet. Various electro-mechanical models have been developed to assess the stress conditions within a volume element inside the lithium filament in the scenario in Fig. 1.8a [53, 58, 55]. In general, the stress conditions depend on solid electrolyte properties, such as surface flaw geometry,

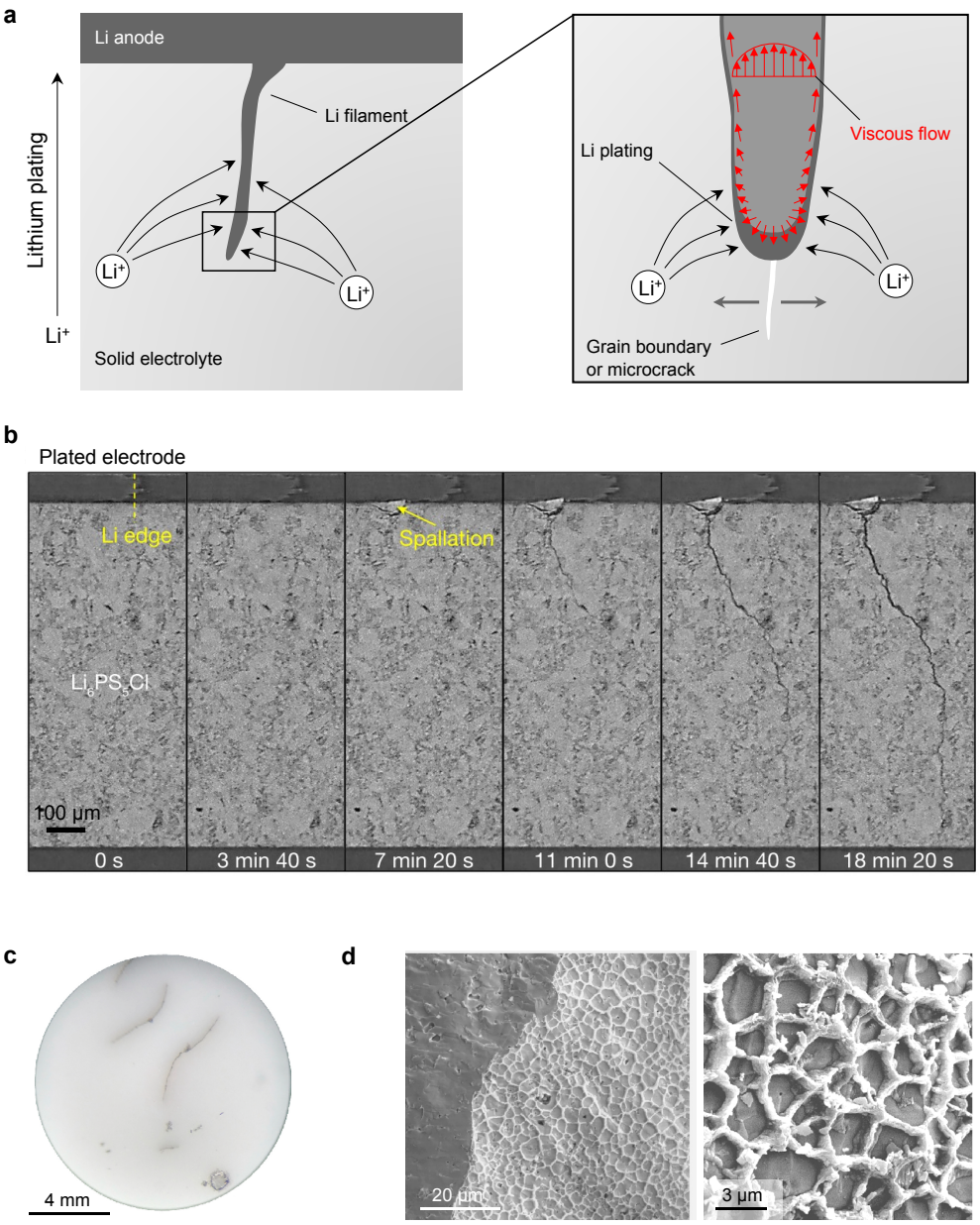


Figure 1.8. Dendritic failure of solid electrolytes. **a**, Simplified schematic of a lithium filament in a solid electrolyte matrix. During lithium plating, current density concentrates at the tip of the filament, resulting in a stress accumulation (red arrows). If the viscous flow of lithium away from the tip is not sufficiently fast, the stress can cause crack initiation and propagation. Adapted with permission from [33]. **b**, X-ray tomography showing the initiation and propagation of a dendritic crack in an argyrodite solid electrolyte. Reproduced with permission from [55]. **c**, Optical image of a cycled solid electrolyte (LLZO) pellet showing the appearance of black linear surface features after plating and **d**, SEM images of the fractured cross section of the pellet showing a lithium web morphology, suggesting that lithium dendrites propagate preferentially along grain boundaries. Adapted with permission from [56].

ionic conductivity, plating current density, as well as on lithium metal diffusion rates and mechanical properties. External stack pressure applied to the cell also plays a role. Once the stress state σ is determined, the criterion for crack extension can be expressed using linear elastic fracture mechanics:

$$\sigma \geq \frac{K_{Ic}}{\gamma\sqrt{\pi a}} \tag{1.4}$$

Here, K_{Ic} is the fracture toughness of the solid electrolyte, γ represents the geometric factor related to the surface flaw shape, a denotes the flaw size. For instance, K_{Ic} is approximately 1.25 MPa $m^{1/2}$ for LLZO, a widely used solid electrolyte discussed in the next section of this chapter. If this criterion is reached, the pressure in the flaw is released by crack growth into the solid electrolyte. This illustrates how a relatively soft metal like lithium can induce mechanical damage and penetrate robust ceramic materials despite its low shear modulus and yield strength. In other reports, a significantly higher yield strength has been found in micron-scale lithium metal compared to bulk lithium metal [59]. This enhanced strength could have important implications on understanding the interfacial mechanics under the operating conditions of a cell and would partially explain why dendrites grow in solid electrolytes [60].

The stress conditions within the lithium dendrite depend on a multitude of parameters, making simple predictions challenging. Nevertheless, qualitative correlations between the critical current density and various parameters have been experimentally verified and align with the proposed models. For instance, the critical current density for dendritic growth tends to be smaller for solid electrolytes with larger defect size, higher defect population density, as well as in those with reduced fracture strength [61, 62, 63]. Efforts have been focused on minimizing the presence of current hot spots on the solid electrolyte surface and on obtaining mechanically resilient ceramic electrolyte formulations. In particular, effective sintering and careful surface preparation of the electrolytes have proven impactful in increasing the attainable critical current density [57, 61, 64]. However, some degree of current concentration at the lithium/solid electrolyte interface is inevitable. Section 1.2 has already illustrated how achieving a complete interfacial contact is nearly impossible even during assembly, due to the microscopic roughness of the solid electrolyte. In addition, void formation during stripping can result in interfacial contact loss and subsequent current intensification at fewer contact points. Referring back to Fig. 1.5b, void formation was evidenced by the cell polarization during stripping, and the cell voltage can be observed to quickly drop to zero as soon as the current direction is switched for the plating step, signalling the growth of dendrites through the solid electrolyte.

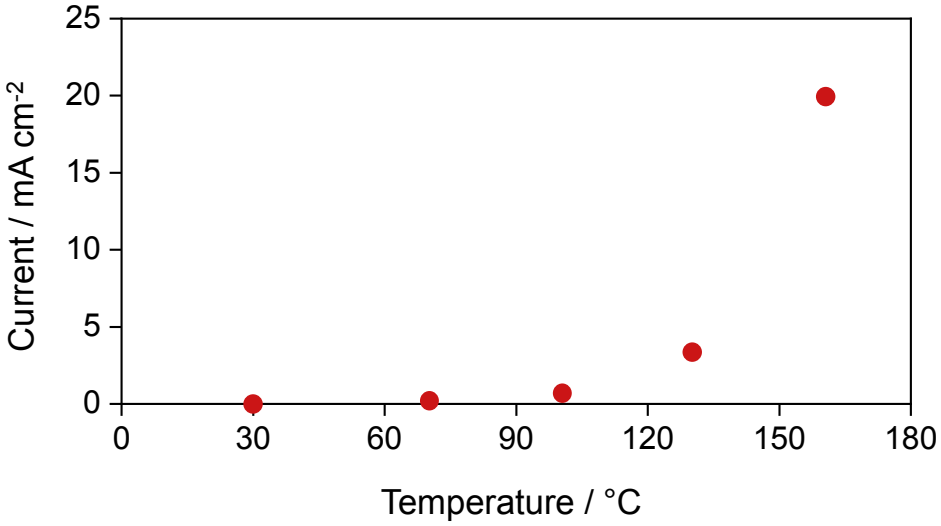


Figure 1.9. Critical current density versus temperature. Critical current density values for the dendritic failure of symmetric lithium metal cell employing an LLZO solid electrolyte. The cells were cycled at 30, 70, 100, 130, 160 °C (lithium's melting temperature is 180 °C). The current values increase exponentially with temperature. Reproduced with permission from [39].

Notably, the critical stripping current for void formation has been shown to have a direct correlation with the critical current density for dendrite penetration during the subsequent plating step [35]. Therefore, any strategy that effectively minimizes void formation can also protect the solid-state cell from dendritic failure. For instance, higher temperatures result in improved critical current densities, as illustrated in Fig. 1.9, thanks to the softening of lithium metal and to the enhanced lithium diffusivity in the anode bulk. The application of a large stack pressure can also prevent current focusing by maintaining a good lithium/solid electrolyte interfacial contact and delay dendrite initiation. On the other hand, an excessive pressure can also drive crack propagation and promote dendrite growth [37]. Building on this, recent research indicates that dendrite initiation and propagation are separate processes, each influenced by parameters in different ways [55]. Specifically, the external stack pressure is critical to avoid dendrite initiation, but should be minimized to prevent dendrite propagation. Balancing external stack pressure during cycling exemplifies the kind of compromises required for an efficient use of solid-state cells.

A different mechanism for the nucleation of lithium filaments has also been proposed, stemming from the residual electronic conductivity of solid electrolytes. This mechanism is sometimes known as mode II, or 'electrical', degradation, opposed to mode I or 'mechanical' degradation illustrated above in Fig. 1.8 [65]. Despite having

low bulk electronic conductivity, typically below 10^{-8} S cm^{-1}, computational studies have revealed that pores and grain boundaries can display reduced electronic band gaps, allowing for small currents to leak from the lithium anode into the solid electrolyte [66, 67]. This enables Li^+ ions to encounter residual electrons at such sites, leading to their premature reduction into lithium metal within the solid electrolyte [68, 69]. The observation of preferential dendrite propagation along grain boundaries (see Fig. 1.5c) supports the notion of higher electronic conductivity in such regions [56]. Moreover, solid electrolytes with larger bulk electronic conductivities have been observed to be more susceptible to dendrite formation, as indicated by operando neutron depth profiling and ex situ electron microscopy [69].

In general, internal lithium plating can occur if the local chemical potential of lithium exceeds the standard chemical potential $\mu_{Li} > \mu^0_{Li}$. The chemical potential of lithium metal μ_{Li} is defined as the sum of the chemical potential of ions and electrons:

$$\mu_{Li} = \widetilde{\mu}_{Li^+} + \widetilde{\mu}_{el} = \mu_{Li^+} + \mu_{el} \tag{1.5}$$

with $\widetilde{\mu}_{Li^+} = \mu_{Li^+} + F\varphi$ = electrochemical potential of lithium ions, $\widetilde{\mu}_{el} = \mu_{el} - F\varphi$ = electrochemical potential of electrons, μ_{Li^+} = chemical potential of lithium ions, μ_{el} = chemical potential of electrons, and φ = galvani potential [25]. From equation 1.5, an increase in μ_{Li} may occur at locations where the ratio between electronic and ionic conductivities is larger than in the bulk of the solid electrolyte, such as at grain boundaries or pores, as displayed in the schematic in Fig. 1.10a. If the μ_{Li} overshoot is sufficiently large to overcome the lithium nucleation barrier, which depends on the local mechanical properties of the solid electrolyte, internal lithium deposition can occur. This can in turn lead to an internal pressure build up and facilitate mechanical degradation of the solid electrolyte, ultimately leading to a dendritic short circuit. However, definitive evidence in support of this electrical degradation mode is lacking. Figure 1.10b illustrates the two different degradation modes.

A single mechanism or explanation may be insufficient to capture the full complexity of the observed dendritic phenomena, and mixed-mode cell failures could be possible. Multiple types of lithium penetration morphologies can be observed even within the same solid electrolyte [71]. Kazyak et al. have classified these into 'straight', 'spalling', 'branching', and 'diffuse' [72]. The prevailing morphology depends on the applied current density and on the impedance at the lithium/solid electrolyte interface, and might originate from different underlying mechanisms. Hence, a comprehensive understanding of lithium dendrite evolution in solid electrolytes is lacking, and the effectiveness of solid electrolytes in preventing dendrite growth at

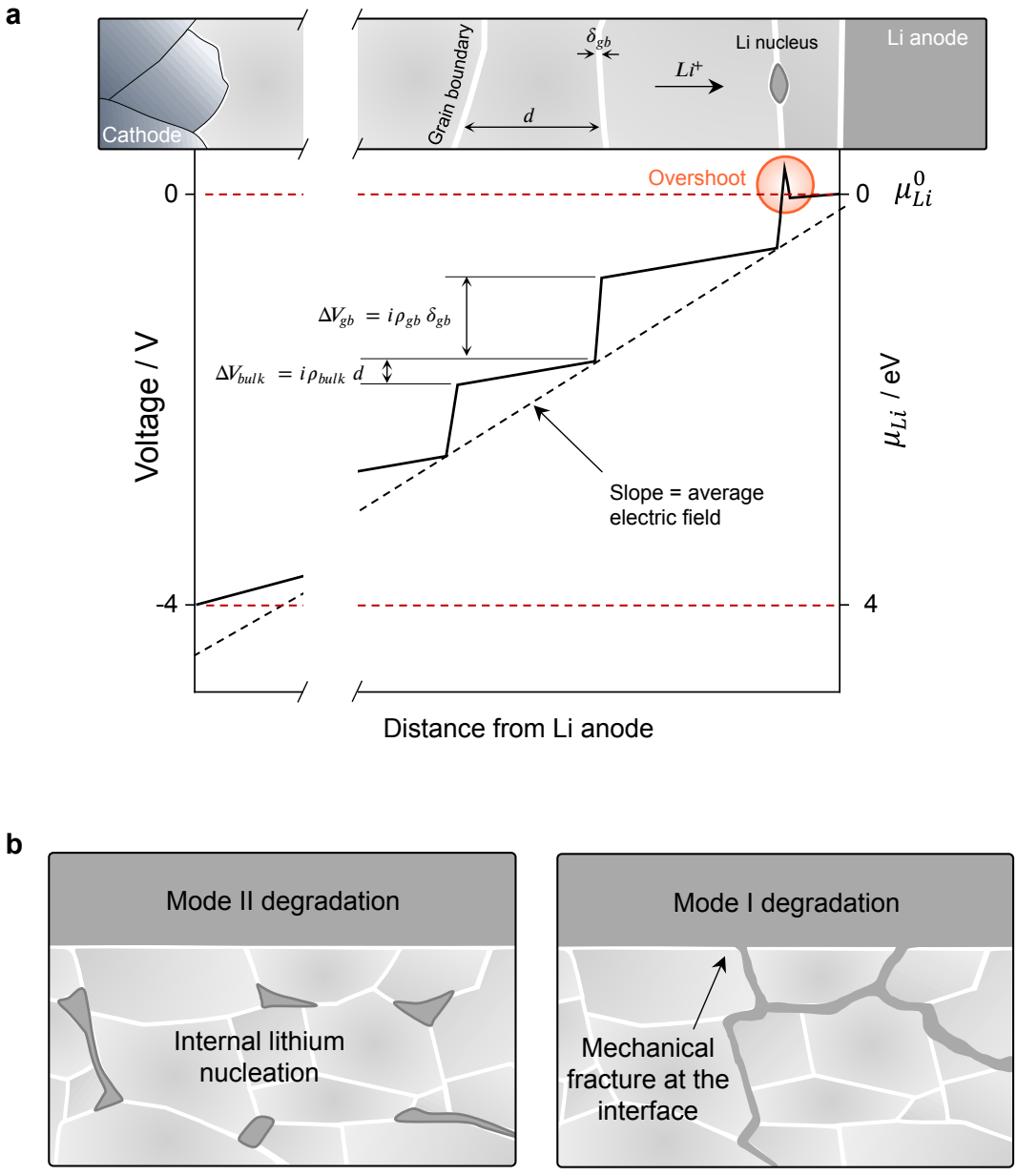


Figure 1.10. Internal lithium deposition. **a**, Qualitative profile of the chemical potential μ_{Li} during lithium plating in a solid-state cell. The standard chemical potential of lithium metal μ^0_{Li} is set to zero. It is assumed that the grain boundaries have a higher electronic/ionic conductivity ratio than the bulk solid electrolyte. An overshoot of μ_{Li} is possible at a grain boundary position close to the lithium metal anode. If the overpotential is sufficiently large, a driving force for the internal lithium nucleation is created. Adapted with permission from [25, 70]. **b**, Schematics of degradation mode I and mode II in solid electrolytes. The occurrence of one or the other depends on electro-chemo-mechanical properties of the lithium/solid electrolyte interface.

practical current densities is still uncertain. Therefore, despite the potential advantages of solid electrolytes in terms of safety and energy density, most solid-state cells exhibit lower capacities and shorter cycle lives compared to batteries based on liquid electrolytes [11, 73]. Moving forward, it is evident that a thorough characterization of both lithium metal and solid electrolytes properties, as well as their interface, is critical for a correct interpretation of cycling results.

Chapter 5 studies more in detail the issue of lithium dendrite propagation in solid electrolytes. In particular, the interface between lithium metal and LLZO solid electrolyte will be investigated after lithium plating to identify the initiation sites of lithium dendrites. The observation that lithium can deposit in occluded porosity in the sub-surface region of the LLZO pellet will be considered in accordance with the electronic degradation theory. Since LLZO serves as the main solid electrolyte in this thesis for investigating lithium stripping and plating behaviour, the next section will provide a detailed introduction to this solid electrolyte chemistry.

1.4 LLZO as model solid electrolyte system

The key component in solid-state batteries is the lithium-ion conducting solid electrolyte, which enables efficient lithium-ion transport between the electrodes. Crystalline inorganic solid electrolytes are characterized by fixed ionic structures that offer open conduction channels, comprising vacant or interstitial sites along which Li^+ ions can diffuse through thermally activated jumps. Due to the small size of Li^+ ions, a rapid conductivity can be achieved.

The most extensively studied inorganic solid electrolytes belong to two classes: oxides and sulfides. The main distinction between these two chemistries arises from the electronegativity difference between oxygen and sulfur atoms. Specifically, the interaction between the more electronegative O^{2-} ions and Li^+ ions is stronger than that between S^{2-} ions and Li^+ ions. Consequently, ionic conductivity in oxide solid electrolytes is typically slower because Li^+ ions have a more limited mobility within the crystal structure. Notably, the highest room temperature Li^+ conductivity reported for an solid electrolyte is 25 mS cm^{-1} in sulfide-type $Li_{9.54}Si_{1.74}P_{1.44}S_{11.7}Cl_{0.3}$, even surpassing that of liquid electrolytes [18].

However, oxides excel in terms of chemical and electrochemical stability. They possess a wider electrochemical stability window, allowing for the creation of cells with a large energy separation between the anode and cathode chemical potentials without inducing electrolyte reduction or oxidation. Sulfides, on the other hand, are

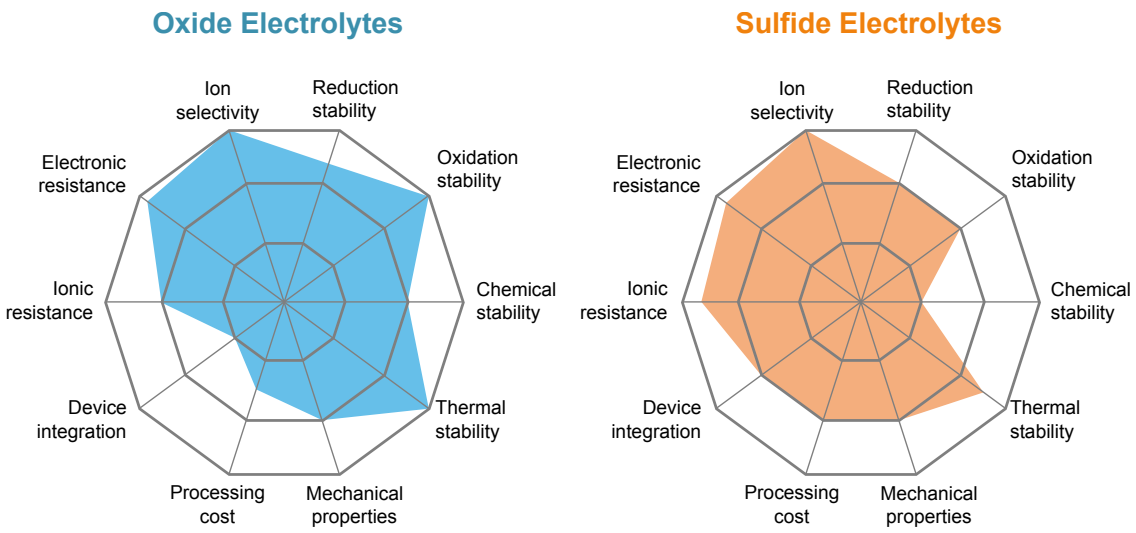


Figure 1.11. Performance of oxide and sulfide solid electrolytes. Spyder plots for oxide and sulfide solid electrolyte materials. The main differences are processing, electrochemical stability and ionic resistance. Reproduced with permission from [74].

constrained by their lower chemical and electrochemical stability, both when interacting with cathode and anode materials. Except for argyrodite (Li_6PS_5X (X = Cl, Br, I))-type electrolytes, which undergo relatively slow reactions at the interface, most sulfide electrolytes tend to decompose rapidly upon contact with lithium metal. Furthermore, their poor air stability leads to the release of toxic H_2S gas and to structural damage and degraded performance, limiting their practical application. Sulfides do offer a good mechanical deformability due to their lower melting temperatures, which allows for an easier mechanical processability and scalable cold-pressing-based fabrication. Moreover, intimate solid-solid contacts with electrode materials is promoted. In contrast, oxides face a processability challenge, often requiring high-temperature sintering to achieve relatively dense pellets.

Thus, each solid electrolyte class exhibits advantages and disadvantages (see Fig. 1.11 for a summary), and a compromise between various solid electrolyte requirements must usually be struck depending on the solid-state battery application. Recent commercialization efforts have primarily focused on sulfide solid electrolytes due to their enhanced ionic conductivity, which is particularly important for a fast kinetics on the cathode side and thus offers a clear advantage when considering overall cell design for high-power applications [47]. However, when assessing the interface between the solid electrolyte and lithium metal anode exclusively, oxides potentially provide a model interface, without introducing reaction layers that can complicate the interpretation

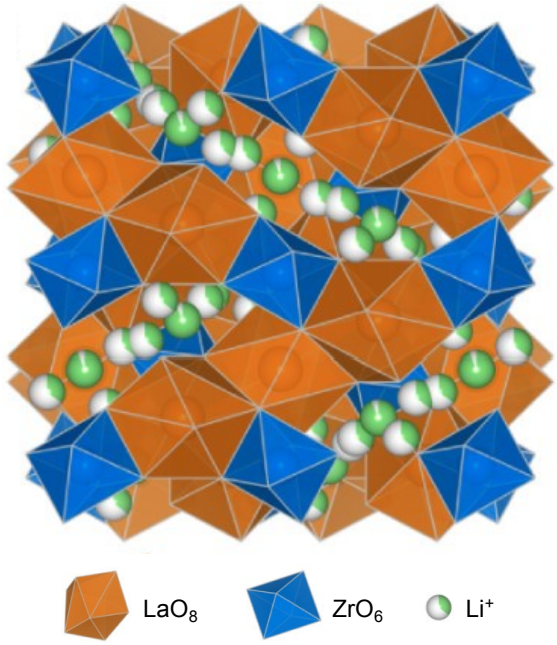


Figure 1.12. LLZO cubic crystal structure. Crystal structure of garnet-type cubic LLZO ($Ia\bar{3}d$). Li^+ ions are shown as partially filled spheres, indicating partial occupancy. La dodecahedra and Zr octahedra are depicted in orange and blue, respectively. Reproduced with permission from [77].

of experimental results. Nevertheless, it is challenging to draw general conclusions as the properties of the anode/solid electrolyte interface are usually case specific.

In this thesis, a lithium garnet oxide solid electrolyte known as LLZO has been employed as a model system. This choice simplifies the interpretation of lithium stripping and plating behaviours, which are analyzed in chapters 4 and 5 respectively. Lithium garnet solid electrolytes have been extensively studied over the last two decades, since the seminal work of Thangadurai et al. reported a garnet-type structure, $Li_5La_3M_2O_{12}$ (M = Nb, Ta), exhibiting a room temperature Li^+ conductivity on the order of 10^{-6} S cm^{-1} [75]. A wide variety of compositions within the garnet family have been since explored for solid-state cells. In particular, it was found that 'Li-stuffed' garnets, containing a greater number of lithium atoms per formula unit, exhibit enhanced ionic conductivity. In 2007, Murugan et al. reported a new garnet-type $Li_7La_3Zr_2O_{12}$ (LLZO) solid electrolyte with a room temperature conductivity of 0.3 mS cm^{-1} [76].

Pure LLZO has only one thermodynamically stable phase at room temperature, the tetragonal phase (space group $I4_1/acd$), characterized by limited ionic conductivity of approximately 10^{-6} S cm^{-1}. However at high temperatures, around 650

°C, LLZO undergoes a phase transformation into the high-conducting cubic phase (space group $Ia\bar{3}d$). The cubic LLZO structure comprises 8-fold coordinated LaO_8 dodecahedra and 6-fold coordinated ZrO_6 octahedra sharing corners within the crystal structure. The Li^+ ions are randomly distributed in the interstitial sites of the structure, along three-dimensional conduction paths, as displayed in Fig. 1.12. Stabilization of the high-temperature cubic phase at room temperature can be achieved by partially substituting one (or more) of the crystal lattice sites with an aliovalent element. Such substitution are carried out to induce the formation of additional lithium vacancies, such that the stabilized cubic phase of Li_7-garnets is actually of the form Li_{7-x}. The introduction of additional lithium vacancies increases the disorder in the garnet structure and results in Li^+ ions hopping from site to site asynchronously, with a significantly lower activation energy than the collective ionic movement taking place in the tetragonal phase [78].

The most common approach involves the partial replacement of Li^+ sites with trivalent metallic cations like Al^{3+}, Ga^{3+} or Fe^{3+}. Four-, penta-, and hexa-valent substitutions in the Zr^{4+} sublattice sites can also lead to the formation of additional lithium vacancies and cubic phase stabilization at room temperature. Substitutions with Nb^{5+}, Ta^{5+}, Sb^{5+}, Mo^{6+}, W^{6+}, amongst others, are often reported [79]. Different LLZO chemical compositions can have slightly different electrochemical and mechanical behaviour. For instance, while LLZO solid electrolytes generally feature a wider electrochemical stability window than most alternatives, the stability of the lithium/solid electrolyte interface depends on the non-lithium cations contained in the solid electrolyte, which may be reduced upon contact with lithium metal as previously discussed. Garnets containing Nb or Ti are more susceptible to reduction by lithium metal [80]. Additionally, studies have shown that the immediate surface (up to five unit cells) of Al-doped LLZO can be reduced upon contact with lithium metal to form the poorly conducting tetragonal LLZO phase [81].

In addition to a good ionic conductivity and electrochemical stability, LLZO exhibits higher fracture toughness than many other solid electrolytes, approximately 1.25 MPa $m^{0.5}$. This characteristic ensures that the applied pressure to a Li/LLZO interface primarily induces lithium creep without compromising the mechanical integrity of the solid electrolyte pellet. Also, LLZO's high thermal stability can further enhance battery safety. Moreover, recent studies have confirmed that the charge transfer resistance at the Li/LLZO interface, representing the resistance to the process described in equation 1.1, is negligibly small ($R_{CT} < 0.1\ \Omega\ cm^{-2}$). This theoret-

ically allows for extremely fast plating and stripping kinetics in the range of several hundreds of mA cm^{-2} without the occurrence of transport limitations [82].

Given these chemical and structural advantages, the Li/LLZO interface serves as a suitable model system for studying kinetic and morphological behaviour inherent to the lithium metal anode. Among various doped LLZO compositions, Ta-doped LLZO $Li_{6.4}La_3Zr_{1.4}Ta_{0.6}O_{12}$ stands out due to its relatively higher room temperature ionic conductivity of approximately 1 mS cm^{-1} [83, 84]. This composition also demonstrates superior electrochemical stability when in contact with lithium metal [80] and has therefore been selected for the present study.

One of the challenges associated with the assembly of a Li/LLZO interface originates from the lithiophobic nature of the LLZO surface, which can prevent lithium metal from adhering to the LLZO pellet. This results in a substantial interfacial resistance. However, this issue is attributable to surface contamination of the LLZO, as pristine LLZO is actually inherently lithiophilic [44]. Initially, LLZO was believed to be chemically stable when exposed to ambient air [76], but in fact recent research has revealed its susceptibility to reacting with H_2O and CO_2, leading to the formation of a lithiophobic surface layer consisting of Li_2CO_3 and LiOH [85, 86]. Fortunately, this surface layer can be effectively removed prior to the assembly of the Li/LLZO interface. The efficacy of various surface treatments is thoroughly assessed in chapter 3, where a detailed analysis of the chemical composition of LLZO surface is conducted.

1.5 Aims and structure of the thesis

This thesis aims to tackle the unique challenges of the Li/LLZO interface, as they have been introduced in this chapter, and showcase the opportunities to achieve high-performing solid-state cells. The main three chapters delve into the three steps that this interface undergoes, namely assembling, lithium stripping and lithium plating, respectively. Chapter 3 sets out to conduct an extensive study of LLZO's surface reactivity, laying the foundation for the subsequent chapters by providing information on the correct protocols for handling and assembling LLZO cells in a glovebox atmosphere. To do so, H_2O and CO_2 gas dosing experiments are performed in a near-ambient pressure X-ray photoelectron spectroscopy chamber. The chapter analyses the impact that LLZO surface contamination has on the interfacial impedance with a lithium metal anode and on the cell cycling performance. It also assesses the effectiveness of different surface treatments that can be used for the removal of surface contaminants. This chapter is instrumental for a better understanding of the

LLZO solid electrolyte and is therefore placed early in the thesis. Furthermore, the ability to treat the LLZO surface to tune the Li/LLZO interfacial impedance will prove valuable in both chapters 4 and 5.

Chapter 4 focuses on exploring the kinetics of lithium stripping. The chapter aims to illustrate the formation of voids in lithium metal, as explained in the previous sections. The stripping behaviour can change upon introduction of a small amount of magnesium in the metallic anode, but its effect is not fully understood. Initially, a comprehensive characterization of the diffusion properties of lithium metal and LiMg alloy anodes is conducted using secondary ion mass spectrometry. This technique is chosen to directly probe lithium diffusivity over large distances in these anode materials, yielding diffusion coefficients relevant to the operation of solid-state cells. Subsequently, the interface morphology during stripping at the interface with LLZO is examined using cryogenic plasma focused-ion beam, to observe the contact loss between the anode and the solid electrolyte. This chapter will explain the role of lithium diffusivity and of interface morphology in determining the stripped capacity of solid-state cells.

Chapter 5 delves into the formation of lithium dendrites during plating. Building on chapter 4, a LiMg anode is employed, and diffusion of magnesium along the freshly plated lithium in the dendrites is promoted. Then, the morphology of initiation sites for dendrites are analysed with energy dispersive X-rays technique and studied with unprecedented resolution. This strategy enables to draw conclusions regarding the mechanism behind dendrite formation.

This thesis aspires to make a meaningful contribution to the understanding of solid-state cell operations. To achieve this, novel instruments such as plasma focused-ion beam and innovative imaging techniques such as electron beam induced current have been employed. Notably, the introduction of a small amount of magnesium in the lithium metal anode is a recurring theme of this thesis, as comparing the behaviour of pure lithium metal and LiMg anodes has led to an enhanced understanding of both the kinetics of lithium stripping and the formation of dendrites during lithium plating. The use of LLZO throughout the thesis facilitates the assembly of a model interface with lithium metal, as explained in the previous section, and allows the study of lithium metal behaviour. Many of the conclusions of the thesis can be however applied to different solid electrolyte systems, albeit with necessary care when considering the possibility of electrochemical reduction of the solid electrolyte or variations in the electrolyte mechanical properties. Building on the findings of these following chapters, a combination of a highly dense LLZO and a meticulous assembly

of the Li/LLZO interface will be indicated in the concluding remarks of this thesis as the most promising strategy to allow cycling of solid-state cells under commercially relevant conditions, such as room temperature and relatively low externally applied stack pressures.

Before delving into the experimental results, chapter 2 provides an overview of the experimental methods critical to this thesis. These methods include processes such as sintering LLZO pellets, casting LiMg alloys, the use of various eletrochemical techniques and of plasma focused-ion beam to study the Li/LLZO interface, amongst others, offering insight into the day-to-day operations of my research.

Chapter 2

Experimental Methods

This chapter provides an overview of the experimental methods employed in this thesis. To begin, the spark plasma sintering processing of LLZO pellets is outlined, elucidating how different pellet densities can be achieved. A comprehensive structural and electrochemical characterization of LLZO is then presented. Secondly, the procedure for casting LiMg alloys is detailed, followed by their characterization using XRD, SEM and XPS techniques. Subsequently, the primary characterization tool employed in this thesis, the PFIB-SIMS instrument, is introduced. We will explore how PFIB-SIMS has been used to measure lithium diffusivity in both lithium metal and LiMg alloys. Afterwards, this chapter delves into the assembly procedure for solid-state Li/LLZO/Li symmetric cells. This starts with the polishing procedure and potential treatments to eliminate LLZO surface contaminants. The subsequent sections detail the initial EIS analysis of the cells and the electrochemical cycling. Finally, the process of automated serial sectioning of LLZO with PFIB is outlined, which has been employed in the thesis to investigate the three-dimensional morphology of lithium dendrites in LLZO.

2.1 Spark plasma sintering of LLZO pellets

$Li_{6.4}La_3Zr_{1.4}Ta_{0.6}O_{12}$ powder (99.9%, Ampcera) with a particle size of 5 μm was used for the preparation of LLZO pellets. Within a glovebox, approximately 2 g of the powder was weighed and subsequently transferred into a graphite die. The die had an internal diameter of 10 mm and was lined with graphite paper. The powder underwent cold pre-pressing at $\sim$ 10 MPa using a manual press. Then the graphite die was taken out of the glovebox and placed into the spark-plasma sintering (SPS) machine (Dr Fritsch DSP 507).

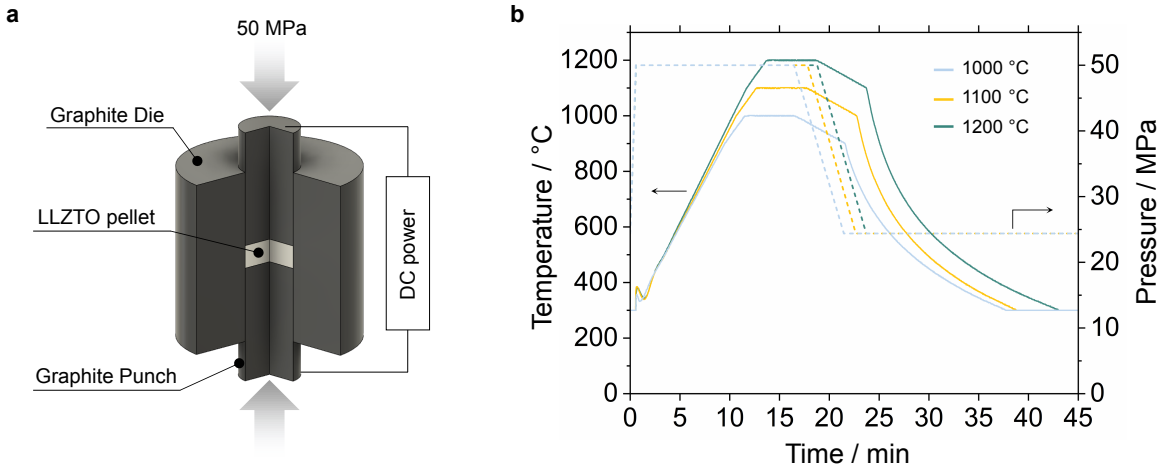
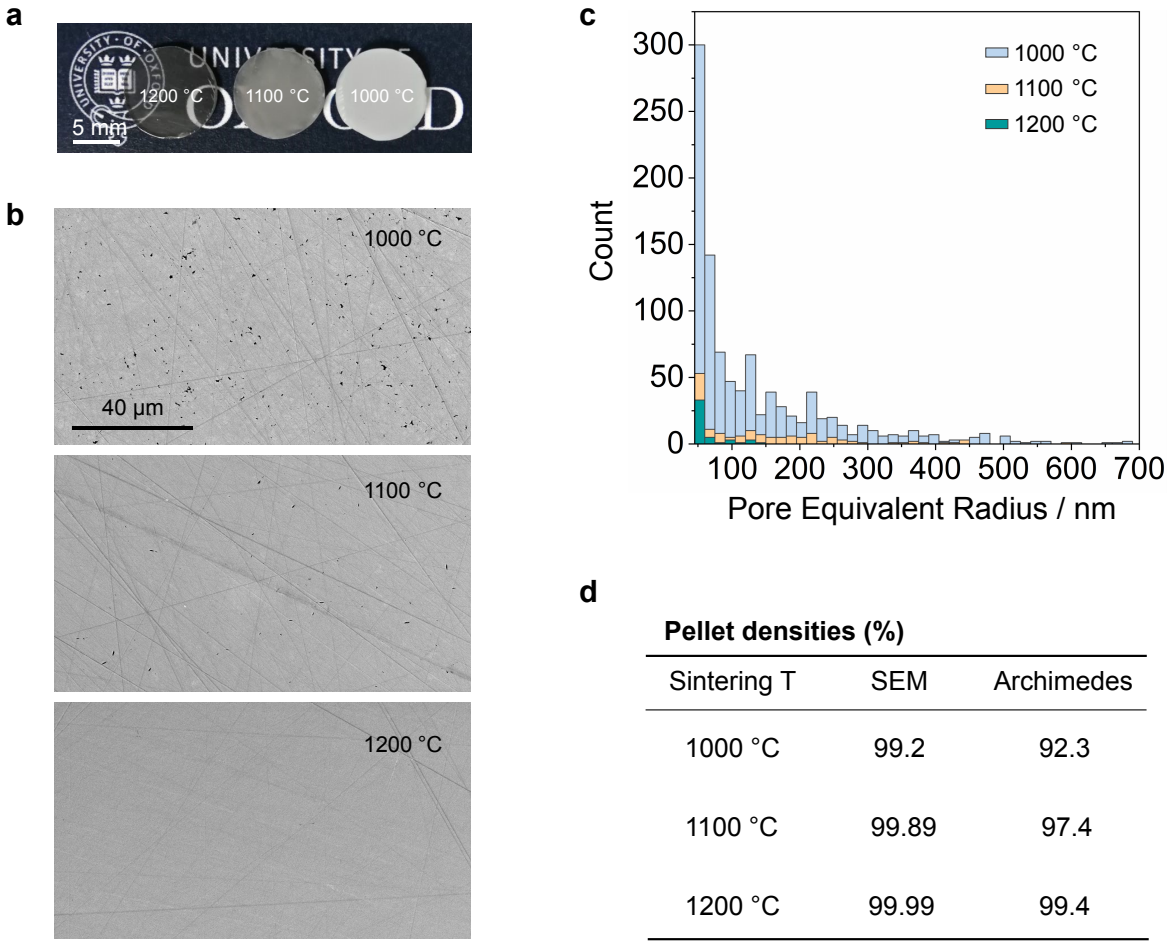


Figure 2.1. Spark plasma sintering of LLZO pellets. **a**, Assembly of the graphite die for SPS. **b**, Temperature and pressure profiles during SPS experiments with different upper sintering temperatures.

The SPS chamber was promptly evacuated to a base pressure of 0.1 mbar to minimize exposure of the LLZO powder to trace moisture and CO_2. During the SPS process, also known as field-assisted sintering technique (FAST), the graphite die containing the initial powder is compressed between two graphite plates. These plates also serve as electrodes, through which a direct current is applied to the graphite die, inducing Joule heating to raise the powder temperature (see the schematic in Fig. 2.1a). This combined compression and Joule heating facilitate the densification of the powder compact. Compared to conventional sintering methods, SPS can achieve nearly theoretical densities at lower sintering temperatures [87]. SPS is advantageous also because it offers a better control of the sintering parameters for the formation of the desired pellet structure. Additionally, Joule heating rates can reach up to 1000 K/min, making the SPS process notably quicker than conventional methods. This not only provides commercial advantages but also mitigates the evaporation of lithium from Li-containing ceramic powders such as LLZO, which can occur at temperatures exceeding 600 °C. Such litihum loss in LLZO can result in reduced Li^+ ionic conductivity in the final pellet [88].

Figure 2.1b illustrates the pressure and temperature profiles applied to the LLZO powders. The powder was gradually compressed to 50 MPa at room temperature. Subsequently, the temperature was raised at a rate of 100 °C/min. The final 100 °C increment used a 200 °C/min rate to prevent temperature overshooting. The powder was held at the designated sintering temperature for 5 minutes and then cooled at 200



Pellet densities (%)

Sintering T	SEM	Archimedes
1000 °C	99.2	92.3
1100 °C	99.89	97.4
1200 °C	99.99	99.4

Figure 2.2. LLZO pellet densities. **a**, Photo of LLZO pellets sintered at different temperatures, hence with different densities. A high density pellet is nearly transparent. **b**, SEM images of the surface of LLZO pellets after polishing. **c**, Porosity analysis based on the SEM surface images. **d**, Pellet densities extracted from the SEM surface images and from the Archimedes method.

°C/min over 100 °C while concurrently reducing the pressure. Finally, the pellet was allowed to naturally cool to room temperature. The upper sintering temperature can be easily adjusted to achieve different pellet densities, as shown in Fig. 2.2. Sintering at 1000, 1100 and 1200 °C yielded pellets with Archimedes densities of 92.3, 97.4, and 99.4%, respectively. Notably, the Archimedes method measures the apparent density of the pellet, representing the ratio of the total pellet mass to its overall volume, including any pores or voids. This value is therefore lower than the true or absolute density of the pellet. On the other hand, densities extracted from secondary electron microscopy (SEM) images are likely to be an overestimation.

Different pellet densities manifest in varying appearances (see the photo in Fig. 2.2a) and surface characteristics, as demonstrated by the SEM images in Fig. 2.2b. LLZO pellets with high density are nearly transparent, such as the ones sintered at 1200 °C, a consequence of their markedly low sample porosity. Pores, as well as secondary phases and other imperfections, can scatter light, causing the LLZO pellet to appear translucent like the ones sintered at 1000 and 1100 °C [89]. The difference in sample density also results in distinct behaviour during cell cycling. A higher level of porosity has been demonstrated to correspond to a lower critical current density for the formation of lithium dendrites through LLZO [62]. Conventional sintering methods typically yield LLZO pellets with much lower densities (60 – 95%) compared to the pellets employed in this thesis [90]. This suggests that the spark plasma sintered LLZO pellets employed in this study exhibit enhanced electrochemo-mechanical performance, as later demonstrated by cycling data in chapters 3 and 5 were LLZO cells are cycled at large current densities. Moreover, SPS also allows comparing the behaviour of pellets with different densities, facilitating a better understanding of the degradation mechanisms at the Li/LLZO interface. For instance, in chapter 5, the fewer number of spallations observed on denser LLZO pellets after lithium plating (Fig. 5.10) crucially contributes to elucidating the spallation formation mechanism. Thus, the ability to finely adjust LLZO density is a valuable advantage offered by the SPS technique.

To ensure phase purity of the sintered LLZO pellets, X-ray diffraction (XRD) measurements were carried using an Empyrean diffractometer with Cu $K_{\alpha 1}$ radiation (Malvern Panalytical). A pure cubic crystal structure is evident in Fig. 2.3a, and no contamination is observed. XRD was carried out for each sintering temperature. The XRD patterns display narrower peaks, indicative of larger grain sizes and lower lattice disorder, in pellets sintered at higher temperatures. The cross sectional SEM

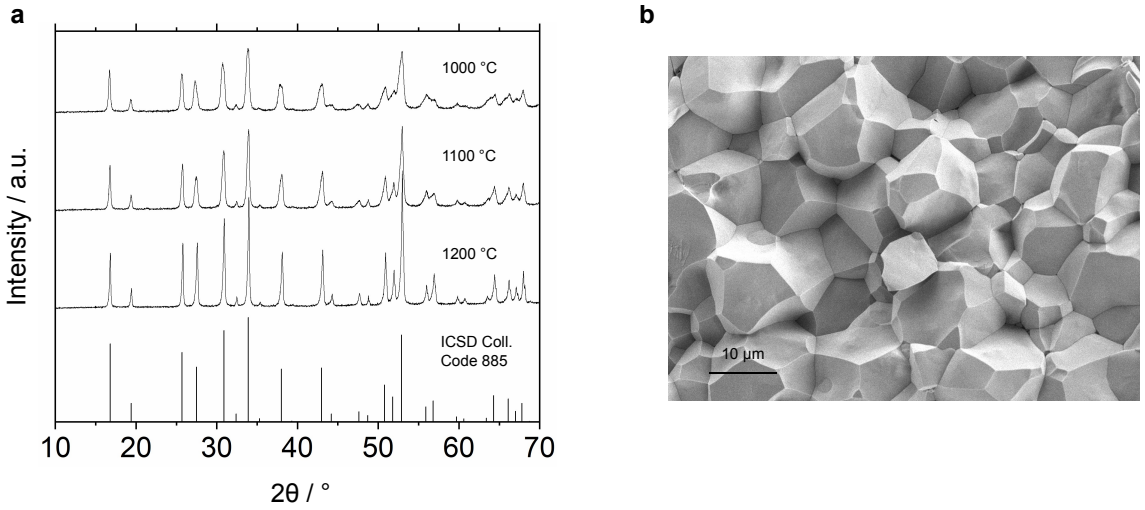


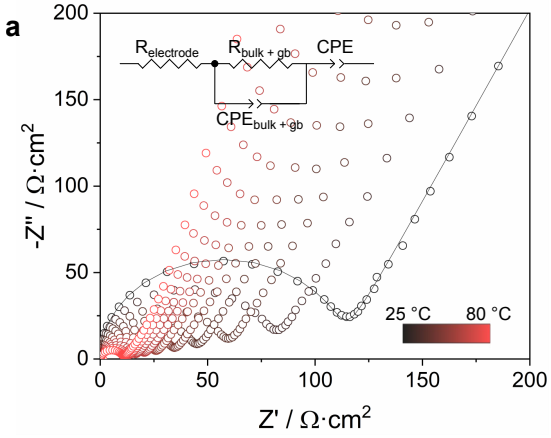
Figure 2.3. XRD spectra of LLZO pellets. **a**, X-ray diffraction spectra of LLZO pellets sintered at different temperatures. Narrower peaks are visible for higher sintering temperatures. **b**, SEM image of a manually fractured cross section of a pellet sintered at 1200 °C.

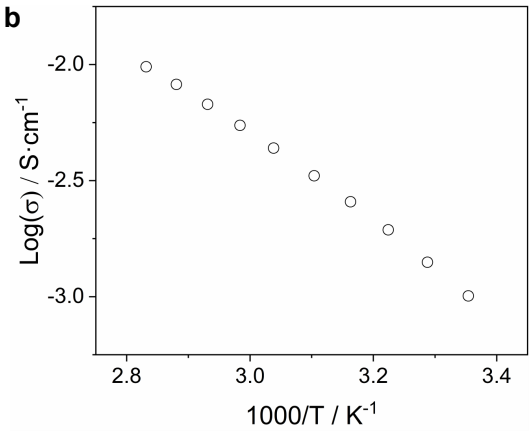
image (Zeiss Merlin SEM) in Fig. 2.3b reveals grains of approximately 10 μm in size for an LLZO pellet sintered at 1200 °C.

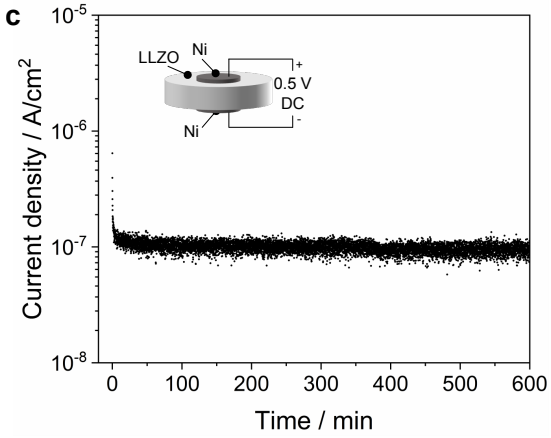
2.2 LLZO ionic and electronic conductivities

When LLZO was first synthesized by Murugan et al. in 2007, it exhibited a Li^+ ionic conductivity of 3×10^{-4} S cm^{-1} at 25 °C [76]. Since then, advancements have been made and the ionic conductivity has been improved through modifications to LLZO chemistry and sintering techniques. Presently, a typical value stands around $\sim 1 \times 10^{-3}$ S cm^{-1}, which aligns with the ionic conductivity of the LLZO pellets employed in this study.

To measure the ionic conductivity, Ni blocking electrodes with a thickness of 100 nm and a diameter of 2 mm were radio frequency sputtered onto both sides of polished LLZO pellets using a sputtering chamber fitted within a glovebox (MB EVAP, MBraun). Subsequently, electrochemical impedance spectroscopy (EIS) was conducted at various temperatures on the Ni/LLZO/Ni cells using an MTZ-35 potentiostat (BioLogic). The corresponding Nyquist plot is reported in Fig. 2.4a, alongside the equivalent circuit used to fit the spectra. The equivalent circuit comprises a single semicircle at higher frequencies, representing the contribution of bulk LLZO and LLZO grain boundaries to the overall impedance, along with a Warburg element capturing the low-frequency tail [91]. The ionic conductivity is derived from $\sigma_{Li^+} = \frac{t}{R \cdot A}$,







d

Pellet conductivities at 30 °C

Sintering T	σ_{Li^+} mS cm^{-1}	σ_{e^-} S cm^{-1}
1000 °C	1.36	$2.19 \cdot 10^{-8}$
1100 °C	1.38	$2.04 \cdot 10^{-8}$
1200 °C	1.41	$1.93 \cdot 10^{-8}$

Figure 2.4. Ionic and electronic conductivity of LLZO. a, Typical EIS spectra at various temperatures for a Ni/LLZO/Ni cell. The inset shows the equivalent circuit model used to fit the spectra. **b**, Typical Arrhenius plot for the LLZO pellets used in this study. **c**, Chronoamperometry experiment for a Ni/LLZO/Ni cell. 0.5 V is applied to the cell and the steady-state current is measured to evaluate the electronic conductivity. **d**, Ionic and electronic conductivities of LLZO pellets sintered at different temperatures, i.e. with different densities as shown in Fig. 2.2.

where t denotes the LLZO thickness, A the area of the Ni electrode, and R the resistance of bulk LLZO. The ionic conductivity varies with temperature according to an Arrhenius law described as $\sigma_{Li^+} = \frac{\sigma_0}{T} \exp^{E_A/k_B T}$. An activation energy E_A of approximately 0.37 eV was deduced from the Arrhenius plot in Fig. 2.4b for the LLZO pellets used in this research, which is in line with literature values [92].

A chronoamperometry experiment was conducted to quantify the electronic conductivity of LLZO. This involves the application of a step potential of 0.5 V to the Ni/LLZO/Ni cells and measurement of the current response with a SP-200 potentiostat (BioLogic). The initial current response in Fig. 2.4c is representative of both Li^+ and electron transport. However, due to the absence of Li^+ supply from the Ni electrodes, the residual steady-state current is purely electronic, and its value can be used to assess the electronic conductivity σ_{e^-}. LLZO is a purely ionic conductor, well-suited for solid-state cells, as the pellets exhibit an exceptionally low electronic conductivity of $\sim 2 \times 10^{-8}$ S cm^{-1}. Nevertheless, recent findings have suggested that LLZO grain boundaries might have a higher σ_{e^-}, enabling some electronic current leakage into the LLZO solid electrolyte at the interface with the lithium metal electrode [69, 93]. This phenomenon could contribute to the nucleation of lithium dendrites in LLZO. Chapter 5 of this thesis will provide additional evidence in support of this hypothesis.

Both the ionic and electronic conductivities of LLZO pellets sintered at different temperatures and employed in this study for the fabrication of solid-state cells are presented in the table in Fig. 2.4d. Notably, values for σ_{Li^+} and σ_{e^-} remain consistent across LLZO pellets sintered at different temperatures, hence with different densities.

2.3 Casting LiMg alloys

LiMg alloys with different magnesium content of 10, 20, and 30 at. % will be used as substrates for the diffusivity experiments and as anode materials in chapters 4 and 5. Lithium metal (foil, 99.9%, Alfa Aesar) and magnesium metal (turnings, 99.98%, Alfa Aesar) were used for casting the alloys in a tube furnace (MTI KSL-1200X-J-UL), which was placed within a glovebox. The lithium metal was heated to 100 °C above the LiMg liquidus temperature in a custom-made stainless-steel crucible lined with stainless-steel foil. For samples containing 20 and 30 at. % Mg, molybdenum foil was used instead of stainless-steel, as reactions were observed between the LiMg melt and steel above 450 °C. After reaching the desired temperature, the molten lithium was extracted from the furnace and any slag was carefully removed using a stainless-steel

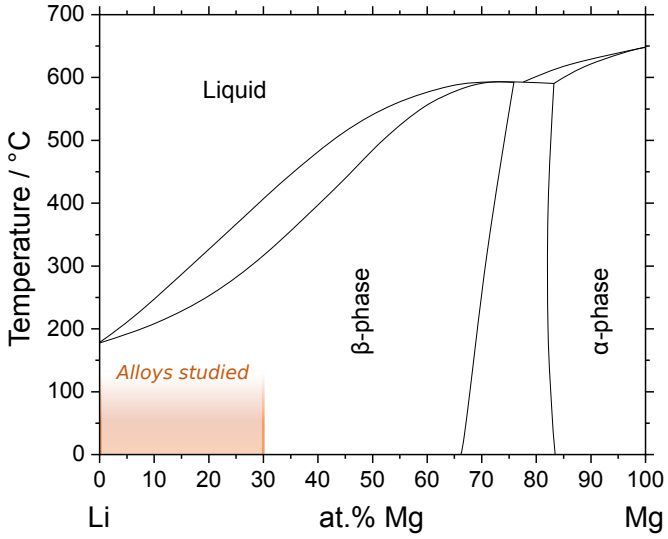


Figure 2.5. LiMg phase diagram., The LiMg binary phase diagram shows the exceptionally wide solubility range of magnesium in lithium, with the β-phase region spanning from 0 to 70 at. % Mg at room temperature [95].

spatula. Subsequently, an appropriate mass of magnesium turnings was fully dissolved in the molten lithium. The crucible was then reintroduced into the furnace for 2 hours before slowly cooling to room temperature. The casting procedure for LiMg alloys was carried out by Jack Aspinall (University of Oxford). Verification of the magnesium content was performed using inductively coupled plasma optical emission spectroscopy (ICP-OES) analysis (PerkinElmer Optima 8000), with the assistance of Stephen Turrell (University of Oxford). This analysis method requires dissolving a known quantity of material in nitric acid and recording emission spectra generated when a small volume of the solution interacts with a plasma. A comparison with emission spectra from a standard solution allows for precise quantification of the concentration of each element in the sample. The magnesium content was confirmed as 10, 21 and 31 at. %, respectively, very close to the targeted amounts.

The LiMg equilibrium binary phase diagram in Fig. 2.5 illustrates the extensive solubility range of magnesium in lithium, with the β-phase region spanning from 0 to 70 at. % Mg at room temperature. The LiMg alloys employed in this study fall within this Li-rich β-phase region. Because this solid solution β-phase extends to pure lithium metal, the crystalline structure of the alloy remains constant when placed in contact with pure lithium metal. Magnesium is the only element that has this property [94], significantly simplifying the measurements of lithium diffusivity in LiMg alloys as performed in chapter 4.

Phase purity analysis of freshly cast LiMg alloys and lithium metal foil was conducted using XRD (Empyrean, Malvern Panalytical). The samples were shielded from atmospheric exposure during XRD measurements using polyimide tape. The XRD patterns reveal a body-centred cubic (BCC) configuration for both lithium metal and LiMg samples. Notably, in Fig. 2.6a, higher magnesium contents lead to XRD peak shifts toward higher 2Θ values, indicating a reduction in lattice parameter with the addition of magnesium. Fig. 2.6b reports the lattice parameters extracted by Rietveld refinement of the XRD patterns.

A Zeiss Merlin SEM was used for imaging the grain size of lithium metal and LiMg alloys. Samples were cut within a glovebox using a fresh microtome blade to expose clean, undamaged surfaces for the visualization of grain boundaries. An argon-filled vessel (Gatan iLoad) was used for air-free transfer of samples to the SEM. All lithium and LiMg samples used for the diffusivity experiments in chapter 4 exhibit large grain sizes (see Fig. 2.6c), minimizing the contribution of grain boundaries to lithium diffusivity.

X-ray photoelectron spectroscopy (XPS) was employed to characterize the surfaces of lithium metal and LiMg alloys, using an ULVAC Phi Versaprobe III XPS with a water-cooled monochromatic Al Kα source (hν 1486.6 eV, 15 kV anode voltage, 25 W beam power). The goal was to discern possible variations in the surface passivation layer that develops within a glovebox environment on the surface of lithium and LiMg samples. Differences in surface passivation would in turn affect the lithium diffusivity in these samples, due to the need for lithium atoms from the tracer thin film to traverse the surface contamination layer (see section 2.4). In the glovebox, freshly cut surfaces were gently scraped with a stainless steel blade just before transferring the samples to the XPS in an argon-filled transfer vessel (ULVAC Phi GmbH, < 1 minute from the glovebox to the XPS chamber), ensuring minimal exposure to air. The samples were electrically connected to the sample holder with conductive carbon tape. In-situ Ar^+ ion beam sputtering was used for depth profiling (4 kV acceleration voltage, 3×3 mm^2 raster, 2.8 μA beam current). XPS data were energy calibrated relative to the O 1s lithium oxide signal at 528.5 eV. Core level spectra were collected with a pass energy of 55 eV and a step size of 0.05 eV/step. The analysis chamber pressure was maintained below $5 \times$ 10e-9 mbar during measurement. Data analysis was performed using the CasaXPS software package [96]. O 1s, Mg KLL, C 1s, Li 1s, and Mg 2p XPS spectra are reported in Fig. 2.3. All samples reveal a similar surface passivation layer, primarily composed of Li_2O, LiOH, and Li_2CO_3. Following 2 minutes of in-situ Ar^+ sputtering, adventitious carbon and carbonate signals diminish

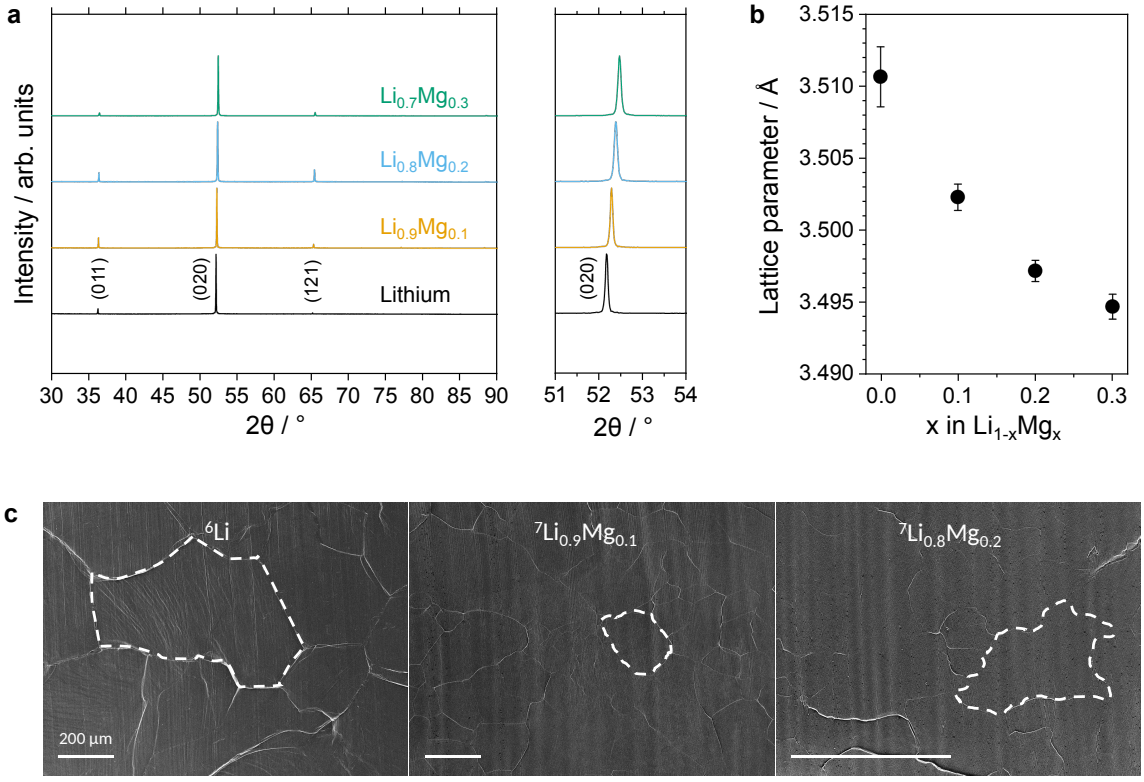


Figure 2.6. XRD and SEM characterization of Li and LiMg alloys. **a**, X-ray diffraction patterns of lithium metal and of the LiMg alloys. **b**, Lattice parameter as a function of magnesium content. **c**, SEM images of ^{6}Li and LiMg alloys. These are the substrates employed for the lithium diffusivity experiments in chapter 4. Notably, the grain size is at least tens of μm for all the samples. The $Li_{0.7}Mg_{0.3}$ alloy is not included here as it was more difficult to manipulate due to its increased hardness.

significantly. Li_2O peak is more persistent, remaining visible throughout sputtering. For all samples, the Li 1s metallic peak emerges after approximately 4 minutes of Ar^+ sputtering, accompanied by the Mg 2p metallic peak in the case of LiMg alloys. The intensity of the magnesium peak correlates, as expected, with the at. % concentration of the LiMg alloy. This chemical composition of the surface passivation layer agrees with prior research on lithium metal [97], which identified an outer layer of lithium hydroxide and carbonate and an inner region rich in lithium oxide. This information will be valuable in chapter 4, where the XPS plots here reproduced will be referred to.

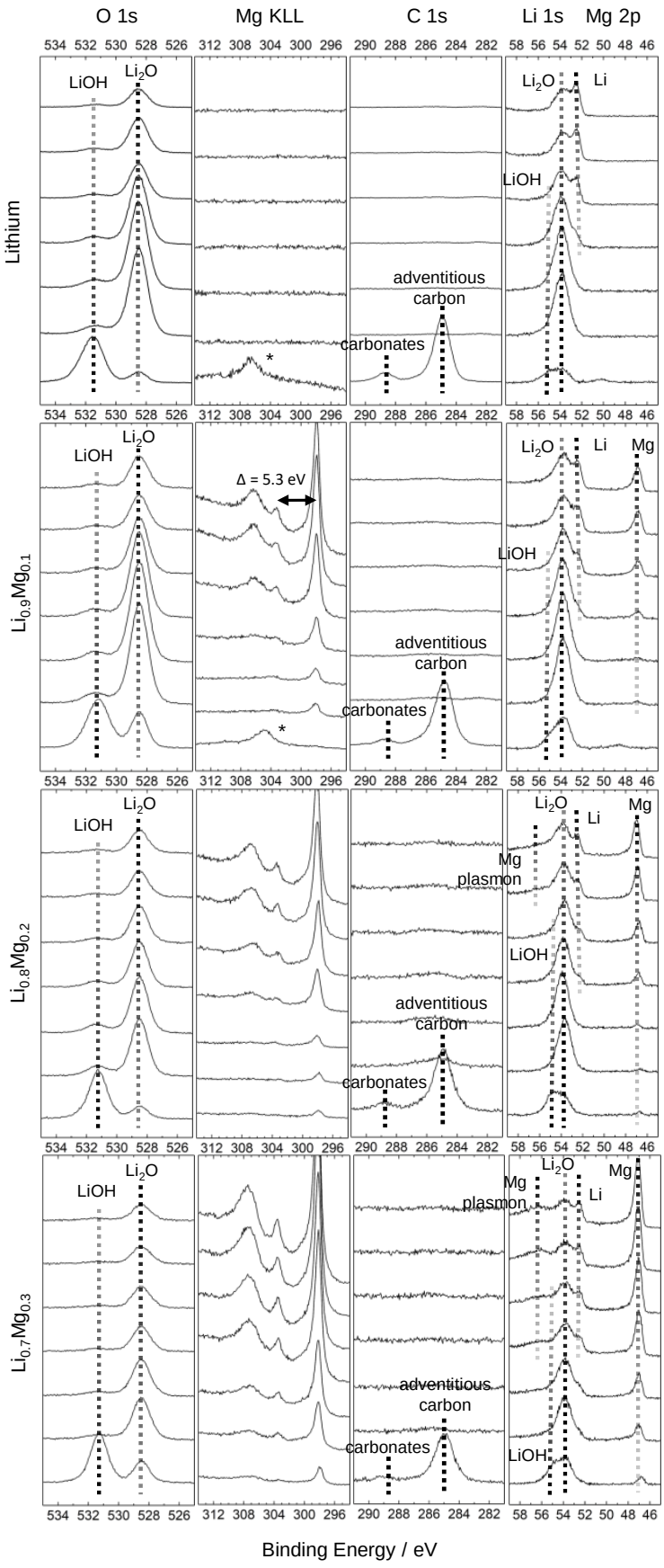


Figure 2.7. XPS depth profiling of Li and LiMg alloys. Full XPS data set for lithium metal, $Li_{0.9}Mg_{0.1}$, $Li_{0.8}Mg_{0.2}$, and $Li_{0.7}Mg_{0.3}$ (panels from top to bottom respectively). The spectrum at the bottom of each panel corresponds to the as-loaded sample, the spectra on top of it correspond to the sample after Ar^+ sputtering. Ar^+ ions with an accelerating voltage of 4 kV and beam current of 7 mA were applied, using the following sputtering steps: 2×2 min, 2×5 min, 2×15 min. *unknown surface species.

2.4 Measuring Li diffusivity with PFIB-SIMS

Lithium metal and LiMg alloys serve as substrates in chapter 4 for measuring the diffusion coefficient of lithium in these materials. In this section, the procedure for evaluating the diffusion coefficient is presented. This procedure involves the deposition of a lithium 'tracer' thin film onto a Li or LiMg substrate. The isotopic composition of the deposited lithium, specifically the ratio of ^{6}Li to ^{7}Li, differs from that of the substrate. Over time, the lithium tracer diffuses from the deposited thin film into the substrate material. The isotopic concentration is tracked through the sample depth using a secondary ion mass spectrometry (SIMS) detector integrated into in a plasma focused-ion beam (PFIB) instrument. Fitting the concentration curves with a solution of Fick's second law yields the diffusion coefficient.

^{6}Li-enriched lithium metal (chunks, 95 at. % ^{6}Li, Sigma Aldrich) and lithium metal granules with a natural isotopic ratio (99%, Sigma Aldrich) were used for thermal evaporation. In this thesis, they are respectively referred to as ^6Li and ^7Li to differentiate them from the pure isotopes. The isotopic content of the as-received lithium metals was confirmed using SIMS. The measured ^{7}Li concentration in the lithium metal granules is 91%, reasonably close to the natural isotopic abundance of 92.5%. The ^{6}Li-enriched material has a ^{6}Li concentration of 95.1%, as specified by the supplier.

The deposition of the tracer thin film was conducted using a thermal evaporator (MB EVAP, MBraun) located within a glovebox. The substrate, freshly cut from either ^6Li or ^{7}LiMg, was gently scratched with a stainless steel blade just before being placed in the thermal evaporation chamber, positioned approximately 20 cm from the evaporation source. The evaporation chamber was promptly evacuated to a background pressure below 10e-5 mbar before initiating the deposition process to minimize any exposure to glovebox contaminants. A quartz crystal microbalance was used to monitor the deposition rate (25 - 30 Å s^{-1}) until a thickness of $\sim$ 3 - 5 μm was achieved. Thinner films would diffuse too rapidly into the substrate even at room temperature, causing loss of the concentration profile. Conversely, thicker films would require extended deposition times, risking excessive thermal heating during evaporation, and would necessitate prolonged SIMS depth profiling. The substrate temperature was monitored by a thermocouple in contact with the substrate surface. The temperature gradually increased from 26 °C (glovebox atmosphere) to a maximum of 35 °C by the end of the evaporation (15 - 20 minutes), at a consistent rate for all substrates used in this study.

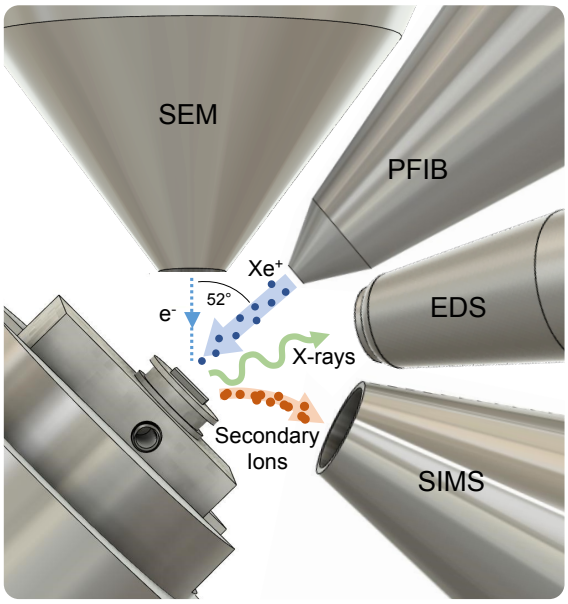


Figure 2.8. Schematic of the PFIB chamber. The PFIB chamber contained EDS and SIMS detectors. Coupled with the possibility of in-situ cross sectioning, the setup allowed for great versatility and novel imaging techniques. The sample stage could also be cooled with liquid nitrogen to minimize beam damage to the sample.

Following thermal evaporation, the samples were swiftly transferred to the PFIB chamber (Helios G4 PFIB CXe DualBeam, Thermo Scientific) in an argon-filled transfer vessel (Gatan iLoad). The PFIB employs a focused Xe^+ ion beam to ablate the sample in-situ. The Xe^+ ion beam is accelerated into the range of 1 - 50 keV, spatially focused to the micrometer range by electrostatic lenses, and rastered across the sample surface. Upon impact, the Xe^+ ions sputter the sample surface, forming a well-defined crater. The PFIB is typically coupled with an SEM column onto a dual platform instrument, where the electron column is mounted vertically and the ion column is at 52 ° from the vertical [98]. By aligning the sample at a stage height where the electron and the ion beams coincide (as shown in Fig. 2.8), PFIB processing and SEM characterization can be co-localized. This configuration enables sectioning of the specimens and innovative imaging of buried features and interfaces.

Xe^+ ion sources, which have been recently developed [99], offer numerous advantages over traditional ion sources such as Ga^+ or He^+. Notably, sputtering with heavier Xe^+ ions yields significantly higher material removal rates compared to Ga^+ milling [100], enabling the preparation of larger samples. An additional benefit of the heavier Xe^+ ion mass is a much shorter trajectory of the ions into the sample,

resulting in reduced ion implantation effects and lower overall damage. The chemically inert nature of Xe gas further minimizes damage to materials sensitive to other ion types. For instance, lithium metal and solid electrolyte materials are prone to damage by Ga^+ ion sources [101]. The superiority of PFIB over other traditional FIBs has also paved the way for the application of the method in large-volume serial section tomography, as further explored in section 2.6 of this chapter.

To evaluate the diffusivity of lithium, the PFIB chamber was equipped with a SIMS detector (Hiden Analytical EQS). The interaction of the Xe^+ ion beam with the sample surface triggers the sputtering of a few top atomic layers, resulting in the emission of positively and negatively charged species (ions and molecular ions). During SIMS analysis, these are collected by the SIMS aperture and channeled through an electric quadrupole mass analyser. This device separates the ions based on the stability of their trajectories in an oscillating electric field. Subsequently, the ions are detected by a microchannel plate detector, which offers lateral resolution. This methodology enables the creation of mass-resolved depth profiles as well as 2D and 3D chemical mappings. Notably, a major advantage of SIMS is its extreme sensitivity and exceptional mass resolution [102]. Additionally, SIMS has the capability to identify light elements, a challenge for X-ray techniques such as energy dispersive X-ray spectroscopy (EDS). This attribute proves invaluable for the study of battery materials. In the context of this study, SIMS allows the precise differentiation of ^6Li and ^7Li isotopes, enabling accurate measurement of the diffusion coefficient.

For the experiments detailed in chapter 4, a 30 kV accelerating voltage and a 4 nA current Xe^+ ion beam was used to sputter the tracer thin film and the lithium or LiMg substrate. These settings were calibrated to ensure a fast removal of lithium with minimal beam damage. The intensities of secondary ions $^6Li^+$ and $^7Li^+$ were recorded for each PFIB slice, constructing a profile as a function of the sputtering time. A typical ion mass spectrum from SIMS analysis is reported in Fig. 2.9a, clearly showing the ion intensities of the $^6Li^+$ and $^7Li^+$ isotopes. The sample was maintained at room temperature throughout the measurement, so inter-diffusion of the thin film and bulk substrate occurred over the course of the experiment. The sputtering area measured 20 $\times$ 20 μm^2, although only about 20% of this area was used for the analysis of the diffusion profile in order to exclude crater edge effects. At the end of each experiment, the craters were examined by SEM to convert the sputtering time to a sputtering rate, assuming a constant sputter rate. This process allows the concentration of secondary ions to be plotted against sample depth. This profile can be fitted via Fick's second law.

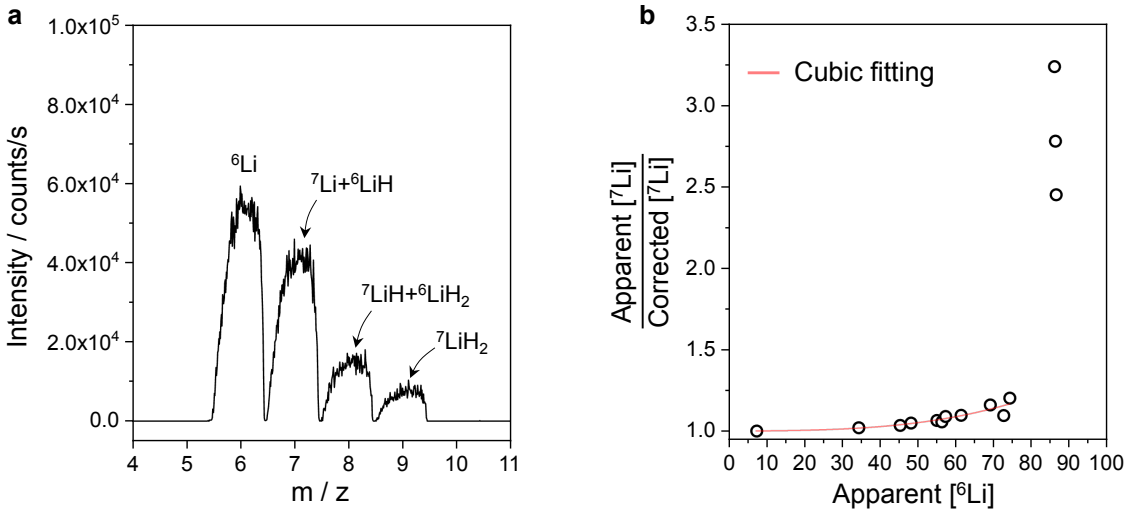


Figure 2.9. LiH correction applied to ion mass spectra. **a**, PFIB-SIMS positive ion mass spectrum (m/z is mass to charge ratio) measured on the surface of a ^{6}Li/^{7}Li isotope heterostructure after 60 minutes from the start of the thermal evaporation of ^{6}Li. A Xe^+ beam with 30 kV acceleration voltage and 4 nA current was directed on a 100 × 100 μm area of the sample. **b**, Correction factor applied to the diffusivity data to take into account the overlap of ^{6}LiH and ^{7}Li signals.

Before fitting, a correction was applied to the $^6Li^+$ and $^7Li^+$ secondary ion intensities to account for the formation of LiH and LiH_2^+ species, resulting from sputtered Li^+ reacting with trace hydrogen that is present even in the ultra-high vacuum conditions of the PFIB chamber. The mass spectrum in Fig. 2.9a displays signals from these hydrogenated species. The ^{7}Li signal overlaps with ^{6}LiH at $m/z = 7$. To address this, the signals for ^{7}LiH + $^6LiH_2$ and $^7LiH_2$ were also collected. Assuming that both lithium isotopes react with the same efficiency with trace hydrogen to form hydrides, it is possible to back-calculate the true amount of ^{7}Li. The ion mass spectrum was collected only on the surface of the samples prior to depth profiling. A correction factor was determined from surface data and is plotted in Fig. 2.9b as a function of the surface ^{6}Li concentration. This correction factor was then applied to the depth profiling SIMS data.

The corrected diffusion profiles were then fitted with the 'thin film' Gaussian solution of Fick's second law:

$$C(x,t) = \frac{N}{\sqrt{\pi D t}} \exp^{\frac{-x^2}{4D_{Li}t}} \tag{2.1}$$

where $C(x,t)$ is the excess lithium isotope concentration in the sample with respect to the background concentration, $N = \int_0^\infty c(x,t)\,dx$ is the total amount of the diffusing

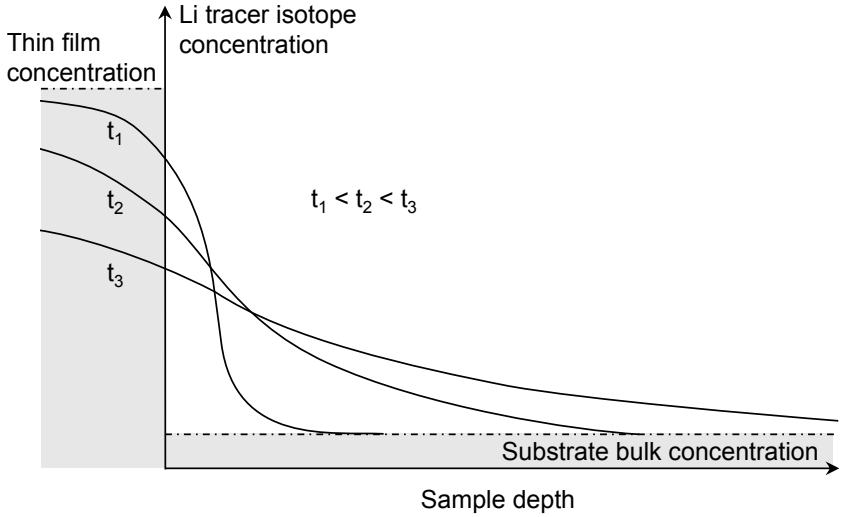


Figure 2.10. Thin film solution to Fick's second law. Qualitative profiles of the tracer isotope concentration across the isotope heterostructure described by the thin film Gaussian solution to Fick's second law. This solution is suitable for the diffusion of a deposited film that is relatively thin compared to the diffusion length into the substrate. Because a fixed amount of tracer isotope is deposited, the surface concentration decreases with time.

species, and D_{Li} is the diffusion coefficient [103]. The diffusion profiles that are well fitted by this solution are qualitatively illustrated in Fig. 2.10. Notably, the surface concentration of the tracer isotope decreases with time. The thin film solution is suitable for isotope diffusion experiments with a fixed amount of diffusing species, i.e. a thin film, where the effects of short circuit diffusion through grain boundaries can be ignored because of the very large grain size in bulk metallic Li and LiMg samples (Fig. 2.6c) [104].

2.5 Assembly and testing of solid-state cells

For the assembly of LLZO-based solid-state cells, the LLZO pellets, sintered according to the procedure in section 2.1, were cut into smaller pieces using a low-speed diamond saw (Buehler IsoMet) to ensure high sample consistency. These smaller pellets were then stored in a glovebox. Before cell assembly, both surfaces of the LLZO pellet were dry polished within the glovebox, initially with SiC paper gradually progressing to p4000 grade and then with a 1 μm diamond lapping film (Kemet), until the surface was visually shiny. Pellets of $\sim$ 1.1 - 1.3 mm thickness were used throughout this study, except for the pellets in chapter 3 which were $\sim$ 0.7 mm thick to minimise

charging effects during XPS analysis. Pellets in chapter 3 were also polished in air before loading them in the XPS chamber, instead of within a glovebox.

The Li/LLZO or LiMg/LLZO interface was promptly assembled right after polishing. The Li or LiMg electrodes were prepared by laminating corresponding pieces with an electric rolling press (MSK-2150-DC) inside a glovebox, reducing their thickness to about 200 μm unless specified otherwhise. The foils were carefully scraped to remove the surface contamination that always form in contact with a glovebox atmosphere, and 2 mm $\varnothing$ electrodes were punched out and gently pressed onto the solid electrolyte after applying 2 mm $\varnothing$ polyimide tape masks. This ensured a constant electrode area during cycling. To evaluate the electrochemical performance of the Li/LLZO interface, two-electrode Li/LLZO/Li cells were assembled. These lithium symmetrical cells are commonly employed in the literature to eliminate the problems related to having a cathode material. All cells were sealed in Mylar pouch bags with Cu current collectors and taken out of the glovebox for testing. The cells were usually left at the testing temperature of 30 °C within a temperature control chamber with an external pressure of 5 MPa for at least 24 hours, to ensure an equilibrium is established at the Li/LLZO interface before electrochemical testing.

As a preliminary test, EIS was often performed to assess the Li/LLZO interfacial impedance. Potentiostatic EIS (PEIS) was conducted on the Li/LLZO/Li cells by applying a sinusoidal voltage perturbation with an amplitude of 10 mV and a frequency range of 3.7 MHz - 1 Hz using an MTZ-35 potentiostat (BioLogic). Galvanostatic EIS (GEIS) was carried out with a BioLogic SP-200 potentiostat by applying a sinusoidal current with a 0.05 mA cm^{-2} amplitude and frequencies ranging from 7 MHz to 500 mHz. The impedance spectra were analysed with the ZView software package. A typical Li/LLZO/Li impedance spectrum is shown in Fig. 2.11a. The spectrum is composed of two semicircles, representing the impedance contributions from the bulk LLZO and LLZO grain boundaries, as well as from the Li/LLZO interface. In Fig. 2.11a, the contribution from the Li/LLZO interface dominates the signal, indicating that the interface exhibits a large resistance to the movement of Li^+ ions.

In fact, as discussed in the introductory chapter, LLZO can react with trace H_2O and CO_2 even during storage in the glovebox to form a surface contamination layer primarily consisting of Li_2CO_3 [86]. Li_2CO_3 is lithio-phobic, resulting in poor wettability of lithium on Li_2CO_3 and, by extension, on LLZO (see Fig. 2.11b) [44]. As a result, the Li/LLZO interfacial impedance of a cell assembled with LLZO is typically very large, ranging from thousands of Ω cm^2 (as in Fig. 2.11a) to tens of

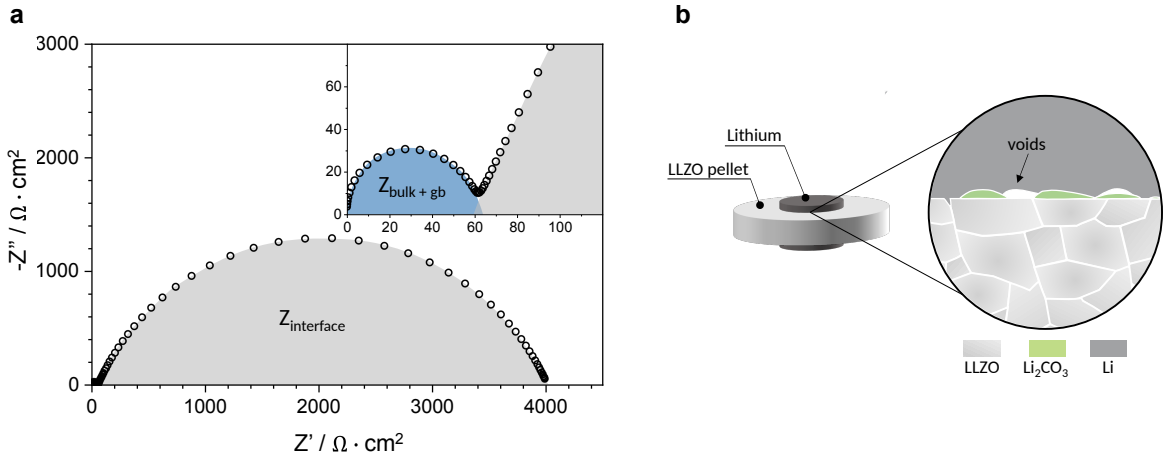


Figure 2.11. Typical EIS of a Li/LLZO/Li cell. **a**, Nyquist plot of a Li/LLZO/Li cell assembled after a simple LLZO polishing step. **b**, Schematic of the assembled Li/LLZO/Li symmetric cell and of the incomplete contact at the Li/LLZO interface.

thousands of Ω cm^2. This detrimentally affects the cell performance, causing uneven lithium plating and stripping due to poor Li/LLZO contact.

A simple polishing step is insufficient for complete removal of the surface Li_2CO_3, as shown in chapter 3. However, LLZO can undergo various surface treatments to effectively remove the surface Li_2CO_3 contamination [105]. In this study, an acid treatment in $HCl_{(aq)}$ was selected to remove the Li_2CO_3 contamination and expose the LLZO surface, significantly reducing the Li/LLZO interfacial impedance to nearly negligible values. During the acid treatment, the polished LLZO was brought outside of the glovebox and immersed in 1M $HCl_{(aq)}$ for 10 seconds. Then, a washing step with ethanol and isopropanol was performed to eliminate any HCl surface residues, and the pellet was dried using an Ar jet. The pellet was immediately (<1 min) loaded back into the glovebox, and Li/LLZO/Li cells were assembled within 5 minutes of the acid treatment. This procedure can decrease the Li/LLZO interfacial resistance by two orders of magnitude, as detailed in chapter 3, which will comprehensively explore the formation and removal of LLZO surface contaminants, analyzing the effectiveness of various surface treatments as well as their limitations.

In some cases, the assembled Li/LLZO/Li cells were subjected to a thermal preconditioning step at 170 °C for 2 hours under a pressure of approximately 2 MPa. This additional step can facilitate the formation of a good interface between the electrodes and the solid electrolyte, further decreasing the Li/LLZO interfacial impedance and creating the optimal starting conditions for cell cycling [39].

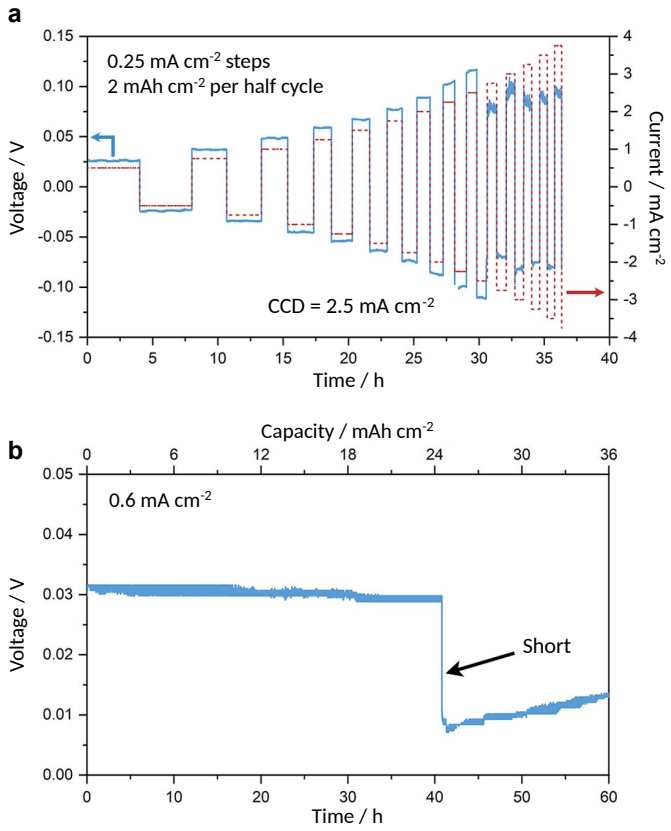


Figure 2.12. Critical current density measurement. **a**, CCD tests of a Li/argyrodite/Li cell. The initial current density is 0.5 mA cm^{-2}, and the current density is increased in 0.25 mA cm^{-2} steps after each cycle, with a half-cycle capacity of 2 mAh cm^{-2}. The CCD for this cell is 2.5 mA cm^{-2}. **b**, Continuous plating at one interface in a Li/argyrodite/Li cell at 0.6 mA cm^{-2} leads to short circuiting after plating over 24 mAh cm^{-2} ($\sim$ 120 μm of lithium plated), showing that the shuttled capacity has a significant impact on the CCD value. Reproduced with permission from [106].

Following the initial EIS characterization, galvanostatic plating/stripping experiments were conducted with either a VMP3 or SP-200 potentiostat (BioLogic). This involved applying a constant current to the Li/LLZO/Li cell and recording the voltage response. This is a simplified version of the real-world battery operation. In the literature, Li/LLZO/Li cells are often tested using critical current density (CCD) measurements, which consists in cycling the cell with a current density that increases in a step-wise manner after each plate/strip cycle. The 'critical' current density is the value at which lithium dendrites penetrate through the solid electrolyte and short-circuit the cell. This CCD measurement represents a straightforward method to assess the performance of the Li/LLZO interface, especially when comparing the CCD values of different cells [107]. However, there is hardly any agreement on the electrochem-

ical protocol for the CCD measurement, especially on the amount of capacity that is plated/stripped at each half-cycle. Since this parameter can significantly impact the formation of voids during stripping, it also influences the obtained CCD values. Furthermore, it has been shown that partial dendrite formation can occur at current rates much lower than the measured CCD, when the amount of plated lithium is too small for the dendrites to reach the opposite side of the cell [106]. These partial dendrites can be stripped during the subsequent half-cycle, leading to the overestimation of the CCD as displayed in Fig. 2.12. Therefore, the voltage profile of CCD measurements should be carefully inspected for partial short-circuits, and CCD values are to be considered prone to error. Some CCD measurements are carried out in chapter 3 to evaluate the effect of LLZO surface treatments on the overall performance of solid-state cells. In this instance, the current density is increased in 0.05 mA cm^{-2} steps after each cycle and the half-cycle capacity is 0.5 mAh cm^{-2}, which is deemed sufficient to create short-circuiting dendrites in LLZO [108].

All the cycling procedures in this thesis were typically carried out at 30 °C within a temperature control chamber and often with a certain external pressure. The specific value of the external pressure varied depending on a case-by-case basis, details of which will be outlined in each chapter. After cycling, the cells were carefully disassembled and then transferred to the designated characterization tool. By manipulating cycling parameters such as current density, temperature, pressure, and more, and by correlating electrochemical results with post-cycling characterization techniques, it was possible to comprehensively assess the cell performance and gain insight into the processes unfolding at the Li/LLZO interface.

2.6 Serial sectioning of LLZO for three-dimensional visualization

As discussed in section 2.4, the versatility of the PFIB instrument and its advantages over more traditional FIBs allow the exploration of novel imaging procedures. Notably, the utilization of the heavier Xe^+ ions leads to an increased material sputtering rate, which facilitates performing large area cross-sectioning while maintaining the nm resolution of an SEM. This capability has opened up new opportunities. For instance, an alternating procedure of PFIB slicing and SEM imaging can be applied to collect a stack of 2D images which can be aligned in sequence to build up a 3D image of the specimen. This technique is described in the literature as serial sectioning or 'slice-and-view'. The serial sectioning routine can be carried out without tilting

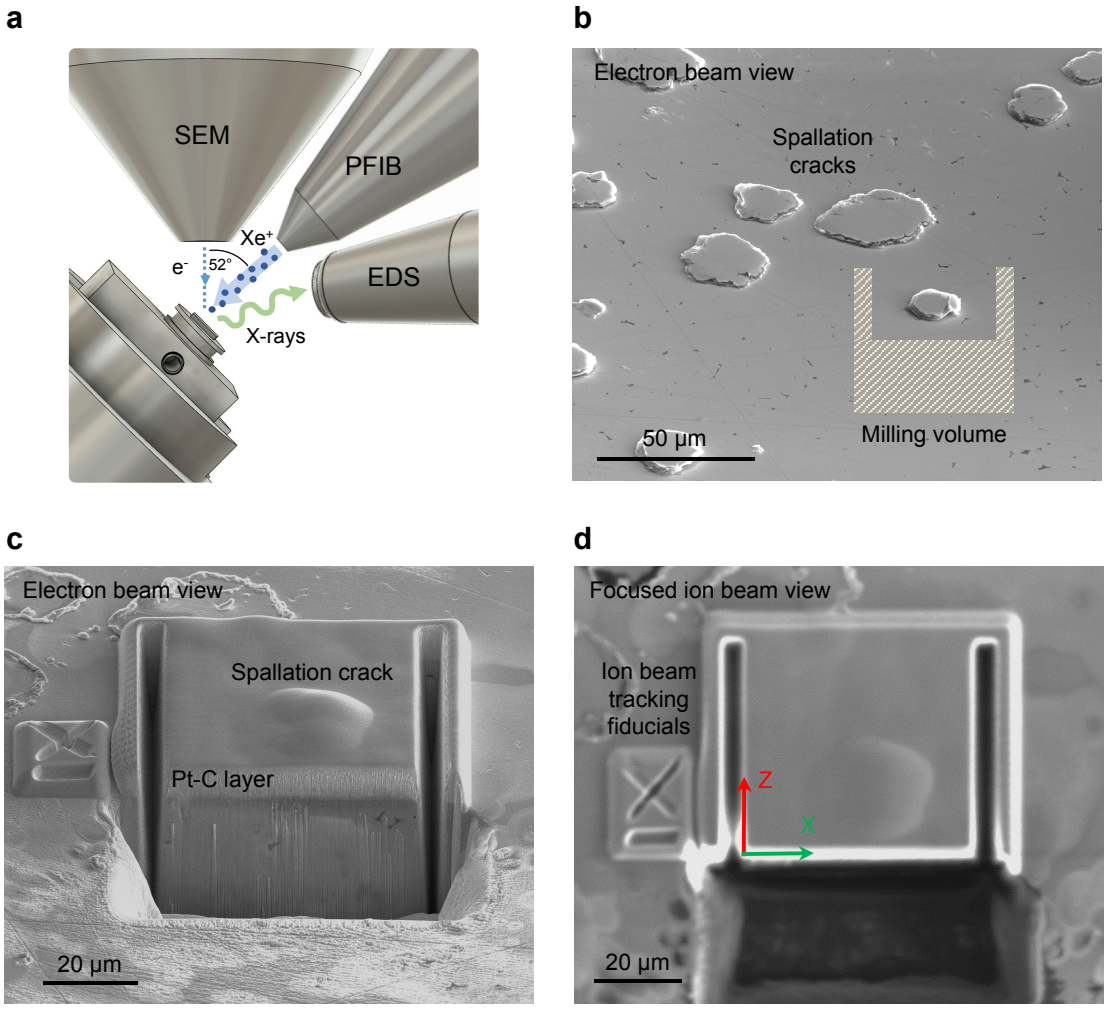


Figure 2.13. PFIB setup for automated serial sectioning. **a**, PFIB setup with the sample surface tilted at 52° with respect to the electron beam. The sample stage can be cooled with liquid nitrogen to minimise beam damage. **b**, SEM surface image of the LLZO surface after plating. The lithium electrode has been peeled off. **c**, Electron beam view of the volume of interest after milling. **d**, PFIB view of the volume of interest. The volume is prepared milling the regions around it with the Xe^+ beam, decreasing the milling current in a stepwise manner to obtain a smooth cross-section.

and repositioning the stage, so that a precise control of the slicing distance down to the 10 nm range can be achieved [109]. Sample drift and instabilities during serial sectioning can be corrected with a high degree of automation, therefore achieving a high-throughput, high-resolution image acquisition process [110].

The same PFIB instrument employed in the experiments for the measurement of lithium diffusivity (Helios G4 PFIB CXe DualBeam, Thermo Scientific) was also utilized for imaging LLZO samples. In chapter 4, serial sectioning of LLZO was carried out to obtain a three-dimensional view of the surface spallation cracks and to explore the morphology of sub-surface features at the nanoscale. The PFIB and EDS setup for serial sectioning is illustrated in Fig. 2.13. After cycling of the LLZO cells, both electrodes were removed to inspect the LLZO surface. The sample was then transferred to the PFIB in an argon-filled vessel (Gatan iLoad). The volume of interest was selected and prepared for serial sectioning as follows. Firstly, a Pt-C layer of approximately 5 μm was deposited with a gas injection system to minimize Xe^+ beam damage. Secondly, a front trench and side trenches were milled to define the block for serial sectioning. Fiducial markers were then milled next to the volume of interest (Fig. 2.13b and c). Finally, a 30 kV, 15 nA Xe^+ beam was used to mill the volume of interest, while a 10 kV, 0.2 - 0.8 nA electron beam was used for secondary electron imaging. Moreover, EDS analysis of the cross-section was conducted to identify the cracks and pores with an above-average magnesium signal, whose significance is explained in chapter 4. The thickness of each PFIB 'slice' was 100 nm. This method allowed the capture of microstructural features at the tens of nanometres to the tens of microns scale.

The 2D secondary electron images were subsequently processed using Avizo 3D (version 2021.2, ThermoFisher Scientific). The procedure is summarized in Fig. 2.14. First, the y-dimension of the SEM images is corrected to account for the 52° tilt between the electron beam and focused ion beam. Then the images are re-aligned one to each other, as some drift can occur during the slicing procedure. The images are processed by applying a background subtraction to remove brightness variation due to shadowing effects. A Fourier transform filter is sometimes applied to remove the vertical curtaining lines, which are an undesirable surface artefact of FIB milling, and a smoothing and noise reduction filter (non-local means filter) is applied to enhance the image quality. The images are then segmented with a semi-automated process to distinguish pores and cracks from bulk LLZO material. Specifically, a thresholding method is first applied, followed by a watershed algorithm or manual segmentation were necessary. Finally, the aligned 2D stack are transformed into a 3D

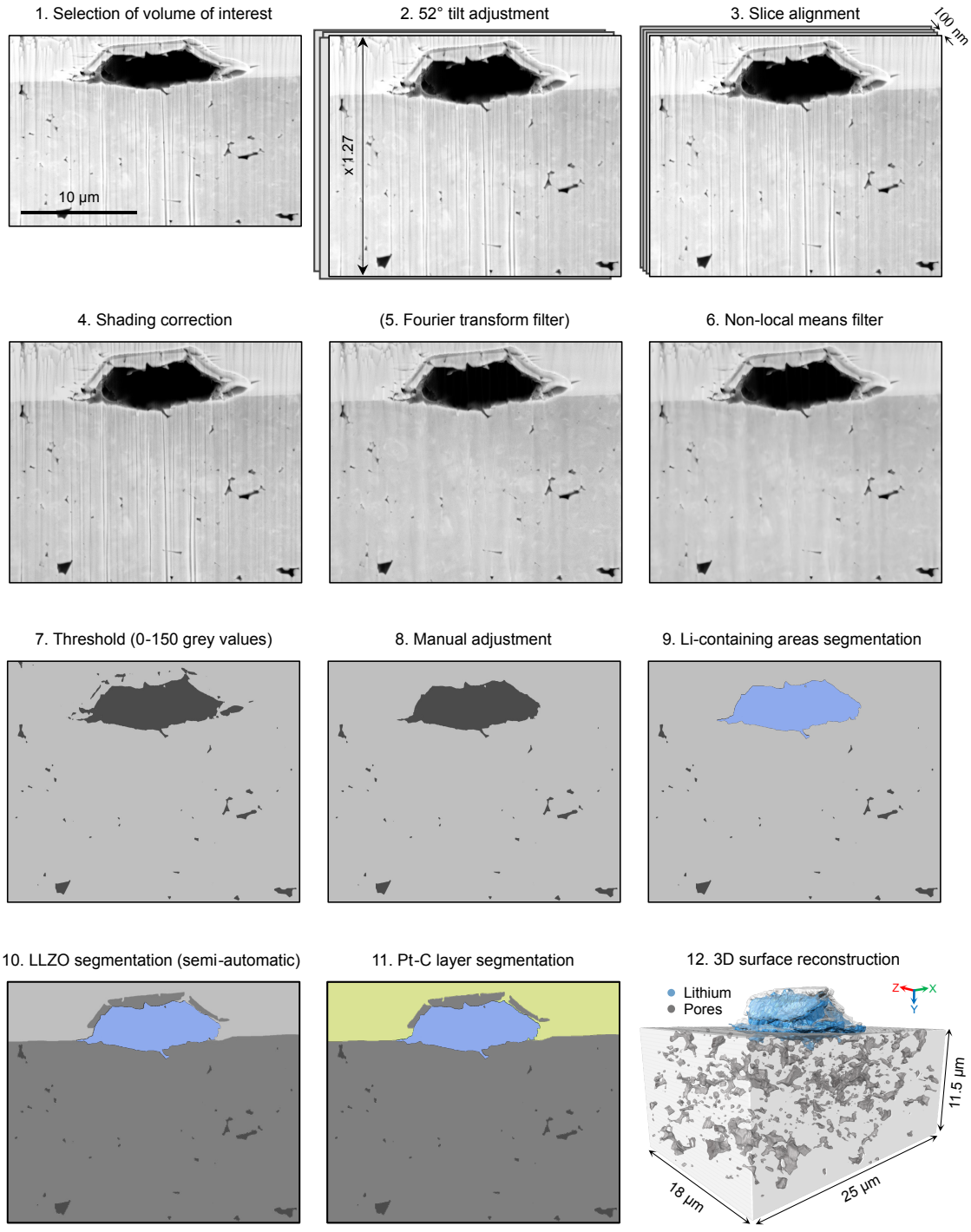


Figure 2.14. Segmentation procedure for 3D volume reconstruction. The stack of 2D SEM cross-sectional images are first aligned, then they undergo a series of processing steps to enhance the image quality. Subsequently, a segmentation procedure is carried out based on a thresholding method to distinguish pores, lithium metal, and LLZO regions. Finally, a 3D view can be reconstructed.

reconstruction, which helps visualize the porosity and lithium metal networks in the solid electrolyte.

Chapter 3

The Removal and Reoccurrence of LLZO Surface Contaminants Under Glovebox Conditions

The reactivity of LLZO surfaces to form Li_2CO_3 and LiOH when exposed to trace amounts of H_2O and CO_2 is a main hurdle towards the commercialization of LLZO-based solid-state battery. Various treatments, including annealing LLZO within a glovebox and acid etching, have been developed in recent years and aim to remove the surface contaminants. However, a comprehensive understanding of the evolving LLZO surface chemistry during and after these treatments is lacking. In this chapter, glovebox H_2O and CO_2 conditions are recreated in a near ambient pressure X-ray photoelectron spectroscopy (NAP-XPS) chamber to analyse the LLZO surface under realistic conditions. These experiments were carried out at the B07-C beamline at the Diamond Light Source synchrotron facility. The NAP-XPS results show that annealing LLZO at 600 °C under glovebox atmosphere indeed effectively eliminates surface contaminants, but a significant level of contamination reappears upon cooling down. In contrast, $HCl_{(aq)}$ acid etching demonstrates superior contamination removal and stable post-treatment surface chemistry. To avoid air exposure during the acid treatment, a H_2O-free HCl solution in diethyl ether is used directly within the glovebox. This novel acid etching strategy delivers the lowest Li/LLZO interfacial resistance.

3.1 Introduction

Initial studies on garnet-type solid electrolytes reported their chemical stability when exposed with ambient air, a characteristic that could significantly benefit manufacturing processes and has contributed to the prominence of these solid electrolytes [76].

However, recent research has revealed that several lithium garnet oxides, including LLZO, undergo a chemical reaction with H_2O and CO_2 in ambient air, leading to the formation of a surface contamination layer primarily comprising Li_2CO_3 and LiOH [85, 86]. This reaction can occur through two distinct pathways. The first pathway involves an initial reaction with moisture, where H^+ protons infiltrate the LLZO lattice and substitute the Li^+ in the tetrahedral sites to form LiOH. Subsequently, LiOH absorbs CO_2 to form Li_2CO_3.

$$Li_7La_3Zr_2O_{12} + xH_2O \rightarrow Li_{7-x}H_xLa_3Zr_2O_{12} + xLiOH \tag{3.1}$$

$$2LiOH + CO_2 \rightarrow Li_2CO_3 + H_2O \tag{3.2}$$

The second pathway involves direct reaction with CO_2, which can be expressed as:

$$Li_7La_3Zr_2O_{12} + xCO_2 \rightarrow Li_{7-2x}La_3Zr_2O_{12-x} + xLi_2CO_3 \tag{3.3}$$

Although the reaction mechanism is still a topic of debate, most studies tend to support a two-step mechanism with water having a catalytic effect on the reaction rate [105, 111, 112].

Leng et al. have revealed that an untreated LLZO surface, when exposed to air for 24 hours, develops a layer of contamination that is 120-160 nm thick, visible on the surface secondary electron microscopy (SEM) images in Fig. 3.1a [113]. In their SEM study, a change in surface morphology is visible after just 10 minutes of air exposure. In other reports, Sharafi et al. have conducted an XPS depth profiling of an LLZO sample after polishing in air and brief storage in a glovebox. They have proposed a multilayer model of surface contaminants, with inner layers richer in LiOH, outer surface layers with a larger Li_2CO_3 content, and absorbed hydrocarbon contamination on the topmost surface. However in this model, illustrated in Fig. 3.1b, the Li_2CO_3, LiOH and LLZO components are simultaneously present in most of the contamination layers. These studies demonstrate that LLZO surface reacts quickly during processing and preparation in air. The reaction follows a diffusion-limited process, so as the contamination layer thickens the reaction rate decreases, and eventually may come to a halt [114].

Surprisingly, it has come to light that even in the supposedly inert atmosphere of an argon-filled glovebox – an environment commonly used for the fabrication and storage of LLZO cells in research settings – the formation of surface LiOH and Li_2CO_3 is still a concern. Despite the stringent efforts to maintain ultra-low moisture levels

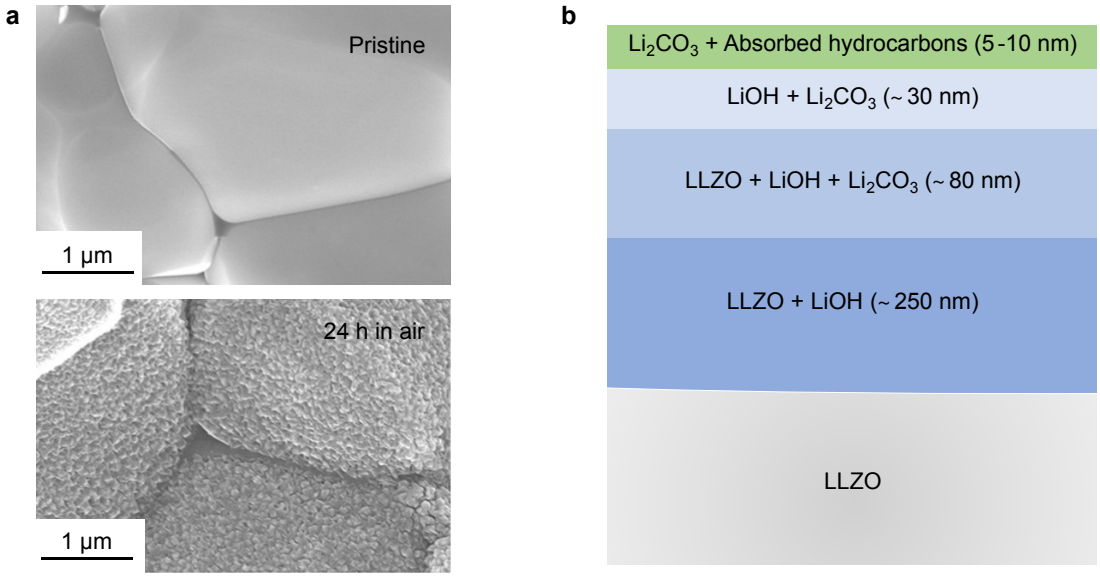


Figure 3.1. LLZO surface after air exposure. **a**, SEM images of a freshly cleaved LLZO surface (top) and after 24 hours storage in ambient air (bottom). Reproduced with permission from [113]. **b**, Proposed schematic of the surface contamination of an LLZO sample after polishing in air and brief storage in a glovebox. The layer thicknesses are estimated by XPS depth profiling of the sample. Reproduced with permission from [112].

(typically < 0.1 ppm of H_2O) in gloveboxes, background trace levels of moisture can creep up due to routine glovebox usage. Additionally, the concentration of CO_2 in gloveboxes is generally not actively controlled or filtered. A non-dispersive infrared CO_2 sensor (Analox) was used to assess CO_2 levels across various gloveboxes used for this work, finding CO_2 concentrations ranging from 1 to 7 ppm. Although these H_2O and CO_2 levels are seemingly negligible compared to the ones in ambient atmosphere (approximately 420 ppm of CO_2 and 10000 ppm of H_2O on average), they are nevertheless adequate to instigate the formation of a contamination layer on the LLZO surface within a remarkably short span. For instance, Yamada et al. found that a clean LLZO surface can accumulate a layer of contamination measuring 4 - 6 nm within as little as 30 minutes of exposure to a glovebox environment [115]. Although glovebox storage does mitigate the reaction kinetics to some extent, it is evident that the contamination process persists, albeit at a somewhat reduced rate compared to open-air exposure.

The presence of Li_2CO_3 and LiOH contaminants on the surface of LLZO poses a substantial challenge. To begin, these contaminants have lower ionic conductivity

compared to LLZO, thereby impeding ion transport across the electrode/LLZO interface [116]. Furthermore, in the context of solid-state cells, LLZO is commonly paired with a lithium metal anode. The contaminants exhibit lithiophobic characteristics, leading to incomplete contact between the LLZO and the lithium metal electrode [44]. Both the low ionic conductivity and lithiophobicity of the contamination layer result in a large Li/LLZO interfacial resistance R_{int}. As a direct consequence, during cycling the local current density at the Li/LLZO interface becomes much larger than the nominal applied value. This localized current density disparity can result in adverse effects, such as cell polarization and formation of lithium dendrites through the solid electrolyte [117], inevitably compromising the overall battery performance. Later in section 3.5 of this chapter, as well as in chapter 5, it will be shown that Li/LLZO/Li cells assembled without any prior LLZO surface treatment are prone to lithium dendrite failure at much smaller nominal current densities compared to cells assembled with surface treated LLZO.

Therefore, the efficient removal of surface contaminants is essential to achieve high-performance LLZO-based solid-state batteries. Several surface treatment methods, including mechanical polishing, annealing, and acid etching, have proven successful in removing the contamination layer, each exhibiting varying levels of effectiveness [105]. A mechanical polishing step is often performed to obtain a planar solid electrolyte surface before cell assembly. While this step can reduce the surface contaminants, it cannot completely eliminate them. This could be due to the presence of contaminants along LLZO grain boundaries, as observed through SEM analysis [85], which may not be removed by a simple polishing step. Therefore, polishing is commonly followed by annealing or acid treatment.

Annealing within the controlled argon atmosphere of a glovebox has been widely adopted in the literature. XPS studies have suggested that equation 3.1 can be reversed and LiOH is removed by heating LLZO up to 500 °C. Higher temperatures appear to be necessary for Li_2CO_3, which decomposes into Li_2O and CO_2 mostly around and above 700 °C [44, 113, 118]. The precise annealing temperature required for complete contamination removal depends on various LLZO characteristics, for instance doping elements and grain size, as well as on the annealing environment. Under ultra-high vacuum (UHV) conditions, where materials volatilize at lower temperatures, annealing at 500 - 600 °C can almost completely remove the surface contaminants [80, 119, 120]. However, to obtain a low interfacial resistance between lithium metal and LLZO, annealing LLZO at 300 - 400 °C in the glovebox atmosphere can be sufficient, as reported in Fig. 3.2a. The improved interfacial contact can also be

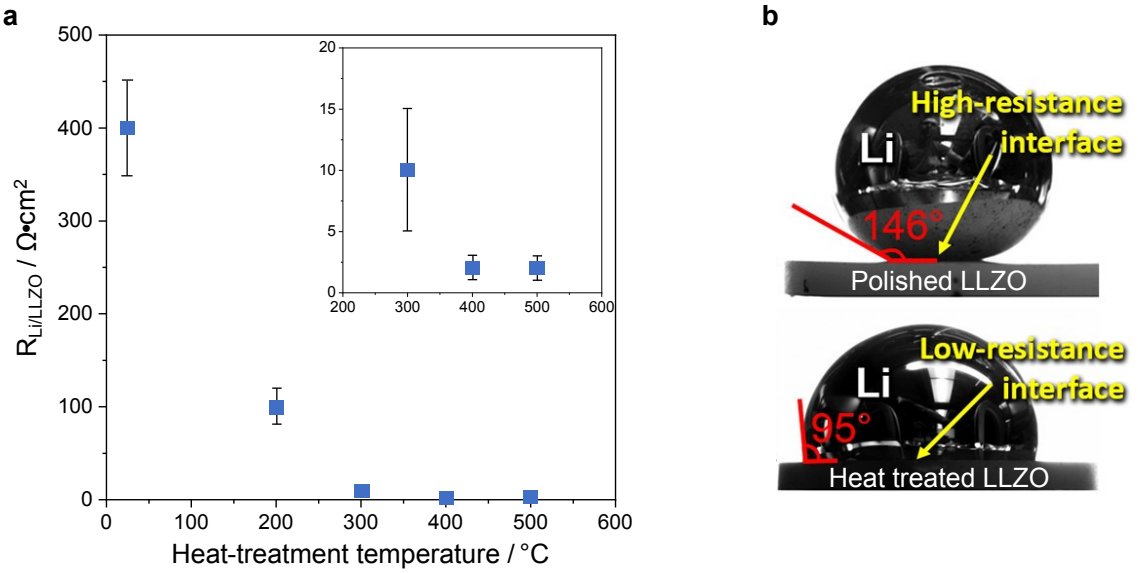


Figure 3.2. Removing lithiophobic surface contaminants via annealing. a, Li/LLZO interfacial resistance versus the LLZO annealing temperature. The EIS was performed on Li/LLZO/Li cells after an additional thermal preconditioning step at 175 °C to soften lithium metal. Error bars represent standard deviations for 3 cells. **b**, Contact angle measurements of molten metallic lithium on an LLZO pellet after polishing in air (top) and after annealing at 500 °C in a glovebox atmosphere. Reproduced with permission from [44].

quantified by contact angle measurements with molten lithium as in Fig. 3.2b, which help visualize the conversion of LLZO surface from lithiophobic to lithiophilic [44].

However, a significant drawback of the heat treatment lies in the potential evaporation of lithium, which can trigger the formation of pyrochlores such as $La_2Zr_2O_7$ on the pellet surface, which possess a lower ionic conductivity [120, 121]. An alternative to annealing, acid etching is particularly appealing due to its simplicity and efficiency [122, 123, 124]. A rapid immersion in a weak aqueous solution such as $HCl_{(aq)}$ can successfully decompose Li_2CO_3 according to:

$$Li_2CO_3 + 2HCl \rightarrow 2LiCl + CO_2 + H_2O \tag{3.4}$$

Following annealing or acid etching, however, there can be a resurgence of contamination before the Li/LLZO interface is assembled. This can occur during the short storing time in the glovebox before cell assembly [80, 115], but also during cooling from the annealing temperature back to room temperature or during the brief contact to air after the acid treatment in $HCl(aq)$. During these transitions, LLZO can be exposed to H_2O and CO_2 leading to unintended surface reactions. Consequently,

even after these treatments, a residual interfacial resistance persists at the Li/LLZO interface.

Adding complexity to the situation, LLZO is often transferred from the glovebox to the characterization instruments like XPS using an O-ring sealed transfer vessel, without independent pumping. Unfortunately, this vessel may allow air leakage even over a short time [125]. As a result, any LLZO surface analyzed after such a transfer is likely to exhibit additional surface LiOH and Li_2CO_3, formed during the transfer process. This intricacy clouds the accurate determination of the origin of these surface contaminants – whether they originated after the surface treatment within the glovebox or during the transfer process. This highlights the necessity for in-situ characterization techniques that can provide a more precise understanding of LLZO surface modifications.

This chapter focuses on the investigation and comparison of annealing and acid etching treatments. To accurately simulate real-world conditions, in-situ NAP-XPS was employed to analyze the LLZO surface chemistry under glovebox-like environments, dosing H_2O vapour and CO_2 gas into the analysis chamber. Heating LLZO to 600 °C under glovebox-like H_2O and CO_2 atmosphere is effective in removing the surface contaminants but, upon cooling back to room temperature, LiOH and Li_2CO_3 promptly reappear as the clean LLZO surface quickly reacts with H_2O and CO_2 at 300 - 400 °C. The final amount of contamination on the LLZO is nonetheless lower than after a simple polishing step in air. In contrast, a rapid acid etching with $HCl_{(aq)}$ can prove more effective in removing the surface contaminants if the LLZO pellet is quickly brought into the glovebox environment after the treatment. Moreover, the surface chemistry remains stable long enough to assemble the Li/LLZO interface. To avoid the short exposure to air after the acid treatment, a novel acid treatment with a solution of HCl in diethyl ether ($HCl_{(Et_2O)}$) was further developed. Being H_2O-free, this treatment can be conducted directly inside a glovebox. The interfacial resistance between lithium and LLZO, which correlates with the amount of lithiophobic Li_2CO_3 and LiOH on the LLZO surface, is at its lowest after the new $HCl_{(Et_2O)}$ treatment.

3.2 Annealing in a glovebox environment

Annealing LLZO within the controlled atmosphere of a glovebox has been widely acknowledged as an effective strategy for the removal of surface Li_2CO_3 and LiOH, leading to a significant reduction of the Li/LLZO interfacial resistance. Nevertheless, this approach is prone to the reformation of Li_2CO_3 and LiOH during the cooling

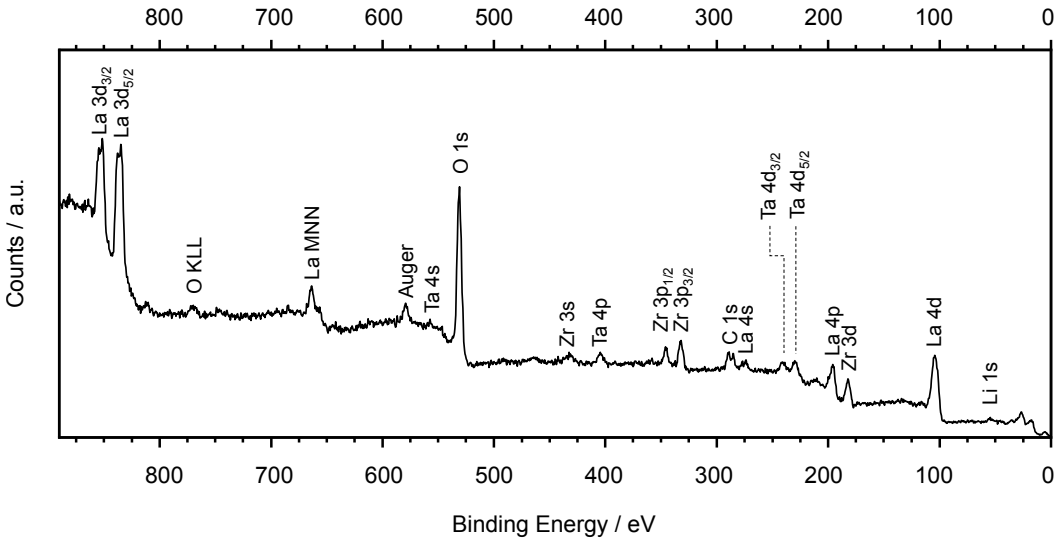


Figure 3.3. XPS survey spectrum of an LLZO pellet polished in air. La, Li, Zr, O, and Ta signals from the LLZO pellet surface are present. No unfamiliar contamination is observed. The spectrum was collected with a 2500 eV incident X-ray energy.

phase, as elucidated in this section. The data presented in this section were collected with assistance from Joshua Gibson, Jack Swallow, and James Tufnail from the University of Oxford.

An LLZO pellet was polished in air following the procedure in section 2.5 and promptly introduced into the NAP-XPS chamber, which was evacuated within 60 seconds. The pellets used in this chapter have been sintered at 1200 °C and are of the highest density (see section 2.1). The O 1s and C 1s signals were collected to study the evolution of surface chemistry throughout the annealing treatment. X-rays with an incident energy of 2500 eV (here referred to as hard X-rays for simplicity) were employed to probe the deeper surface layers with a probing depth of approximately 15 nm. During cooling, softer X-rays were also used, tuning the incident energy to achieve a kinetic energy of the ejected photoelectrons of $\sim$ 315 eV, thereby probing approximately the topmost 3 nm of the LLZO surface. The initial O 1s and C 1s spectra under UHV conditions ($\sim$ 3e-8 mbar) at 30 °C are reported at the bottom of Fig. 3.4a and b for the hard and soft X-rays respectively.

Let us first delve into the hard X-ray data. A survey spectrum is reported in Fig. 3.3. Signals from La, Li, Zr, O, and Ta, the main elements of LLZO, are observed, and no unfamiliar contamination could be detected. Zooming in, the O 1s spectrum in Fig. 3.4a exhibits a large peak (B.E. $\sim$ 531.4 eV) with a smaller low-energy shoulder attributed to LLZO lattice oxygen (B.E. $\sim$ 528.9 eV). This shape correlates very well

with previously published data where, in many cases, the high-energy peak has been fitted with both Li_2CO_3 and LiOH with a peak separation of approximately 0.9 eV [80, 112]. In our case at 30 °C, the LiOH peak has zero intensity, suggesting that after polishing in air the primary surface impurity is Li_2CO_3. The C 1s spectrum was fitted with -CO_3, C-OH, and adventitious C-C/C-H peaks.

Following the preliminary characterization in UHV, a glovebox-like environment was reproduced in the NAP-XPS chamber by introducing small quantities of CO_2 gas and H_2O vapour. CO_2 was dosed in the pumped NAP-XPS chamber through a mass flow controller at 0.22 sccm, corresponding to a constant chamber pressure of 4e-3 mbar. H_2O vapour was then immediately introduced through a manually controlled leak valve connected to a quartz tube containing water, until a total chamber pressure of 5e-3 mbar was obtained. Both the CO_2 and H_2O lines were continuously flushed and evacuated before opening to the NAP-XPS chamber, to minimize the chance of introducing external air-borne contamination in the chamber. These pressures correspond to 4 ppm of CO_2 and 1 ppm of H_2O, which simulate the values normally found in an operating glovebox, where the LLZO annealing treatment is usually carried out.

The LLZO pellet was then heated to 600 °C at a rate of 10 °C/min. The temperature was monitored with a thermocouple in contact with the sample holder surface. The data collection took $\sim$ 3 min for O 1s and 4 min for C 1s, therefore the temperature reported for each spectrum in Fig. 3.4 is an average. During this heating step, the O 1s spectrum shows an increase in the LLZO signal, while the surface Li_2CO_3 gradually decomposes with temperature. The signal evolves to some extent also at lower temperatures, although the primary temperature window for Li_2CO_3 decomposition is in the range of 400 - 500 °C. This is validated by the C 1s signal, where the -CO_3 peak essentially disappears around those temperatures. The C-C/C-H peak also decreases in intensity alongside the -CO_3 signal, meaning that adventitious carbon species are also leaving the LLZO surface. Above 400 °C, a small LiOH peak becomes evident at $\sim$ 530.5 eV within the O 1s spectrum. It is important to emphasize the inherent dynamic equilibrium between the decomposition and reformation processes of surface contaminants. The direction and kinetics of reactions 3.1 and 3.2 are dependent not only on temperature but also on the availability of reactants. As Li_2CO_3 starts to display considerable decomposition above 400 °C, the pristine LLZO surface comes into contact with the H_2O and CO_2 introduced in the NAP-XPS chamber. Under these specific conditions, LLZO appears to react with H_2O resulting in the formation of a minor quantity of LiOH. However, this LiOH does not seem to react

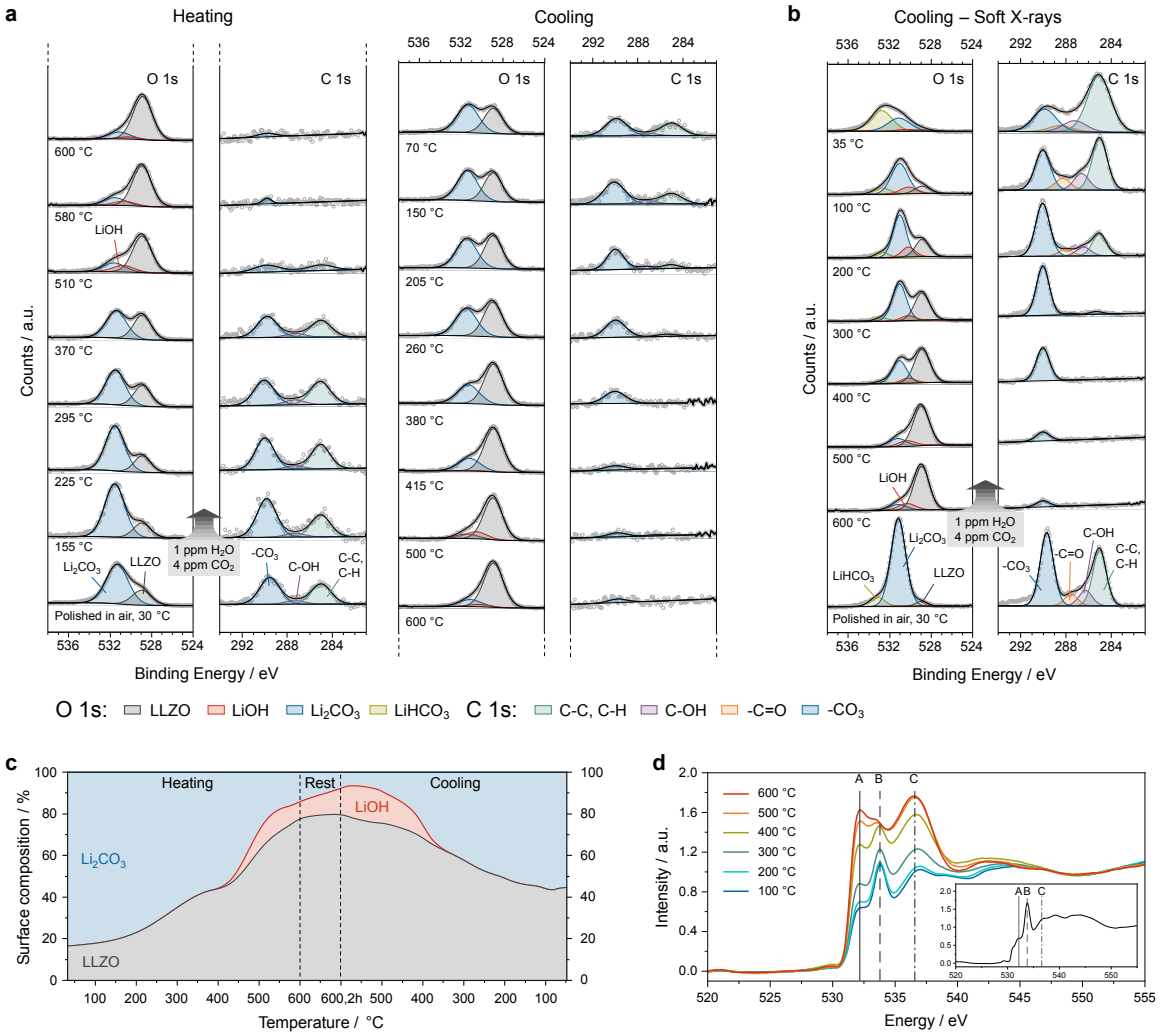


Figure 3.4. Evolution of LLZO surface chemistry during annealing. **a**, Hard XPS O 1s and C 1s spectra collected from an LLZO pellet during annealing treatment. The bottom spectra on the left correspond to the polished pellet analysed under UHV conditions and at room temperature. The subsequent spectra are collected while heating and cooling the sample in a glovebox-like atmosphere (1 ppm of H_2O, 4 ppm of CO_2). The Li_2CO_3 signal decreases while heating and grows back during cooling. **b**, Soft XPS O 1s and C 1s spectra. The bottom spectra correspond to the surface signals after polishing. Above them, signals collected every 100 °C upon cooling the LLZO pellet back to room temperature. The Li_2CO_3 peak gradually increases and overwhelms the LLZO and LiOH signals, eventually merging with a growing $LiHCO_3$ signal at lower temperatures. **c**, Trend of the relative concentration of surface contaminants with temperature, obtained from the hard X-ray XPS signals, coming from the top $\sim$ 15 nm of the surface. **d**, O K-edge XANES spectra for an LLZO pellet during cooling from 600 °C in a glovebox-like atmosphere. Key spectral features are highlighted as A (solid line), B (dashed line) and C (dotted-dashed line). Inset: spectra for an as-loaded LLZO pellet, with the same features highlighted.

with CO_2 to increase the amount of surface Li_2CO_3, which instead keeps decreasing. At 600 °C, the O 1s spectrum shows a prevalent LLZO peak with negligible Li_2CO_3 and LiOH signals, whereas the C 1s signal assumes a mostly flat profile. Annealing was stopped at 600 °C, as the XPS signals were quite stable. The evolution of LLZO, Li_2CO_3, and LiOH signals can be visualised in Fig. 3.4c. Another LLZO sample underwent heating up to 750 °C, yet beyond 600 °C we observed only a small increase in the LLZO O 1s peak from 79 % to 85 %, and the shape of the spectrum remains the same (Fig. 3.5). Therefore, for this study, we consider annealing at 600 °C as sufficient to achieve a clean LLZO surface and prevent excessive vaporisation of lithium metal form the near-surface regions, as suggested in previous reports [120].

The sample was left at 600 °C for 2 hours, after which it gradually cooled back to room temperature. As the temperature decreased from 500 to 350 °C, the intensity of the LiOH signal diminishes while the Li_2CO_3 signal grows back. This could be attributed to the reaction between LiOH and CO_2 as in equation 3.1. The Li_2CO_3 signal gradually intensifies as the temperature decreases to 200 °C, below which all signals are quite stable. The -CO_3 peak in the C 1s signal also re-emerges, as well as the C-C/C-H peak. The latter resurgence may be attributed to the re-deposition of carbonaceous contaminants from the NAP-XPS chamber, a phenomenon that would possibly be even more pronounced in a real glovebox environment.

During cooling, soft X-ray spectra were also collected every 100 °C interval to elucidate the evolution of the topmost 3 nm of the LLZO pellet (Fig. 3.4b). The data obtained from soft X-rays largely corroborate the findings obtained from hard X-rays. At 600 °C, the LLZO surface features only minor LiOH and Li_2CO_3 peaks. Upon cooling, the LiOH signal remains relatively small while the Li_2CO_3 peak grows strongly in intensity. Around 200 °C the LLZO and LiOH peaks begin to attenuate, meaning that Li_2CO_3 now covers most of the topmost surface. Below 200 °C, an additional peak emerges in the O 1s spectrum at higher binding energy of $\sim$ 532.8 eV. This peak was assigned to the hydrated form of Li_2CO_3, lithium bicarbonate ($LiHCO_3$), which can form according to:

$$Li_2CO_3 + CO_2 + H_2O \rightarrow 2LiHCO_3 \tag{3.5}$$

Xu et al. showed that this reaction occurs below 85 °C [126]. It is possible that during cooling the topmost LLZO surface is at a slightly colder temperature than that of the bulk, justifying the appearance of $LiHCO_3$ peak at higher sample bulk temperatures. The monohydrated form of LiOH might also exist as $LiOH{\cdot}H_2O$ [113, 127, 128, 129], but an additional peak was not used in the model. The $LiHCO_3$ peak was also visible

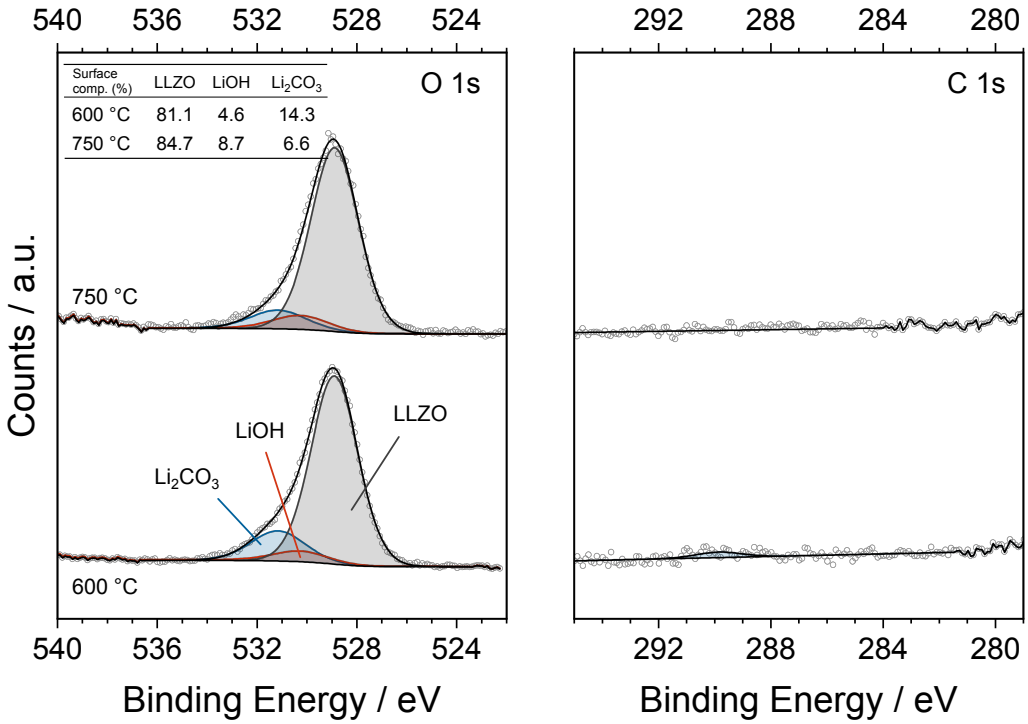


Figure 3.5. Comparison between annealing at 600 °C and 750 °C. Hard XPS O 1s and C 1s spectra of LLZO annealed up to 600 °C or 750 °C. Annealing to 750 °C slightly decreases the Li_2CO_3 surface contamination.

in the spectrum after polishing LLZO in air, reported at the bottom of Fig. 3.5b, which shows a predominant Li_2CO_3 peak. After cooling, at temperatures below 100 °C, $LiHCO_3$ and Li_2CO_3 completely cover the LLZO surface. Pristine LLZO is still present beneath the topmost surface as shown by the hard X-ray data. The C 1s soft X-ray spectrum similarly grows back during cooling, and can be fitted by a four-peak model, including a -C=O peak.

X-ray absorption near-edge spectroscopy (XANES) data were also collected during cooling from 600 °C and are reported in Fig. 3.5d. These were collected at 100 °C increments in-step with the XPS measurements shown in the other panels of Fig. 3.5. Surface sensitive total electron yield mode was utilized, giving a probing depth of < 10 nm. The three significant peaks within the O K-edge spectra are assigned as LLZO at 532.2 eV (A, solid line), Li_2CO_3 at 533.8 eV (B, dashed line), and an additional peak at energies of 535.8 eV (C, dotted-dashed line) [130, 131]. Given the changing growth of LiOH in the XPS data, we interpret the peak at C to correspond to LiOH within this volume-averaged probe of the sample. At 600 °C, the intensity of the LLZO (A) and LiOH (C) peaks are increased relative to the Li_2CO_3 (B). During cooling, the relative intensity of Li_2CO_3 (B) increases at the expense of LLZO (A). The LiOH (C)

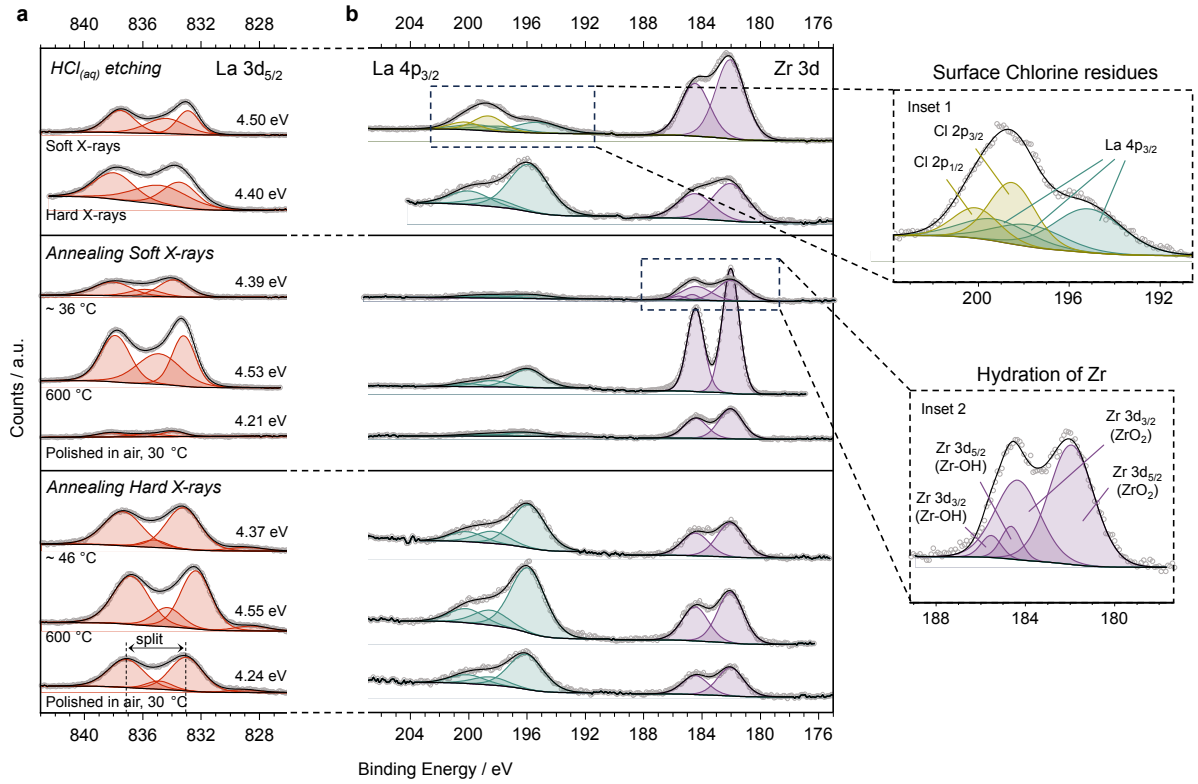


Figure 3.6. Lanthanum and zirconium chemical environments. **a**, La $3d_{5/2}$ XPS spectra collected from LLZO pellets at different stages of the surface treatments. From bottom to top, annealing hard X-ray spectra, annealing soft X-ray spectra, and $HCl_{(aq)}$ etching spectra. The values of the La $3d_{5/2}$ multiplet energy splitting are reported above each spectrum on the right. **b**, La $4p_{3/2}$ and Zr 3d XPS spectra. The soft X-ray spectrum collected after $HCl_{(aq)}$ etching contains a contribution from Cl 2p, shown in detail in inset 1. Inset 2 reports the change in soft X-ray Zr 3d signal after annealing. The change can be explained by a slight hydration of Zr.

peak also reduces, which may be explained as this component converting to Li_2CO_3 as discussed above for the XPS results. The Li_2CO_3 (B) peak shifts by + 0.1 eV at around 400 °C, while the LiOH peak (C) shifts by about + 0.2 eV. The inset in Fig. 3.5d shows the as-loaded sample, acting as a pristine control sample, with the previously discussed three major components highlighted at the same energies. Comparing the sample at 100 °C and as-loaded, it appears that the relative intensity between LLZO (A) and Li_2CO_3 (B) peaks is reduced after annealing, suggesting the treatment has reduced the carbonate component of the sample, without removing it entirely.

For a more comprehensive characterization, La $3d_{5/2}$, La $4p_{3/2}$, and Zr 3d XPS spectra were collected after LLZO polishing, at 600 °C, and once more after cooling

to room temperature. Both the hard and soft X-ray data are shown in the two bottom panels in Fig. 3.6. The La $3d_{5/2}$ multiplet splitting can offer some insight into the oxidation state of La [132, 119]. Existing literature suggests a multiplet split between 3.7 and 4.1 eV for $La(OH)_3$ and La carbonates (potentially $La_2O_2(CO)_3$), and between 4.3 and 4.9 eV for La_2O_3 [133, 134]. As reported in Fig. 3.6, the split before annealing is $\sim$ 4.2 eV, suggesting the presence of a mixture of La oxide and hydroxide/carbonates environments. At 600 °C, when the LLZO surface is mainly free of contaminants, the splitting increases to a range of 4.5 - 4.6 eV. This value more closely aligns with that of La_2O_3, indicative of La in the chemical environment of the LLZO lattice. After cooling to room temperature, the splitting decreases back to $\sim$ 4.4 eV. Therefore, the La $3d_{5/2}$ multiplet splitting qualitatively agrees with the evolution of surface contamination as suggested by O 1s and C 1s signals. The observed splitting is similar for both hard and soft X-ray data.

As for the La $4p_{3/2}$ and Zr 3d spectra, Fig 3.6b shows that the hard X-ray spectra remain consistent during annealing. Interestingly, the soft X-ray Zr 3d spectrum slightly changes after cooling the LLZO pellet to room temperature. The high-energy peak, sitting at $\sim$ 184.4 eV, has increased in intensity. Since the ratio between Zr $3d_{5/2}$ and $3d_{3/2}$ is fixed at 2:3, due to the degeneracies of the spin-orbit split levels (see inset 2 in Fig. 3.6b), it was necessary to include an additional doublet peak at higher binding energies that we assigned to an hydrated form of ZrO_2, as previously reported [135]. Hence, it is likely that upon cooling the topmost surface layer of LLZO evolves with a complex chemistry, including modifications to the La and Zr chemical environments. This could happen during the protonation of LLZO, i.e. the H^+/Li^+ exchange as in equation 3.1. The O 1s spectrum in Fig. 3.5b may contain some minor contributions from La carbonates or hydroxyls, as well as from Zr hydroxide. This would introduce an additional layer of complexity to the peak model, but more detailed information on the La $3d_{5/2}$ and Zr evolution will be necessary to confirm this hypothesis.

This section demonstrated the efficacy of annealing to 600 °C in a glovebox-like environment in eliminating surface Li_2CO_3 from a contaminated LLZO surface. However, the results have also showed that the pristine LLZO surface that is revealed at elevated temperatures is more susceptible to reaction with even low levels of H_2O and CO_2, facilitating the reformation of surface contaminants upon cooling the LLZO pellet to room temperature. A recent study reported similar findings when annealing and subsequently cooling LLZO under different gas environments, including a 1:1 mixture of H_2O and CO_2 at a total pressure of 1 mbar [120]. Investigating the

reactivity of LLZO at the realistic partial pressures found in a glovebox environment, i.e. in the order of 10e-3 mbar such as in this chapter, provides additional information on a widely adopted LLZO surface treatment. From Fig. 3.4 and later on Fig. 3.9, one can notice that the quantity of surface Li_2CO_3 following cooling back after annealing remains lower than the initial amount following air polishing. This explains how annealing LLZO can lead to a reduced Li/LLZO interfacial resistance. The next section will showcase the potential of acid etching to yield an even more pristine LLZO surface. Notably, acid etching operates at room temperature, where a pristine LLZO surface is less reactive with glovebox contaminants compared to its behaviour at high temperatures during the annealing treatment.

3.3 Acid etching in $HCl_{(aq)}$

Pioneering work by Huo et al. and subsequent studies have demonstrated the efficacy of rapid acid treatment in $HCl_{(aq)}$ or $H_2SO_{4(aq)}$ to remove the surface Li_2CO_3, leading to a more favorable Li/LLZO interface [122, 123, 124]. This treatment involves briefly immersing the LLZO pellet in the acid aqueous solution, often followed by a washing step with alcohols to eliminate residual HCl from the surface. Subsequently, a quick drying step with blown air or inert gas is conducted before introducing the LLZO into the glovebox. The simplicity and efficiency of the rapid acid treatment make it particularly appealing. However, as this treatment entails contact between LLZO and an aqueous solution followed by a short air exposure to bring the LLZO pellet back in the glovebox, there is a possibility of some surface contamination reforming on the pellet [122, 123]. Still, the treatment can be effective if the time taken to transfer the LLZO into the glovebox following the acid treatment is minimized. Furthermore, once the LLZO is in the glovebox environment its reactivity with H_2O and CO_2 at room temperature is reduced, as this section will elucidate.

To compare the efficiency of acid etching with that of the annealing treatment, an LLZO pellet was polished in air and immersed it in 1 M $HCl_{(aq)}$ for 10 seconds. This immersion time was specifically selected as it was found to efficiently remove the surface contamination leaving the LLZO surface undamaged. Figure 3.8 shows that longer etching times can result in the surface damage of LLZO. Following the immersion in $HCl_{(aq)}$, a washing step with ethanol and isopropanol was performed to remove any HCl residues, and the pellet was dried with an argon jet. Then it was immediately (< 1 min) loaded into the NAP-XPS system. Comparing the O 1s signal after acid etching (Fig. 3.7) and after air polishing (previously shown in Fig.

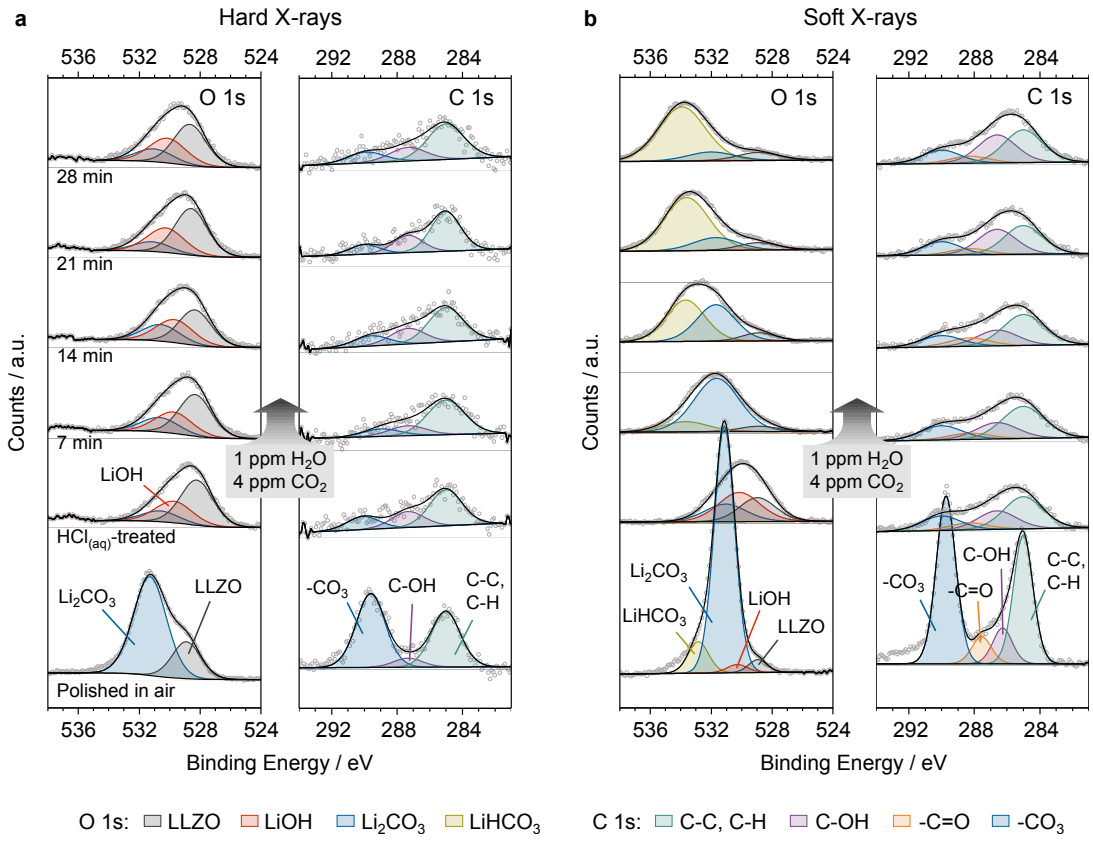


Figure 3.7. Introducing LLZO in the 'glovebox' after $HCl_{(aq)}$ etching. Hard and soft XPS O 1s and C 1s signals collected from LLZO pellets following acid treatment in $HCl_{(aq)}$. For comparison, the bottom spectra correspond to pellets polished in air. The spectra above them are collected first under UHV conditions and then in a glovebox-like atmosphere (1 ppm of H_2O, 4 ppm of CO_2).

3.4a and b, and now reported at the bottom of Fig. 3.7) reveals a stark contrast. The hard X-ray data now exhibit a strong LLZO peak, with comparatively smaller Li_2CO_3 and LiOH peaks. The presence of LiOH, which is absent after air polishing, might originate from the contact of LLZO with H_2O in the acid solution. Surface contamination, including $LiHCO_3$, is more prominent in the soft X-ray data, but the LLZO peak is still visible. This is corroborated by the C 1s signals, where the $-CO_3$ peak is relatively small. Moreover, La $3d_{5/2}$ spectra in Fig. 3.6a show a multiplet splitting of $\sim$ 4.6 eV, suggesting that the acid etching can reveal the pristine LLZO surface. In Fig. 3.6b the La $4p_{3/2}$ soft X-ray signal includes a doublet peak that can be assigned to Cl 2p (see inset 1). The washing step after acid etching has not rinsed away all of the chloride anions, which however are present only on the very top surface and in minor quantities.

After this preliminary characterization, 1 ppm of CO_2 and 4 ppm of H_2O were

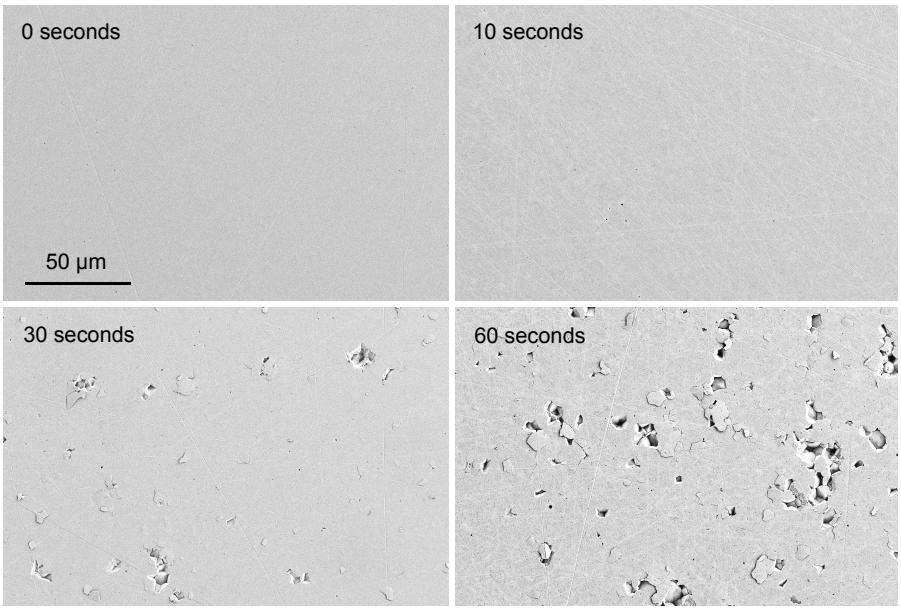


Figure 3.8. LLZO surface SEM images after different $HCl_{(aq)}$ etching times. The top left panel shows the surface SEM image of a pristine polished LLZO pellet. After 10 seconds of immersion in $HCl_{(aq)}$, the LLZO surface looks similar to the pristine one. However, longer etching times of 30 and 60 seconds can cause pitting and result in a significant surface damage.

dosed into the NAP-XPS chamber to simulate introducing the acid-treated LLZO pellet into a glovebox, following the same procedure detailed in section 3.2. XPS measurements were conducted at 7-minute intervals for nearly 30 minutes, which would be enough time to assemble the Li/LLZO interface in the glovebox. Minimal changes are observed in both O 1s and C 1s hard X-ray spectra during this period (Fig. 3.7a). Therefore, these results suggest that the LLZO surface obtained through acid etching remains relatively uncontaminated after introduction in a glovebox environment. However, some change is visible in the very topmost surface layers during storage in the glovebox-like environment. The soft X-ray O 1s spectrum changes shape and gradually shifts towards higher binding energies (Fig. 3.7b). This was explained as the reaction of LiOH to form Li_2CO_3 as in equation 3.2. Then the Li_2CO_3 peak slowly merges into the $LiHCO_3$ peak at even higher binding energies, which slowly overshadows the other signals. The resulting surface spectrum after 30 minutes of glovebox storage resembles that after cooling down from the annealing treatment (Fig. 3.4b).

The XPS data presented in this section suggest that acid etching LLZO in $HCl_{(aq)}$ cannot achieve the same degree of contamination removal that is achieved at 600

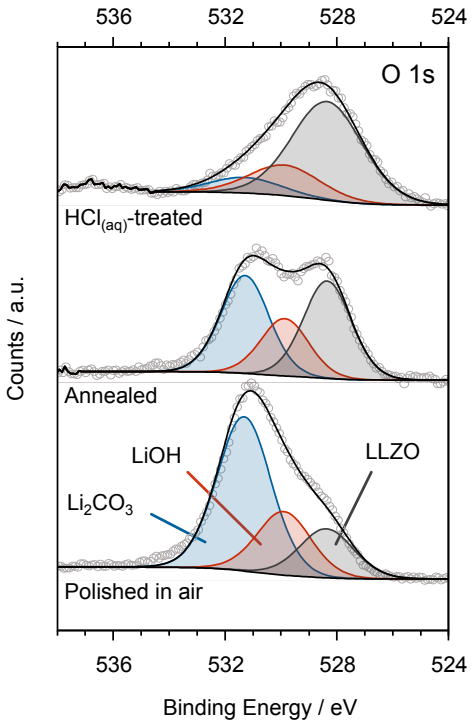


Figure 3.9. Comparison between annealing and $HCl_{(aq)}$ etching. XPS O 1s spectra of LLZO pellets after different surface treatments. The acid treatment in $HCl_{(aq)}$ is superior in removing the surface contaminants Li_2CO_3 and LiOH.

°C during the annealing treatment. However, considering that surface contamination reappears during cooling from 600 °C, acid etching actually proves to be more effective than the annealing treatment. Moreover, once the acid-treated LLZO is reintroduced into the glovebox environment, the growth of the surface contaminants occurs at a slow rate. In fact, the deeper LLZO surface layers ($\sim$ 20 nm) remain unchanged during 30 minutes of glovebox storage. Figure 3.9 compares the O 1s spectra from LLZO pellets 'just before cell assembly' within the glovebox, showing that the degree of surface contamination is lower for an acid-treated LLZO pellet. The small amount of surface contamination on the acid-treated pellet might be due to the brief air exposure necessary to return the LLZO to the glovebox after immersion in the $HCl_{(aq)}$ solution. Next section demonstrates that the Li/LLZO interface can be further improved by performing the acid treatment directly within the glovebox environment using a H_2O-free acid solution.

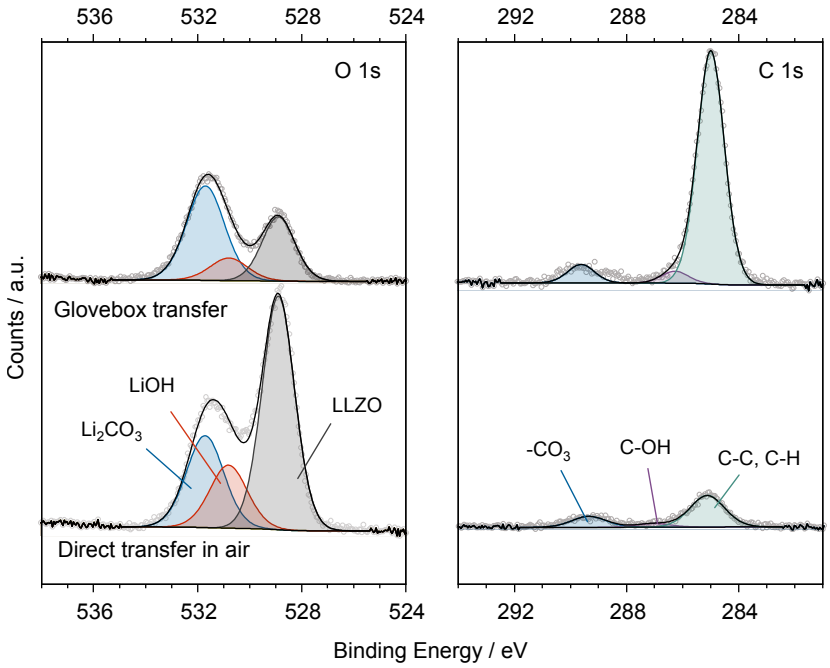


Figure 3.10. Additional contamination during glovebox transfer. XPS O 1s and C 1s spectra collected from LLZO pellets after acid treatment in $HCl_{(aq)}$. For the bottom spectra, the LLZO was immediately loaded in the XPS (< 1 min) after the surface treatment in air. For the top spectra, the LLZO pellet was promptly loaded in the glovebox (< 1 min) after the surface treatment, and then transferred to the XPS in a sealed vessel. The LLZO that was loaded via the glovebox exhibits a significantly larger surface contamination.

3.4 Acid etching in $HCl_{(Et_2O)}$

To prevent air exposure of LLZO following the acid treatment, we employed a solution of HCl in diethyl ether ($HCl_{(Et_2O)}$), which is compatible for use within a controlled glovebox environment. In this section, NAP-XPS is not used to track the evolution of the LLZO surface chemistry subsequent to $HCl_{(Et_2O)}$ etching. The reason for this lies in the fact that the NAP-XPS chamber was not directly connected to a glovebox where the $HCl_{(Et_2O)}$ etching could be performed. Although sealed transfer vessels are frequently used to transfer samples between the glovebox and the XPS setup, we have observed that a significant additional surface contamination can develop during during the transfer to the XPS in the sealed vessel, which would complicate the surface analysis (see Fig. 3.10). The sensitivity of lithium solid electrolyte surfaces to trace amounts of H_2O and CO_2 leaking in the air-free holder has also been documented in a previous study by Gibson et al. [125]. Thus, the utilization of XPS was deemed inappropriate for investigating the $HCl_{(Et_2O)}$ acid treatment. Instead, electrochemical

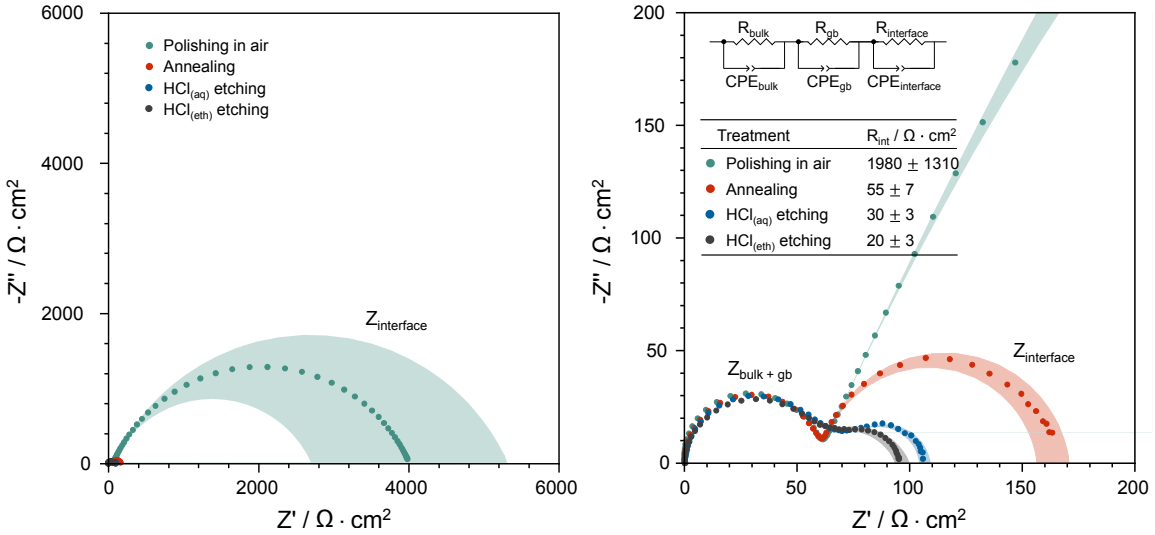


Figure 3.11. Electrochemical impedance spectroscopy of Li/LLZO/Li cells. EIS spectra of Li/LLZO/Li cells assembled after LLZO was subjected to the various surface treatments. The graph on the right is a zoomed-in version of the graph on the left. The equivalent circuit model used to fit the spectra is shown in the inset. The values of R_{int} are also reported in the inset table. The resistance of the Li/LLZO interface scales with the degree of surface contamination left on the LLZO.

impedance spectroscopy (EIS) of Li/LLZO/Li cells was collected to demonstrate the efficacy of $HCl_{(Et_2O)}$ etching in eliminating surface contamination and preventing its reformation. EIS spectra were fitted to quantify the Li/LLZO interfacial impedance, which is directly proportional to the degree of contamination present on the LLZO surface.

Therefore, Li/LLZO/Li cells were assembled using LLZO pellets that had undergone various surface treatment methods to remove the surface contaminants. At least 3 cells were assembled for each surface treatment. For the annealing treatment, LLZO pellets were polished in air following the procedure in section 2.5 and were introduced into a glovebox with values of moisture and CO_2 similar to those used for the NAP-XPS studies (O_2 and $H_2O \sim 1$ ppm, $CO_2 \sim 4$ ppm). The LLZO pellets were promptly heated to 600 °C with a 10 °C/min rate in a box furnace (MTI), using an alumina crucible lined with gold foil. The pellet was left at 600 °C for 2 hours, before cooling it back to room temperature over a period of 4 hours. Both the heating and cooling profiles resemble the ones followed for the NAP-XPS experiments. After cooling, the Li/LLZO/Li cell was immediately assembled (see section 2.5 for the assembly procedure).

The $HCl_{(aq)}$ treatment also followed the steps used for the NAP-XPS study. Specif-

ically, the LLZO was polished in air, immersed for 10 seconds in 1 M $HCl_{(aq)}$, washed with ethanol and isopropanol, and dried with an argon jet. Then it was quickly brought into the glovebox and the cell was assembled within 5 minutes of the acid treatment. For the $HCl_{(Et_2O)}$ treatment, the LLZO pellet underwent a polishing step in air before being brought into the glovebox and immersed in 1 M $HCl_{(Et_2O)}$ for 10 minutes. Li_2CO_3 is nearly insoluble in ethers, possibly explaining the longer immersion time needed with $HCl_{(Et_2O)}$ [136]. Subsequently, a washing process with dry ethanol and isopropanol was performed, followed by careful drying with an argon jet. Then the Li/LLZO/Li cell was immediately assembled. EIS was carried out as outlined in section 2.5.

The outcomes of this investigation are summarized in Fig. 3.11, which shows the Li/LLZO/Li impedance spectra. To interpret the data, an equivalent circuit model comprising of three semicircles (RC elements) was used. Two semicircles are used to fit the high-frequency data, representing the impedance inherent to the bulk LLZO material and the LLZO grain boundaries. The third semicircle was used for the low-frequency data, which represents the Li/LLZO interface contribution. From this data, it is possible to quantify the resistance to Li^+ ion transport across a singular Li/LLZO interface. The interfacial resistance values are reported in Fig. 3.11. A Li/LLZO interface assembled with an LLZO pellet subject solely to air polishing exhibits a R_{int} value of 1980 ± 1310 Ω cm^2. The annealing treatment managed to significantly lower this value to 55 ± 7 Ω cm^2, while acid etching in $HCl_{(aq)}$ yielded a value of 30 ± 3 Ω cm^2. Notably, the acid treatment involving $HCl_{(Et_2O)}$ resulted in the most favourable outcome, with the lowest interfacial resistance of 20 ± 3 Ω cm^2. This discernible reduction in interfacial resistance is attributed to a lower degree of contamination present on the LLZO surface. As is well-established, a lower R_{int} invariably translates to improved cell performance [117], emphasizing the critical role that the Li/LLZO interface plays in enhancing the overall efficiency of the battery.

3.5 Conclusions

This chapter assessed the efficacy of different treatments in mitigating surface contamination on LLZO SEs. Interestingly, it was observed that the commonly used method of annealing at high temperatures to remove the surface contaminants has a significant drawback; upon cooling the LLZO pellet back to room temperature, both Li_2CO_3 and LiOH promptly re-form. This could also affect the sintering process of LLZO powder to produce solid electrolyte pellets, where sintering temperatures reach

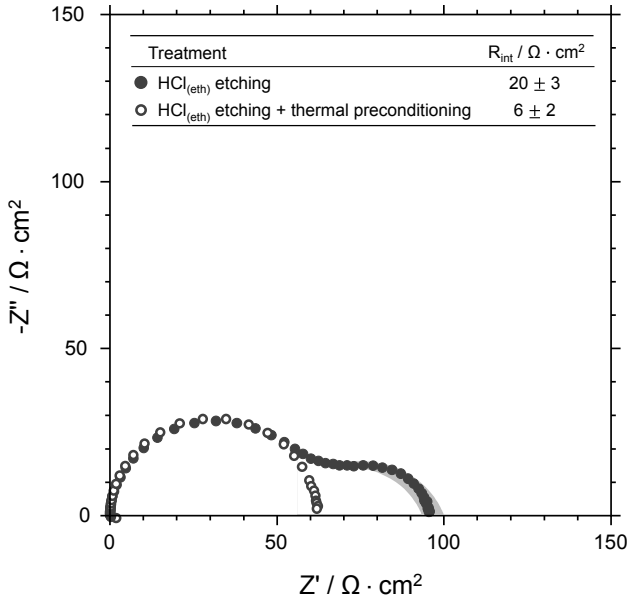


Figure 3.12. Thermal conditioning of the Li/LLZO interface. After acid etching of the LLZO pellet, a thermal conditioning of the Li/LLZO/Li cell at $\sim$ 170 °C for 2 hours results in a further decrease in the Li/LLZO interfacial resistance.

up to 1200 °C. Depending on the sintering atmosphere, the cooling of LLZO samples within the furnace could trigger the formation of Li_2CO_3 and other contaminants, which might also remain trapped in the LLZO porosity as recently suggested [93]. Further studies are required to investigate the potential impact of this phenomenon on the pellet performance as solid electrolyte.

In contrast, a rapid acid treatment using $HCl_{(aq)}$ yields a cleaner LLZO surface by maintaining the pellet at room temperature throughout the procedure, hence slowing down the kinetics of reaction between LLZO and trace CO_2 and H_2O. However, the brief exposure to air during transfer to the glovebox reduces the efficacy of the treatment, allowing the resurface of some superficial contamination. Furthermore, the effectiveness of this treatment is influenced by variations in air moisture and CO_2 content, meaning the LLZO is exposed to an environment which is difficult to control. Therefore, performing the acid treatment directly in a glovebox proves to be a more effective strategy to remove the surface contaminants. The novel acid treatment using $HCl_{(Et_2O)}$ within a glovebox shows superior results, demonstrating the lowest Li/LLZO interfacial resistance among the tested methods. This indicates its efficiency in removing surface Li_2CO_3 and LiOH and significantly preventing their reformation. Thus, R_{int} values follow this order: $HCl_{(Et_2O)} < HCl_{(aq)} <$ annealing. The R_{int} can be further reduced after cell assembly by heating the cell to 170 °C

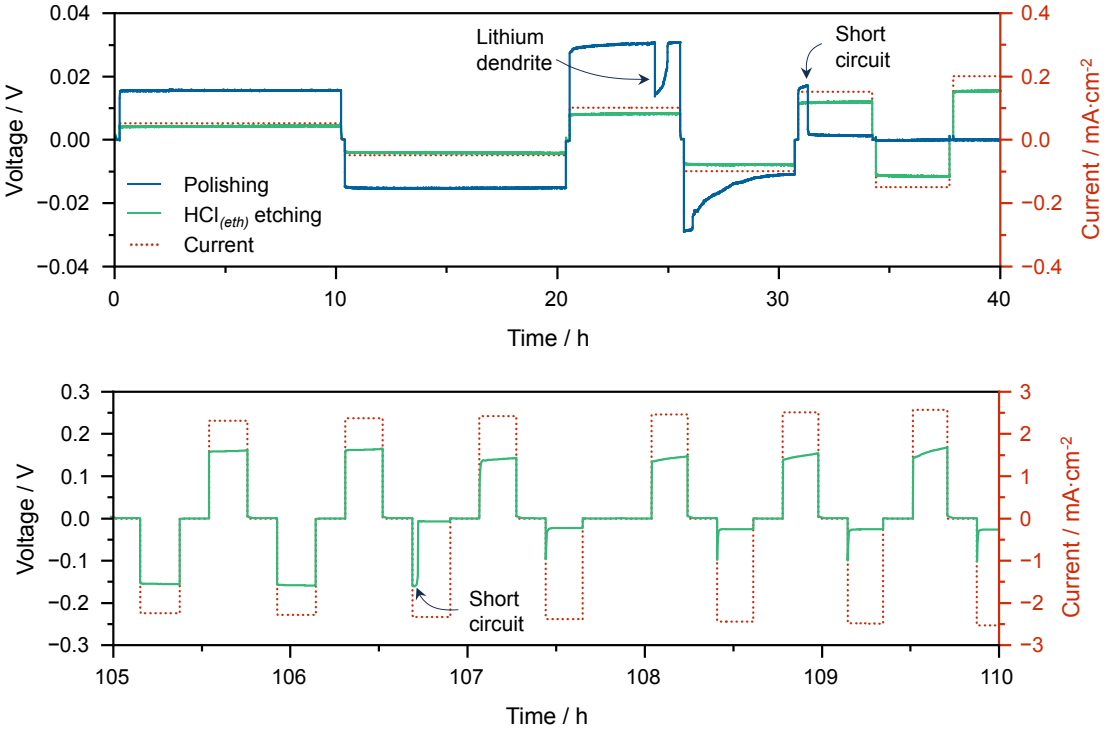


Figure 3.13. Critical current density measurements. Galvanostatic lithium plating and stripping of two different Li/LLZO/Li cells. LLZO underwent no treatment (blue line) or $HCl_{(Et_2O)}$ etching (green line). Both cells underwent a thermal preconditioning at 170 °C. The current density was increased by 0.05 mA cm^{-2} after each cycle, until a short circuit occurred. A capacity of 0.5 mAh cm^{-2} was plated or stripped during each half cycle. The cells were cycled at 30 °C and with 1 MPa of external stack pressure. The untreated LLZO cell fails at 0.1 mA cm^{-2}, whereas the surface treated LLZO cell undergoes short circuiting at 2.35 mA cm^{-2}.

for a few hours [39]. This thermal conditioning softens the lithium metal electrodes, allowing them to flow into microscopic interfacial gaps, ultimately leading to nearly zero interfacial resistance (see Fig. 3.12).

This chapter also highlights the significance of conducting in-situ characterization of LLZO surfaces and showcases the potential of NAP-XPS to provide insight into the timescales required for surface passivation within a glovebox environment. This information is important for optimizing LLZO treatment and storage protocols. Using this instrument, the detailed evolution of LLZO surface chemistry was comprehensively captured. For instance, the XPS data reveals a correlation between the growth of the Li_2CO_3 signal and the reduction of the LiOH signal, confirming that the formation of Li_2CO_3 might follow the reaction path outlined in equation 3.2. Additionally, it was possible to detect the presence of an additional high binding energy peak forming on

the topmost surface of LLZO upon exposure to the glovebox environment. This peak was attributed to lithium hydrocarbonate, potentially resulting from the reaction between Li_2CO_3 and H_2O. Over extended storage periods, this hydrocarbonate could contribute to the growth of the Li_2CO_3 surface layer.

The vulnerability of LLZO SEs to surface contamination, even in environments conventionally considered controlled and inert such as gloveboxes, was a crucial consideration when carrying out the research presented in this thesis. The recurring formation of surface LiOH and Li_2CO_3 highlights the need for meticulous handling and storage protocols, which have been employed in the subsequent chapters. These protocols are essential to minimize the impact of LLZO surface reactions, which can significantly influence the performance and reliability of LLZO solid-state cells. Figure 3.13 presents critical current density (CCD) measurements for Li/LLZO/Li cells assembled with two different LLZO pellets. This test involves increasing the current density in a stepwise manner after each plating/stripping cycle until a short circuit arises due to lithium dendrite growth within the pellet. Despite the limitations of CCD measurements, as discussed in section 2.5, this method provides a straightforward means of assessing the performance of Li/LLZO interfaces. In the CCD measurements in Fig. 3.13, one LLZO pellet received no surface treatment, while the other LLZO underwent $HCl_{(Et_2O)}$ acid etching. Both Li/LLZO/Li cells underwent subsequent preconditioning at 170 °C to improve the interfacial impedance. Notably, for the same applied current, the polarization of the cell (i.e., voltage) differs due to the varying Li/LLZO interfacial resistance. The CCD value for the cell with untreated LLZO, representing the current density at which lithium dendrite penetration causes cell failure, is 0.1 mA cm^{-2}. This value increases to 2.35 mA cm^{-2}, an order of magnitude higher, for the cell with acid-treated LLZO. This experiment underscores the significance of the lithium/solid electrolyte interface for the performance of solid-state cells.

Subsequent chapters will employ acid etching in 1 M $HCl_{(aq)}$ as the chosen surface treatment for removing surface contaminants from LLZO pellets. This treatment was selected for its effectiveness, simplicity and cost-efficiency. By combining this acid etching with thermal preconditioning of the cell at 170 °C, and a high-density spark plasma sintered LLZO pellet, an optimal Li/LLZO interface can be achieved with almost negligible interfacial resistance. This opened up new possibilities for cycling protocols of Li/LLZO/Li cells, leading to a better understanding of the Li/LLZO interface behaviour during lithium plating and stripping.

For instance, chapter 4 employs such Li/LLZO/Li cells to investigate the mechanics of lithium metal and LiMg stripping at relatively high current densities of 1 mA cm^{-2}. The only way for previous studies to achieve these current density values without failure due to lithium dendrites, was by introducing an interlayer between the lithium electrode and LLZO to enhance interfacial contact. In chapter 4, however, high-current stripping of pristine Li/LLZO interfaces was possible owing to the optimal cell assembly protocol developed in this study.

In chapter 5, the use of acid-treated LLZO cells will enable the assessment of the 'critical' current density required for the formation of spallations on the LLZO surface. These spallations represent the initial morphology of lithium dendrites. In cases of cells with nearly zero interfacial impedance, the applied current density closely aligns with the local current density at the Li/LLZO interface, therefore making this evaluation feasible.

Chapter 4

On the Relative Importance of Li Bulk Diffusivity and Interface Morphology in Determining the Stripped Capacity of Metallic Anodes

As described in section 1.2, lithium metal self-diffusion is too slow to sustain stripping at large current densities at the interface with LLZO. The resulting formation of voids in the lithium metal electrode is a major limiting factor for the power density of solid-state cells. The enhanced morphological stability of some lithium alloy electrodes has prompted questions on the role of lithium diffusivity in these materials. In this chapter, the lithium diffusivity in LiMg alloys is investigated by an isotope tracer method, revealing that, contrary to previous reports, the presence of magnesium slows down the diffusion of lithium. For large stripping currents the delithiation process is diffusion-limited, hence a lithium metal electrode yields a larger capacity than a LiMg electrode. However, at lower currents we explain the apparent contradiction that more lithium can be extracted from LiMg electrodes by showing that the alloy can maintain a more geometrically stable diffusion path to the solid electrolyte surface so that the effective lithium diffusivity is improved.

4.1 Introduction

In solid-state cells using lithium metal as the anode, the atomic diffusivity of lithium within the bulk of the electrode is often a limiting factor in determining the cycling behaviour. Specifically, a fast bulk diffusivity of lithium atoms is crucial to maintain

a stable interface between the lithium metal electrode and the solid electrolyte under realistic cycling current densities [25, 26]. As an example, a diagram of the evolution of the Li/LLZO interface during cycling is illustrated in Fig 4.1. Stripping a lithium metal anode involves the migration of lithium ions into the solid electrolyte and the creation of vacancies at the surface of the lithium electrode. If the diffusion of lithium atoms from the bulk electrode towards the surface is not fast enough to replenish these vacancies, the Li/LLZO contact may be lost at the atomic scale. As previously discussed in section 1.2, vacancies can then cluster to form voids, leading to macroscopic contact loss and to an increase in the Li/LLZO interfacial impedance [34, 49]. This could ultimately lead to cell failure in subsequent cycles, as the local plating current density would intensify beyond the nominally applied value, thereby promoting the formation of lithium dendrites [35]. This phenomenon was elaborated in the introductory chapter 1. The flux of lithium ions into the solid electrolyte is proportional to the stripping current density i according to:

$$J_{Li^+} = \frac{i}{z \cdot F} \tag{4.1}$$

Here, z represents the valence of the mobile ion (1 in this case), and F is Faraday's constant. Thus, higher currents will strip lithium atoms from the metallic anode at a faster rate.

On the other side of the interface, within the lithium metal electrode, the flux of lithium atoms, in the absence of external pressure, is proportional to the lithium diffusion coefficient D_{Li} according to Fick's laws of diffusion. An external pressure would introduce additional creep effects, enhancing the effective flux of lithium atoms toward the solid electrolyte. As mentioned in the introduction to this thesis, external stack pressures in the order of a few megapascal have indeed been effective in preventing contact loss at the Li/LLZO interface [34]. Nonetheless, it remains unclear whether this appraoch would be a practically viable to prevent void formation at commercially relevant current densities of > 4 mA cm^{-2}, which would require very large stack pressures. Notably, electric vehicle requirements stipulate battery stack pressures below 1 MPa [31].

Hence, to maintain a morphologically stable interface, rapid Fickian diffusion of lithium atoms to the interface is needed to avoid local accumulations of vacancies, and understanding the factors governing this diffusion flux is paramount. In monatomic metals like lithium, the bulk atomic diffusion process - referred to as

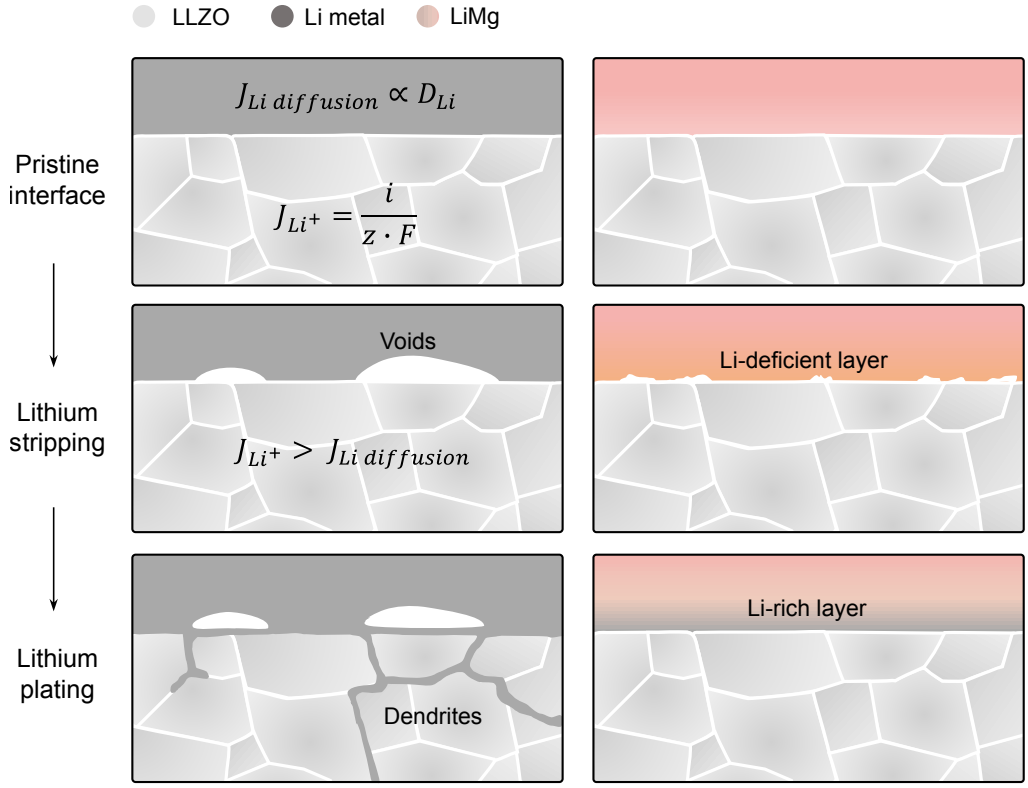


Figure 4.1. Schematic of Li/LLZO and LiMg/LLZO interfaces A balance of fluxes dictates the evolution of the Li/LLZO interface during cycling. In the electrode, the flux of lithium atoms is proportional to lithium diffusion coefficient as dictated by Fick's laws. In the solid electrolyte, the flux of lithium ions is proportional to the current density. If $J_{Li^+} > J_{Li}$, a loss of contact at the Li/LLZO interface will develop in the shape of voids. During the subsequent plating, the formation of lithium dendrites is more likely. In the case of lithium alloys such as LiMg, a more stable interfacial contact has been often attributed to a larger lithium diffusion coefficient D_{Li}^{alloy} than that in pure lithium metal.

self-diffusion - involves exchanging an atom with an adjacent vacancy. At the intermediate temperatures where batteries operate, this vacancy is typically a monovacancy [137]. This process has been previously investigated with nuclear magnetic resonance [138, 139, 140], tracer isotope mass spectrometry [141], and first-principles calculations [137, 142]. From these studies the lithium self-diffusion coefficient in lithium metal, denoted as D_{Li}, falls within the range of 10^{-11} – 10^{-10} cm^2 s^{-1} at room temperature, albeit with some variations due to different methods and experimental conditions, as summarised by Krauskopf et al. [41]. According to the defect relaxation model proposed by Schmalzried and Janek and previously introduced in section 1.2 [27], wherein $i_{crit} \propto \sqrt{D_{Li}}$, the critical stripping current for void formation

i_{crit} at room temperature and zero external pressure would lie in the range of 50 - 200 μA cm^{-2} for the mentioned D_{Li} values.

On the other hand, employing lithium alloys has been shown to help form a more stable interface with solid electrolytes. Various lithium alloys have been used as anodes [41, 143, 144, 145, 146] or as interlayers between lithium metal and solid electrolytes [147, 148, 149, 150, 151, 152]. The enhanced morphological stability of the interface is often attributed to a fast lithium diffusivity within the alloy [45, 144, 147, 152]. During stripping, vacancies formed at the interface would be quickly replenished, curbing void formation, as depicted in Fig. 4.1. During plating the fast lithium diffusion into the bulk of the alloy helps maintain the lithium activity at the interface below one, limiting an excessive accumulation of lithium atoms at the interface.

Previous studies exploring various lithium alloys have reported lithium diffusivities that significantly surpass lithium self-diffusivity. Chemical diffusion coefficients in these studies have ranged from 10^{-8} to 10^{-6} cm^2 s^{-1} at room temperature [48, 152, 153, 154, 155]. This phenomenon is somewhat surprising, as conventional wisdom suggests that alloying lithium with a solute of higher melting point typically reduces diffusivity rates, owing to a decrease in homologous temperature. However, it is worth noting that these reported values are often derived from indirect measurements, as elaborated below. A summary of reported lithium diffusivity values from previous studies can be found in Fig. 4.2, along with corresponding references in Table B.1 in appendix B. Notably, these values vary by several orders of magnitude even for the same lithium alloy system. Such uncertainty can be attributed to the use of diverse techniques for measuring diffusion coefficients. In particular, electrochemical methods such as galvanostatic or potenstiostatic intermittent titration techniques (GITT or PITT) are extensively employed for this purpose due to their relatively simplicity, but they represent an indirect approach to measuring diffusion coefficients. In these methods, the material of interest is employed as an electrode in an electrochemical cell and these methods are based on analyzing the voltage (current) relaxation response of the electrode after the application of a current (voltage) pulse. Utilizing these methods involves making several assumptions about the material and its interaction with the electrolyte [156]. They also require careful experimental design and intricate data fitting processes. A recent review by Kang et al. [157] has highlighted possible systematic errors in the implementation of these methods, explaining the uncertainties in Fig. 4.2. These methods have mostly yielded large diffusion coefficients, which are

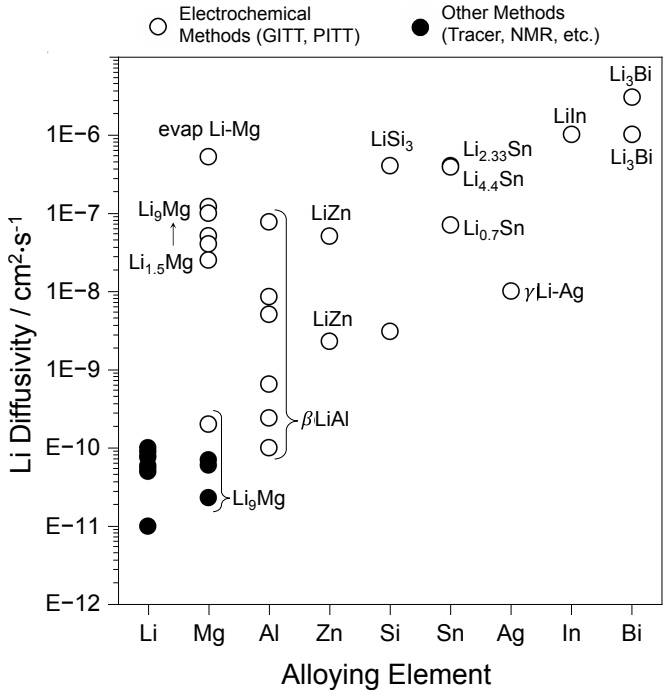


Figure 4.2. Literature survey of Li diffusivity in Li alloys. Lithium diffusion coefficients for various Li-alloying elements. Table B.1 contains the corresponding references. Most of the diffusion coefficients have been obtained with electrochemical methods such as GITT and PITT. A significant uncertainty exists in the diffusivity values even for the same alloy composition.

frequently cited to explain the enhanced morphological stability of lithium alloys at the interface with solid electrolytes [45, 144, 147, 152].

Among these lithium alloys, the LiMg system has attracted particular interest [143, 158, 159]. Magnesium exhibits an exceptionally broad solubility range in lithium, with the β-phase region spanning from 0 to 70 at. % Mg (see the phase diagram in Fig. 2.5) [95]. This suggests the absence of a phase transformation during electrochemical cycling of LiMg, leading to an enhanced microstructural stability [41]. The coexistence of two phases with different molar volumes would instead cause inhomogeneous volume change in the anode. Moreover, magnesium is a light element and LiMg alloys have a potential of ~ 0 V versus Li/Li$^+$, both desirable properties for optimising the cell energy density [94]. However, discrepancies concerning the values of lithium diffusivity in LiMg alloys exist in the literature. While nuclear magnetic resonance [160] and neutron tomography [161] have yielded diffusion coefficients around 10^{-11} cm^2 s^{-1}, PITT studies have reported values in the range of 10^{-8} - 10^{-7} cm^2 s^{-1} [162]. A LiMg electrode exhibiting such fast lithium diffusivity could sustain a critical stripping current for void formation i_{crit} one order of magnitude higher than

a lithium metal electrode, according to $i_{crit} \propto \sqrt{D_{Li}}$ as in equation 1.2 [26].

Given the importance of understanding the role of lithium diffusivity in governing the morphology of the electrode/solid electrolyte interface, this chapter aims to resolve the inconsistency in the literature values by performing direct measurements of lithium diffusivity in elemental lithium and in LiMg alloys with up to 30 at. % Mg. For this purpose, an isotope tracer method is employed, which couples two materials with different stable isotope concentrations, known as isotope heterostructures, and tracks the isotopic diffusion. To ensure intimate contact between these two materials, thermal evaporation is used to deposit a thin film of the tracer isotope onto bulk samples of varying isotopic concentrations, according to the Experimental Methods section 2.4. A secondary ion mass spectrometry (SIMS) detector, integrated in a plasma focused-ion beam (PFIB) apparatus as depicted schematically in Fig. 4.3a, is used to track the isotopic concentration as a function of depth. From this data, the diffusion coefficient can be derived. Notably, this direct measure of tracer diffusive flux over the micron scale renders the diffusion coefficient obtained by SIMS sensitive to microstructural features like grain boundaries, dislocations, etc. This sensitivity makes it a good measure of the transport processes specifically within the anode metal. By contrast, methods such as nuclear magnetic resonance provide a measure of the random atomic-scale displacement over shorter distances, thus yielding a diffusion coefficient sensitive to a single or few atomic jumps only. Furthermore, the SIMS technique is also preferred over electrochemical methods, which only indirectly determine the chemical diffusion coefficient using models reliant on multiple underlying assumptions, such as an ideal electrode/electrolyte interaction, that must be fulfilled for accurate diffusion measurements [157].

Based on the SIMS analysis conducted in this chapter, the lithium diffusivity observed in LiMg alloys aligns with the lower end of the literature values and is approximately one order of magnitude slower than lithium self-diffusion in lithium metal. This suggests that any improvement in the performance of a solid-state cell featuring a LiMg alloy anode does not arise from enhanced lithium diffusivity. In fact, within this chapter, an LLZO solid electrolyte is employed with a pure lithium or a LiMg alloy anode. The objective is to investigate the influence of lithium bulk diffusivity on determining the maximum capacity that can be extracted from the anode. The experimental results reveal distinct behaviours of the two anodes depending on the applied stripping current density. At relatively large stripping current densities, a higher capacity can be stripped from a pure lithium metal anode, benefiting from its faster lithium diffusivity, compared to a LiMg alloy anode. However, the LiMg alloy

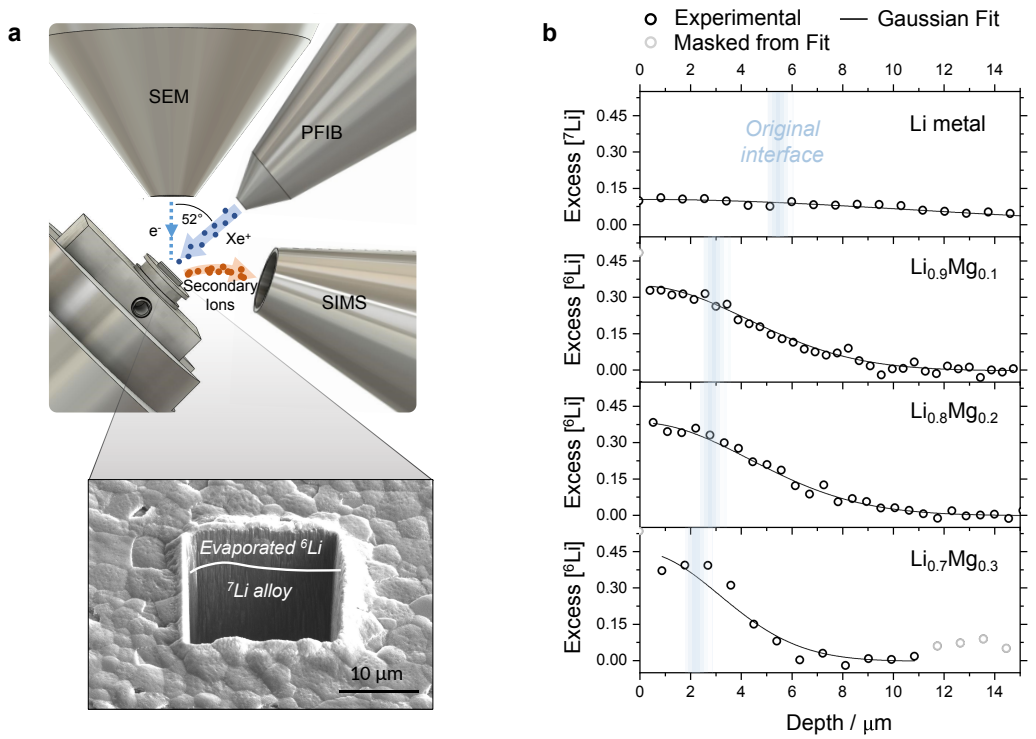


Figure 4.3. Lithium diffusion profiles. **a**, Experimental setup for the measurement of the lithium diffusivity with a SIMS detector fitted in the PFIB chamber. A crater is sputtered on the ^{6}Li/^{7}LiMg heterostructure and the isotopic concentration is tracked across the crater depth. **b**, SIMS diffusion profiles of the excess concentration of the tracer isotope into the substrate taken 60 minutes from the start of the tracer deposition. From the top: ^{7}Li into ^6Li, then ^{6}Li into $^7Li_{1-x}Mg_x$ with x = 0.1, 0.2, and 0.3. The position of the original interface between the tracer and the substrate was inferred by cross sectional secondary electron imaging.

anode demonstrates superior performance to a pure lithium anode at lower stripping current densities, and in the absence of external pressure. This is attributed to a more stable morphological interfacial contact with LLZO, as investigated through cryogenic PFIB sectioning.

4.2 Lithium diffusivity measured by SIMS

To investigate self-diffusion in lithium metal, a thin film of ^7Li $\sim$ 5 μm thick was thermally evaporated onto ^6Li (see section 2.4 in chapter 2 for details on experimental procedure). In this chapter, italics are used to distinguish lithium isotopes, ^{7}Li and ^{6}Li, from lithium metal with the natural isotopic abundance, ^7Li, or from lithium metal isotopically enriched with ^{6}Li, ^6Li. To measure diffusion in ^{7}LiMg alloys, ^6Li

was evaporated onto the alloy surface. Here the isotope effect is neglected, i.e. the possibility of ^{6}Li diffusing faster than ^{7}Li due to the difference in their masses, as the reported difference [140] lies within the error bars of diffusion coefficients determined by most methods. Care was taken to perform all the operations in an inert glove-box with < 0.1 ppm values of O_2 and H_2O, and the surface contamination that can develop on lithium and LiMg substrates during storage was removed with a scalpel immediately prior to thermal evaporation. Naturally, as soon as the thermal evaporation process begins, interdiffusion of the two stable lithium isotopes also starts. A small increase in substrate temperature was detected during evaporation of the isotope thin film (as reported in section 2.4), meaning the initial diffusion rate was slightly accelerated. Figure 4.3b shows typical diffusion profiles of the isotope tracer into different substrates taken 60 minutes from the start of the thermal evaporation. The excess concentration of the isotope tracer was fitted with the Gaussian solution of Fick's second law, as reported in section 2.4. This solution is suitable for isotope diffusion experiments with a fixed amount of diffusing species, i.e. a thin film, like in this case. The first data points in the diffusion profiles can lie at an artificially high value due to the effect of surface oxygen contamination on the sputter yield, and these points were removed from the Gaussian fitting.

The diffusion profile of ^{7}Li into ^6Li in Fig. 4.3b results in the calculation of a lithium self-diffusion (tracer diffusion) coefficient, D^*_{Li}, of $(1.6 \pm 0.1) \times 10^{-10}$ cm^2 s^{-1}, which is in reasonable agreement with previous literature reports [141]. However, the lithium diffusivity does not increase in the LiMg alloys, which have measured intrinsic diffusion coefficients for Li, D_{Li}, of (2.4 ± 0.1), (2.6 ± 0.1), and $(1.4 \pm 0.2) \times 10^{-11}$ cm^2 s^{-1} for 10, 20 and 30 at. % Mg alloys respectively, based on the diffusion profiles in Fig. 4.3b. This slower diffusivity can also be seen in Fig. 4.3b by the fact that the surface concentration of the tracer isotope on the LiMg alloys is greater in all cases than on the elemental lithium metal. Additional SIMS diffusion profiles are reported in Fig. 4.4. These are profiles of ^{6}Li into LiMg alloys, taken at different times after the start of the tracer deposition, specifically after 60, 120, and 180 minutes. It is possible to observe the typical evolution of diffusion profiles as described by the Gaussian solution to Fick's second law, with the surface tracer concentration decreasing with time as previously illustrated in Fig. 2.10. There is reasonable agreement amongst the diffusion coefficients obtained from the Gaussian fitting for the same LiMg alloy.

To interpret the SIMS data, we note that the β-phase in LiMg alloys is a substitutional solid solution, and since the Goldschmidt radii of Li and Mg differ by only

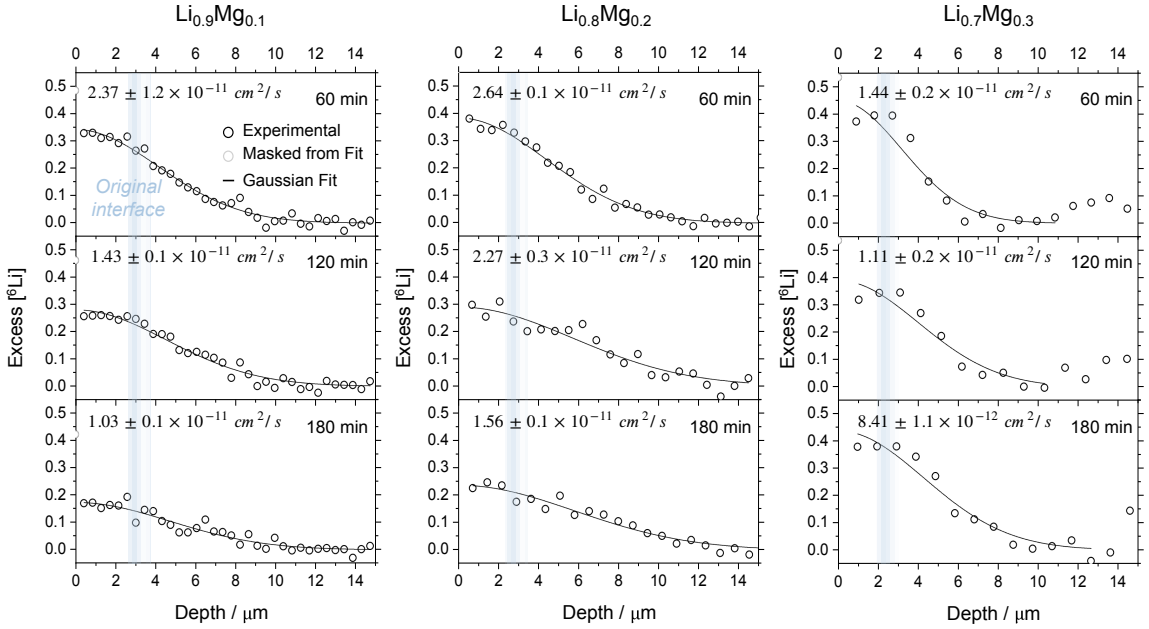


Figure 4.4. Evolution of Li diffusion profiles in LiMg alloys with time. SIMS diffusion profiles of the excess concentration of the ^{6}Li isotope into $^7Li_{1-x}Mg_x$ with x = 0.1, 0.2, and 0.3 (panels from left to right). The profiles were taken on each sample 60, 120, and 180 minutes from the start of the tracer deposition (panels from top to bottom). The lithium diffusion coefficient D_{Li} obtained from the Gaussian fitting is reported above each diffusion profile. There is reasonable agreement between the diffusion coefficients measured from the same sample. The position of the original interface between the tracer and the substrate was inferred by cross sectional secondary electron imaging.

a few percent we may assume that lithium diffuses in LiMg by the same vacancy mechanism as in elemental lithium. Another possible difference between the lithium metal and LiMg alloy materials that might influence the measured diffusivity is the grain size, but as shown in Fig. 2.6 this is in the order of 100 microns in all materials, so that the grain boundary contribution to the overall diffusion fluxes should be both similar and negligible. We note here that when considering a lithium flux diffusing into a LiMg alloy there is a compositional gradient that should introduce an associated activity gradient (hence the use of the label intrinsic diffusion coefficient, D_{Li}), but that in general adding a higher melting point element, B, to a lower melting point matrix, A, should decrease the value of D_A.

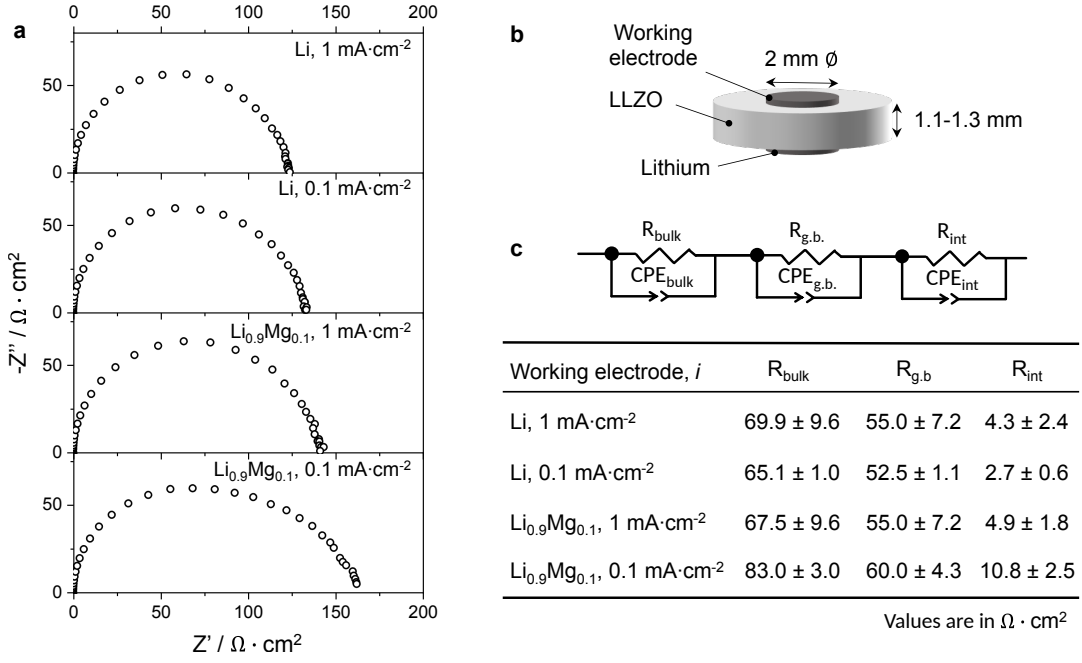
The D_{Li} values agree with the more conservative literature values on LiMg alloys, such as Korblein et al. ($< 7 \times 10^{-11}$ cm^2 s^{-1} using nuclear magnetic resonance) [160] and Zhang et al. (6×10^{-11} cm^2 s^{-1} using neutron tomography) [161], as well as with the study on LiMg in contact with a solid electrolyte by Krauskopf et al. (3

$\times$ 10^{-11} cm^2 s^{-1}) [41]. The discrepancy with the literature showing faster lithium diffusivity in LiMg alloys obtained by PITT might be explained by the fact that the diffusion coefficients obtained by electrochemical methods are strongly influenced by the microstructure of the alloys used and their surface morphology, with larger diffusion coefficients for more porous structures (like the ones studied by Gole et al.) [155, 162]. In fact, for such methods the knowledge of the true alloy surface area is needed to calculate the diffusion coefficient [156]. This and other sources of uncertainties can alter the diffusivity values measured by electrochemical titration methods by as much as four orders of magnitude [157], while tracer diffusion methods like the one employed here directly probe the bulk diffusivity without the need for model assumptions.

4.3 Implications for solid-state batteries

In the context of the performance of solid-state batteries, the lithium self-diffusivity D^*_{Li} found in this chapter is expected, based on the model proposed by Schmalzried and Janek [26], to be insufficient for maintaining a stable interface between a lithium metal electrode and a solid electrolyte, even at small current densities (50 - 200 μA cm^{-2}). Consequently, during the stripping process, voids are likely to form unless significant external pressure is applied [26]. The smaller D_{Li} values observed in LiMg alloys suggest even slower lithiation and delithiation kinetics in these alloy anodes. This observation is confirmed in this section by performing stripping experiments using both lithium and $Li_{0.9}Mg_{0.1}$ electrodes in contact with an LLZO solid electrolyte. No external pressure was applied during stripping, so that the flux of lithium atoms in the anode is solely dependent on lithium diffusivity, with any effect of creep deformation ruled out.

Initially, a stripping current density of 1 mA cm^{-2} was applied to Li/LLZO/Li and LiMg/LLZO/Li cells. The current was maintained until the cells exhibited a polarization exceeding 4 V, therefore assessing the maximum capacity that can be stripped from the anode. These cells featured an optimal initial interface between the electrodes and LLZO, achieved through the acid treatment of LLZO (described in section 2.5) to remove surface contamination, primarily consisting of Li_2CO_3 and LiOH as detailed in chapter 3. Additionally, a thermal preconditioninig step at 170 °C, described in section 2.5, was carried out, resulting in negligible initial Li/LLZO and LiMg/LLZO interfacial impedances. This allowed the investigation of the electrode/LLZO interfacial stability at relatively large stripping currents, previously in-



Working electrode, *i*	R_{bulk}	$R_{g.b}$	R_{int}
Li, 1 mA·cm^{-2}	69.9 ± 9.6	55.0 ± 7.2	4.3 ± 2.4
Li, 0.1 mA·cm^{-2}	65.1 ± 1.0	52.5 ± 1.1	2.7 ± 0.6
$Li_{0.9}Mg_{0.1}$, 1 mA·cm^{-2}	67.5 ± 9.6	55.0 ± 7.2	4.9 ± 1.8
$Li_{0.9}Mg_{0.1}$, 0.1 mA·cm^{-2}	83.0 ± 3.0	60.0 ± 4.3	10.8 ± 2.5

Values are in Ω · cm^2

Figure 4.5. Starting EIS spectra of LLZO cells with negligible R_{int}. **a**, Electrochemical impedance spectroscopy performed on the solid-state cells prior to the stripping experiments in Fig. 4.6, labelled as: working electrode, current density. **b**, Two-electrode cell schematics where the working electrode is either pure lithium metal or a LiMg alloy. **c**, Equivalent circuit model for the fitting of electrochemical impedance spectra and table with bulk, grain boundary, and interfacial resistance (single interface) values obtained by the fitting. The starting interfacial resistance values are very small thanks to the acid etching surface treatment of the LLZO pellets.

accessible. Figure 4.5 shows the initial electrochemical impedance spectroscopy (EIS) data for the cells employed in this section, along with their corresponding R_{int} vaues.

Figure 4.6a presents the potential profiles of LLZO cells during stripping at 1 mA cm^{-2}. The cells were maintained at 30 °C and without external stack pressures throughout the stripping experiments. Upon reaching a cell polarization of 4 V, the current was stopped and the cells were meticulously disassembled within a glovebox. Careful handling of the samples ensured that the unadulterated electrode/LLZO interface could be investigated. The samples were then transferred to the same PFIB instrument used for the lithium diffusivity experiment, now equipped with a cryogenic stage. Cross-sectioning of the Li/LLZO and LiMg/LLZO interfaces was performed at -150 °C to prevent beam damage and partial melting of the lithium or LiMg electrodes.

The polarization of the cell observed in the voltage profiles results from a decrease in lithium concentration at the solid electrolyte surface. This process appears dif-

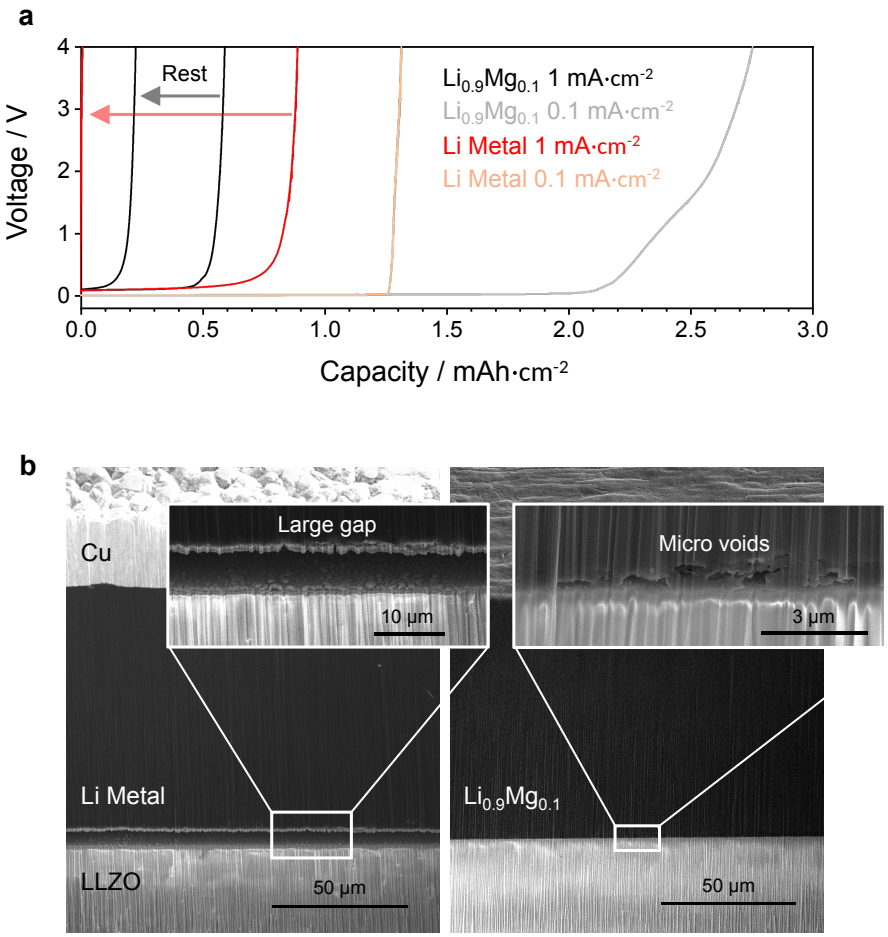


Figure 4.6. Stripping of Li and $Li_{0.9}Mg_{0.1}$ electrodes. **a**, Stripping experiments for lithium and $Li_{0.9}Mg_{0.1}$ electrodes at 1 mA cm^{-2} and 0.1 mA cm^{-2}. The cells were cycled at 30 °C and without external pressure. The counter electrode was lithium metal. For 1 mA cm^{-2}, after the cut-off voltage of 4 V was reached the cell was rested for 2 hours, then stripping was repeated. **b**, Secondary electron images of cryogenic PFIB cross sections of the working electrodes after the first stripping step at 1 mA cm^{-2}. A large, continuous gap is formed between lithium and LLZO, while a more localised porosity is present in the $Li_{0.9}Mg_{0.1}$ electrode.

ferently at a Li/LLZO or LiMg/LLZO interface. Cryogenic PFIB cross sectioning (Fig. 4.6b) reveals that for the pure lithium metal electrode, the polarization is due to the formation of large voids and almost complete loss of contact. In contrast, the presence of magnesium, which is not stripped, encourages the preservation of a more stable contact morphology between the $Li_{0.9}Mg_{0.1}$ alloy and LLZO. The increase in polarization is a result of the lithium concentration reduction in the alloy. Therefore, while lithium is stripped from both electrodes at the same rate, the use of $Li_{0.9}Mg_{0.1}$ mitigates the formation of large voids. However, its slower bulk lithium diffusivity D_{Li} limits the capacity extracted from the alloy. This cycling performance is validated using at least two cells of each type. Interestingly, if the $Li_{0.9}Mg_{0.1}$ electrode is rested for a few hours after the initial delithiation, lithium can diffuse back to the LLZO surface due to the maintained diffusion path, allowing for some additional capacity to be extracted in a subsequent stripping step (Fig. 4.6a). In contrast, the complete loss of contact between the lithium metal electrode and LLZO, which is not recovered in the absence of external pressure, precludes any further stripping even after a resting period.

Potential profiles for stripping at 0.1 mA cm^{-2} are also reported in Fig. 4.6a. When a smaller stripping current is applied, a lithium metal electrode achieves only a slightly higher capacity than with a 1 mA cm^{-2} current, suggesting the formation of a similar number of voids after reaching the same stripped capacity, in the absence of an external pressure. In contrast, the capacity extracted from the $Li_{0.9}Mg_{0.1}$ electrode is more than four times higher compared to that at 1 mA cm^{-2}, as a consequence of the ability of $Li_{0.9}Mg_{0.1}$ to retain good contact with the solid electrolyte. This result suggests that when the delithiation rate is low enough to allow the bulk diffusion of lithium atoms to supply a sufficient flux to the interface, it is the morphological stability of the interfacial contact that becomes a more critical factor in determining the final capacity. LiMg electrodes with 20 and 30 at. % Mg were not considered here due to their higher hardness, making solid-state cell assembly more challenging. Nonetheless, all the LiMg alloys mentioned above exhibit comparable diffusion coefficients, suggesting a similar delithiation behaviour in contact with LLZO.

It is important to note that in real operating conditions, the alloy electrode would experience a variation in the lithium activity that is difficult to predict. These variations might alter lithium diffusivity (D_{Li} should depend on the local lithium concentration) and charge transfer efficiency [41, 163]. However, based on the results presented above and from prior studies [41, 160, 162], it is expected that the diffusion coefficient would decrease with increasing magnesium content. This would be

consistent with the steep increase in the melting temperature, as compositions with higher melting points generally have lower atom mobility (see phase diagram in Fig. 2.5). Nevertheless, LiMg alloys appear to provide lithium atoms in the bulk of the anode continuous access to the solid electrolyte surface through the partly delithiated LiMg phase, while lithium diffusion through a void in the lithium electrode is clearly impeded.

Consequently, the behaviour of LiMg alloys can be understood by considering an *effective* lithium diffusivity that accounts for both the bulk lithium diffusivity and the way in which the different void morphologies affect the contact area between the electrode and the solid electrolyte. When voids form in a lithium metal electrode, its *effective* diffusivity rapidly decreases. In contrast, a LiMg electrode has a smaller initial *effective* diffusivity, but its interface morphology remains more stable over cycling, thus enhancing the capacity at small stripping rates.

4.4 Interface contamination

During the lithium diffusivity experiments, great care was taken to minimize contamination at the interface between the evaporated tracer thin films and the ^{6}Li or ^{7}LiMg substrates. Lithium and LiMg alloy samples react rapidly with trace moisture, oxygen, carbon dioxide, and nitrogen in a glovebox and even in the vacuum environment of the thermal evaporation chamber, as noted in previous studies [125, 164]. Mindful of this, exposure of the freshly prepared lithium and LiMg alloy surfaces to the glovebox atmosphere was kept to a minimum duration (less than one minute) before evacuating the thermal evaporation chamber. However, the presence of some contamination is inevitable. Hence, the measured lithium diffusivity is likely an underestimation, as lithium tracer atoms have an interface to cross.

To assess the impact of contamination on the measured lithium diffusivity, Fig. 4.7a illustrates a comparison of two diffusion profiles of ^{7}Li into ^{6}Li where the ^{6}Li substrate was prepared in glovebox atmospheres with different contamination levels before depositing the ^{7}Li tracer. For a glovebox atmosphere containing approximately 1 ppm of H_2O and O_2, the ^{18}O signal collected with SIMS exhibits a substantial peak at the original ^{7}Li - ^{6}Li interface position. This directly confirms the contamination of the ^{6}Li surface in the less well controlled environment, even during the brief sample loading time. Notably, oxygen is known to significantly enhance the ionization probability of electropositive elements [102]. As a result, excess [^{7}Li] data points at the interface do not follow the diffusion profile and were excluded from the Gaussian

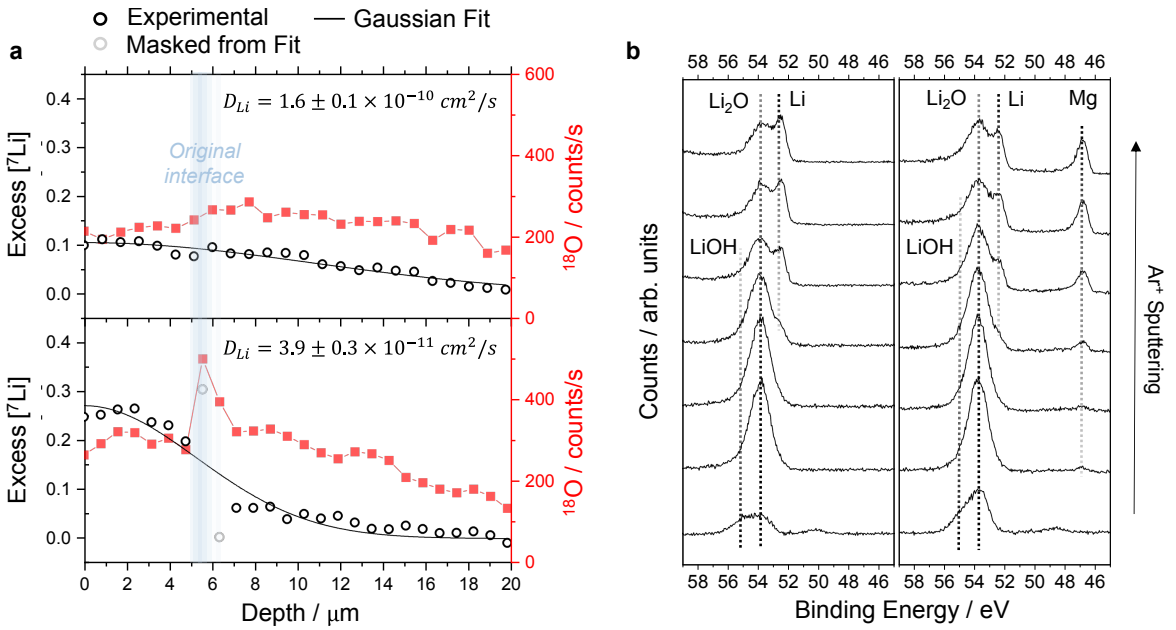


Figure 4.7. Effect of glovebox atmosphere on Li diffusivity. **a**, Diffusion profile of ^{7}Li into ^6Li including the ^{18}O SIMS signal at 60 min after the start of the tracer deposition. Top panel: ^6Li substrate prepared in a glovebox atmosphere with < 0.1 ppm H_2O and O_2 (same profile as in Fig. 4.3b). Bottom panel: glovebox atmosphere with ~ 1 ppm of H_2O and O_2. **b**, XPS signal of the Li 1s and Mg 2p regions for fresh surfaces of ^6Li (left) and $^7Li_{0.9}Mg_{0.1}$ (right). Ar^+ ions were used for depth profiling with the following sputtering steps: 2×2 min, 2×5 min, 2×15 min. The bottom spectra represent the surface of the sample before the sputtering step. The LiOH peak might contain some Li_2CO_3 contributions.

fitting. In this scenario, the measured diffusion coefficient is one order of magnitude lower than the value reported in section 4.2, highlighting the substantial impact that even a small amount of contamination can have on the measured lithium diffusivity. The good agreement of our results in section 4.2 with most of the literature data on direct measurements of lithium diffusivity suggests that the amount of contamination under well-controlled glovebox conditions does not appear to strongly distort the lithium diffusivity measurements.

Furthermore, the levels of surface contamination on both ^6Li and LiMg surfaces were analysed by X-ray photoelectron spectroscopy (XPS). Figure 4.7b illustrates the XPS spectra of the Li 1s and Mg 2p regions for pure lithium and $Li_{0.9}Mg_{0.1}$ samples. Freshly cut surfaces were quickly transferred from the glovebox to the XPS chamber within an argon-filled transfer vessel to minimize contact with atmospheric contaminants. Despite these precautions, the XPS results indicate that even fresh surfaces contain some signals from lithium oxide and from lithium hydroxide or carbonate,

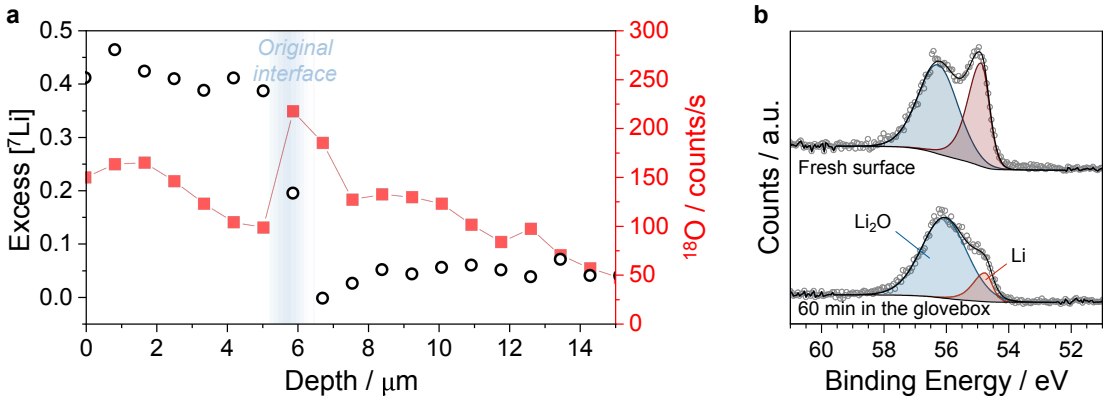


Figure 4.8. Long exposure to optimal glovebox environment. **a**, Diffusion profile of ^{7}Li into ^{6}Li including the ^{18}O SIMS signal at 60 min after the start of the tracer deposition. The ^{6}Li was exposed to a glovebox atmosphere of $<$ 0.1 ppm H_2O and O_2 for 60 minutes. Note how this exposure hinders the diffusion of the ^{7}Li tracer film. **b**, XPS spectra of the Li 1s region for a fresh ^{6}Li surface (top) and after 60 minutes of glovebox exposure. The spectra were collected after approximately 30 minutes of Ar^+ sputtering.

which can be challenging to distinguish. In situ Ar^+ sputtering in the XPS chamber can reveal the underlying metallic signal [97], which is exposed after the same duration of Ar^+ sputtering for all samples (see Fig. 2.3 in the Experimental Methods chapter 2 for the full XPS data set). Therefore, since the same contaminant species are seen across all surfaces, with a similar evolution upon Ar^+ sputtering, we conclude that the impact of unavoidable surface contamination on the measurements of lithium diffusivity is likely similar for both lithium metal and LiMg alloys.

An additional experiment was conducted to assess the effect of more severe lithium surface contamination on lithium diffusivity. A ^{6}Li freshly cut surface was left exposed to the glovebox atmosphere (with $<$ 0.1 ppm H_2O and O_2) for an extended period of 60 minutes. Then, the ^{7}Li tracer thin film was thermally evaporated and the isotope heterostructure was analysed by PFIB-SIMS. Figure 4.8a displays the ^{7}Li concentration depth profile after 60 minutes from the start of the evaporation. The profile reveals a sharp step at the contaminated $^{7}Li/^{6}Li$ interface, representing a barrier to the diffusing species. In Fig. 4.8b, the XPS of the ^{6}Li surface exposed to the glovebox for 60 minutes is compared to the spectrum of a fresh ^{6}Li surface, following approximately 30 minutes of in-situ Ar^+ sputtering in the XPS chamber. A significant amount of Li_2O remains on the lithium metal exposed to the glovebox, while the metallic lithium peak is more pronounced on a freshly cut lithium piece. Therefore, achieving accurate control of the glovebox atmosphere and minimizing

exposure time are both essential for the successful measurement of lithium diffusion coefficients with SIMS.

4.5 Conclusions

This chapter investigated the diffusivity of lithium in pure lithium and in LiMg alloys containing 10, 20, and 30 at. % Mg with an isotope tracer method, employing SIMS to track the isotope diffusion. In contrast to certain literature reports, the lithium diffusivity in LiMg is notably slower compared to lithium self-diffusion, with approximate values of 2×10^{-11} and 1.6×10^{-10} cm^2 s^{-1} respectively. This information is significant for the design of solid-state batteries. To date, the stable electrode/electrolyte interface and good cycling performance of cells constructed with a wide range of lithium alloys have often been attributed to faster lithium diffusivity. The experiments in this chapter show that this suggestion must be challenged. Despite the smaller lithium bulk diffusion rate, a LiMg alloy can deliver a considerably larger stripping capacity than a lithium metal electrode when operated at relatively low current densities. This behaviour was elucidated by revealing that the LiMg alloy maintains a stable interfacial contact with the LLZO solid electrolyte, so that lithium atoms can continuously diffuse to the electrolyte surface. In essence, it is the improved morphology of the interface that provides operational stability.

In contrast, the presence of large voids in the lithium metal electrode impedes the transport of lithium atoms, even though the bulk diffusion coefficient in the anode is greater. However, at larger stripping current densities, the slower bulk diffusion kinetics in the LiMg alloy electrode eventually restricts the stripping capacity so that, under these conditions, a lithium metal electrode outperforms the LiMg alloy. The comparison between pure lithium and LiMg stripping behaviours can be understood in terms of an effective diffusivity, which depends on the cross-sectional area available for diffusion into the solid electrolyte (see Fig. 4.9).

It is worth repeating that these experiments were conducted in the absence of external pressures to rule out creep effects. In practical solid-state cells, some pressure would be commonly applied, partially closing the voids at the Li/LLZO interface. Nevertheless, very high stack pressures would be necessary to counteract the rate of void formation during stripping, in particular at commercially relevant current densities exceeding 4 mA cm^{-2}. Therefore, this study remains relevant also in this scenario, where voids would likely still develop. At such large current densities, LiMg alloys may not be suitable because of their lower diffusivity. Hence, the search for

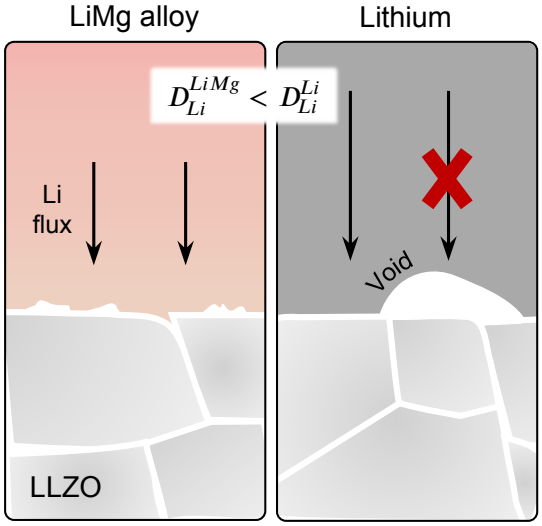


Figure 4.9. Effective diffusivity at the metallic anode/LLZO interface. An effective diffusivity across the metallic anode/LLZO interface can be defined as the lithium diffusivity in the electrode but reduced by a factor which takes into account the cross-sectional interfacial area with LLZO. Because lithium diffusivity in LiMg alloys is slower than in pure lithium, the effective diffusivity of a pristine interface is also slower in LiMg. However, as stripping goes on and bigger voids are formed at the pure lithium/LLZO interface, the effective diffusivity of pure lithium decreases and can fall below that of LiMg alloys, which maintain a more stable contact area.

a lithium alloy with a fast lithium bulk diffusivity is still important, not only for its influence during lithium stripping but also to keep the lithium activity at the interface below 1 during lithium plating. To do so, isotope tracer methods can be useful to probe the bulk diffusivity directly, without relying on model assumptions.

Lastly, a small amount of unavoidable surface contamination from the glovebox atmosphere does not appear to suppress the diffusion of lithium. However, a more serious surface reaction, resulting from either a contaminated glovebox atmosphere or prolonged exposure to a well-controlled atmosphere, can markedly hinder lithium diffusivity across the isotope heterostructure interface. As discussed in chapter 3 for the surface contamination of LLZO, careful handling of air-sensitive materials is critical even in the supposedly inert atmosphere of a glovebox, and a small amount of contamination should always be taken into account. The surface contamination on metallic anodes may have an impact on the effective diffusivity of lithium across the electrode/LLZO interface, and affect the stripping and plating performance of solid-state cells. Further investigations into this matter may prove beneficial to the battery research community.

The study of lithium diffusivity in LiMg outlined in this chapter will prove valuable

also in the following chapter, which investigates the initiation of dendrites on the surface of LLZO during lithium plating.

Chapter 5

Initiation of Dendritic Failure of LLZO via Sub-Surface Lithium Deposition

The formation of lithium dendrites through the solid electrolyte during plating constitutes a primary challenge for the widespread adoption of power-dense solid-state cells. Remarkably, there is still no definitive understanding of the mechanism behind dendrite formation. The primary suspect for the initiation of dendrites appears to be inhomogeneities at the Li/LLZO interface, where the plating current can intensify, causing a pressure build-up that can lead to mechanical damage and initiate a dendrite. This chapter aims to shed light on the origin of lithium dendrites in LLZO by investigating the Li/LLZO interface after dendritic cell failure. Plasma focused-ion beam (PFIB) is employed to image the sub-surface region of LLZO, which plays a crucial role in this process.

This chapter serves as natural continuation of the previous one, which focused on lithium stripping, in particular on the interplay between lithium diffusivity in the bulk electrode and morphological stability of the electrode/LLZO interface. For that purpose, it compared the behaviour of LiMg alloys with that of pure lithium metal electrode to achieve a better understanding of the behaviour of pure lithium metal itself. Likewise, in the following sections, comparing LiMg/LLZO and Li/LLZO interfaces during plating provides valuable insights into the behaviour of pure lithium metal. In particular, it will prove crucial when characterizing the initial stages of dendrite formation on the LLZO surface.

5.1 Introduction

Lithium filaments or 'dendrites' can penetrate through a solid electrolyte such as LLZO even at relatively small current densities, resulting in the premature failure of the cell [165, 166]. As previously discussed in the introduction to this thesis, the precise mechanism underlying the formation of these lithium dendrites is a subject of ongoing debate, but it is generally accepted that they tend to initiate preferentially at current hot spots situated at the interface between the lithium electrode and the solid electrolyte [26, 167]. These hot spots can arise due to various inhomogeneities, including grain boundaries, microcracks on the solid electrolyte surface, or areas with poor interfacial solid-solid contact [39, 53, 65]. Here, the pressure generated by plated lithium can either create new cracks or extend existing microcrack, thereby establishing a self-sustaining mechanism that cascades throughout the solid electrolyte [55, 58].

Recently, it has been proposed that lithium may also plate internally within occluded regions in the SE, without a direct electrical connection to the plating electrode [69, 70, 168, 169, 170]. While the electrical conductivity of bulk SEs is typically insufficient to allow isolated lithium plating, with values ranging between 10^{-8} and 10^{-10} S cm^{-1} [171, 172, 173], reduced band gaps at grain boundaries and pore surfaces could facilitate current leakage, making these regions susceptible to such phenomenon [66, 67, 93, 174, 175, 176]. The pressure build-up resulting from isolated lithium deposition could lead to localized mechanical damage within the solid electrolyte, consequently promoting the propagation of lithium dendrites. However, the existing literature lacks clear data that unequivocally demonstrate the feasibility of isolated lithium deposition. In general, distinguishing between isolated lithium deposits and lithium dendrites connected to the plating electrode presents a formidable challenge. X-ray tomography has traditionally been the primary tool for obtaining three-dimensional insights into the solid electrolyte and investigating internal lithium deposition. However, this approach has limitations, including low resolution and low phase contrast between metallic lithium and ceramic materials [62, 177, 178]. Therefore, additional evidence is crucial to substantiate the possibility of isolated lithium deposition in various solid electrolyte materials and to elucidate the relative importance of the two degradation modes, specifically dendrite propagation due to electrical degradation or classical mechanical fracture.

In this chapter, high-resolution PFIB analysis is employed to examine both the surface and sub-surface regions of LLZO pellets after lithium plating. Circular pothole

cracks or 'spallations' can be observed on the LLZO surface after peeling off the plating electrode. PFIB sectioning is used to investigate the morphology of these spallation cracks, revealing the presence of freshly plated lithium metal within them, which appears to have fractured the LLZO surface from within. To validate the physical isolation of freshly plated lithium from the plating electrode, a plating electrode containing 10 at. % of Mg was used, and magnesium diffusion through the plated lithium was tracked by energy dispersive X-ray spectroscopy (EDS) analysis. While magnesium diffusion is observed in the plated lithium connected to the LiMg electrode, pure lithium metal is found filling the early-stage cracks in the sub-surface volume. In addition, to gain a better understanding of the relationship between the isolated lithium deposition and the propagation of lithium dendrites, electron beam induced current imaging (EBIC) was employed on LLZO pellets following short-circuiting by lithium dendrites. This technique uses the secondary electron microscopy (SEM) electron beam to probe the electrical continuity between the surface cracks on the plating side and the lithium counter electrode. This novel approach confirmed that the spallation cracks on the LLZO surface can be the origin of short-circuiting lithium dendrites. Therefore, a theory is proposed whereby the isolated lithium deposition within the sub-surface region of the LLZO pellet causes the surface cracking and that the plating current focusing at these locations facilitates the propagation of lithium dendrites from the crack tips into the SE.

5.2 Spalling of LLZO during lithium plating

While LLZO holds promise as a suitable solid electrolyte, it appears to exhibit a great susceptibility to the formation of lithium dendrites, similarly to other solid electrolytes. The critical current density (CCD) values for LLZO often fall below 1 mA cm^{-2} [107]. When a Li/LLZO/Li cell is cycled at a current density exceeding a 'critical' value, lithium dendrites can grow from the electroplating working electrode (Li-WE in this chapter, as shown in Fig. 5.1a) and reach the stripping counter electrode (Li-CE), effectively causing a short-circuit. This results in almost the entire current flowing through the short-circuit, leading to cell failure. The growth of lithium dendrites can be detected by operando galvanostatic electrochemical impedance spectroscopy (GEIS) during a single plating step [179]. GEIS consists in applying a sinusoidal current perturbation and measuring the output voltage. This technique is typically preferred over PEIS, the potenstiostatic counterpart, for tracking impedance changes operando, by superimposing the AC current perturbation on a DC current.

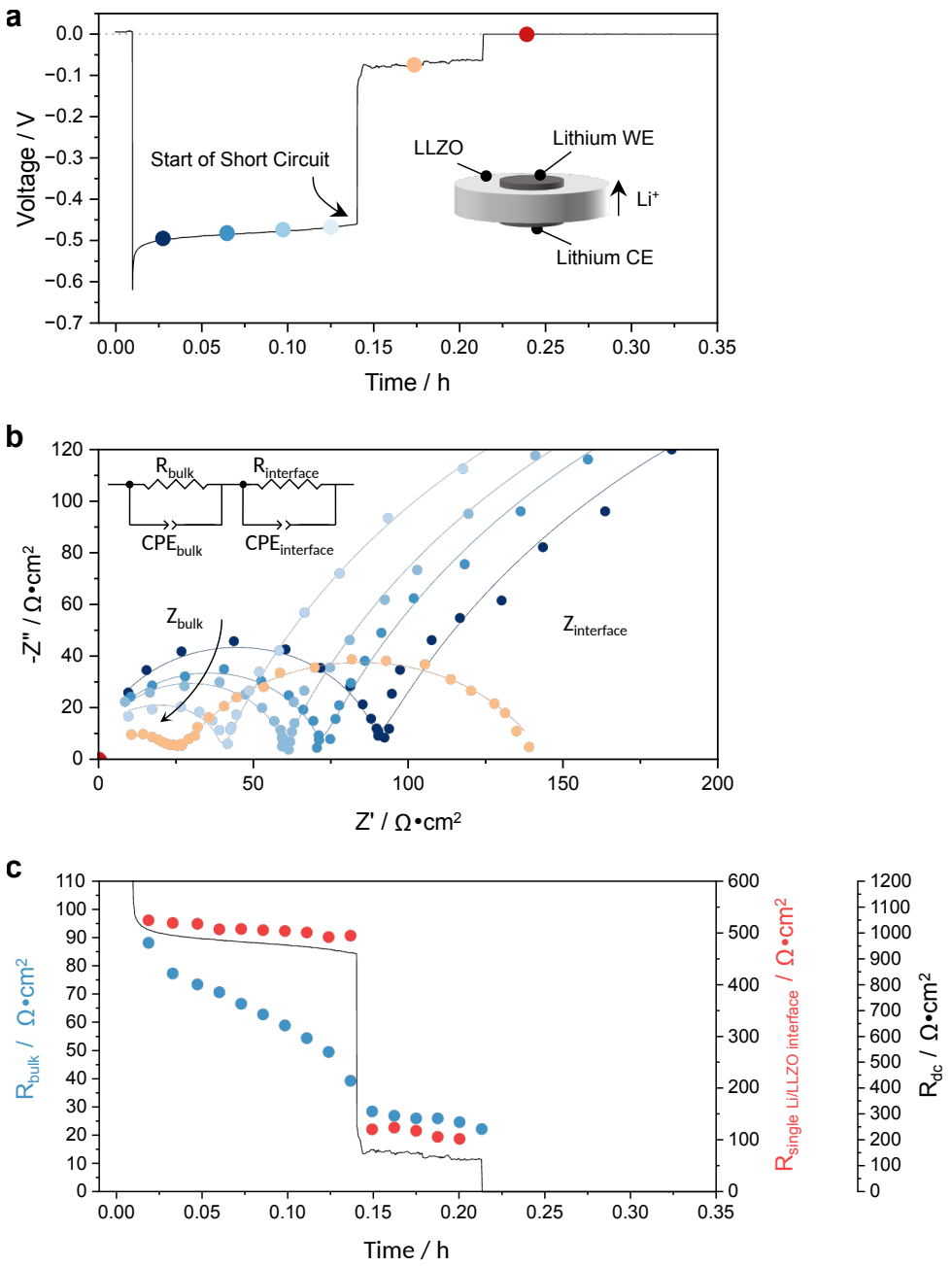


Figure 5.1. Tracking lithium dendrites with GEIS. a, Voltage versus time plot for the plating step of a Li/LLZO/Li cell at 0.5 mA cm^{-2} and 5 MPa stack pressure. The inset shows the symmetric cell setup, where the lithium WE is at the plating side. **b**, GEIS spectra corresponding to each coloured dot in **a**, and the equivalent circuit model used to fit them. **c**, GEIS spectra were collected every 20 seconds during plating, and the fitted R_{bulk} and R_{int} are here compared to the DC resistance of the cell.

Figure 5.1b shows the GEIS spectra of a Li/LLZO/Li cell acquired while plating lithium at 0.5 mA cm^{-2}. Similarly to PEIS Nyquist plots encountered before (Figs. 2.11 and 3.11), a typical GEIS spectrum of a Li/LLZO/Li cell comprises two semi-circles: one at high-frequency and one at low-frequency, corresponding to the bulk LLZO and the Li/LLZO interface, respectively [26]. The inset in Fig. 5.1b illustrates the equivalent circuit model used to fit the GEIS spectra and extract R_{bulk} and R_{int} values, whose evolution during plating is presented in Fig. 5.1c. The bulk LLZO contribution R_{bulk} gradually decreases in magnitude, indicating a reduction of the Ohmic resistance and, consequently, a decrease in the effective distance between the electrodes. This is due to lithium deposition in the LLZO, in the form of lithium dendrites or isolated lithium deposits. The initial decrease in R_{int}, although relatively smaller than that of R_{bulk}, can be explained by an improvement of the Li/LLZO contact resulting from lithium deposition. Eventually, a sudden drop in impedance, concurrent with a reduction in the DC resistance of the cell, signifies complete short-circuit of the cell. In the case of this specific cell, a partial short-circuit occurred at 0.14 h, before a complete cell failure.

It is essential to note that the Li/LLZO/Li cell was assembled without any pre-treatment to improve the Li/LLZO interfacial contact, such as the ones discussed in chapter 3. LLZO surface contaminants, such as Li_2CO_3 and LiOH, are lithiophobic and impede proper contact between lithium and LLZO, resulting in the initial R_{int} of a few hundred Ω cm^{-2} observed in Fig. 5.1b. In the first three sections of this chapter, a lithiophobic LLZO was intentionally used to facilitate the removal of the Li-WE after the cell short-circuit for inspection of the LLZO surface. The Li-WE was simply peeled off the LLZO pellet, often leaving very few lithium residues on the LLZO surface. The performance of the LLZO cell was compromised by the presence of surface contaminants, as a nominal plating current of 0.5 mA cm^{-2} was sufficiently large to induce dendritic growth. A surface-treated LLZO can reach higher critical current densities (see Fig. 3.13). However, this compromise was made to enable easy access to the LLZO surface after dendritic failure. Section 5.5 of this chapter employs acid-treated LLZO cells and it demonstrates that the LLZO failure mechanism remains the same, although a larger nominal current density is required to initiate it. Moreover, a large R_{int} can also develop during stripping of a Li/LLZO interface with nearly zero starting R_{int}, assembled with a surface-treated LLZO (see Fig. 5.2), using a relatively large current density of 2 mA cm^{-2}. In this scenario, the exponential increase in R_{int} is ascribed to the formatio of voids at the Li/LLZO interface, resulting in a short-circuit due to dendrite formation on the subsequent plating step [35], as

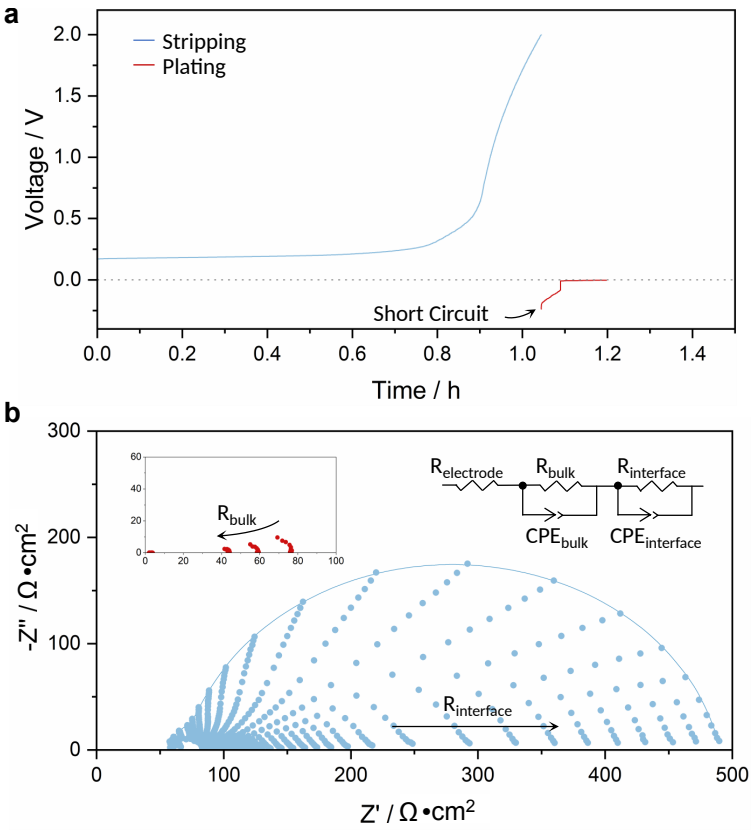


Figure 5.2. Cycling of a Li/LLZO/Li cell with nearly zero starting R_{int}. **a**, Voltage profile for the stripping and plating of a Li/LLZO/Li cell where the LLZO was subjected to $HCl_{(aq)}$ acid treatment prior to cell assembly, in order to remove the lithiophobic surface contaminants and obtain a nearly zero starting R_{int} (4 Ω cm^{-2}). The cell was cycled at 2 mA cm^{-2} and 5 MPa of stack pressure. **b**, GEIS spectra were taken at constant intervals during cycling and show a large increase in R_{int}. This results in the cell polarization visible in **a**. A short-circuit immediately occurs upon switching the current sign, due to the growth of lithium dendrites. During this process, the bulk impedance decreases as shown in the inset.

explained in sections 1.2 and 1.3. Therefore, none of the LLZO cell configurations studied here appears to avoid short-circuiting failure under commercially relevant cycling conditions.

After removing the Li-WE, circular cracks ranging from $\sim$ 5 to 100 μm in diameter can be observed on the LLZO surface, as shown in Fig. 5.3a. These cracks are similar to those recently reported in various SEs as spallations or spallation cracks [71, 72, 180, 181, 182]. PFIB sectioning of one of these surface spallation cracks reveals freshly plated lithium metal that seems to have extruded from beneath the surface and emerged out of the crack. PFIB serial sectioning was employed to study the three-dimensional view of such cracks, as depicted in Fig. 5.3b. A comprehensive account

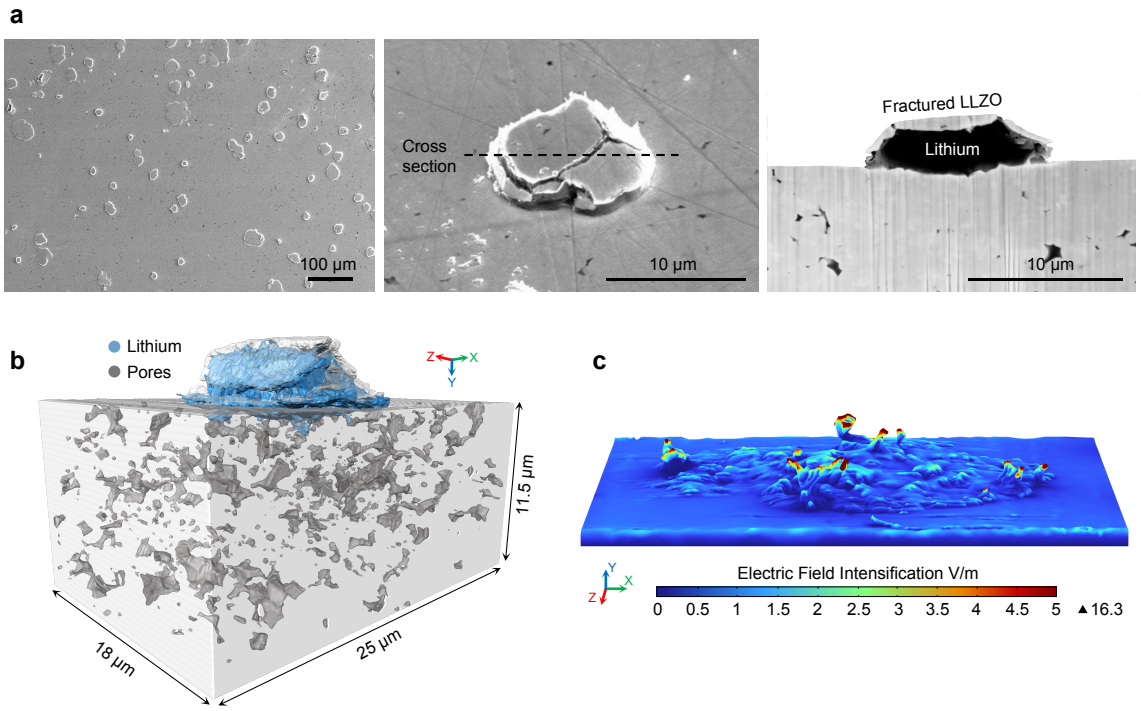


Figure 5.3. Spallation cracks on the LLZO surface after lithium plating. **a**, SEM images of the LLZO surface after short-circuit and peeling off the Li-WE, with a cross-section showing the fractured LLZO surface and the lithium metal below it. **d**, Three-dimensional view of the spallation crack shown in **c** and of the sub-surface porosity. **e**, Finite element modeling of the electric field distribution based on the reconstructed spallation crack in **d** (note the inversion of the direction of the y axis).

of the three-dimensional reconstruction procedure can be found in section 2.6. From the three-dimensional views, these cracks appear to be predominantly intergranular, running through previously isolated sub-surface pores located at grain boundary triple junctions. The LLZO pellets employed in this chapter were sintered at 1000 °C and have an Archimedes' density of 92.3% (see section 2.1 for the sintering procedure). These pellets exhibit larger sub-surface pores, facilitating the investigation of the pore contents using PFIB-EDS. These pores, typically featuring a concave geometry with pointed edges, appear to contain lithium metal, thus representing sharp lithium protrusions into the SE, where the geometrical concentration of the plating current would occur.

Finite element modeling of the electric field based on the crack surface reconstructed in Fig. 5.3b was carried out by Dr. Guanchen Li (University of Glasgow). COMSOL Multiphysics was employed to simulate the electric field within a rectangular solid electrolyte block, sandwiched between two voltage-biased lithium electrodes.

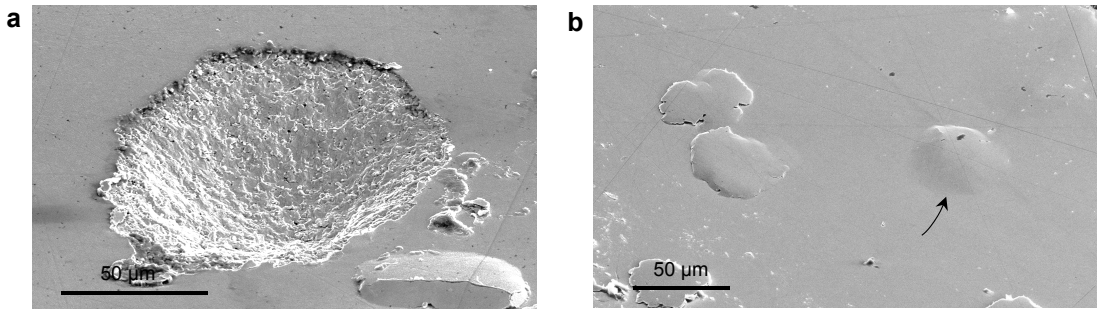


Figure 5.4. Additional SEM images of spallations. **a**, Large crater left on the LLZO surface after peeling the Li-WE off. The peeling process removed the fractured LLZO cap. Such spallations, going deep into the SE, can represent a spot for significant current intensification. **b**, Early-stage spallations, one of which (arrowed) appears to not yet have cracked the LLZO surface.

Specifically, Laplace's equation, $\nabla^2\Phi = 0$, governed the electric potential in the electrolyte Φ. Dirichlet boundary conditions (constant potential) were imposed at the lithium/solid electrolyte interface and no-flux Neumann conditions ($\overrightarrow{\nabla}\Phi = 0$) at other boundaries.

The modeling work demonstrated that the electric field in the spallation crack can be much greater than in the bulk of the SE, reaching an intensification of up to 16.3 V/m at the tip of some Li-filled pores connected to the spallation crack, as illustrated in Fig. 5.3c. The electric field is directly proportional to the local current density according to Ohm's law $\overrightarrow{i} = \sigma\overrightarrow{\nabla}\Phi$, so the plating current density in the spallation region must have been larger than the nominally applied value. The volume of lithium plated in the spallation crack in Figs. 5.3a and 5.3b is indeed larger than that expected from the nominal plated capacity for this specific sample (note that the cross-sectional images are tilted by 52° so the true vertical dimension is obtained by multiplying by 1.27). Considering that larger and deeper spallation cracks can be found on the LLZO surface after plating, such as the one in Fig. 5.4a, these surface cracks evidently represent hot spots of current intensification.

Similar spallation cracks are also observed when the Li-WE is left on the LLZO pellet, and the buried Li/LLZO interface is cross-sectioned with PFIB. For this cell, a lithium metal electrode of 50 μm thickness was used to facilitate the PFIB cross sectioning. Figure 5.5 shows SEM and EDS characterization of two spallation features, demonstrating that any mechanical damage introduced by peeling the Li-WE off is not the cause of these features. Moreover, EDS lanthanum maps confirm that the fractured LLZO surface is pushed into the lithium electrode. Considering that

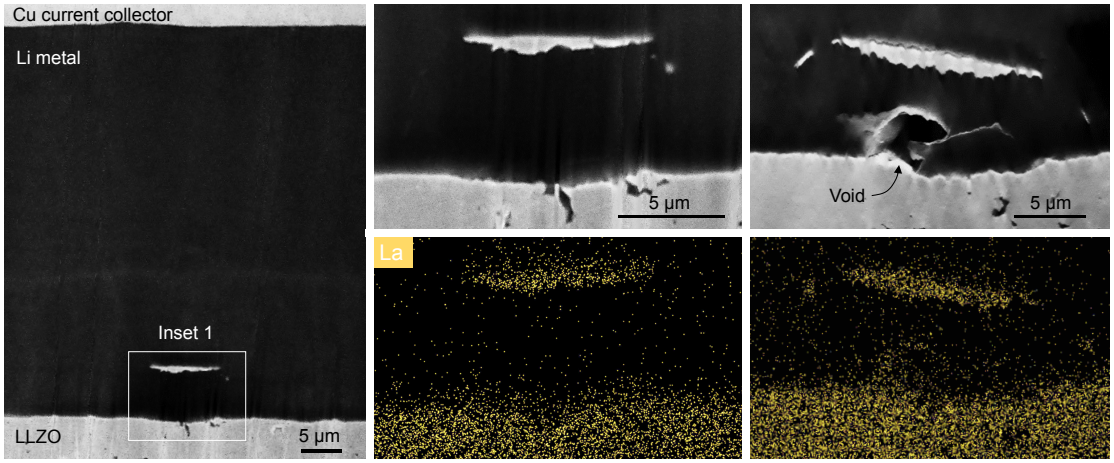


Figure 5.5. Spallation cracks at the buried Li/LLZO interface. SEM and EDS images of spallation cracks visible after lithium plating at the Li/LLZO interface, which was cross-sectioned with PFIB without peeling the lithium electrode off. The location of the fractured LLZO cap is confirmed by the La maps. This suggests that peeling off the lithium electrode introduces no or little mechanical damage, while it allows an easier access to the LLZO surface. The lithium plated below the spallation on the right contains a void, which has likely formed during plating.

5 MPa of external pressure was applied during plating, the pressure build-up from the freshly plated lithium must have been substantial. This could result from a very high local current density. For one of the spallations in Fig. 5.5, it appears that the lithium electrode could not deform quickly enough to accommodate the freshly plated lithium, resulting in the plated lithium being not fully dense, as a void can be observed. Additionally, clear indentations were observed on the surface of the peeled Li-WE, where the fractured LLZO surface was pushed into the soft lithium (Fig. 5.6).

In this section, removing the Li-WE allowed the investigation of the LLZO surface and sub-surface regions following dendritic failure, providing an unprecedented level of insight into the morphology of spallation cracks. The data collected suggest that spallations form at the plated interface due to a pressure build-up of lithium, which fractures the LLZO surface and pushes it into the lithium electrode. Among the many spallation cracks considered, some have not yet cracked to the LLZO surface, as seen for instance in Fig. 5.4b. These appear to be early-stage spallations that, with further plating, will eventually develop into fully formed circular cracks. The lithium contained in the spallations represents a protrusion into the LLZO sub-surface, so these cracks could serve as preferential site for the growth of lithium dendrites - as demonstrated in the next section.

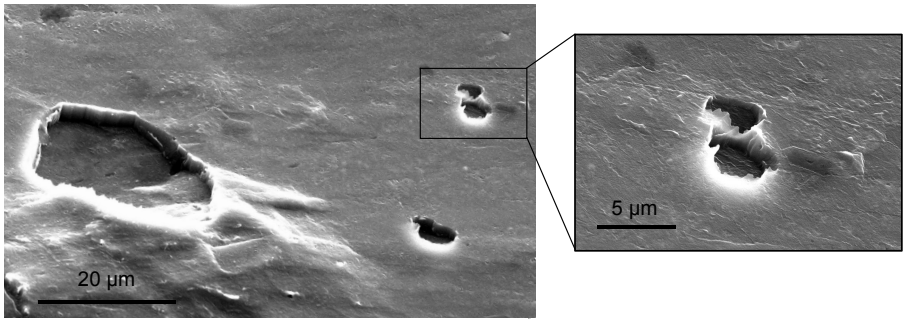


Figure 5.6. Indentations on the peeled lithium electrode surface. SEM images of the Li-WE surface showing indentations left by the fractured LLZO, which is pushed into the soft electrode by the lithium freshly plated in the spallation cracks.

5.3 Locating the short-circuiting dendrite

X-ray tomography may be employed to investigate the presence of lithium dendrites originating from the surface spallation cracks. However, the X-ray attenuating properties of LLZO make imaging of buried lithium challenging. Therefore, Electron Beam Induced Current (EBIC) imaging was used instead, with help from Yifu Shi (University of Oxford). EBIC is an SEM-based technique commonly applied to characterize semiconductor devices, usually a Schottky or pn-junction [183]. When the electron beam illuminates the semiconductor specimen, it induces the generation of electron-hole pairs, some of which can be collected at the EBIC device contacts, giving rise to a photocurrent. By scanning the electron beam, a two dimensional map of collected current is constructed, allowing the visualization of the collection efficiency of charge carriers within the semiconductor device.

In this section, EBIC imaging was utilized in a novel manner to characterize LLZO cells short-circuited by dendrites. Specifically, EBIC was used to assess the electrical continuity between the lithium metal contained in surface spallations on the plating side and the lithium counter electrode. Figures 5.7a and b depict the voltage profile and PEIS spectra for a Li/LLZO/Li cell subjected to a plating step until a short-circuit occurred. Subsequently, the Li-WE was carefully peeled off and the Li-CE was electrically connected to an SEM sample holder using a drop of Ag paste. The sample was then loaded into a Zeiss NVision 40 FIB-SEM equipped with a tungsten micromanipulator (Oxford Instruments Omniprobe100). There was a brief exposure to air for a few seconds during the loading process. The tungsten

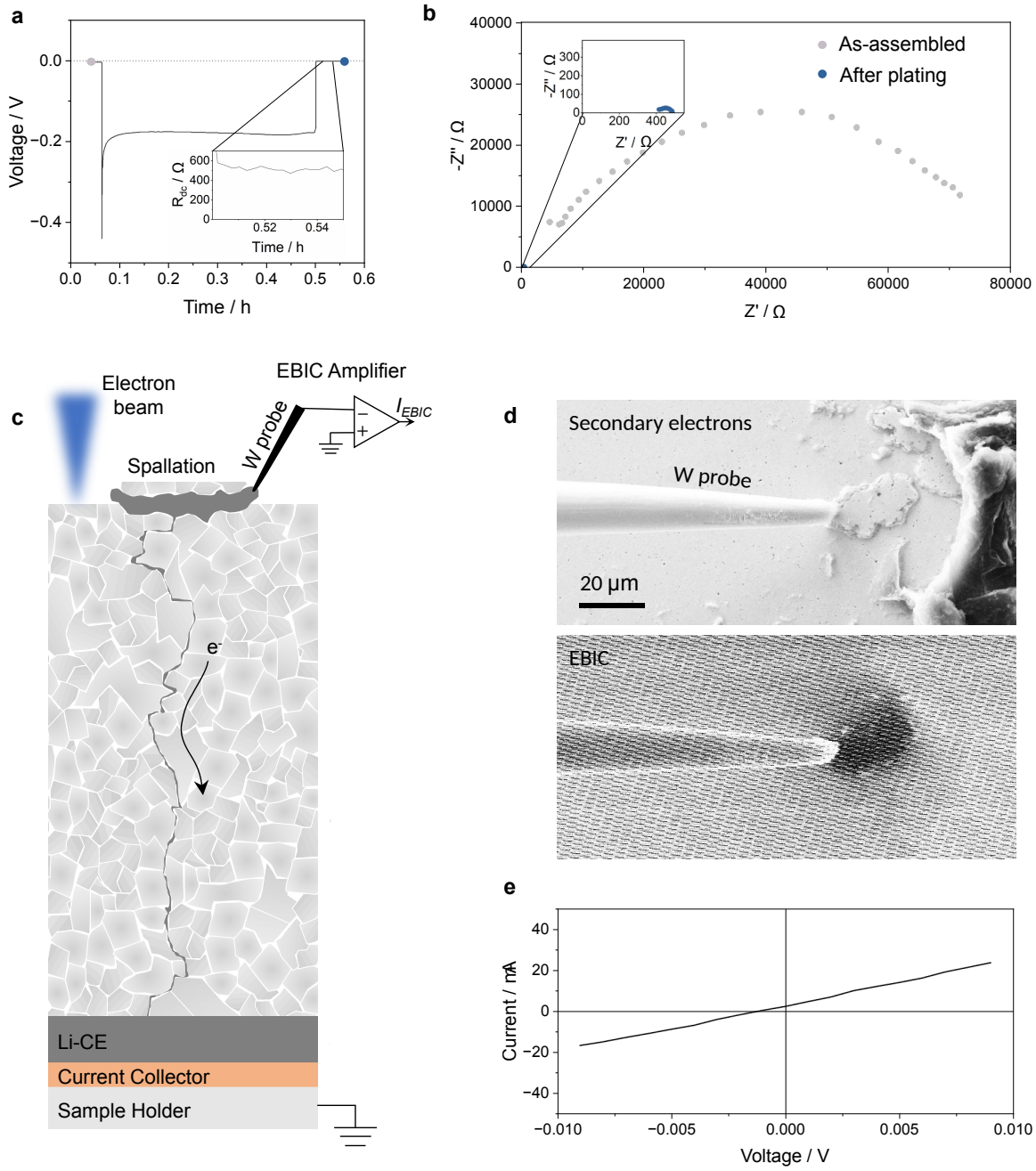


Figure 5.7. EBIC imaging of a surface spallation connected to the short-circuiting dendrite. **a**, Voltage profile of the Li/LLZO/Li cell used for the EBIC experiment. The cell shorted at 0.5 h, after which the cell resistance was $\sim$ 480 Ω. **b**, PEIS spectra before and after the plating step. **c**, Schematic of the experimental setup: a W microprobe is in contact with lithium metal extruding from the surface spallation crack. Excess electrons from the electron beam can be collected at the Li-CE through the short-circuiting lithium dendrite, with the circuit completed through the W microprobe and the current amplifier. **d**, SEM and EBIC images showing a current contrast arising at the surface spallation, indicating electrical connection between the spallation and the Li-CE. **e**, I-V curve of the lithium dendrite showing resistive behaviour.

microprobe was carefully connected to the lithium metal extruding from a spallation crack on the LLZO surface and then to the grounded SEM sample stage through a current amplifier (Point Electronic), while the Li-CE is in contact with the SEM sample stage (see the schematic in Fig. 5.7c). A lithium dendrite originating from the spallation crack and extending to the Li-CE would effectively close the electrical circuit. When the electron beam illuminates the spallation crack region, a portion of the excess electrons is collected at the device contacts, resulting in a current. EBIC map images were acquired at an accelerating voltage of 20 kV and analyzed using the DISS 5 software package (Point Electronic). A large accelerating voltage was selected to ensure an adequate number of electrons reached the lithium contained within the spallation crack.

Figure 5.7d shows a spallation crack exhibiting dark contrast as excess electrons are collected by the SEM sample stage through the lithium dendrite, confirming that the lithium within this surface crack is electrically connected to a short-circuiting lithium dendrite proceeding from the surface crack. It is important to note that the Li-WE diameter was limited to 100 μm by using a polyimide tape laser-cut mask to define the electrode area. This limitation ensured that the number of surface spallation cracks to probe with EBIC was no more than ten. Only one spallation on the surface of this specific LLZO pellet exhibited a dark contrast in EBIC mode. The I-V curve in Fig. 5.7e, measured through the EBIC contacts, reveals a lithium dendrite resistance of 440 Ω. This value aligns well with the cell resistance following short-circuiting, which was measured at 487 Ω as reported in the inset in Fig. 5.7a. Assuming a straight pure lithium dendrite running through the LLZO pellet, its diameter would be approximately 500 nm. However, in reality, a network of irregular filaments with smaller diameter typically extends through the LLZO pellet [72].

Following the EBIC analysis, PFIB was employed to cross-section the sub-surface region beneath the spallation crack. As anticipated, it was possible to identify a narrow crack with a diameter ranging from 50 to 100 nm running through the LLZO porosity (Fig. 5.8). Locating this dendritic crack with X-ray tomography would be extremely challenging, as high-resolution PFIB was necessary to visualize the thin crack. Therefore, the unconventional use of EBIC imaging in this section was essential to demonstrate that the short-circuiting failure of LLZO likely originates from the tip of the surface spallation cracks, where the current density is at its maximum.

In another short-circuited LLZO cell, a macroscopic crack could be observed running through some surface spallations (Fig. 5.9a). The crack was subsequently manually cleaved in a glovebox, revealing that it contained lithium metal and it extended

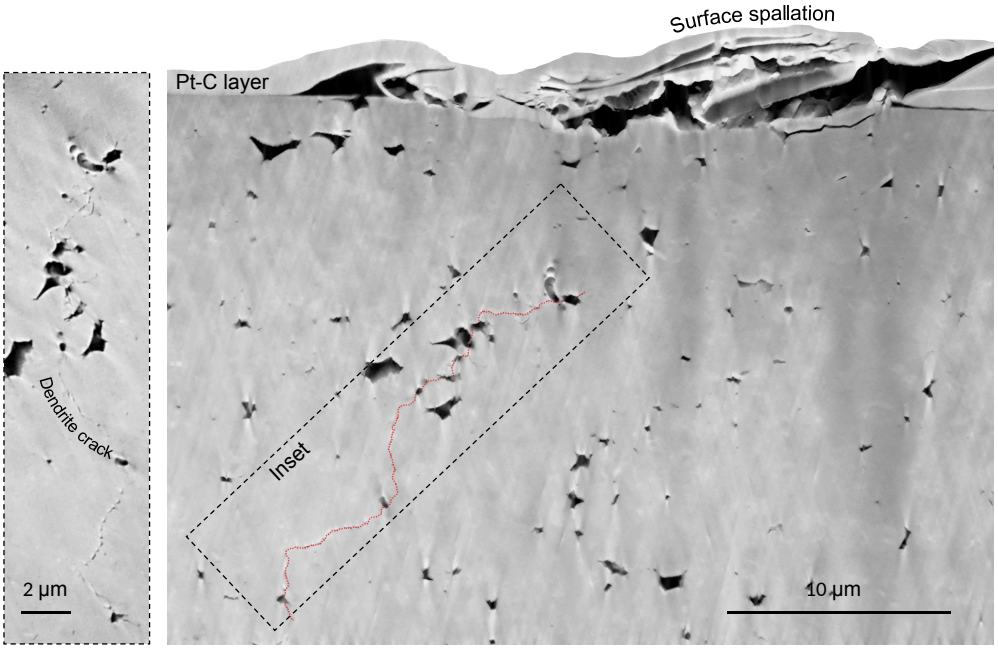


Figure 5.8. Cross section of the spallation crack after EBIC. The PFIB cross section of the surface spallation reveals a thin crack extending into the LLZO pellet. The image was post-processed to remove the vertical curtaining lines.

from the surface spallations through the entire LLZO pellet (see Fig. 5.9b). It is likely that a significant amount of lithium was plated within this crack before the final short-circuit occurred, and the combined pressure from lithium plating and from the external stack pressure applied to the Li/LLZO/Li cell ultimately opened the crack so that it became visible at a macroscopic level. This observation suggests that surface spallations not only represent a spot for the concentration of current density, as demonstrated by the modeling in section 5.2, but also serve as stress concentration points on the polished LLZO surface. The interaction of these two factors determines the growth of dendrites through the solid electrolyte.

5.4 Using magnesium to look for isolated lithium deposits

The growth of a transverse dendrite crack from a surface spallation is consistent with prior research on Li_6PS_5Cl solid electrolyte [180], as reported for instance in Fig. 1.8b in the introduction chapter of this thesis. Nevertheless, the mechanism responsible for the formation of these spallation cracks has been so far unclear. Considering that

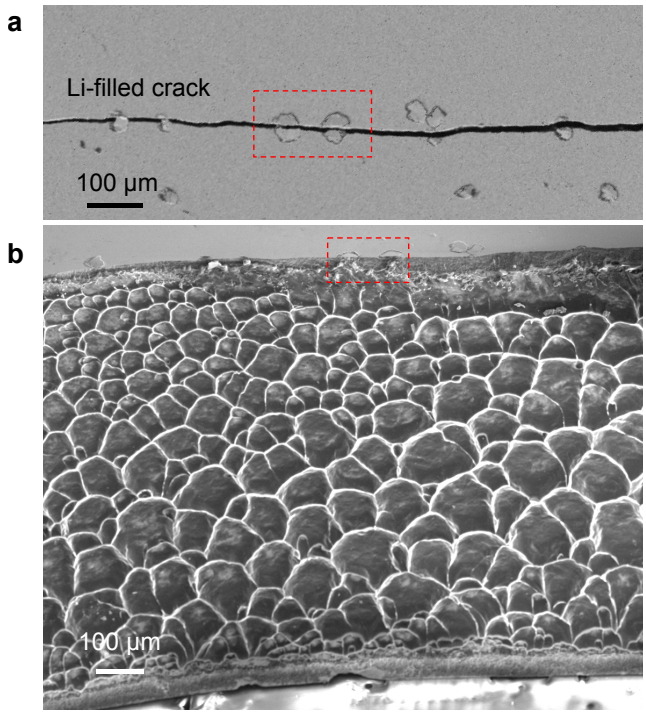


Figure 5.9. Macroscopic lithium-filled dendritic crack. **a**, SEM image of the surface of a short-circuited LLZO pellet. A large crack runs through some surface spallations, suggesting that they represent hot-spots for the focusing of both electrical current density and mechanical stress. **b**, The pellet was manually cleaved to reveal that the crack is full of lithium, which displays the typical cone fracture morphology of a ductile metal. The spallation cracks are still visible on the top surface.

these surface features seem to play a significant role in the initiation of dendritic cell failure, a more comprehensive investigation into their origins became imperative. The morphology of early-stage spallation cracks, such as those illustrated in Fig. 5.4b, suggests an internal and isolated origin of the pressure build-up that ultimately causes the crack to open to the LLZO surface. This agrees with earlier studies that hint at the possibility of electronic leakage currents in the solid electrolyte and the formation of lithium deposits within occluded pores, as reviewed in section 5.1.

In addition, it was found that the population density of the spallation cracks decreases as pellet density increases. Surface SEM images of LLZO pellets after dendritic failure are presented in Fig. 5.10a. These pellets were sintered at different temperatures and therefore have different densities, as detailed in section 2.1. Notably, the number of surface spallation cracks significantly decreases in denser pellets. This suggests that the pressure build-up leading to the LLZO surface cracking may occur within sub-surface porosity.

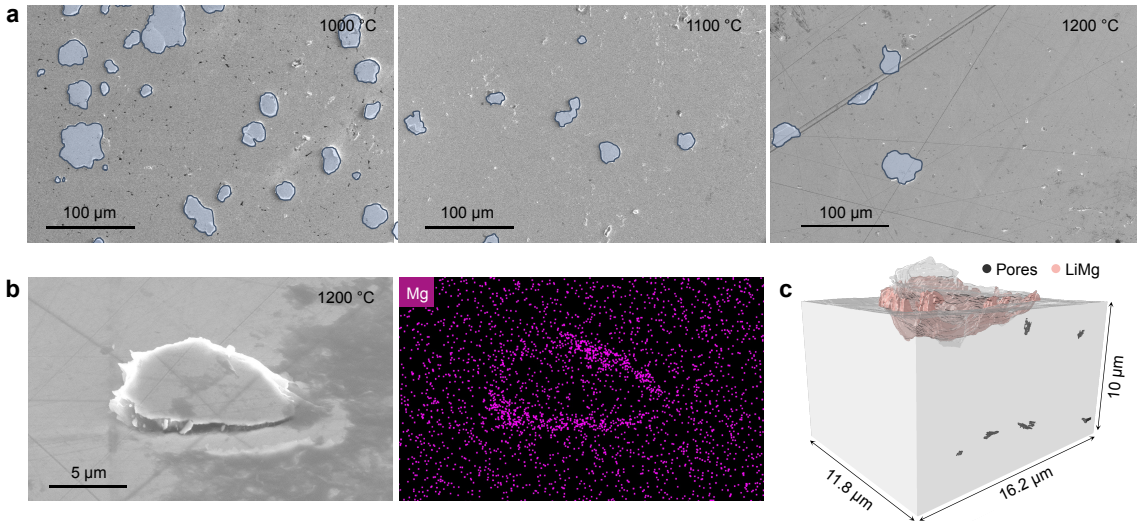


Figure 5.10. Population density of surface spallation cracks with LLZO density. **a**, SEM images of the LLZO surface after dendritic failure, showing that as the LLZO density increases with sintering temperature, the number of surface spallation cracks decreases. **b**, SEM and EDS images and **c**, three-dimensional reconstruction of a spallation crack on a $> 99\%$ dense LLZO pellet, sintered at 1200 °C. The pellet was assembled with a LiMg-WE, so magnesium could diffuse into the freshly plated lithium in the crack.

Therefore, this section embarks on an investigation of early-stage spallations in search for isolated internal lithium deposition. However, despite the high spatial resolution of PFIB, there remains a possibility of a narrow lithium path, invisible to SEM, connecting the lithium in the surface crack to the Li-WE, even when the lithium deposit appears isolated. The impossibility of detecting lithium with EDS analysis makes the investigation even more challenging. Consequently, instead of employing a pure Li-WE, a LiMg alloy containing 10 at. % Mg was utilized as working electrode. From the secondary ion mass spectrometry data in chapter 4, the diffusivity of lithium in LiMg alloys is quite fast, although not as fast as lithium self-diffusivity. Moreover, when pure lithium and LiMg are placed in contact, the interdiffusion of lithium and magnesium occurs. This motivated the use of a LiMg-WE here. Magnesium will spontaneously diffuse into plated lithium that is physically, i.e. electrically, connected to the LiMg-WE because of the magnesium compositional gradient. Subsequently, EDS can be used to unequivocally detect the presence of magnesium. Moreover, the addition of 10 at. % Mg only marginally increases the anode voltage by a few meV and is not expected to alter the electrodeposition behavior [41]. The mechanical behaviour of such LiMg alloy is also very similar to that of pure lithium.

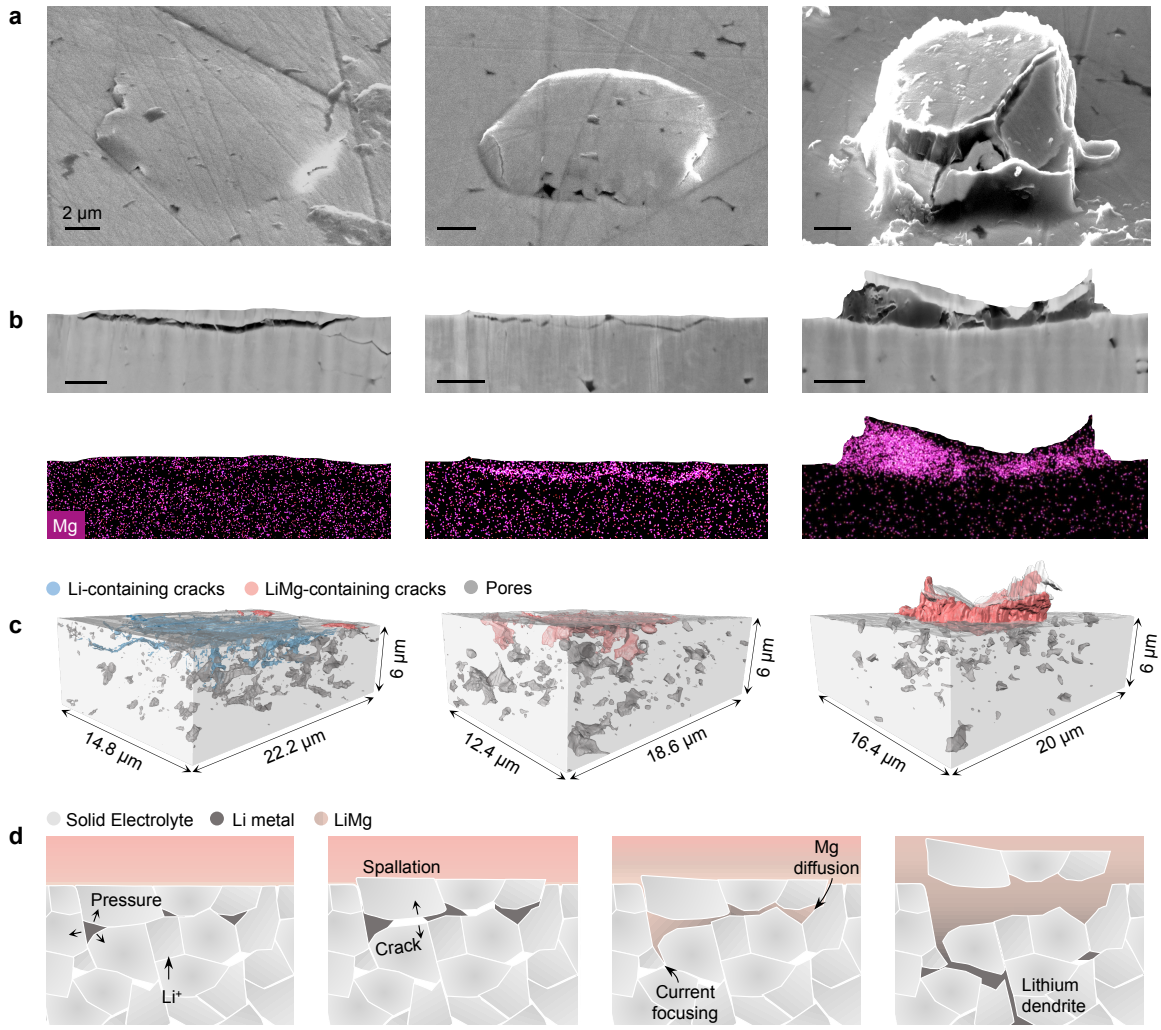


Figure 5.11. Different stages of the formation of surface spallations at the LiMg/LLZO interface. **a**, SEM images of three different spallation cracks found on the LLZO surface after short-circuiting of a LiMg/LLZO/Li cell and peeling off the LiMg-WE. **b**, Cross-sectional SEM and EDS images showing the diffusion of magnesium in some Li-filled cracks, those in which lithium was physically connected to the LiMg-WE. The Pt-C protective layer deposited prior to PFIB sectioning has slightly modified the appearance of the fractured LLZO. **c**, Three-dimensional views of the surface cracks identifying those filled with Li or LiMg. **d**, Schematic with the proposed formation mechanism and evolution of a spallation crack at the LiMg/LLZO interface.

A LiMg/LLZO/Li cell was assembled, and lithium was plated at the LiMg/LLZO interface until a short-circuit occurred. The LiMg-WE was peeled off after a period of at least 15 days, to allow sufficient time for magnesium to diffuse through the freshly plated lithium. Figure 5.11a displays three spallation cracks found on the surface of the same LLZO pellet, representing different stages of crack development. The initial spallation crack (on the left of Fig. 5.11a) has not yet fully developed. However, PFIB cross-sectioning reveals the presence of some lithium metal within the spallation, although not uniformly distributed throughout the entire crack (Fig. 5.11b). No magnesium signal could be detected, implying that the lithium metal in the crack has not come into direct contact with the LiMg-WE. In contrast, magnesium is found to have diffused into the lithium within the second crack, which thus must have been in contact with the LiMg electrode. Finally, the fully developed spallation crack contains a substantial amount of lithium metal, and the existence of a channel for the diffusion of magnesium into the crack can be expected. Indeed, EDS analysis exhibits a strong magnesium signal. The three-dimensional reconstructions of these spallation cracks obtained by automated serial sectioning of LLZO are reported in Fig. 5.11c. It should be noted that the possibility of magnesium content in the early-stage spallation crack being below the sensitivity threshold of EDS analysis cannot be ruled out. Nevertheless, magnesium appears to readily diffuse within narrow cracks filled with lithium, as demonstrated in the second spallation crack in Fig. 5.11. In this crack, magnesium was also detected in certain pores located further away from the LLZO surface and connected to the spallation through a very thin crack, as reported in Fig. 2.13d in the Experimental Methods chapter.

The proposed evolution of a spallation crack for a LiMg/LLZO/Li cell is illustrated schematically in Fig. 5.11d. Lithium plating within the sub-surface porosity of the LLZO pellet results in an internal pressure build-up exceeding the fracture strength of the solid electrolyte, leading to crack formation. As more lithium is plated within the crack, the fractured LLZO surface is pushed into the soft Li-WE, connecting the lithium within the crack to the LiMg-WE, thereby creating a channel for magnesium diffusion. From this point onward, lithium will preferentially plate inside these cracks, where it is confined to a small volume, and the substantial pressure build-up drives further crack growth.

These findings show that LLZO appears to be susceptible to isolated lithium deposition. Moreover, the presence of spallation cracks on the solid electrolyte surface may serve as evidence for the ability of lithium to deposit within occluded sub-surface porosity. Similar spallation cracks were also observed on the surface of Na β-Al_2O_3, a

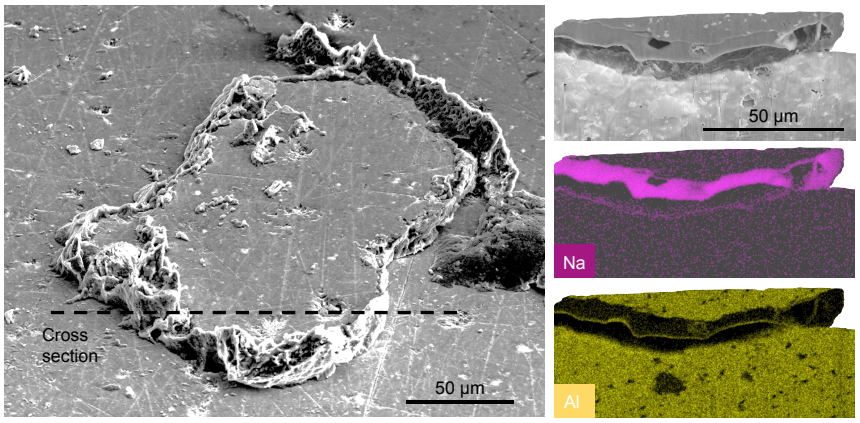


Figure 5.12. Spallation crack on the surface of Na β-Al_2O_3. **a**, SEM and EDS images of the surface and cross-section of a Na β-Al_2O_3 pellet. The pellet was cycled in a symmetric Na/β-Al_2O_3/Na cell configuration until short-circuit, then the plated Na-WE was peeled off. A large spallation crack is visible where Na metal has plated between the pellet and the fractured surface, similar to the LLZO behaviour.

sodium-ion conducting solid electrolyte. Na β-Al_2O_3 pellets were procured by Ionotec, and Na/β-Al_2O_3/Na symmetric cells were assembled and subjected to a plating step at 0.5 mA cm^{-2}, following the same procedure outlined for lithium cells. Figure 5.12 shows the SEM surface image and PFIB cross-section of a spallation crack on the Na β-Al_2O_3 surface following short-circuiting. EDS analysis confirms the presence of sodium metal within the spallation crack. It is worth noting that Na β-Al_2O_3 solid electrolytes were extensively studied before the advent of the lithium-ion cells and are already known to be susceptible to isolated internal deposition of sodium metal [184, 185]. The presence of spallations on various solid electrolytes indicates that the mechanism for the initiation of dendritic failure proposed in this chapter might be extended to systems other than LLZO.

5.5 Current density dependency of the formation of spallations

The conditions for internal lithium deposition appear to be met almost instantaneously upon the application of current to the cell. Figure 5.13a displays the EIS for a LiMg/LLZO/Li cell before and after only 10 μAh of lithium plating. Both R_{bulk} and R_{int} decrease after plating, as discussed in section 5.2, however the cell has not yet experienced a short-circuit. After removing the LiMg electrode, early-stage spallation cracks are observed on the LLZO pellet, such as the one in Fig. 5.13b. This

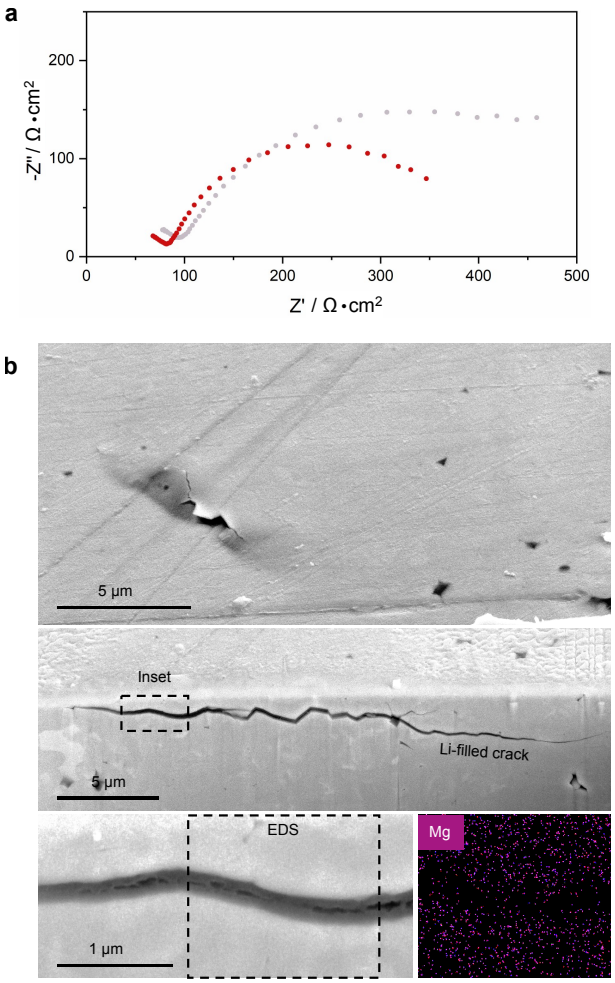


Figure 5.13. LLZO spalling after 10 μAh cm^{-2} of plated capacity. **a**, PEIS spectra of a LiMg/LLZO/Li cell before and after 10 μAh cm^{-2} of capacity plated at 0.5 mA cm^{-2}. R_{bulk} decreases after plating, but the cell has not short-circuited. **b**, Surface SEM and cross-section of a spallation crack after peeling off the LiMg-WE, confirming the presence of sub-surface lithium at a very early stage of plating. The magnesium EDS signal is absent from the lithium plated in the crack.

spallation was cross-sectioned using the PFIB equipped with a cryo-stage, keeping the sample stage at -150 °C to ensure that the presence of lithium within the crack is not due to beam damage [186]. The serrated crack shape suggests it developed mainly intergranularly. Lithium metal appears to be indeed already present within the spallation, although magnesium was not detected by EDS analysis throughout the crack, suggesting that lithium had not come into contact with the LiMg-WE. These findings can help explaining the propensity for dendrite formation in LLZO at small nominal current densities. In fact, as soon as the current is applied, the local current value immediately diverges from the nominal one due to the intensification at the spallation crack tips.

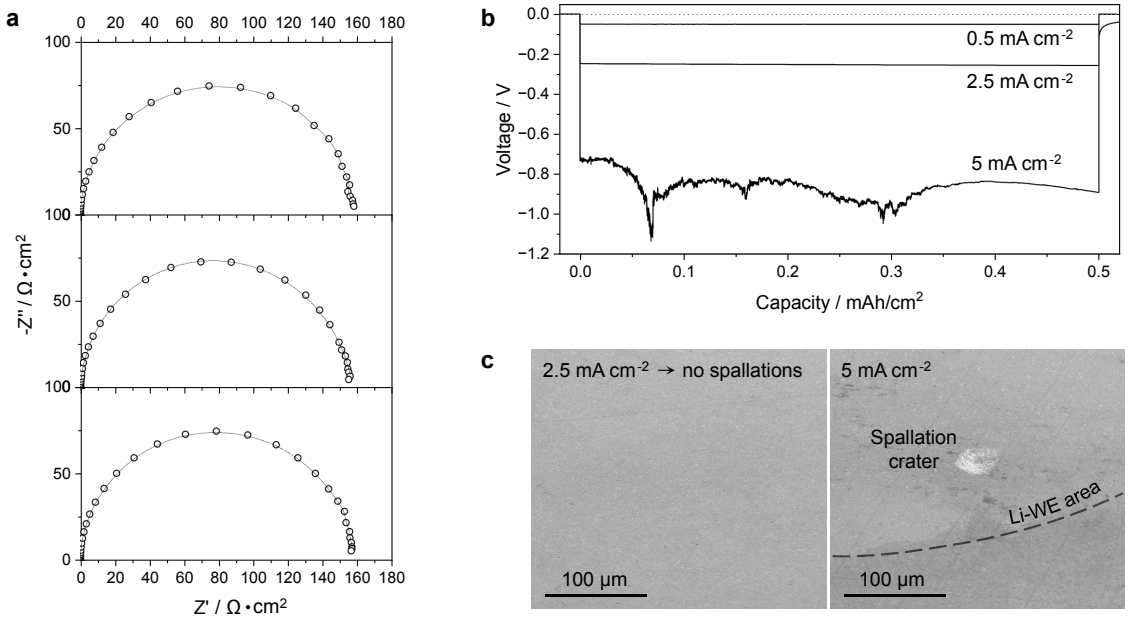


Figure 5.14. Current dependency of the spalling process. **a**, EIS profiles of the cells assembled with acid-treated LLZO and cycled at 0.5, 2.5, and 5 mA cm^{-2} (from top to bottom). The starting Li/LLZO interfacial impedance R_{int} is lower than 6 Ω cm^{-2} for all cells. **b**, Voltage traces at different plating current densities for the Li/LLZO/Li cells assembled with acid-treated LLZO. **c**, SEM surface images of the different LLZO pellets after plating 1 mAh cm^{-2} and dissolving the plating lithium electrode in ethanol.

At this point, it became pertinent to investigate whether there exists a minimum current density for the formation of surface spallations. However, the initial interfacial resistance R_{int} between Li or LiMg and LLZO for the cells employed so far in this chapter was relatively large, rendering the local plating current density value difficult to pinpoint. Therefore, an acid treatment with $HCl_{(aq)}$ was performed to chemically remove the lithiophobic LLZO surface contaminants, as already discussed in section 3.11. Moreover, thermal preconditioning was applied to the Li/LLZO/Li cells which led to a nearly zero starting R_{int}, as illustrated by the PEIS in Fig. 5.14a. This ensured that the local plating current density for these cells would not diverge significantly from the nominal value. Subsequently, 1 mAh cm^{-2} of lithium capacity was plated at various current densities, specifically at 0.5, 2.5, and 5 mA cm^{-2}. The good Li-WE/LLZO interfacial contact meant that peeling off the Li-WE was not feasible, hence it was dissolved in ethanol in order to expose the LLZO surface. While surface spallations and dendrites readily formed on an untreated LLZO pellet at a nominal applied current density of 0.5 mA cm^{-2}, as demonstrated in the previous

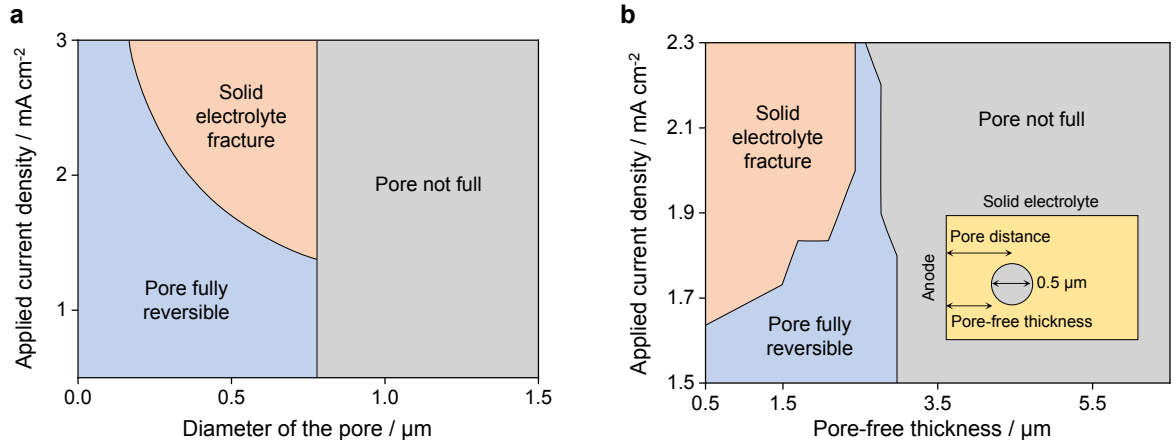


Figure 5.15. Modeling internal lithium deposition in a pore. **a**, Evolution of pores in a solid electrolyte as a function of pore diameter and applied current density for a deposited lithium capacity of 4 mAh cm^{-2}. Sufficiently large pores are never filled upon charging (grey area). In the blue area, pores will be filled but the pressure build-up is not sufficient to fracture the solid electrolyte. For conditions in the orange area the pores will fracture. **b**, Evolution of pores as a function of pore-free thickness and applied current density (deposited lithium capacity of 4 mAh cm^{-2}). The inset describes the pore geometry. Adapted with permission from [168].

sections, no spallations are now visible on the acid-treated LLZO pellet cycled at 0.5 and 2.5 mA cm^{-2}, and the voltage trace remains stable throughout the plating step (Fig. 5.14b). In contrast, a few spallation craters are visible on the LLZO surface after plating at 5 mA cm^{-2} (Fig. 5.14c). The LLZO cap has been removed by the ethanol washing step. The craters are primarily located near the edge of the Li-WE, where the current density is largest. It is worth noting that even at 5 mA cm^{-2} and 1 mAh cm^{-2} of plated capacity no complete short-circuit occurred, although voltage instability indicates some level of dendritic growth.

The cycling data strongly suggest the existence of a 'critical' current density for the formation of surface spallations and, according to the proposed mechanism for the formation of such spallations, for the deposition of lithium in occluded pores within the solid electrolyte. The current-dependent behaviour for isolated lithium deposition agrees well with prior modeling work [168]. In this work, Tu et al. modeled the sub-surface porosity of a solid electrolyte during a lithium plating step, accounting for a partial electronic conductivity in the solid electrolyte. Depending on the applied current density, plated lithium capacity, pore dimension and position with respect to the interface with the lithium metal anode, and solid electrolyte fracture toughness, it is possible to determine whether the pressure build-up in the pore resulting from the

internal lithium deposition will generate a crack in the solid electrolyte. Figure 5.15 illustrates some of this findings, and the order of magnitude of the applied current density aligns with the values found in this chapter.

5.6 Conclusions

This chapter contributes to the understanding of the short-circuiting mechanism of LLZO and of the relationship between isolated lithium deposition and the nucleation of lithium dendrites. Automated serial sectioning of LLZO with PFIB in combination with EDS analysis allows the visualization of the initiation of dendritic failure with good spatial resolution. We reveal that, above a certain plating current density, spallation cracks form at the interface between LLZO pellets and the plating electrode. These cracks contain freshly plated lithium that appears to have first plated within the solid electrolyte without physical contact with the electrode. When a LiMg plating electrode is used, magnesium can diffuse into plated lithium that is in physical contact with the electrode, and this diffusion of magnesium can be tracked with EDS analysis. The absence of magnesium in the early-stage spallation cracks demonstrates the physical isolation of these volumes of lithium, indicating that the development of the cracks on the LLZO surface is directly associated with the deposition of isolated lithium metal in the sub-surface porosity.

We propose that the pressure build-up in a sub-surface Li-filled LLZO pore can be released by opening a circular crack on the solid electrolyte surface. Then lithium metal preferentially plates in the newly formed crack, which becomes a hot spot for the intensification of both electrical current density and mechanical stress. The insertion of lithium generates further internal pressure and drives crack growth along the mechanically weakest path, eventually creating a continuous short-circuiting path of lithium metal. A novel technique, EBIC imaging, was employed to verify that the lithium in the surface spallation cracks can indeed be electrically connected to the short-circuiting lithium dendrite, thus demonstrating that the spallations are directly correlated to the failure of the cell.

The observation that dendrites originate from surface spallations is consistent with a recently proposed two-step mechanism for dendrite initiation and propagation in solid electrolytes [55]. This chapter shows how the isolated lithium deposits play a role for the initiation of dendrites, emphasizing the significance of limiting this isolated lithium deposition to suppress LLZO failure. This can be achieved, for instance, by enhancing solid electrolyte density, which will have the additional benefit of improving

the solid electrolyte mechanical properties. Using spark plasma sintering, or any other sintering method where pressure is applied at high temperatures, proves valuable in this regard.

Another way to minimize internal lithium deposition is by reducing the local current density at the Li/LLZO interface. This can be achieved by optimizing the interfacial solid-solid contact, for instance through a careful LLZO surface preparation as demonstrated in section 5.5 and as previously discussed in chapter 3. The starting R_{int} plays indeed a critical role in the Li/LLZO interfacial behaviour, and decreasing the R_{int} value is an effective way to limit the formation of spallations and ultimately of dendrites at commercially significant current densities.

Future studies should focus on optimizing both the solid electrolyte density and the interfacial contact with lithium metal anodes, in order to improve the performance of solid-state batteries. Moreover, the precise mechanism of current leakage in solid electrolytes remains not fully understood and should be the subject of further investigations.

Chapter 6

Concluding Remarks and Outlook

Solid-state batteries featuring lithium metal anodes hold the potential to supplant conventional lithium-ion batteries due to their prospects for higher energy and power densities, enhanced safety, and prolonged durability when compared to their liquid-based counterparts. Nevertheless, it has become increasingly evident that many challenges akin to those affecting liquid electrolyte batteries also impede the performance of solid-state batteries. Above all, the formation of lithium dendrites during plating, which afflicts even the most robust ceramic solid electrolytes. Additionally, the presence of solid-solid contacts poses a unique challenge for solid-state cells, a complication absent in liquid electrolyte systems. In fact, most of the remaining issues in solid-state cells can be traced back to a lack of interfacial contact. This thesis has undertaken the investigation of some of these challenges and some solutions have been proposed.

Chapter 3 primarily delved into the hurdles immediately arising upon the assembly of a lithium/solid electrolyte interface, and in particular in the context of LLZO solid electrolytes. LLZO's susceptibility to trace H_2O and CO_2 exceeds expectations, resulting in the rapid formation of a surface contamination layer even within a controlled glovebox environment. To gain insights into LLZO's surface chemistry evolution under such environment, in-situ gas dosing experiments with H_2O and CO_2 were conducted in a near-ambient pressure XPS chamber. In particular, LLZO surface was studied during and after common surface treatments such as annealing and acid etching, which are widely used in the literature to remove the surface contaminants. The lithiophobic nature of these contaminants detrimentally affects the interfacial impedance with lithium metal, ultimately limiting safe cycling current densities. To mitigate this issue, a novel acid etching method using a diethyl ether solution directly within a glovebox was proposed, demonstrating superior results in term of LLZO surface cleanliness and critical current density measurements.

Despite XPS and EIS data suggesting some level of LLZO surface contamination is always inevitable, acid etching of LLZO and subsequent thermal conditioning of the Li/LLZO interface at 170 °C can effectively reduce the interfacial impedance to nearly zero. Therefore, at a commercial level, it is likely that heating or even melting lithium metal is necessary for its integration with lithium garnet solid electrolytes, to facilitate its flow into microscopic interfacial gaps, preventing the formation of point interfacial contacts. Still, careful temperature and pressure engineering is essential to maintain the morphological stability during stripping and avoid local electric field concentration during battery operation.

Lithium stripping was the subject of Chapter 4, which provided a comparative analysis between pure lithium metal and LiMg alloys. A comprehensive characterization of lithium diffusivity in both metallic anodes was undertaken using an isotope tracer method via PFIB-SIMS, which allows for a straightforward determination of lithium diffusion coefficients. Lithium diffusivity in LiMg alloys was found to be approximately one order of magnitude lower than in pure lithium metal. This difference rationalized the larger capacity stripped from pure lithium anodes compared to LiMg at a stripping current density of 1 mA cm^{-2}. However, a larger capacity is stripped from LiMg at relatively lower current densities, a phenomenon elucidated with PFIB cross-sectional imaging. Thanks to the presence of Mg, LiMg/LLZO interfacial contact is maintained upon stripping, whereas large voids form in lithium metal anodes. The concept of effective diffusivity was introduced, considering that voids hinder lithium diffusion across the interface into the solid electrolyte. This chapter challenged the notion that improved cycling performance in cells constructed with lithium alloys is solely connected to faster lithium diffusivity.

At the same time, chapter 4 underscored the need for enhanced lithium diffusivity within the anode. Hence the search for lithium alloys exhibiting improved diffusivity is still ongoing, with Li-Ag and Li-In systems appearing promising. As for the Li-Mg system, a well-conceived cycling procedure could leverage the extra capacity attainable from LiMg anodes after a brief resting period, as explained in section 4.3. Further investigations should explore the evolution of magnesium content at the LLZO surface to determine whether lithium-poor phases nucleate during stripping and assess the alloy's integrity during plating.

Chapter 5 tackled the formation of lithium dendrites during plating. The extensive investigation of spallation cracks morphology led to the hypothesis of an initial internal lithium plating process at the onset of plating, due to the non-negligible electrical conductivity of LLZO. This process results in pressure build-up in pores

near the LLZO surface but not directly in contact with the lithium metal anode. Subsequently, circular cracks form on the LLZO surface, releasing the accumulated pressure to the LLZO surface. Once the lithium within the spallation crack connects with the anode, a stronger electrical field concentrates at the small diameter and large curvature of the spallation tip, leading to further pressure build-up and eventual cracking throughout the solid electrolyte pellet. Whether internal lithium deposition precedes crack propagation remains uncertain, but recent studies suggest that dendrite propagation is primarily governed by mechanical stress release principles. However, limiting the leakage of current into the sub-surface region of the solid electrolyte can delay the initiation and ultimately the propagation of dendrites.

In conclusion, this thesis findings emphasize the necessity to optimize both the solid electrolyte sintering process, achieving over 99% density, and the cleanliness of the interfacial contact with lithium metal anodes. The combined pursuit of these objectives has the potential to inhibit dendritic failure and enhance solid-state battery performance. For the first objective, while spark plasma sintering offers high density, exploring cost-effective sintering processes with higher throughput is crucial. New sintering processes will likely lead to changes in some material parameters. As for the interfacial contact, careful surface processing and cell assembly are necessary, but chapter 3 demonstrates that a nearly pristine interface can be achieved.

The promise of solid-state batteries may not yet be fully realized, and compromises may be necessary. Nonetheless, significant progress has been made in understanding interfacial dynamics on both the anode and cathode sides, with noteworthy achievements such as the development of all-solid-state batteries showcasing high energy density, coulombic efficiency, and cycle life. Thus, it appears that the challenges facing solid-state cells are gradually transitioning from fundamental scientific hurdles to more manageable manufacturing problems, marking a promising evolution in the field.

Appendix A

XPS and XANES data analysis

XPS data collection and analysis

X-ray photoelectron spectra were collected at the Diamond Light Source B07-C beamline (experiment no. SI 33570-1). The incident X-ray energy was set to 2500 eV to probe the deeper surface layer of $\sim$ 15 nm. A fixed incident energy results in slightly different probing depth for the various elements, varying from 10 nm for La 3d to 15 nm for Li 1s assuming a pristine LLZO surface. For the soft X-rays, the incident energy was instead tuned so that the kinetic energy of the ejected photoelectrons probed was fixed at 315 eV for all the elements and the escape depth was $\sim$ 3 nm. This corresponds to the following incident energies: La 3d 1160 eV, O 1s 850 eV, C 1s 600 eV, Zr 3d 500 ev. The pass energy for hard X-rays was 60 eV, while for soft X-rays it was 30 eV. Survey measurements were conducted with a step size of 0.5 eV, while core level spectra had a step size of 0.1 eV.

The data analysis was carried out with CasaXPS [96]. Shirley backgrounds and GL(30) line shapes were used to fit the peaks, unless otherwise specified. The following model constraints were applied to the O 1s spectra. The Li_2CO_3 peak was fixed at LiOH + 0.9 eV [80, 112], while $LiHCO_3$ was fixed at LiOH + 2.6 eV. For the hard X-ray data, the full width half maxima of the surface contaminants peaks were constrained to be 1.15 times that of the LLZO lattice oxide peak, while for the soft X-ray data they were constrained to be equal to the LLZO peak. For C 1s spectra, a linear background was used. Here, full width half maxima were constrained to be equal.

La $3d_{5/2}$ and La $4p_{3/2}$ spectra were fitted with a three-peak model, according to Sunding et al. [132]. The Cl $2p_{3/2}$ surface contamination was fitted with a doublet peak. Cl $2p_{1/2}$ area was constrained to be half of Cl $2p_{3/2}$, same full width half maxima, a doublet splitting of 1.6 eV. Zr 3d spectra were fitted with a doublet peak

with a 2.4 eV splitting [135]. A background subtraction was performed for a better visualization of the XPS data, as the background intensity can vary depending on temperature and charging effects. The C 1s spectra were energy calibrated with reference to the C-C/C-H peak at 285.0 eV, while the O 1s spectra to the lattice oxygen peak at 528.9 eV.

XANES data collection

X-ray absorption near-edge spectra (XANES) were collected at the Diamond Light Source B07-C beamline. The oxygen K-edge was collected in total electron yield mode over the 520 to 555 eV range. The data was plotted normalised in the Athena XAS software, setting E_0 to the first peak of the derivative, and calculating pre- and post-edge lines from -13.4 to -3.4 eV and 15.0 to 21.6 eV from E_0 respectively.

Appendix B

Literature survey of lithium diffusivity in lithium alloys

Figure 4.2 from section 4.1 reported a literature survey of lithium diffusion coefficients. Here, a table contains references to the previous studies on lithium diffusivity. Notably, various lithium alloys seem to have lithium diffusivities significantly exceeding lithium self-diffusivity. However, it is worth noting that these reported values are often derived from indirect measurements, such as GITT and PITT.

Table B.1. Lithium diffusion coefficients reported in the literature for various lithium alloys.

Material	D_{Li} / $cm^2\ s^{-1}$	Method	Reference
Li	5.6e-11	Sand's Equation	Jow and Liang [49]
Li	5e-11	Tracer Technique	Lodding et al. [141]
Li	7.8e-11	NMR	Messer and Noack [138]
Li	9e-11	Spin Lattice Relaxation	Heitjans et al. [187]
Li	5e-11	NMR	Mali et al. [140]
Li	5.9e-11	NMR	Fischer et al. [139]
Li	0.1 - 1e-10	Ab-Initio Force Constant	Frank et al. [142]
Li	7.65e-11	cBω model	Dologlou [188]
βLi-Mg	2.3e-11	Sand's Equation	Krauskopf et al. [41]
βLi-Mg	7e-11	Spin Lattice Relaxation	Korblein et al. [160]
βLi-Mg	6e-11	Neutron Tomography	Zhang et al. [161]
βLi-Mg	2e-10	PITT	Zhang et al. [161]
Li-Mg (evaporated)	1.2e-7	GITT	Shi et al. [162]
$Li_{0.9}Mg_{0.1}$	9.89e-8	GITT	Shi et al. [162]
$Li_{0.8}Mg_{0.2}$	5.1e-8	GITT	Shi et al. [162]
$Li_{0.7}Mg_{0.3}$	4e-8	GITT	Shi et al. [162]
$Li_{0.6}Mg_{0.4}$	2.5e-8	GITT	Shi et al. [162]

βLi-Al	7.7e-8	PITT	Baranski and Fawcett [189]
βLi-Al	5.06e-9	PITT	Jow and Liang [48]
βLi-Al	8.48e-9	GITT	Jow and Liang [48]
βLi-Al	1e-10	PITT	Kumagai et al. [190]
βLi-Al	2.4e-10	Impedance Method	Kumagai et al. [190]
$Li_{0.7}Sn$	6 - 8e-8	GITT	Wang et al. [154]
$Li_{2.33}Sn$	3 - 5e-7	GITT	Wang et al. [154]
$Li_{4.4}Sn$	1.8 - 5.9e-7	GITT	Huggins [153]
Li-Ga (46-56 at. % Li)	1e-6	GITT	Hiratani et al. [191]
Li-In (47-63 at. % Li)	1e-6	GITT	Hiratani et al. [191]
Li-In (75-85 at. % Li)	1e-6	GITT	Hiratani et al. [191]
Li-Bi (75-85 at. % Li)	1e-6	GITT	Hiratani et al. [191]
Li_3Bi (75-85 at. % Li)	1 - 3e-6	GITT	Hiratani et al. [45]
LiZn (75-85 at. % Li)	0.9 - 2.3e-9	GITT	Huggins [153]
LiZn (evaporated)	0.1 - 5.1e-8	GITT	Gole et al. [155]
$LiSi_3$	3 - 5e-7	GITT	Wang et al. [154]
Li-Si	0.1 - 6e-9	GITT	Tan et al. [192]
Li-Ag	1e-8	GITT	Jin et al. [152]

Bibliography

[1] Ghassan Zubi, Rodolfo Dufo-López, Monica Carvalho, and Guzay Pasaoglu. The lithium-ion battery: State of the art and future perspectives. *Renewable and Sustainable Energy Reviews*, 89:292–308, 2018.

[2] Rosamaria Fong, Ulrich Von Sacken, and Jeff R Dahn. Studies of lithium intercalation into carbons using nonaqueous electrochemical cells. *Journal of The Electrochemical Society*, 137(7):2009, 1990.

[3] Hong Li. Practical evaluation of Li-ion batteries. *Joule*, 3(4):911–914, 2019.

[4] Paul Albertus, Susan Babinec, Scott Litzelman, and Aron Newman. Status and challenges in enabling the lithium metal electrode for high-energy and low-cost rechargeable batteries. *Nature Energy*, 3(1):16–21, 2018.

[5] Mario Marinaro, Dominic Bresser, Engelbert Beyer, Peter Faguy, Kei Hosoi, Hong Li, Julija Sakovica, Khalil Amine, Margret Wohlfahrt-Mehrens, and Stefano Passerini. Bringing forward the development of battery cells for automotive applications: perspective of R&D activities in China, Japan, the EU and the USA. *Journal of Power Sources*, 459:228073, 2020.

[6] Jürgen Janek and Wolfgang G Zeier. A solid future for battery development. *Nature energy*, 1(9):1–4, 2016.

[7] Wenzhuo Cao, Jienan Zhang, and Hong Li. Batteries with high theoretical energy densities. *Energy Storage Materials*, 26:46–55, 2020.

[8] J-M Tarascon and Michel Armand. Issues and challenges facing rechargeable lithium batteries. *nature*, 414(6861):359–367, 2001.

[9] Kevin N Wood, Malachi Noked, and Neil P Dasgupta. Lithium metal anodes: toward an improved understanding of coupled morphological, electrochemical, and mechanical behavior. *ACS Energy Letters*, 2(3):664–672, 2017.

[10] Dingchang Lin, Yayuan Liu, and Yi Cui. Reviving the lithium metal anode for high-energy batteries. *Nature nanotechnology*, 12(3):194–206, 2017.

[11] Theodosios Famprikis, Pieremanuele Canepa, James A Dawson, M Saiful Islam, and Christian Masquelier. Fundamentals of inorganic solid-state electrolytes for batteries. *Nature materials*, 18(12):1278–1291, 2019.

[12] Thomas Schmaltz, Tim Wicke, Lukas Weymann, Philipp Voß, Christoph Neef, and Axel Thielmann. Solid-state battery roadmap 2035+. 2022.

[13] John B Goodenough and Youngsik Kim. Challenges for rechargeable Li batteries. *Chemistry of materials*, 22(3):587–603, 2010.

[14] Darren HS Tan, Ying Shirley Meng, and Jihyun Jang. Scaling up high-energy-density sulfidic solid-state batteries: a lab-to-pilot perspective. *Joule*, 6(8):1755–1769, 2022.

[15] Alberto Varzi, Rinaldo Raccichini, Stefano Passerini, and Bruno Scrosati. Challenges and prospects of the role of solid electrolytes in the revitalization of lithium metal batteries. *Journal of Materials Chemistry A*, 4(44):17251–17259, 2016.

[16] Jeffrey W Fergus. Ceramic and polymeric solid electrolytes for lithium-ion batteries. *Journal of Power Sources*, 195(15):4554–4569, 2010.

[17] Wenjia Zhao, Jin Yi, Ping He, and Haoshen Zhou. Solid-state electrolytes for lithium-ion batteries: fundamentals, challenges and perspectives. *Electrochemical Energy Reviews*, 2:574–605, 2019.

[18] Yuki Kato, Satoshi Hori, Toshiya Saito, Kota Suzuki, Masaaki Hirayama, Akio Mitsui, Masao Yonemura, Hideki Iba, and Ryoji Kanno. High-power all-solid-state batteries using sulfide superionic conductors. *Nature Energy*, 1(4):1–7, 2016.

[19] Syed Atif Pervez, Musa Ali Cambaz, Venkataraman Thangadurai, and Maximilian Fichtner. Interface in solid-state lithium battery: challenges, progress, and outlook. *ACS applied materials & interfaces*, 11(25):22029–22050, 2019.

[20] Shuo Wang, Qiang Bai, Adelaide M Nolan, Yunsheng Liu, Sheng Gong, Qiang Sun, and Yifei Mo. Lithium chlorides and bromides as promising solid-state

chemistries for fast ion conductors with good electrochemical stability. *Angewandte Chemie International Edition*, 58(24):8039–8043, 2019.

[21] William D Richards, Lincoln J Miara, Yan Wang, Jae Chul Kim, and Gerbrand Ceder. Interface stability in solid-state batteries. *Chemistry of Materials*, 28(1):266–273, 2016.

[22] Yizhou Zhu, Xingfeng He, and Yifei Mo. Strategies based on nitride materials chemistry to stabilize Li metal anode. *Advanced Science*, 4(8):1600517, 2017.

[23] Darren HS Tan, Abhik Banerjee, Zheng Chen, and Ying Shirley Meng. From nanoscale interface characterization to sustainable energy storage using all-solid-state batteries. *Nature nanotechnology*, 15(3):170–180, 2020.

[24] Simon Randau, Dominik A Weber, Olaf Kötz, Raimund Koerver, Philipp Braun, André Weber, Ellen Ivers-Tiffée, Torben Adermann, Jörn Kulisch, Wolfgang G Zeier, et al. Benchmarking the performance of all-solid-state lithium batteries. *Nature Energy*, 5(3):259–270, 2020.

[25] Thorben Krauskopf, Felix H Richter, Wolfgang G Zeier, and Jurgen Janek. Physicochemical concepts of the lithium metal anode in solid-state batteries. *Chemical reviews*, 120(15):7745–7794, 2020.

[26] Thorben Krauskopf, Hannah Hartmann, Wolfgang G Zeier, and Jurgen Janek. Toward a fundamental understanding of the lithium metal anode in solid-state batteries – an electrochemo-mechanical study on the garnet-type solid electrolyte $Li_{6.25}Al_{0.25}La_3Zr_2O_{12}$. *ACS applied materials & interfaces*, 11(15):14463–14477, 2019.

[27] H Schmalzried and J Janek. Chemical kinetics of phase boundaries in solids. *Berichte der Bunsengesellschaft für physikalische Chemie*, 102(2):127–143, 1998.

[28] M Meyer, H Rickert, and U Schwaitzer. Investigations on the kinetics of the anodic dissolution of lithium at the interface Li/Li3N. *Solid State Ionics*, 9:689–693, 1983.

[29] Dheeraj Kumar Singh, Till Fuchs, Christian Krempaszky, Boris Mogwitz, Simon Burkhardt, Felix H Richter, and Jürgen Janek. Overcoming anode instability in solid-state batteries through control of the lithium metal microstructure. *Advanced Functional Materials*, 33(1):2211067, 2023.

[30] Dheeraj Kumar Singh, Till Fuchs, Christian Krempaszky, Pascal Schweitzer, Christian Lerch, Felix H Richter, and Jürgen Janek. Origin of the lithium metal anode instability in solid-state batteries during discharge. *Matter*, 6(5):1463–1483, 2023.

[31] Paul Albertus, Venkataramani Anandan, Chunmei Ban, Nitash Balsara, Ilias Belharouak, Josh Buettner-Garrett, Zonghai Chen, Claus Daniel, Marca Doeff, Nancy J Dudney, et al. Challenges for and pathways toward Li-metal-based all-solid-state batteries. *ACS Energy Letters*, 6(4):1399–1404, 2021.

[32] Alvaro Masias, Nando Felten, Regina Garcia-Mendez, Jeff Wolfenstine, and Jeff Sakamoto. Elastic, plastic, and creep mechanical properties of lithium metal. *Journal of materials science*, 54(3):2585–2600, 2019.

[33] William S LePage, Yuxin Chen, Eric Kazyak, Kuan-Hung Chen, Adrian J Sanchez, Andrea Poli, Ellen M Arruda, MD Thouless, and Neil P Dasgupta. Lithium mechanics: roles of strain rate and temperature and implications for lithium metal batteries. *Journal of The Electrochemical Society*, 166(2):A89–A97, 2019.

[34] Michael J Wang, Rishav Choudhury, and Jeff Sakamoto. Characterizing the Li-solid-electrolyte interface dynamics as a function of stack pressure and current density. *Joule*, 3(9):2165–2178, 2019.

[35] Jitti Kasemchainan, Stefanie Zekoll, Dominic Spencer Jolly, Ziyang Ning, Gareth O Hartley, James Marrow, and Peter G Bruce. Critical stripping current leads to dendrite formation on plating in lithium anode solid electrolyte cells. *Nature materials*, 18(10):1105–1111, 2019.

[36] Xin Zhang, Q Jane Wang, Katharine L Harrison, Scott A Roberts, and Stephen J Harris. Pressure-driven interface evolution in solid-state lithium metal batteries. *Cell Reports Physical Science*, 1(2), 2020.

[37] Jean-Marie Doux, Han Nguyen, Darren HS Tan, Abhik Banerjee, Xuefeng Wang, Erik A Wu, Chiho Jo, Hedi Yang, and Ying Shirley Meng. Stack pressure considerations for room-temperature all-solid-state lithium metal batteries. *Advanced Energy Materials*, 10(1):1903253, 2020.

[38] Kostiantyn V Kravchyk, Faruk Okur, and Maksym V Kovalenko. Break-even analysis of all-solid-state batteries with Li-garnet solid electrolytes. *ACS Energy Letters*, 6(6):2202–2207, 2021.

[39] Asma Sharafi, Harry M Meyer, Jagjit Nanda, Jeff Wolfenstine, and Jeff Sakamoto. Characterizing the Li–Li7La3Zr2O12 interface stability and kinetics as a function of temperature and current density. *Journal of Power Sources*, 302:135–139, 2016.

[40] Wahid Zaman, Le Zhao, Tobias Martin, Xin Zhang, Zhanjiang Wang, Q Jane Wang, Stephen Harris, and Kelsey B Hatzell. Temperature and pressure effects on unrecoverable voids in Li metal solid-state batteries. *ACS Applied Materials & Interfaces*, 2023.

[41] Thorben Krauskopf, Boris Mogwitz, Carolin Rosenbach, Wolfgang G Zeier, and Jürgen Janek. Diffusion limitation of lithium metal and Li–Mg alloy anodes on LLZO type solid electrolytes as a function of temperature and pressure. *Advanced Energy Materials*, 9(44):1902568, 2019.

[42] Bryan Kinzer, Andrew L Davis, Thorben Krauskopf, Hannah Hartmann, William S LePage, Eric Kazyak, Jürgen Janek, Neil P Dasgupta, and Jeff Sakamoto. Operando analysis of the molten Li/LLZO interface: understanding how the physical properties of Li affect the critical current density. *Matter*, 4(6):1947–1961, 2021.

[43] Dominic Spencer Jolly, Ziyang Ning, Gareth O Hartley, Boyang Liu, Dominic LR Melvin, Paul Adamson, James Marrow, and Peter G Bruce. Temperature dependence of lithium anode voiding in argyrodite solid-state batteries. *ACS Applied Materials & Interfaces*, 13(19):22708–22716, 2021.

[44] Asma Sharafi, Eric Kazyak, Andrew L Davis, Seungho Yu, Travis Thompson, Donald J Siegel, Neil P Dasgupta, and Jeff Sakamoto. Surface chemistry mechanism of ultra-low interfacial resistance in the solid-state electrolyte Li7La3Zr2O12. *Chemistry of Materials*, 29(18):7961–7968, 2017.

[45] Masahiko Hiratani, Katsuki Miyauchi, and Tetsuichi Kudo. Effect of a lithium alloy layer inserted between a lithium anode and a solid electrolyte. *Solid State Ionics*, 28:1406–1410, 1988.

[46] Hanyu Huo and Jürgen Janek. Solid-state batteries: from 'all-solid'to 'almost-solid'. *National Science Review*, 10(6):nwad098, 2023.

[47] Dengxu Wu, Liquan Chen, Hong Li, and Fan Wu. Solid-state lithium batteries-from fundamental research to industrial progress. *Progress in Materials Science*, page 101182, 2023.

[48] TR Jow and CC Liang. Lithium-aluminum electrodes at ambient temperatures. *Journal of The Electrochemical Society*, 129(7):1429, 1982.

[49] TR Jow and CC Liang. Interface between solid electrode and solid electrolyte–a study of the Li/LiI(Al2O3) solid-electrolyte system. *Journal of The Electrochemical Society*, 130(4):737, 1983.

[50] Charles Monroe and John Newman. The impact of elastic deformation on deposition kinetics at lithium/polymer interfaces. *Journal of The Electrochemical Society*, 152(2):A396, 2005.

[51] Daxian Cao, Xiao Sun, Qiang Li, Avi Natan, Pengyang Xiang, and Hongli Zhu. Lithium dendrite in all-solid-state batteries: growth mechanisms, suppression strategies, and characterizations. *Matter*, 3(1):57–94, 2020.

[52] Xinyou Ke, Yan Wang, Liming Dai, and Chris Yuan. Cell failures of all-solid-state lithium metal batteries with inorganic solid electrolytes: lithium dendrites. *Energy Storage Materials*, 33:309–328, 2020.

[53] Luis Barroso-Luque, Qingsong Tu, and Gerbrand Ceder. An analysis of solid-state electrodeposition-induced metal plastic flow and predictions of stress states in solid ionic conductor defects. *Journal of The Electrochemical Society*, 167(2):020534, 2020.

[54] Kevin N Wood, Eric Kazyak, Alexander F Chadwick, Kuan-Hung Chen, Ji-Guang Zhang, Katsuyo Thornton, and Neil P Dasgupta. Dendrites and pits: untangling the complex behavior of lithium metal anodes through operando video microscopy. *ACS central science*, 2(11):790–801, 2016.

[55] Ziyang Ning, Guanchen Li, Dominic LR Melvin, Yang Chen, Junfu Bu, Dominic Spencer-Jolly, Junliang Liu, Bingkun Hu, Xiangwen Gao, Johann Perera, et al. Dendrite initiation and propagation in lithium metal solid-state batteries. *Nature*, 618(7964):287–293, 2023.

[56] Eric Jianfeng Cheng, Asma Sharafi, and Jeff Sakamoto. Intergranular Li metal propagation through polycrystalline Li6.25Al0.25La3Zr2O12 ceramic electrolyte. *Electrochimica Acta*, 223:85–91, 2017.

[57] Tushar Swamy, Richard Park, Brian W Sheldon, Daniel Rettenwander, Lukas Porz, Stefan Berendts, Reinhard Uecker, W Craig Carter, and Yet-Ming Chiang. Lithium metal penetration induced by electrodeposition through solid electrolytes: example in single-crystal Li6La3ZrTaO12 garnet. *Journal of The Electrochemical Society*, 165(16):A3648–A3655, 2018.

[58] Lukas Porz, Tushar Swamy, Brian W Sheldon, Daniel Rettenwander, Till Frömling, Henry L Thaman, Stefan Berendts, Reinhard Uecker, W Craig Carter, and Yet-Ming Chiang. Mechanism of lithium metal penetration through inorganic solid electrolytes. *Advanced Energy Materials*, 7(20):1701003, 2017.

[59] Chen Xu, Zeeshan Ahmad, Asghar Aryanfar, Venkatasubramanian Viswanathan, and Julia R Greer. Enhanced strength and temperature dependence of mechanical properties of Li at small scales and its implications for Li metal anodes. *Proceedings of the National Academy of Sciences*, 114(1):57–61, 2017.

[60] Pallab Barai, Anh T Ngo, Badri Narayanan, Kenneth Higa, Larry A Curtiss, and Venkat Srinivasan. The role of local inhomogeneities on dendrite growth in LLZO-based solid electrolytes. *Journal of the Electrochemical Society*, 167(10):100537, 2020.

[61] Yaoyu Ren, Yang Shen, Yuanhua Lin, and Ce-Wen Nan. Direct observation of lithium dendrites inside garnet-type lithium-ion solid electrolyte. *Electrochemistry Communications*, 57:27–30, 2015.

[62] Fengyu Shen, Marm B Dixit, Xianghui Xiao, and Kelsey B Hatzell. Effect of pore connectivity on Li dendrite propagation within LLZO electrolytes observed with synchrotron X-ray tomography. *ACS Energy Letters*, 3(4):1056–1061, 2018.

[63] Qingsong Tu, Luis Barroso-Luque, Tan Shi, and Gerbrand Ceder. Electrodeposition and mechanical stability at lithium-solid electrolyte interface during plating in solid-state batteries. *Cell Reports Physical Science*, 1(7), 2020.

[64] Nathan J Taylor, Sandra Stangeland-Molo, Catherine G Haslam, Asma Sharafi, Travis Thompson, Michael Wang, Regina Garcia-Mendez, and Jeff Sakamoto. Demonstration of high current densities and extended cycling in the garnet Li7La3Zr2O12 solid electrolyte. *Journal of Power Sources*, 396:314–318, 2018.

[65] Geoff McConohy, Xin Xu, Teng Cui, Edward Barks, Sunny Wang, Emma Kaeli, Celeste Melamed, X Wendy Gu, and William C Chueh. Mechanical regulation of lithium intrusion probability in garnet solid electrolytes. *Nature energy*, 8(3):241–250, 2023.

[66] Hong-Kang Tian, Bo Xu, and Yue Qi. Computational study of lithium nucleation tendency in $Li_7La_3Zr_2O_{12}$ (LLZO) and rational design of interlayer materials to prevent lithium dendrites. *Journal of Power Sources*, 392:79–86, 2018.

[67] Hong-Kang Tian, Zhe Liu, Yanzhou Ji, Long-Qing Chen, and Yue Qi. Interfacial electronic properties dictate Li dendrite growth in solid electrolytes. *Chemistry of Materials*, 31(18):7351–7359, 2019.

[68] Frederic Aguesse, William Manalastas, Lucienne Buannic, Juan Miguel Lopez del Amo, Gurpreet Singh, Anna Llordés, and John Kilner. Investigating the dendritic growth during full cell cycling of garnet electrolyte in direct contact with Li metal. *ACS applied materials & interfaces*, 9(4):3808–3816, 2017.

[69] Fudong Han, Andrew S Westover, Jie Yue, Xiulin Fan, Fei Wang, Miaofang Chi, Donovan N Leonard, Nancy J Dudney, Howard Wang, and Chunsheng Wang. High electronic conductivity as the origin of lithium dendrite formation within solid electrolytes. *Nature Energy*, 4(3):187–196, 2019.

[70] R Raj and J Wolfenstine. Current limit diagrams for dendrite formation in solid-state electrolytes for Li-ion batteries. *Journal of Power Sources*, 343:119–126, 2017.

[71] Motohiro Nagao, Akitoshi Hayashi, Masahiro Tatsumisago, Tsukasa Kanetsuku, Tetsuya Tsuda, and Susumu Kuwabata. In situ SEM study of a lithium deposition and dissolution mechanism in a bulk-type solid-state cell with a Li_2S–P_2S_5 solid electrolyte. *Physical Chemistry Chemical Physics*, 15(42):18600–18606, 2013.

[72] Eric Kazyak, Regina Garcia-Mendez, William S LePage, Asma Sharafi, Andrew L Davis, Adrian J Sanchez, Kuan-Hung Chen, Catherine Haslam, Jeff Sakamoto, and Neil P Dasgupta. Li penetration in ceramic solid electrolytes: operando microscopy analysis of morphology, propagation, and reversibility. *Matter*, 2(4):1025–1048, 2020.

[73] Jun Ma, Bingbing Chen, Longlong Wang, and Guanglei Cui. Progress and prospect on failure mechanisms of solid-state lithium batteries. *Journal of Power Sources*, 392:94–115, 2018.

[74] Arumugam Manthiram, Xingwen Yu, and Shaofei Wang. Lithium battery chemistries enabled by solid-state electrolytes. *Nature Reviews Materials*, 2(4):1–16, 2017.

[75] Venkataraman Thangadurai, Heiko Kaack, and Werner JF Weppner. Novel fast lithium ion conduction in garnet-type Li5La3M2O12 (M = Nb, Ta). *Journal of the American Ceramic Society*, 86(3):437–440, 2003.

[76] Ramaswamy Murugan, Venkataraman Thangadurai, and Werner Weppner. Fast lithium ion conduction in garnet-type Li7La3Zr2O12. *Angewandte Chemie International Edition*, 46(41):7778–7781, 2007.

[77] Fabian A Garcia Daza, Mauricio R Bonilla, Anna Llordés, Javier Carrasco, and Elena Akhmatskaya. Atomistic insight into ion transport and conductivity in Ga/Al-substituted Li7La3Zr2O12 solid electrolytes. *ACS applied materials & interfaces*, 11(1):753–765, 2018.

[78] Chengwei Wang, Kun Fu, Sanoop Palakkathodi Kammampata, Dennis W McOwen, Alfred Junio Samson, Lei Zhang, Gregory T Hitz, Adelaide M Nolan, Eric D Wachsman, Yifei Mo, et al. Garnet-type solid-state electrolytes: materials, interfaces, and batteries. *Chemical reviews*, 120(10):4257–4300, 2020.

[79] Evgeniya Il'ina. Recent strategies for lithium-ion conductivity improvement in Li7La3Zr2O12 solid electrolytes. *International Journal of Molecular Sciences*, 24(16):12905, 2023.

[80] Yisi Zhu, Justin G Connell, Sanja Tepavcevic, Peter Zapol, Regina Garcia-Mendez, Nathan J Taylor, Jeff Sakamoto, Brian J Ingram, Larry A Curtiss, John W Freeland, et al. Dopant-dependent stability of garnet solid electrolyte interfaces with lithium metal. *Advanced Energy Materials*, 9(12):1803440, 2019.

[81] Cheng Ma, Yongqiang Cheng, Kuibo Yin, Jian Luo, Asma Sharafi, Jeff Sakamoto, Juchuan Li, Karren L More, Nancy J Dudney, and Miaofang Chi. Interfacial stability of Li metal–solid electrolyte elucidated via in situ electron microscopy. *Nano letters*, 16(11):7030–7036, 2016.

[82] Thorben Krauskopf, Boris Mogwitz, Hannah Hartmann, Dheeraj K Singh, Wolfgang G Zeier, and Jürgen Janek. The fast charge transfer kinetics of the lithium metal anode on the garnet-type solid electrolyte Li6.25Al0.25La3Zr2O12. *Advanced Energy Materials*, 10(27):2000945, 2020.

[83] Yutao Li, Jian-Tao Han, Chang-An Wang, Hui Xie, and John B Goodenough. Optimizing Li+ conductivity in a garnet framework. *Journal of Materials Chemistry*, 22(30):15357–15361, 2012.

[84] Travis Thompson, Asma Sharafi, Michelle D Johannes, Ashfia Huq, Jan L Allen, Jeff Wolfenstine, and Jeff Sakamoto. A tale of two sites: on defining the carrier concentration in garnet-based ionic conductors for advanced Li batteries. *Advanced Energy Materials*, 5(11):1500096, 2015.

[85] Ying Jin and Paul J McGinn. Li7La3Zr2O12 electrolyte stability in air and fabrication of a Li/Li7La3Zr2O12/Cu0.1V2O5 solid-state battery. *Journal of power sources*, 239:326–331, 2013.

[86] Lei Cheng, Ethan J Crumlin, Wei Chen, Ruimin Qiao, Huaming Hou, Simon Franz Lux, Vassilia Zorba, Richard Russo, Robert Kostecki, Zhi Liu, et al. The origin of high electrolyte–electrode interfacial resistances in lithium cells containing garnet type solid electrolytes. *Physical Chemistry Chemical Physics*, 16(34):18294–18300, 2014.

[87] Olivier Guillon, Jesus Gonzalez-Julian, Benjamin Dargatz, Tobias Kessel, Gabi Schierning, Jan Räthel, and Mathias Herrmann. Field-assisted sintering technology/spark plasma sintering: mechanisms, materials, and technology developments. *Advanced Engineering Materials*, 16(7):830–849, 2014.

[88] Seung-wook Baek, Jae-Myung Lee, Tae Young Kim, Min-Sang Song, and Youngsin Park. Garnet related lithium ion conductor processed by spark plasma sintering for all solid state batteries. *Journal of Power Sources*, 249:197–206, 2014.

[89] Weichang Guo, Fei Shen, Jiawei Liu, Yifei Chen, Hong Guo, Jieda Yan, Yuting Yin, Bo He, and Xiaogang Han. Preparation of transparent LLZTO electrolyte and its application in the observation of Li dendrite. *Ceramics International*, 48(13):18949–18955, 2022.

[90] Hongzheng Zhu and Jian Liu. Emerging applications of spark plasma sintering in all solid-state lithium-ion batteries and beyond. *Journal of Power Sources*, 391:10–25, 2018.

[91] Pooja Vadhva, Ji Hu, Michael J Johnson, Richard Stocker, Michele Braglia, Dan JL Brett, and Alexander JE Rettie. Electrochemical impedance spectroscopy for all-solid-state batteries: theory, methods and future outlook. *ChemElectroChem*, 8(11):1930–1947, 2021.

[92] Alfred Junio Samson, Kyle Hofstetter, Sourav Bag, and Venkataraman Thangadurai. A bird's-eye view of li-stuffed garnet-type Li7La3Zr2O12 ceramic electrolytes for advanced all-solid-state Li batteries. *Energy & Environmental Science*, 12(10):2957–2975, 2019.

[93] Chao Zhu, Till Fuchs, Stefan AL Weber, Felix H Richter, Gunnar Glasser, Franjo Weber, Hans-Jürgen Butt, Jürgen Janek, and Rüdiger Berger. Understanding the evolution of lithium dendrites at $Li_{6.25}Al_{0.25}La_3Zr_2O_{12}$ grain boundaries via operando microscopy techniques. *Nature Communications*, 14(1):1300, 2023.

[94] Mark N Obrovac and Vincent L Chevrier. Alloy negative electrodes for Li-ion batteries. *Chemical reviews*, 114(23):11444–11502, 2014.

[95] AA Nayeb-Hashemi, JB Clark, and AD Pelton. The Li-Mg (lithium-magnesium) system. *Bulletin of Alloy Phase Diagrams*, 5(4):365–374, 1984.

[96] Neal Fairley, Vincent Fernandez, Mireille Richard-Plouet, Catherine Guillot-Deudon, John Walton, Emily Smith, Delphine Flahaut, Mark Greiner, Mark Biesinger, Sven Tougaard, et al. Systematic and collaborative approach to problem solving using x-ray photoelectron spectroscopy. *Applied Surface Science Advances*, 5:100112, 2021.

[97] Svenja-K Otto, Yannik Moryson, Thorben Krauskopf, Klaus Peppler, Joachim Sann, Jurgen Janek, and Anja Henss. In-depth characterization of lithium-metal surfaces with XPS and ToF-SIMS: toward better understanding of the passivation layer. *Chemistry of Materials*, 33(3):859–867, 2021.

[98] Nabil Bassim, Keana Scott, and Lucille A Giannuzzi. Recent advances in focused ion beam technology and applications. *Mrs Bulletin*, 39(4):317–325, 2014.

[99] NS Smith, WP Skoczylas, SM Kellogg, DE Kinion, PP Tesch, O Sutherland, Ane Aanesland, and RW Boswell. High brightness inductively coupled plasma source for high current focused ion beam applications. *Journal of Vacuum Science & Technology B: Microelectronics and Nanometer Structures Processing, Measurement, and Phenomena*, 24(6):2902–2906, 2006.

[100] Jinqiao Liu, Ranming Niu, Ji Gu, Matthew Cabral, Min Song, and Xiaozhou Liao. Effect of ion irradiation introduced by focused ion-beam milling on the mechanical behaviour of sub-micron-sized samples. *Scientific Reports*, 10(1):10324, 2020.

[101] Xiangchen Hu, Yuan Lu, Yu Chen, Zeyu Wang, Yuanqi Huang, Wei Liu, and Yi Yu. High-quality TEM specimen preparation for lithium-ion conducting solid electrolytes by low-energy ion milling. *Ultramicroscopy*, page 113823, 2023.

[102] Alfred Benninghoven, FG Rudenauer, and Helmut W Werner. *Secondary ion mass spectrometry: basic concepts, instrumental aspects, applications and trends*. John Wiley and Sons, New York, NY, 1987.

[103] John Crank. *The mathematics of diffusion*. Oxford university press, 1979.

[104] RTP Whipple. CXXXVIII. concentration contours in grain boundary diffusion. *The London, Edinburgh, and Dublin Philosophical Magazine and Journal of Science*, 45(371):1225–1236, 1954.

[105] Hanyu Huo, Jing Luo, Venkataraman Thangadurai, Xiangxin Guo, Ce-Wen Nan, and Xueliang Sun. Li2CO3: a critical issue for developing solid garnet batteries. *ACS Energy Letters*, 5(1):252–262, 2019.

[106] John A Lewis, Chanhee Lee, Yuhgene Liu, Sang Yun Han, Dhruv Prakash, Emily J Klein, Hyun-Wook Lee, and Matthew T McDowell. Role of areal capacity in determining short circuiting of sulfide-based solid-state batteries. *ACS applied materials & interfaces*, 14(3):4051–4060, 2022.

[107] Yang Lu, Chen-Zi Zhao, Hong Yuan, Xin-Bing Cheng, Jia-Qi Huang, and Qiang Zhang. Critical current density in solid-state lithium metal batteries: mechanism, influences, and strategies. *Advanced Functional Materials*, 31(18):2009925, 2021.

[108] Matthias Klimpel, Huanyu Zhang, Maksym V Kovalenko, and Kostiantyn V Kravchyk. Standardizing critical current density measurements in lithium garnets. *Communications Chemistry*, 6(1):192, 2023.

[109] Marco Cantoni and Lorenz Holzer. Advances in 3D focused ion beam tomography. *Mrs Bulletin*, 39(4):354–360, 2014.

[110] TL Burnett, Ron Kelley, Bart Winiarski, L Contreras, Michael Daly, Ali Gholinia, MG Burke, and PJ Withers. Large volume serial section tomography by Xe Plasma FIB dual beam microscopy. *Ultramicroscopy*, 161:119–129, 2016.

[111] Lei Cheng, Cheng Hao Wu, Angelique Jarry, Wei Chen, Yifan Ye, Junfa Zhu, Robert Kostecki, Kristin Persson, Jinghua Guo, Miquel Salmeron, et al. Interrelationships among grain size, surface composition, air stability, and interfacial resistance of Al-substituted Li7La3Zr2O12 solid electrolytes. *ACS applied materials & interfaces*, 7(32):17649–17655, 2015.

[112] Asma Sharafi, Seungho Yu, Michael Naguib, Marcus Lee, Cheng Ma, Harry M Meyer, Jagjit Nanda, Maiofang Chi, Donald J Siegel, and Jeff Sakamoto. Impact of air exposure and surface chemistry on Li–Li7La3Zr2O12 interfacial resistance. *Journal of Materials Chemistry A*, 5(26):13475–13487, 2017.

[113] Jin Leng, Huaying Wang, Hongmei Liang, Zunqiu Xiao, Shitong Wang, Zhongtai Zhang, and Zilong Tang. Storage of garnet solid electrolytes: insights into air stability and surface chemistry. *ACS Applied Energy Materials*, 5(4):5108–5116, 2022.

[114] Nina Hoinkis, Jorg Schuhmacher, Sebastian Leukel, Christoph Loho, Andreas Roters, Felix H Richter, and Jurgen Janek. Particle size-dependent degradation kinetics of garnet-type Li6.5La3Zr1.5Ta0.5O12 solid electrolyte powders in ambient air. *The Journal of Physical Chemistry C*, 2023.

[115] Hirotoshi Yamada, Tomoko Ito, Sanoop Palakkathodi Kammampata, and Venkataraman Thangadurai. Toward understanding the reactivity of garnet-type solid electrolytes with H2O/CO2 in a glovebox using x-ray photoelectron

spectroscopy and electrochemical methods. *ACS applied materials & interfaces*, 12(32):36119–36127, 2020.

[116] Siqi Shi, Yue Qi, Hong Li, and Louis G Hector Jr. Defect thermodynamics and diffusion mechanisms in Li2CO3 and implications for the solid electrolyte interphase in Li-ion batteries. *The Journal of Physical Chemistry C*, 117(17):8579–8593, 2013.

[117] Florian Flatscher, Martin Philipp, Steffen Ganschow, H Martin R Wilkening, and Daniel Rettenwander. The natural critical current density limit for Li7La3Zr2O12 garnets. *Journal of Materials Chemistry A*, 8(31):15782–15788, 2020.

[118] Yutao Li, Xi Chen, Andrei Dolocan, Zhiming Cui, Sen Xin, Leigang Xue, Henghui Xu, Kyusung Park, and John B Goodenough. Garnet electrolyte with an ultralow interfacial resistance for Li-metal batteries. *Journal of the American Chemical Society*, 140(20):6448–6455, 2018.

[119] Rowena H Brugge, Federico M Pesci, Andrea Cavallaro, Christopher Sole, Mark A Isaacs, Gwilherm Kerherve, Robert S Weatherup, and Ainara Aguadero. The origin of chemical inhomogeneity in garnet electrolytes and its impact on the electrochemical performance. *Journal of Materials Chemistry A*, 8(28):14265–14276, 2020.

[120] Sundeep Vema, Farheen N Sayed, Supreeth Nagendran, Burcu Karagoz, Christian Sternemann, Michael Paulus, Georg Held, and Clare P Grey. Understanding the surface regeneration and reactivity of garnet solid-state electrolytes. *ACS Energy Letters*, 8:3476–3484, 2023.

[121] Xiao Huang, Jiawen Tang, Yongjian Zhou, Kun Rui, Xin Ao, Yan Yang, and Bingbing Tian. Developing preparation craft platform for solid electrolytes containing volatile components: experimental study of competition between lithium loss and densification in Li7La3Zr2O12. *ACS Applied Materials & Interfaces*, 14(29):33340–33354, 2022.

[122] Hanyu Huo, Yue Chen, Ning Zhao, Xiaoting Lin, Jing Luo, Xiaofei Yang, Yulong Liu, Xiangxin Guo, and Xueliang Sun. In-situ formed Li2CO3-free garnet/Li interface by rapid acid treatment for dendrite-free solid-state batteries. *Nano Energy*, 61:119–125, 2019.

[123] Munekazu Motoyama, Yuki Tanaka, Takayuki Yamamoto, Nobuo Tsuchimine, Susumu Kobayashi, and Yasutoshi Iriyama. The active interface of Ta-doped Li7La3Zr2O12 for Li plating/stripping revealed by acid aqueous etching. *ACS Applied Energy Materials*, 2(9):6720–6731, 2019.

[124] Sewon Kim, Ju-Sik Kim, Lincoln Miara, Yan Wang, Sung-Kyun Jung, Seong Yong Park, Zhen Song, Hyungsub Kim, Michael Badding, JaeMyung Chang, et al. High-energy and durable lithium metal batteries using garnet-type solid electrolytes with tailored lithium-metal compatibility. *Nature Communications*, 13(1):1883, 2022.

[125] Joshua S Gibson, Sudarshan Narayanan, Jack EN Swallow, Pardeep Kumar-Thakur, Mauro Pasta, Tien-Lin Lee, and Robert S Weatherup. Gently does it!: in situ preparation of alkali metal–solid electrolyte interfaces for photoelectron spectroscopy. *Faraday Discussions*, 236:267–287, 2022.

[126] Zhenhua Xu, Haijun Zhang, Ruiyuan Wang, Wenjun Gui, Guofeng Liu, and Ying Yang. Systemic and direct production of battery-grade lithium carbonate from a saline lake. *Industrial & Engineering Chemistry Research*, 53(42):16502–16507, 2014.

[127] Wenhao Xia, Biyi Xu, Huanan Duan, Xiaoyi Tang, Yiping Guo, Hongmei Kang, Hua Li, and Hezhou Liu. Reaction mechanisms of lithium garnet pellets in ambient air: the effect of humidity and CO2. *Journal of the American Ceramic Society*, 100(7):2832–2839, 2017.

[128] DD Williams and RR Miller. Effect of water vapor on the LiOH-CO2 reaction. dynamic isothermal system. *Industrial & Engineering Chemistry Fundamentals*, 9(3):454–457, 1970.

[129] Wei-Guo Wang, Xian-Ping Wang, Yun-Xia Gao, Jun-Feng Yang, and Qian-Feng Fang. Investigation on the stability of Li5La3Ta2O12 lithium ionic conductors in humid environment. *Frontiers of Materials Science in China*, 4:189–192, 2010.

[130] Gulin Vardar, William J Bowman, Qiyang Lu, Jiayue Wang, Richard J Chater, Ainara Aguadero, Rachel Seibert, Jeff Terry, Adrian Hunt, Iradwikanari Waluyo, et al. Structure, chemistry, and charge transfer resistance of the interface between Li7La3Zr2O12 electrolyte and LiCoO2 cathode. *Chemistry of Materials*, 30(18):6259–6276, 2018.

[131] Nian Zhang, Xinghui Long, Zhi Wang, Pengfei Yu, Fudong Han, Jiamin Fu, GuoXi Ren, Yanru Wu, Shun Zheng, Wencheng Huang, et al. Mechanism study on the interfacial stability of a lithium garnet-type oxide electrolyte against cathode materials. *ACS Applied Energy Materials*, 1(11):5968–5976, 2018.

[132] MF Sunding, K Hadidi, S Diplas, OM Løvvik, TE Norby, and AE Gunnæs. XPS characterisation of in situ treated lanthanum oxide and hydroxide using tailored charge referencing and peak fitting procedures. *Journal of Electron Spectroscopy and Related Phenomena*, 184(7):399–409, 2011.

[133] Jerry Pui Ho Li, Xiaohong Zhou, Yaoqi Pang, Liang Zhu, Evgeny I Vovk, Linna Cong, Alexander P van Bavel, Shenggang Li, and Yong Yang. Understanding of binding energy calibration in XPS of lanthanum oxide by in situ treatment. *Physical Chemistry Chemical Physics*, 21(40):22351–22358, 2019.

[134] Mathias Fingerle, Christoph Loho, Thimo Ferber, Horst Hahn, and René Hausbrand. Evidence of the chemical stability of the garnet-type solid electrolyte Li5La3Ta2O12 towards lithium by a surface science approach. *Journal of Power Sources*, 366:72–79, 2017.

[135] MA Gondal, TA Fasasi, Umair Baig, and A Mekki. Effects of oxidizing media on the composition, morphology and optical properties of colloidal zirconium oxide nanoparticles synthesized via pulsed laser ablation in liquid technique. *Journal of Nanoscience and Nanotechnology*, 18(6):4030–4039, 2018.

[136] Zheng-Guo Xu and Shu-Ying Sun. Preparation of battery-grade lithium carbonate with lithium-containing desorption solution. *Metals*, 11(9):1490, 2021.

[137] V Schott, M Fähnle, and PA Madden. Theory of self-diffusion in alkali metals: I. results for monovacancies in Li, Na, and K. *Journal of Physics: Condensed Matter*, 12(7):1171, 2000.

[138] R Messer and F Noack. Nuclear magnetic relaxation by self-diffusion in solid lithium: T1-frequency dependence. *Applied physics*, 6:79–88, 1975.

[139] D Marion Fischer, Peter Duwe, Sylvio Indris, and Paul Heitjans. Tracer diffusion measurements in solid lithium: a test case for the comparison between NMR in static and pulsed magnetic field gradients after upgrading a standard solid state NMR spectrometer. *Solid State Nuclear Magnetic Resonance*, 26(2):74–83, 2004.

[140] M Mali, J Roos, M Sonderegger, D Brinkmann, and P Heitjans. 6Li and 7Li diffusion coefficients in solid lithium measured by the NMR pulsed field gradient technique. *Journal of Physics F: Metal Physics*, 18(3):403, 1988.

[141] A Lodding, JN Mundy, and A Ott. Isotope inter-diffusion and self-diffusion in solid lithium metal. *physica status solidi (b)*, 38(2):559–569, 1970.

[142] W Frank, U Breier, C Elsässer, and M Fähnle. First-principles calculations of absolute concentrations and self-diffusion constants of vacancies in lithium. *Physical review letters*, 77(3):518, 1996.

[143] Chunpeng Yang, Hua Xie, Weiwei Ping, Kun Fu, Boyang Liu, Jiancun Rao, Jiaqi Dai, Chengwei Wang, Glenn Pastel, and Liangbing Hu. An electron/ion dual-conductive alloy framework for high-rate and high-capacity solid-state lithium-metal batteries. *Advanced Materials*, 31(3):1804815, 2019.

[144] Mintao Wan, Sujin Kang, Li Wang, Hyun-Wook Lee, Guangyuan Wesley Zheng, Yi Cui, and Yongming Sun. Mechanical rolling formation of interpenetrated lithium metal/lithium tin alloy foil for ultrahigh-rate battery anode. *Nature Communications*, 11(1):829, 2020.

[145] Shuting Luo, Zhenyu Wang, Xuelei Li, Xinyu Liu, Haidong Wang, Weigang Ma, Lianqi Zhang, Lingyun Zhu, and Xing Zhang. Growth of lithium-indium dendrites in all-solid-state lithium-based batteries with sulfide electrolytes. *Nature Communications*, 12(1):6968, 2021.

[146] John A Lewis, Kelsey A Cavallaro, Yuhgene Liu, and Matthew T McDowell. The promise of alloy anodes for solid-state batteries. *Joule*, 6(7):1418–1430, 2022.

[147] Minghui He, Zhonghui Cui, Cheng Chen, Yiqiu Li, and Xiangxin Guo. Formation of self-limited, stable and conductive interfaces between garnet electrolytes and lithium anodes for reversible lithium cycling in solid-state batteries. *Journal of Materials Chemistry A*, 6(24):11463–11470, 2018.

[148] Hiroyuki Koshikawa, Shoichi Matsuda, Kazuhide Kamiya, Masaru Miyayama, Yoshimi Kubo, Kohei Uosaki, Kazuhito Hashimoto, and Shuji Nakanishi. Electrochemical impedance analysis of the Li/Au-Li7La3Zr2O12 interface during Li dissolution/deposition cycles: effect of pre-coating Li7La3Zr2O12 with Au. *Journal of Electroanalytical Chemistry*, 835:143–149, 2019.

[149] Wei Luo, Yunhui Gong, Yizhou Zhu, Yiju Li, Yonggang Yao, Ying Zhang, Kun Fu, Glenn Pastel, Chuan-Fu Lin, Yifei Mo, et al. Reducing interfacial resistance between garnet-structured solid-state electrolyte and li-metal anode by a germanium layer. *Advanced Materials*, 29(22):1606042, 2017.

[150] Yang Lu, Xiao Huang, Yadong Ruan, Qingsong Wang, Rui Kun, Jianhua Yang, and Zhaoyin Wen. An in situ element permeation constructed high endurance Li–LLZO interface at high current densities. *Journal of Materials Chemistry A*, 6(39):18853–18858, 2018.

[151] Kun Fu, Yunhui Gong, Boyang Liu, Yizhou Zhu, Shaomao Xu, Yonggang Yao, Wei Luo, Chengwei Wang, Steven D Lacey, Jiaqi Dai, et al. Toward garnet electrolyte–based li metal batteries: an ultrathin, highly effective, artificial solid-state electrolyte/metallic Li interface. *Science Advances*, 3(4):e1601659, 2017.

[152] Song Jin, Yadong Ye, Yijie Niu, Yansong Xu, Hongchang Jin, Jinxi Wang, Zhaowei Sun, Anmin Cao, Xiaojun Wu, Yi Luo, et al. Solid–solution-based metal alloy phase for highly reversible lithium metal anode. *Journal of the American Chemical Society*, 142(19):8818–8826, 2020.

[153] Robert A Huggins. Lithium alloy negative electrodes. *Journal of Power Sources*, 81:13–19, 1999.

[154] Jiqiang Wang, ID Raistrick, and Robert A Huggins. Behavior of some binary lithium alloys as negative electrodes in organic solvent-based electrolytes. *Journal of the Electrochemical Society*, 133(3):457, 1986.

[155] James L Gole, Zhong Shi, and Meilin Liu. Generation of highly porous Li–Mg and Li–Zn alloys from kinetically controlled lithiation. *Philosophical Magazine B*, 81(2):119–131, 2001.

[156] Werner Weppner and Robert A Huggins. Determination of the kinetic parameters of mixed-conducting electrodes and application to the system Li3Sb. *Journal of The Electrochemical Society*, 124(10):1569, 1977.

[157] Stephen Dongmin Kang and William C Chueh. Galvanostatic intermittent titration technique reinvented: part I. A critical review. *Journal of The Electrochemical Society*, 168(12):120504, 2021.

[158] Kun Fu, Yunhui Gong, Zhezhen Fu, Hua Xie, Yonggang Yao, Boyang Liu, Marcus Carter, Eric Wachsman, and Liangbing Hu. Transient behavior of the metal interface in lithium metal–garnet batteries. *Angewandte Chemie International Edition*, 56(47):14942–14947, 2017.

[159] Yan Xu, Shuyang Zhao, Guangmin Zhou, Wei Chen, Fei Zhou, Ze Rong, Yang Wu, Jia Li, Jinghua Guo, and Yuegang Zhang. Solubility-dependent protective effects of binary alloys for lithium anode. *ACS Applied Energy Materials*, 3(3):2278–2284, 2020.

[160] A Korblein, P Heitjans, H-J Stockmann, F Fujara, H Ackermann, W Buttler, K Dorr, and H Grupp. Diffusion processes in solid Li-Mg and Li-Ag alloys and the spin-lattice relaxation of 8Li. *Journal of Physics F: Metal Physics*, 15(3):561, 1985.

[161] Y Zhang, KS Ravi Chandran, M Jagannathan, HZ Bilheux, and JC Bilheux. The nature of electrochemical delithiation of Li-Mg alloy electrodes: neutron computed tomography and analytical modeling of Li diffusion and delithiation phenomenon. *Journal of The Electrochemical Society*, 164(2):A28, 2016.

[162] Zhong Shi, Meilin Liu, Devang Naik, and James L Gole. Electrochemical properties of Li-Mg alloy electrodes for lithium batteries. *Journal of Power Sources*, 92(1-2):70–80, 2001.

[163] Yang Lu, Chen-Zi Zhao, Rui Zhang, Hong Yuan, Li-Peng Hou, Zhong-Heng Fu, Xiang Chen, Jia-Qi Huang, and Qiang Zhang. The carrier transition from Li atoms to Li vacancies in solid-state lithium alloy anodes. *Science advances*, 7(38):eabi5520, 2021.

[164] Kevin N Wood and Glenn Teeter. XPS on Li-battery-related compounds: analysis of inorganic SEI phases and a methodology for charge correction. *ACS Applied Energy Materials*, 1(9):4493–4504, 2018.

[165] Jürgen Janek and Wolfgang G Zeier. Challenges in speeding up solid-state battery development. *Nature Energy*, 8:1–11, 2023.

[166] Kelsey B Hatzell, Xi Chelsea Chen, Corie L Cobb, Neil P Dasgupta, Marm B Dixit, Lauren E Marbella, Matthew T McDowell, Partha P Mukherjee, Ankit Verma, Venkatasubramanian Viswanathan, et al. Challenges in lithium metal anodes for solid-state batteries. *ACS Energy Letters*, 5(3):922–934, 2020.

[167] Hongchun Wang, Haowen Gao, Xiaoxuan Chen, Jianping Zhu, Wangqin Li, Zhengliang Gong, Yangxing Li, Ming-Sheng Wang, and Yong Yang. Linking the defects to the formation and growth of Li dendrite in all-solid-state batteries. *Advanced Energy Materials*, 11(42):2102148, 2021.

[168] Qingsong Tu, Tan Shi, Srinath Chakravarthy, and Gerbrand Ceder. Understanding metal propagation in solid electrolytes due to mixed ionic-electronic conduction. *Matter*, 4(10):3248–3268, 2021.

[169] Jian Gao, Jianxun Zhu, Xiaolei Li, Junpeng Li, Xiangxin Guo, Hong Li, and Weidong Zhou. Rational design of mixed electronic-ionic conducting Ti-doping $Li_7La_3Zr_2O_{12}$ for lithium dendrites suppression. *Advanced Functional Materials*, 31(2):2001918, 2021.

[170] Minghao Sun, Tiefeng Liu, Yifei Yuan, Min Ling, Nan Xu, Yanyan Liu, Lijing Yan, Hui Li, Chengyong Liu, Yingying Lu, et al. Visualizing lithium dendrite formation within solid-state electrolytes. *ACS Energy Letters*, 6(2):451–458, 2021.

[171] Henrik Buschmann, Janis Dölle, Stefan Berendts, Alexander Kuhn, Patrick Bottke, Martin Wilkening, Paul Heitjans, Anatoliy Senyshyn, Helmut Ehrenberg, Andriy Lotnyk, et al. Structure and dynamics of the fast lithium ion conductor '$Li_7La_3Zr_2O_{12}$'. *Physical Chemistry Chemical Physics*, 13(43):19378–19392, 2011.

[172] Bowen Shao, Yonglin Huang, and Fudong Han. Electronic conductivity of lithium solid electrolytes. *Advanced Energy Materials*, 13(16):2204098, 2023.

[173] Martin Philipp, Bernhard Gadermaier, Patrick Posch, Ilie Hanzu, Steffen Ganschow, Martin Meven, Daniel Rettenwander, Günther J Redhammer, and H Martin R Wilkening. The electronic conductivity of single crystalline Ga-stabilized cubic $Li_7La_3Zr_2O_{12}$: a technologically relevant parameter for all-solid-state batteries. *Advanced materials interfaces*, 7(16):2000450, 2020.

[174] Travis Thompson, Seungho Yu, Logan Williams, Robert D Schmidt, Regina Garcia-Mendez, Jeff Wolfenstine, Jan L Allen, Emmanouil Kioupakis, Donald J Siegel, and Jeff Sakamoto. Electrochemical window of the Li-ion solid electrolyte $Li_7La_3Zr_2O_{12}$. *ACS Energy Letters*, 2(2):462–468, 2017.

[175] Xiaoming Liu, Regina Garcia-Mendez, Andrew R Lupini, Yongqiang Cheng, Zachary D Hood, Fudong Han, Asma Sharafi, Juan Carlos Idrobo, Nancy J Dudney, Chunsheng Wang, et al. Local electronic structure variation resulting in Li 'filament' formation within solid electrolytes. *Nature Materials*, 20(11):1485–1490, 2021.

[176] Hyungjun Kim, Patrick Conlin, Matthew Bergschneider, Hayoung Chung, Sung Youb Kim, Suk Won Cha, Maenghyo Cho, and Kyeongjae Cho. First principles study on Li metallic phase nucleation at grain boundaries in a lithium lanthanum titanium oxide (LLTO) solid electrolyte. *Journal of Materials Chemistry A*, 11(6):2889–2898, 2023.

[177] Jared Tippens, John C Miers, Arman Afshar, John A Lewis, Francisco Javier Quintero Cortes, Haipeng Qiao, Thomas S Marchese, Claudio V Di Leo, Christopher Saldana, and Matthew T McDowell. Visualizing chemomechanical degradation of a solid-state battery electrolyte. *ACS Energy Letters*, 4(6):1475–1483, 2019.

[178] Shuai Hao, Josh J Bailey, Francesco Iacoviello, Junfu Bu, Patrick S Grant, Dan JL Brett, and Paul R Shearing. 3D imaging of lithium protrusions in solid-state lithium batteries using X-ray computed tomography. *Advanced Functional Materials*, 31(10):2007564, 2021.

[179] Thorben Krauskopf, Rabea Dippel, Hannah Hartmann, Klaus Peppler, Boris Mogwitz, Felix H Richter, Wolfgang G Zeier, and Jürgen Janek. Lithium-metal growth kinetics on LLZO garnet-type solid electrolytes. *Joule*, 3(8):2030–2049, 2019.

[180] Ziyang Ning, Dominic Spencer Jolly, Guanchen Li, Robin De Meyere, Shengda D Pu, Yang Chen, Jitti Kasemchainan, Johannes Ihli, Chen Gong, Boyang Liu, et al. Visualizing plating-induced cracking in lithium-anode solid-electrolyte cells. *Nature Materials*, 20(8):1121–1129, 2021.

[181] Rishav Choudhury, Michael Wang, and Jeff Sakamoto. The effects of electric field distribution on the interface stability in solid electrolytes. *Journal of The Electrochemical Society*, 167(14):140501, 2020.

[182] Jun Zhao, Yongfu Tang, Qiushi Dai, Congcong Du, Yin Zhang, Dingchuan Xue, Tianwu Chen, Jingzhao Chen, Bo Wang, Jingming Yao, et al. In situ observation of Li deposition-induced cracking in garnet solid electrolytes. *Energy & Environmental Materials*, 5(2):524–532, 2022.

[183] Ruinan Zhou, Mingzhe Yu, David Tweddle, Phillip Hamer, Daniel Chen, Brett Hallam, Alison Ciesla, Pietro P Altermatt, Peter R Wilshaw, and Ruy S Bonilla. Understanding and optimizing EBIC pn-junction characterization from modeling insights. *Journal of Applied Physics*, 127(2):024502, 2020.

[184] TB Tang and MM Chaudhri. Electrical degradation of β-alumina. *Journal of Materials Science*, 17:157–163, 1982.

[185] LC De Jonghe, L Feldman, and A Beuchele. Slow degradation and electron conduction in sodium/beta-aluminas. *Journal of Materials Science*, 16:780–786, 1981.

[186] Jungwoo Z Lee, Thomas A Wynn, Marshall A Schroeder, Judith Alvarado, Xuefeng Wang, Kang Xu, and Y Shirley Meng. Cryogenic focused ion beam characterization of lithium metal anodes. *ACS Energy Letters*, 4(2):489–493, 2019.

[187] P Heitjans, A Korblein, H Ackermann, D Dubbers, F Fujara, and H-J Stockmann. Self-diffusion in solid lithium probed by spin-lattice relaxation of 8Li nuclei. *Journal of Physics F: Metal Physics*, 15(1):41, 1985.

[188] E Dologlou. Self-diffusion in solid lithium. *Glass Physics and Chemistry*, 36:570–574, 2010.

[189] AS Baranski and WR Fawcett. The formation of lithium-aluminum alloys at an aluminum electrode in propylene carbonate. *Journal of The Electrochemical Society*, 129(5):901, 1982.

[190] N Kumagai, Yoshio Kikuchi, K Tanno, F Lantelme, and M Chemla. Electrochemical investigation of the diffusion of lithium in β-LiAl alloy at room temperature. *Journal of applied electrochemistry*, 22:728–732, 1992.

[191] M Hiratani, K Miyauchi, Y Ito, K Kanehori, F Kirino, and T Kudo. Solid state lithium battery, U.S. Patent 4 645 726, Feb. 1987.

[192] Darren HS Tan, Yu-Ting Chen, Hedi Yang, Wurigumula Bao, Bhagath Sreenarayanan, Jean-Marie Doux, Weikang Li, Bingyu Lu, So-Yeon Ham, Baharak Sayahpour, et al. Carbon-free high-loading silicon anodes enabled by sulfide solid electrolytes. *Science*, 373(6562):1494–1499, 2021.